

FTS THESIS  
502.82 KE  
30001005559168  
Ke. Pu Chun  
Near-field scanning optical  
microscopy with laser  
trapping

# Near-Field Scanning Optical Microscopy with Laser Trapping

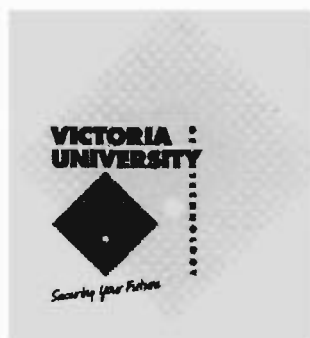
*A thesis submitted*

*by*

Pu Chun Ke

*for the degree of*

Doctor of Philosophy



School of Communications and Informatics  
Victoria University of Technology  
Australia

# Declaration

I, Pu Chun Ke, declare that this thesis entitled

**“Near-field scanning optical microscopy with laser trapping”**

is my own work and has not been submitted previously, in whole or in part, in respect of any other academic award.

Pu Chun Ke



/  
School of Communications and Informatics  
Victoria University of Technology  
Australia

July, 2000

*For my family*

# Abstract

**T**HIS thesis is concerned with a comprehensive understanding of particle-trapped near-field scanning optical microscopy. This technique is unique in that it relies on the collection of scattered evanescent waves from a sample with a laser-trapped particle. In comparison with the other forms of near-field scanning optical microscopy with a tapered fibre or a metallic needle probe, particle-trapped near-field scanning optical microscopy offers several advantages such as no need of distance control, high signal collection efficiency, and easy replacement of a particle probe.

In consideration of the major problems of particle-trapped near-field scanning optical microscopy such as low signal strength and low transverse scanning speed due to the use of a dielectric particle, a two-dimensional laser-trapped metallic particle is proposed as a near-field probe for imaging. This proposal is based on the fact that a metallic particle possesses a high reflection capacity that may lead to efficient near-field Mie scattering. Furthermore, surface plasmon resonance can be excited for metallic particles, which may improve signal strength further. Since the transverse trapping efficiency of a metallic particle increases with the numerical aperture of a trapping objective, a high scanning speed and a high signal-to-noise ratio can be obtained simultaneously for near-field imaging with a laser-trapped metallic particle.

Two major aspects, laser trapping and near-field Mie scattering of metallic particles, are considered in our study of particle-trapped near-field scanning optical microscopy. Specifically, the fundamental issues of laser trapping such as apodization of a high numerical aperture trapping objective, spherical aberration induced by index

mismatch, and the effect of numerical aperture on the transverse trapping efficiency of a metallic particle, are investigated in detail. In terms of near-field Mie scattering, signal strength and depolarisation of scattered evanescent waves are characterised with respect to particle size for image improvement.

The main results attained from this research are summarised as follows:

1. The maximum transverse trapping efficiency increases with the numerical aperture of a trapping objective for a laser-trapped metallic particle, while it decreases for a dielectric particle. As a result, a high scanning speed and a high signal-to-noise ratio can be obtained simultaneously for near-field imaging with a laser-trapped metallic particle.
2. A metallic particle shows a higher scattering efficiency than a dielectric particle of the same size. Consequently image contrast in particle-trapped near-field scanning optical microscopy is significantly improved with a laser-trapped metallic particle.
3. For particle-trapped near-field scanning optical microscopy, both signal strength and noise level affect imaging. Although the strength of scattered evanescent wave increases with the size of a laser-trapped particle, there exists an optimal image contrast for a particle of a particular size when the detector sensitivity is given.
4. Evanescent waves scattered by laser-trapped dielectric and metallic particles are depolarised. In particular, the degree of polarisation increases with the size of a dielectric particle while it decreases with the size of a metallic particle. Depolarised photons carry less information of an object, and can be suppressed by a polarisation-gating method for imaging enhancement. Applying a

polarisation-gating method to near-field imaging with a laser-trapped metallic particle provides advantages in achieving better contrast and resolution.

Throughout our study, we have demonstrated that using metallic particles is feasible for the applications of particle-trapped near-field scanning optical microscopy. Our investigation has confirmed that the use of a metallic particle leads to enhanced image quality and increased scanning speed for image acquisition. Imaging with trapped metallic particles provides advantages since photons scattered by small metallic particles are less depolarised and may carry more information of the original signal from a sample.

# Acknowledgment

I am sincerely indebted to all the people who helped me during the course of my PhD study. Special thanks are dedicated to my supervisor Professor Min Gu whose guidance, cultivation, patience and vision have made today possible. Great appreciation goes to Professor David Booth for lending me a photomultiplier tube, a device from his deft hands, which served my research well.

I would like to thank Dr. Xiaosong Gan for his help on numerical simulations and Dr. Steven Schilders for his assistance on experimental setup and Labview programming. Thanks are also given to my coworkers Dr. Ming Gun Xu, Mr. Daniel Day, Mr. Damian Bird, Mrs. Nicoleta Dragomir, Mr. Dru Morrish, and Mr. Djenan Ganic in the Optoelectronic Imaging Group, and the fellow postgraduate students at the Optical Technology Research Laboratory for forming such a competitive and friendly environment that made my research life enjoyable. I truly appreciate the enormous help from the technical staff Mr. Alex Shelamoff, Mr. Donald Ermel, Mr. Mark Kivinen, Mr. Hayrettin Arisoy, and Mr. Abdurrahman Kuzucu on the construction of the optical and mechanical apparatus I requested. The financial support from an Australian Postgraduate Award and the travel fund from the School of Communications and Informatics at Victoria University are sincerely acknowledged.

Finally, I would like to express my forever gratitude to my parents for teaching me to value education and for their care and love ever since my childhood. The enormous support from my two sisters is passionately acknowledged. My nephews Joman, Yezi and my niece Danni, I love you all. No words can portray my sincere gratefulness to my intelligent wife who has shared all the happiness and sorrows with me over these tough years. Without her love, sacrifice, understanding and encouragement, this thesis would have been impossible.

# Table of Contents

<b>DECLARATION</b> .....	i
<b>ABSTRACT</b> .....	ii
<b>ACKNOWLEDGMENT</b> .....	v
<b>TABLE OF CONTENTS</b> .....	vi
<b>CHAPTER 1</b>	
<b>INTRODUCTION</b>	
1.1 INTRODUCTION .....	1
1.2 OBJECTIVE OF THE RESEARCH .....	2
1.3 PREVIEW OF THE THESIS .....	4
<b>CHAPTER 2</b>	
<b>LITERATURE REVIEW OF NEAR-FIELD SCANNING OPTICAL MICROSCOPY</b>	
2.1 INTRODUCTION .....	7
2.2 NEAR-FIELD SCANNING OPTICAL MICROSCOPY .....	8
2.2.1 PRINCIPLE OF NSOM .....	9
2.2.1.1 NEAR-FIELD AND FAR-FIELD .....	9
2.2.1.2 PRINCIPLE OF NSOM .....	10
2.2.2 CLASSIFICATION OF NSOM .....	10
2.2.2.1 CLASSIFICATION OF NSOM BASED ON PROBE TYPES .....	10
2.2.2.1.1 <i>PHOTON-TUNNELLING NSOM (APERTURE-TYPE)</i> .....	11
2.2.2.1.2 <i>VIBRATING METALLIC TIP SHEAR-FORCE NSOM (APERTURELESS-TYPE)</i> .....	13
2.2.2.1.3 <i>ATOMIC FORCE MICROSCOPY-BASED NSOM (APERTURE- OR APERTURELESS-TYPE)</i> .....	14
2.2.2.2 CLASSIFICATION OF NSOM BASED ON SIGNAL COLLECTION MODES .....	15
2.3 NSOM WITH LASER TRAPPING .....	16
2.3.1 APPLICATIONS OF LASER TRAPPING IN NEAR-FIELD IMAGING .....	17
2.3.1.1 FORCE MICROSCOPY WITH LASER TRAPPING .....	17
2.3.1.2 OPTICAL MICROSCOPY WITH LASER TRAPPING .....	18
2.3.2 PRINCIPLE OF PARTICLE-TRAPPED NSOM .....	19
2.4 LASER TRAPPING .....	21
2.4.1 PRINCIPLE OF LASER TRAPPING .....	22
2.4.2 CHARACTERISATION OF TRAPPING FORCE .....	23
2.4.2.1 THEORETICAL APPROACHES FOR TRAPPING FORCE .....	24
2.4.2.1.1 <i>RAY-OPTICS MODEL</i> .....	24
2.4.2.1.2 <i>ELECTROMAGNETIC WAVE APPROACH</i> .....	29
2.4.2.1.3 <i>COMPARISON OF DIFFERENT APPROACHES</i> .....	31
2.4.2.2 EFFECT OF LIGHT DISTRIBUTION IN THE FOCAL REGION OF A TRAPPING OBJECTIVE .....	32

2.4.2.2.1 SINE CONDITION .....	33
2.4.2.2.2 EFFECT OF SPHERICAL ABERRATION INDUCED BY REFRACTIVE-INDEX MISMATCH .....	36
2.4.2.2.3 COMPENSATION FOR SPHERICAL ABERRATION BY A CHANGE IN TUBE LENGTH .....	39
2.4.2.3 EFFECT OF BROWNIAN MOTION .....	40
2.4.3 LASER TRAPPING OF METALLIC PARTICLES .....	41
2.5 NEAR-FIELD MIE SCATTERING .....	43
2.5.1 MIE SCATTERING AND NEAR-FIELD MIE SCATTERING .....	43
2.5.2 THEORETICAL APPROACHES .....	45
2.5.2.1 MULTIPOLE EXPANSION METHOD .....	46
2.5.2.2 MULTIPLE MULTIPOLE (MMP) METHOD .....	48
2.5.2.3 DISCUSSION .....	49
2.5.3 EXPERIMENTS ON NEAR-FIELD MIE SCATTERING .....	49
2.6 SUMMARY .....	50

## CHAPTER 3

### LASER TRAPPING WITH A HIGH NUMERICAL APERTURE OBJECTIVE

3.1 INTRODUCTION .....	51
3.2 SINE CONDITION OBEYED BY A TRAPPING OBJECTIVE .....	52
3.2.1 AXIAL AND TRANSVERSE TRAPPING FORCES OBEYING THE SINE AND TANGENT CONDITIONS .....	52
3.2.2 CONCLUSION .....	58
3.3 TRAPPING FORCE IN THE PRESENCE OF SPHERICAL ABERRATION CAUSED BY REFRACTIVE-INDEX MISMATCH .....	59
3.3.1 EXPERIMENT .....	59
3.3.2 CALCULATION OF LIGHT DISTRIBUTION IN THE FOCAL REGION .....	64
3.3.3 COMPENSATION FOR SPHERICAL ABERRATION IN TERMS OF CHANGE IN TUBE LENGTH .....	68
3.4 DISCUSSION .....	70
3.5 CONCLUSION .....	72

## CHAPTER 4

### CHARACTERISATION OF TRAPPING FORCE ON METALLIC MIE PARTICLES

4.1 INTRODUCTION .....	73
4.2 PRINCIPLE OF LASER TRAPPING OF METALLIC MIE PARTICLES .....	74
4.3 CALCULATION OF TRAPPING FORCE ON METALLIC MIE PARTICLES .....	75
4.4 EFFECT OF NUMERICAL APERTURE ON TRANSVERSE TRAPPING EFFICIENCY .....	82
4.4.1 THEORETICAL RESULTS .....	82
4.4.2 EXPERIMENTAL RESULTS .....	84
4.4.3 DISCUSSION .....	88
4.5 ENHANCEMENT OF TRANSVERSE TRAPPING EFFICIENCY FOR METALLIC PARTICLES WITH AN ANNULAR LENS .....	91
4.6 CONCLUSION .....	97

**CHAPTER 5****NEAR-FIELD IMAGING WITH METALLIC PARTICLES: EFFECT OF SIGNAL STRENGTH**

5.1 INTRODUCTION .....	98
5.2 STRENGTH OF SCATTERED EVANESCENT WAVES WITH LASER-TRAPPED METALLIC PARTICLES .....	99
5.2.1 EXPERIMENT.....	99
5.2.2 DISCUSSION.....	104
5.3 ENHANCED IMAGE CONTRAST OF PARTICLE-TRAPPED NSOM WITH LASER-TRAPPED METALLIC PARTICLES .....	105
5.3.1 IMAGE CONTRAST OF PARTICLE-TRAPPED NSOM WITH DIELECTRIC PARTICLES .....	106
5.3.1.1 MEASUREMENT OF IMAGE CONTRAST WITH TRAPPED DIELECTRIC PARTICLES OF DIFFERENT SIZES.....	106
5.3.1.2 DISCUSSION .....	108
5.3.2 IMAGE CONTRAST OF PARTICLE-TRAPPED NSOM WITH METALLIC PARTICLES .....	110
5.3.2.1 MEASUREMENT OF IMAGE CONTRAST WITH TRAPPED METALLIC PARTICLES OF DIFFERENT SIZES.....	110
5.3.2.2 DISCUSSION.....	113
5.4 IMAGING ENHANCEMENT FOR A PRISM SURFACE WITH LASER-TRAPPED METALLIC PARTICLES .....	114
5.5 CONCLUSION.....	115

**CHAPTER 6****NEAR-FIELD IMAGING WITH METALLIC PARTICLES: EFFECT OF DEPOLARISATION**

6.1 INTRODUCTION .....	117
6.2 EVANESCENT WAVES ON A PRISM SURFACE ON THE POLARISATION STATES OF ILLUMINATION .....	118
6.2.1 PHASE SHIFT OF EVANESCENT WAVES .....	118
6.2.2 MEASUREMENT OF THE PHASE SHIFT OF EVANESCENT WAVES .....	123
6.3 DEPOLARISATION OF SCATTERED EVANESCENT WAVES .....	126
6.3.1 DEPOLARISATION OF EVANESCENT WAVES SCATTERED BY TRAPPED DIELECTRIC PARTICLES.....	126
6.3.2 DEPOLARISATION OF EVANESCENT WAVES SCATTERED BY TRAPPED METALLIC PARTICLES .....	132
6.4 IMAGING OF PARTICLE-TRAPPED NSOM BY POLARISATION-GATING.....	139
6.4.1 POLARISATION-GATING FOR IMAGING WITH LASER-TRAPPED DIELECTRIC PARTICLES .....	140
6.4.2 POLARISATION-GATING FOR IMAGING WITH LASER-TRAPPED METALLIC PARTICLES ..	142
6.5 POLARISATION-GATING FOR IMAGING OF A PRISM SURFACE WITH LASER-TRAPPED METALLIC PARTICLES.....	145
6.6 CONCLUSION.....	147

**CHAPTER 7**

**CONCLUSION**

7.1 THESIS CONCLUSION ..... 149  
7.2 FUTURE WORK ..... 151

**BIBLIOGRAPHY** ..... 154

**LIST OF FIGURES**..... 163

**LIST OF TABLES**..... 173

**LIST OF SYMBOLS**..... 174

**PUBLICATIONS OF THE AUTHOR** ..... 178

# CHAPTER ONE

## Introduction

### 1.1 Introduction

**T**HE advent of near-field optical scanning microscopy (NSOM) in the 1980's [Pohl *et al.*, 1984] has drastically changed our view of the microscopic world. It opens up vast new opportunities for extracting fine information from a sample under inspection with resolution beyond the diffraction limit [Betzig *et al.*, 1991]. Unlike conventional optical microscopy that relies predominantly on the use of a microscope objective for signal collection, near-field imaging is obtained via probing evanescent photons localised in the near-field region of a sample under study. The characteristics of a near-field probe, in the form of an open aperture or a scatterer, determines primarily image quality such as image resolution and contrast in NSOM [Paesler and Moyer, 1996].

Recently, laser-trapped Mie (diameter  $\phi \gg \lambda$ , where  $\lambda$  is the wavelength of illumination) and Rayleigh (diameter  $\phi \ll \lambda$ ) particles have been utilised as near-field probes and their capabilities in near-field imaging have been demonstrated [Malmqvist and Hertz, 1994; Kawata *et al.*, 1994; Sugiura *et al.*, 1997]. In particular, in the approach of Kawata *et al.*, a dielectric particle is trapped in two-dimension (2D) against a sample under the radiation pressure caused by a highly focused laser beam [Kawata *et al.*, 1994]. The distance between the particle and the sample is maintained to be zero

during a scanning process by focusing the trapping laser beam below the central equatorial plane of the particle. Imaging of a sample is achieved by collecting the evanescent photons scattered by a laser-trapped particle.

This imaging scheme, termed as particle-trapped NSOM, has inherited the merits of the laser trapping technique such as its noninvasive access to a sample, which is particularly of interest to biological applications. Particle-trapped NSOM is simple since no distance regulation is needed. A trapping objective of high numerical aperture (NA) also serves for signal collection with an efficiency higher than that provided by a tapered fibre [van Labeke and Barchiesi, 1993] or a low NA lens [Inouye and Kawata, 1994]. The problem of probe damage, as frequently occurred in the other forms of NSOM, could be avoided since a particle probe may be readily replaced by another particle in a sample solution. Those unique features of particle-trapped NSOM provide enormous chances for the study of near-field physics.

## 1.2 Objective of the research

Although particle-trapped NSOM is an appealing tool because of the advantages described in section 1.1, there are still a few problems to be solved for the further development of this technique. Firstly, signal scattered by a trapped dielectric particle is not strong for image construction since a dielectric particle is refractive. Secondly, although imaging of particle-trapped NSOM uses a high NA objective, the transverse trapping efficiency of a dielectric particle decreases with the NA of a trapping objective. In other words, a compromise must be made in between signal strength and scanning speed, which results in degraded imaging performance.

Fortunately, those problems in particle-trapped NSOM may be avoidable with the employment of a laser-trapped metallic particle. Compared with dielectric particles, metallic particles, especially noble metallic particles, have small skin depths and are less transmissive [Born and Wolf, 1997]. In other words, metallic particles may scatter more efficiently than dielectric particles. As will be introduced in Chapter 4, transverse trapping force (or scanning speed) on a metallic particle increases with the NA of a trapping objective. As a result, fast imaging and high signal-to-noise ratio can be obtained simultaneously for near-field imaging with laser-trapped metallic particles. With the use of a trapped metallic particle, surface plasmon resonance may be excited, which could enhance the strength of the scattered signal.

The objective of our research is to investigate particle-trapped NSOM with the use of a laser-trapped metallic particle. Two major aspects related to the image formation of particle-trapped NSOM, the trapping performance and the scattering of evanescent waves, are examined for metallic particles in comparison with those obtained for dielectric particles. In particular, the following issues are addressed regarding the topic of laser trapping; apodization of a high NA trapping objective that determines the light distribution in the focal region of the objective; the refractive-index mismatch that affects light intensity and trapping force; and the effect of the NA of a trapping objective on trapping force.

It is known from Mie theory that scattering of a propagating wave introduces depolarisation [Born and Wolf, 1997]. Depolarisation also occurs to the evanescent waves scattered by small particles [Chew *et al.*, 1979]. In our study, both depolarisation and signal strength of scattered evanescent waves, which affect the image formation of

particle-trapped NSOM, are characterised for trapped metallic particles of different sizes. Our investigation of the scattering of evanescent waves is conducted mainly within the frame of experimentation due to the complicity involved.

### 1.3 Preview of the thesis

Based on the objective described in the last section, we structure our thesis as follows:

- Chapter 1 contains an introduction to our research scheme. The advantages of particle-trapped NSOM for near-field imaging are listed with the problems pointed out. Consequently, the objective of our research is stated and the structure of the thesis is outlined.
- Chapter 2 presents an overview of the concepts, principles and classifications of NSOM. The advantages and drawbacks of individual imaging techniques are discussed. An introduction to the principle of particle-trapped NSOM is then presented. To understand this technique, the principle and development of laser trapping of small particles including metallic particles are reviewed. In particular, a comparison of trapping force between metallic and dielectric particles is given. Because of the importance of near-field Mie scattering for image formation in particle-trapped NSOM, we present in this chapter a review of theoretical and experimental work on scattering of evanescent waves by small particles.
- Chapters 3 and 4 deal with the fundamentals of laser trapping including apodization and refractive-index mismatch. In particular, in Chapter 3, the sine condition obeyed by a high NA objective [Sheppard and Gu, 1993] is

examined for the quantitative characterisation of trapping force. The effect of spherical aberration induced by refractive-index mismatch [Török *et al.*, 1995] is characterised for estimating the effective trapping power in the focal region of a trapping objective. Based on this investigation, the principle of tube length change for compensation for spherical aberration [Sheppard and Gu, 1991] is demonstrated and the improved transverse trapping force is measured. As a foundation of our study, Chapter 4 deals with the detailed force evaluation for trapped metallic particles. The effect of the NA of a trapping objective on the transverse trapping force on metallic particles is investigated with the consideration of spherical aberration. A method based on the use of an annular lens is proposed and demonstrated for improving the transverse trapping force on a metallic particle.

- Chapters 5 and 6 contribute to an investigation into near-field scattering with trapped metallic particles. Chapter 5 focuses on the effect of signal strength on near-field imaging with trapped metallic particles. The dependence of signal strength and image contrast on the size of a laser-trapped metallic particle is compared with that for dielectric particles. An optimal image contrast is obtained for a particle of a particular size and a detector of a given sensitivity. The image enhancement with the use of a metallic particle instead of a dielectric particle is demonstrated evidently by imaging evanescent wave interference patterns and the surface structure of a prism. Chapter 6 presents an investigation into the depolarisation of evanescent waves scattered by laser-trapped metallic particles and its impact on image formation. The degree of polarisation of near-field Mie scattering is characterised for metallic particles of different sizes. The different behaviour

of the depolarisation between dielectric and metallic particles is discussed in terms of high scattering efficiency and excited surface plasmon resonance associated with metallic particles. A polarisation-gating method based on the utilisation of polarised and/or less depolarised photons for improving image quality is demonstrated.

- Chapter 7 summarises the significance of the main results obtained in this research. Future work on particle-trapped NSOM is discussed.

## CHAPTER TWO

# Literature Review of Near-Field Scanning Optical Microscopy

### 2.1 Introduction

**R**ESearch of near-field imaging has been prosperous over the last two decades, driven by the progress of material science and surface physics [Betzig and Trautman, 1992]. As a result, the family of near-field scanning optical microscopy (NSOM) has grown rapidly, including photon-tunnelling NSOM, vibrating metallic tip shear-force NSOM, atomic force microscopy-based NSOM, and their miscellaneous variations [Paesler and Moyer, 1996]. In general, each imaging technique has its own features and is suitable for particular occasions and samples.

Recently, using a laser-trapped particle as a near-field probe for NSOM has been demonstrated [Malmqvist and Hertz, 1994; Kawata *et al.*, 1994]. This novel technique, termed as particle-trapped NSOM, relies on collecting scattered evanescent waves from a sample with a laser-trapped particle and allows remote sensing (imaging) of a sample that is mechanically unreachable.

For the development of particle-trapped NSOM, one should be attentive to the existing problems and the fundamental issues of this technique. This chapter is therefore to provide the essential background knowledge for this study through an overview of the recent development of NSOM. In section 2.2, we introduce the key concepts and the

imaging mechanisms of NSOM. The advantages and drawbacks associated with individual near-field imaging techniques are discussed. Based on this introduction, the principle of particle-trapped NSOM is described in section 2.3. A comparison of this technique with the other forms of NSOM is summarised to reveal its unique features. Consequently, the problems associated with particle-trapped NSOM are pointed out. To understand the imaging mechanism of particle-trapped NSOM, laser trapping technique and near-field Mie scattering are reviewed in sections 2.4 and 2.5, respectively.

## 2.2 Near-field scanning optical microscopy

Optical microscopy is useful for the study of the microscopic world owing to its versatility, ease-of-use, and low cost features [Betzig and Trautman, 1992]. The growing demand of high spatial resolution of modern optical and surface science has inspired the emergence of such advanced imaging techniques as confocal microscopy [Minsky, 1957] and NSOM [Pohl *et al.*, 1984; Betzig *et al.*, 1991; Girard and Dereux, 1996]. In particular, NSOM has significantly pushed imaging resolution down to the level of tens of nanometres, which is far beyond the diffraction limit [Betzig *et al.*, 1991]. As a result, NSOM has found itself versatile applications in surface chemistry (e.g., single-molecule detection and fluorescence imaging of polymer films), biology (e.g., NSOM imaging of single proteins and photosynthetic membranes), materials science (e.g., photoconductivity measurements and waveguide analysis), and information storage (e.g., near-field magneto-optics data storage) [Betzig and Trautman, 1992].

## 2.2.1 Principle of NSOM

### 2.2.1.1 Near-field and far-field

The concepts of optical near-field and far-field are essential for the understanding of NSOM. As illustrated in Fig. 2.1, an opaque screen with an aperture of sub-wavelength is illuminated with an incident plane wave [Betzig and Trautman, 1992]. The light field transmitted through the aperture comprises both longitudinal evanescent and transverse propagating components. The intensity of the evanescent wave along the longitudinal direction follows

$$I = I_0 \exp(-2\alpha z), \quad (2.1)$$

where  $I_0$  is the light intensity at the output of the aperture, and  $\alpha$  the attenuating factor of the evanescent wave field related to the physical properties of the incident plane wave (e.g., wavelength and polarisation) and the medium (e.g., absorption and scattering) where an evanescent wave arises.

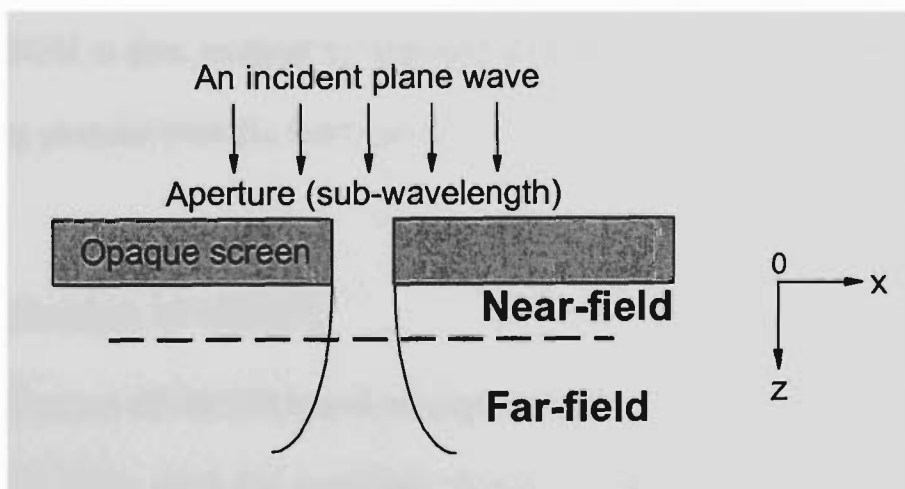


Fig. 2.1 Concepts of near-field and far-field (after Betzig and Trautman, 1992).

Because of the exponential decay of light intensity, evanescent wave can barely travel beyond a particular distance originated from the aperture. The region inside and outside this critical range (less than half the illumination wavelength in normal case) is

consequently termed as the near-field and far-field regions of the aperture, respectively. To obtain signal of high spatial frequencies, a small probe that can be physically placed in the near-field region of a sample (in this case, an aperture) is essential.

### 2.2.1.2 Principle of NSOM

In conventional optical microscopy, imaging is performed by collecting the propagating photons from a sample under study. The non-propagating components, in the form of evanescent waves, are relinquished in the detecting process as they are strictly localised in the optical near-field [Betzig and Trautman, 1992; Paesler and Moyer, 1996]. The evanescent photons, however, carry information on fine structures of a sample and therefore are vital for high-resolution imaging. The idea of NSOM is to utilise these evanescent photons by introducing a near-field probe of sub-wavelength in close proximity to a sample under study. In the presence of this probe, the evanescent photons from the sample are converted to propagating ones by scattering or waveguiding. Imaging of NSOM is then realised by scanning a probe across a sample and collecting the propagating photons with far-field optics.

## 2.2.2 Classification of NSOM

### 2.2.2.1 Classification of NSOM based on probe types

Based on probe types used for near-field imaging, one can group NSOM into two divisions: aperture and apertureless NSOM [Paesler and Moyer, 1996]. For the family of aperture-type NSOM, the commonly used probes are tapered fibre tips [Betzig and Trautman, 1992] and sub-wavelength apertures [Leviatan, 1986], while the typical probes for apertureless-type NSOM are semiconductor tips [Zenhausen *et al.*, 1994],

metallic needles [Inouye and Kawata, 1994], and semiconductor [Mertz *et al.*, 1994] or metallic [Bachelot *et al.*, 1995] cantilevers.

In the following, we shall briefly review three representative forms of NSOM: photon-tunnelling NSOM (aperture-type) [Reddick *et al.*, 1990; de Fornel *et al.*, 1993], vibrating metallic tip NSOM (apertureless-type) [Inouye and Kawata, 1994], and the newly developed atomic force microscopy-based NSOM (aperture- or apertureless-type) [Ohta and Kusumi, 1997]. Though their imaging mechanisms are markedly different, the superior capacities in acquiring fine information from a sample enable these types of NSOM the most commonly adopted for near-field research.

#### 2.2.2.1.1 Photon-tunnelling NSOM (aperture-type)

Ever since the invention of NSOM, the use of a fibre probe has been a conventional approach for high-resolution imaging [Betzig *et al.*, 1991; van Labeke and Barchiesi, 1993]. This is because optical fibres are inexpensive waveguides that can be served as illumination sources or collecting components (see Fig. 2.2). In practice, a fibre probe is produced by heating and stretching a single-mode optical fibre with an infrared laser beam or an arc discharge device, and then processed using chemical etching [Betzig *et al.*, 1991]. To prevent light leakage, the surrounding of a fibre tip is usually coated with some opaque metallic materials (e.g. aluminium [Betzig and Trautman, 1992] or silver [Vikram and Witherow, 1999]).

Fig. 2.2 illustrates a schematic diagram of photon-tunnelling NSOM where a fibre probe acts as a collecting component for near-field imaging. The evanescent photons from a sample, generated with an illumination laser beam under the condition

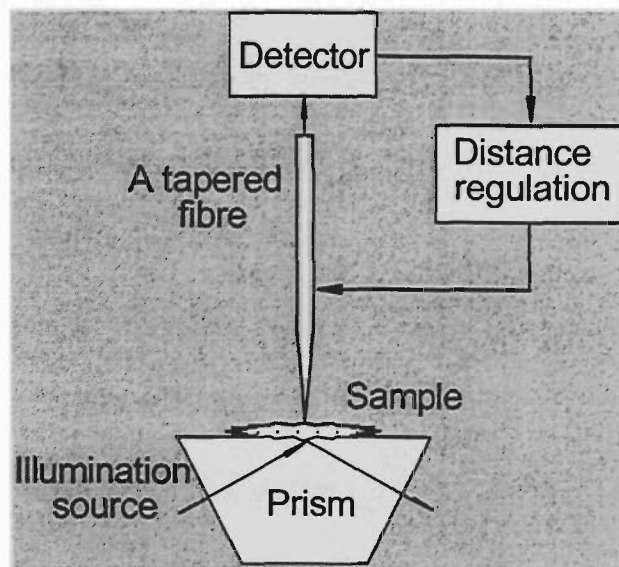


Fig. 2.2 Schematic diagram of photon-tunnelling NSOM.

of total internal reflection, are coupled (tunnelled) to a far-field detector via the fibre probe. The vertical motion of the fibre tip is controlled by a distance regulation mechanism based on feedback electronics. Imaging is performed by raster scanning the fibre tip in close vicinity to the sample. This type of NSOM can be operated at a constant height or a constant gap mode.

For the applications of fibre probes in NSOM including photon-tunnelling NSOM, the inherent problems are low optical throughput and poor signal collection efficiency because of the low numerical aperture (NA) of a fibre probe and heat dissipation in the tapered region of a fibre probe induced by metallic coating [Partovi *et al.*, 1999]. Another concern is that they are fragile to use and hardly reproducible, which is a major dilemma for practical users.

### 2.2.2.1.2 Vibrating metallic tip NSOM (apertureless-type)

Fig. 2.3 illustrates another type of NSOM, vibrating metallic tip NSOM. In this case, near-field imaging of a sample is realised by collecting the scattered evanescent photons from a sample with a sharpened metallic needle. This arrangement allows for imaging of a localised area with structures much smaller than the illumination wavelength through perturbation to the local optical field with a metallic tip. By monitoring the signal at the perturbation frequency, resolution beyond the diffraction limit can be reached. The specular reflection of the illumination light is removed from detection by making the angle of incidence larger than the collection angle of a low NA objective lens [Inouye and Kawata, 1994].

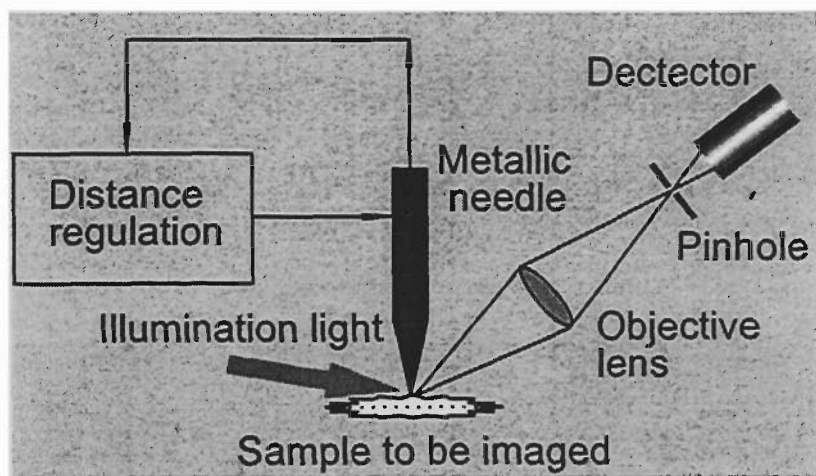


Fig. 2.3 Schematic diagram of vibrating metallic tip NSOM (after Inouye and Kawata, 1994).

Compared with the use of aperture-type NSOM, the use of a metallic needle may not only increase the lifetime of a near-field probe but also ensure the enhancement of the strength of the scattered evanescent waves from a sample under inspection. Under the resonance condition, the evanescent field surrounding the probe tip can be much enhanced due to the excitation of surface plasmon polaritons and image quality can be

substantially improved [Novotny *et al.*, 1998]. Similar to photon-tunnelling NSOM, apertureless-type NSOM can also be operated at a constant height mode or a constant gap mode depending on the mechanism of shear-force detection [Hatano *et al.*, 1998]. Apertureless-type NSOM has now been widely adopted by researchers in near-field optics [Zenhausern *et al.*, 1994; Gleyzes *et al.*, 1995].

Although its merit is significant, the use of a metallic probe in apertureless-type NSOM frequently interferes with the optical near-field. Under this circumstance, the “optical” image obtained is coupled with the topographic information of a sample under study. This artefact needs to be expelled from optical images; otherwise it will increase the difficulty for image processing and analysis.

#### 2.2.2.1.3 Atomic force microscopy-based NSOM (aperture- or apertureless-type)

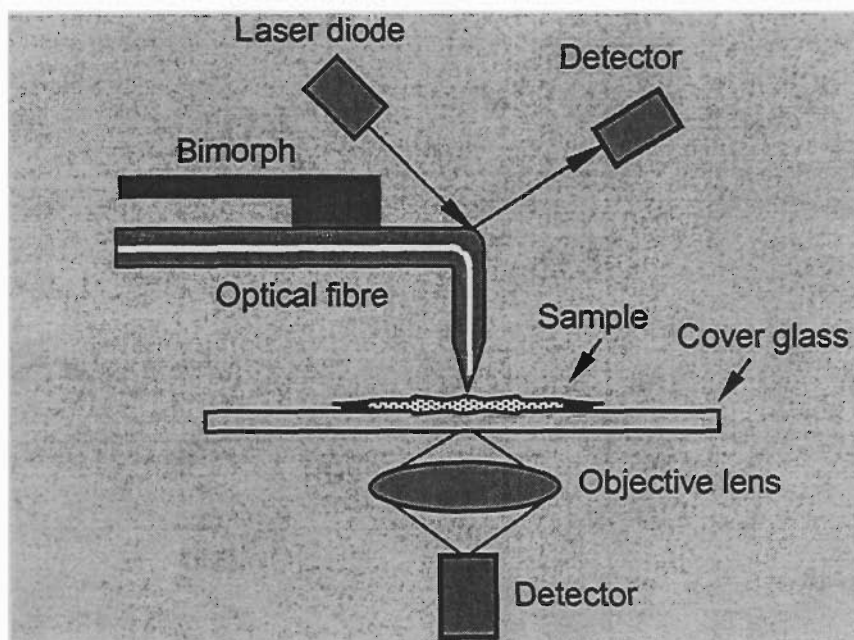


Fig. 2.4 Scheme of atomic force microscopy-based NSOM (after Ohta and Kusumi, 1997).

The combination of atomic force microscopy (AFM) [Binnig *et al.*, 1986] with NSOM is a recent development. This arrangement enables the simultaneous acquisitions of both topographic and optical images of a sample, which is obviously advantageous over the other forms of NSOM [Ohta and Kusumi, 1997]. As shown in Fig. 2.4, a bent optical fibre mounted on a bimorph is vibrated vertically against a sample under inspection. A laser beam incident on the fibre cantilever is reflected to a detector to build up a surface image of the sample with resolution at an atomic level (few nanometres). An optical image of the sample is simultaneously obtained via transmission NSOM that utilises the bent fibre as an illumination source for the sample. In addition to a fibre probe, a metallic cantilever can also be served as a near-field probe for AFM-based NSOM. Depending on the probe type, AFM-based NSOM possesses the advantages and disadvantages as summarised individually for aperture- and apertureless-type NSOM.

#### 2.2.2.2 Classification of NSOM based on signal collection modes

Depending on the configurations of the collection optics, one can classify NSOM as either a reflection mode (top part of Fig. 2.5) or a transmission mode (bottom part of Fig. 2.5) [Paesler and Moyer, 1996]. Fig. 2.5 illustrates a general arrangement of a sample, collection optics, and detectors for NSOM with a fibre probe. The criterion for adopting a reflection or transmission mode for NSOM lies in the optical property of a sample to be imaged. In many occasions, the spatial frequency information contained in the signal transmitted through a sample represents the most important data. In collecting the signal from a sample in a transmission mode, a high NA microscope objective is often used. In a reflection mode configuration such as vibrating metallic tip NSOM, an objective of low NA is employed to attain a long working distance,

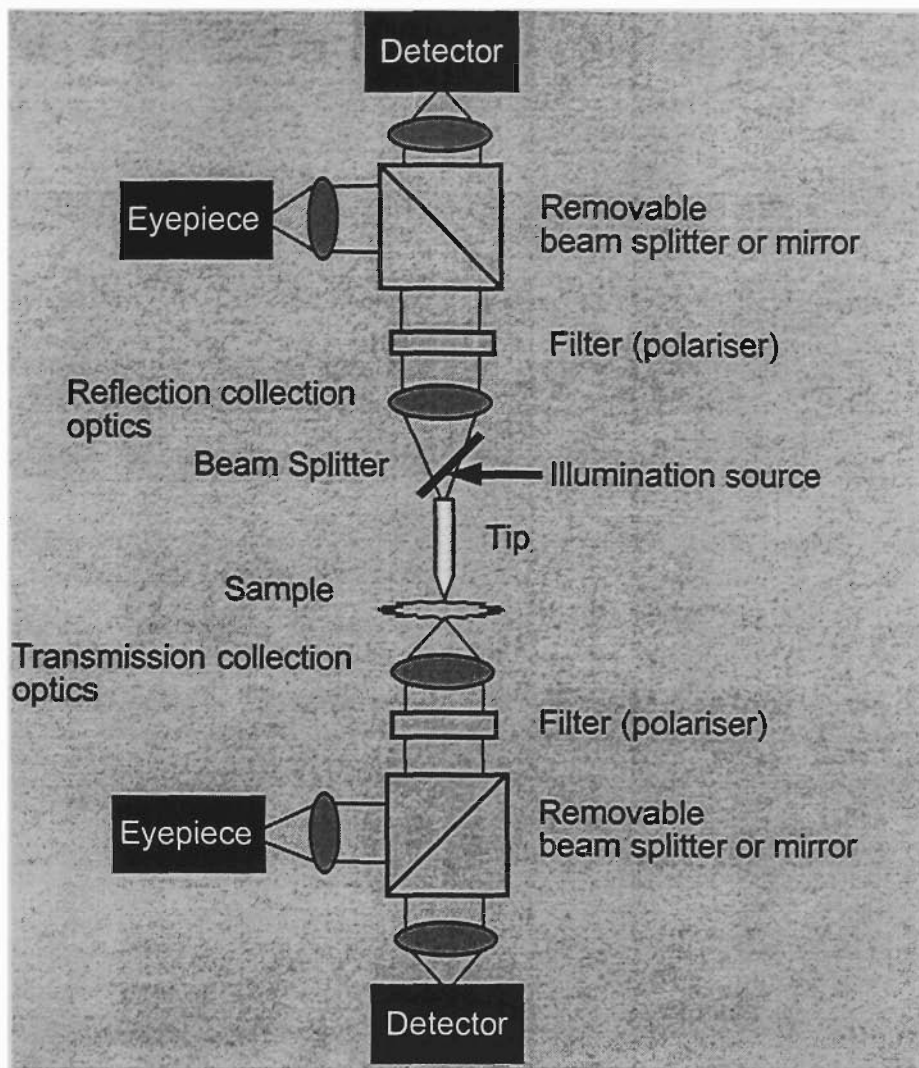


Fig. 2.5 Schematic diagram of the essential optical elements of NSOM (after Paesler and Moyer, 1996).

and the probe tip mounted between a sample and an objective may be bent to provide optical access [Tsai and Guo, 1997]. Simultaneous operation of NSOM in reflection and transmission is possible and provides the freedom in selecting image of better contrast without moving a sample [Wei *et al.*, 1996].

### 2.3 NSOM with laser trapping

The use of a laser-trapped particle as a sensing element for high-resolution microscopic imaging was innovated in early 1990's [Ghislain and Webb, 1993]. Since a laser-trapped particle can be remotely controlled in two or three dimensions with a high

accuracy and the trapped particle itself can act as an efficient scatterer, laser trapping has provided a novel approach for signal acquisition in both force microscopy and optical microscopy.

## 2.3.1 Applications of laser trapping in near-field imaging

### 2.3.1.1 Force microscopy with laser trapping

Recently, it has been demonstrated in the mechanical measurements of individual biomolecules that an optical trap can act as not only a noninvasive micromanipulator but also a force transducer [Ashkin *et al.*, 1990; Block *et al.*, 1990; Kuo and Sheetz, 1993; Svoboda *et al.*, 1993; Finer *et al.*, 1994; Miyata *et al.*, 1995; Simmons *et al.*, 1996; Visscher *et al.*, 1996]. The use of an optically trapped object as a sensing probe for scanning force microscopy, which detects the interaction between a sample and a probe, was reported by Ghislain and Webb [Ghislain and Webb, 1993]. Compared with a mechanical cantilever that converts force into displacement, the spring constant (stiffness) of an optically trapped probe is reduced by three to four orders of magnitude while high resonance frequency is retained. This is desirable as a small spring constant improves sensitivity as well as isolates vibration noise. In addition, laser trapping has an advantage that the spring constant of a trap can be instantly changed during the measurement by varying the laser power. By employing a three-dimensional (3D) trapped dielectric bead as a position sensor, applications of laser trapping in scanning force microscopy and evanescent wave microscopy have become possible [Florin *et al.*, 1996; Friese *et al.*, 1999]. It was found that with a laser-trapped metallic particle, the lateral spring constant of an optical trap can be reduced to  $10^{-6}$  N/m, which detects force as small as  $10^{-13}$  N [Higurashi *et al.*, 1999].

### 2.3.1.2 Optical microscopy with laser trapping

The motivation of utilising laser trapping for optical imaging is to perform high-resolution imaging of materials. In 1992, Malmqvist and Hertz proposed a novel optical imaging method using an axially trapped dielectric particle as an illumination source for a sample under study [Malmqvist and Hertz, 1992]. In 1994, Malmqvist and Hertz further demonstrated that near-field imaging of a sample could be achieved with an axially trapped frequency-doubled dielectric particle as an illumination source [Malmqvist and Hertz, 1994].

However, the microscope proposed by Malmqvist and Hertz suffers from low resolution due to the Brownian motion of a trapped particle. This is because that the evanescent wave of a sample is extremely sensitive to the axial position of a trapped particle, and therefore the axial displacement of a trapped particle may severely degrade image resolution.

Recently, Kawata *et al.* used a two-dimensional (2D) laser-trapped dielectric particle as a near-field probe [Kawata *et al.*, 1994]. With this form of NSOM (referred to as particle-trapped NSOM in this thesis), spatial resolution of less than 100 nm was demonstrated. Near-field imaging was also reported with an axially trapped metallic Rayleigh particle [Sugiura *et al.*, 1997]. The particle probe was lifted against the bottom surface of a sample by the axial gradient force. Two laser beams of different wavelengths were employed for trapping and illumination, respectively, using a single high NA objective. However, image resolution obtained with this imaging system was not quite satisfactory possibly due to the collection of light scattered directly from the sample.

Compared with conventional stylus-based NSOM that is restricted to mechanical access to smooth surfaces, the use of a laser-trapped particle enables noninvasive imaging of surfaces and objects in a solution. The axial pushing force acting on a trapped particle eliminates the requirement of distance control. The problem of probe deterioration may be avoided since plenty of particles are available for injection in the trap. Furthermore, accidental collisions with an object will not result in probe or object destruction due to the elastic nature of laser trapping. Finally, shape and material of a particle probe can be more easily controlled than that of stylus-based NSOM, thus providing more freedom for experimenting.

### 2.3.2 Principle of particle-trapped NSOM

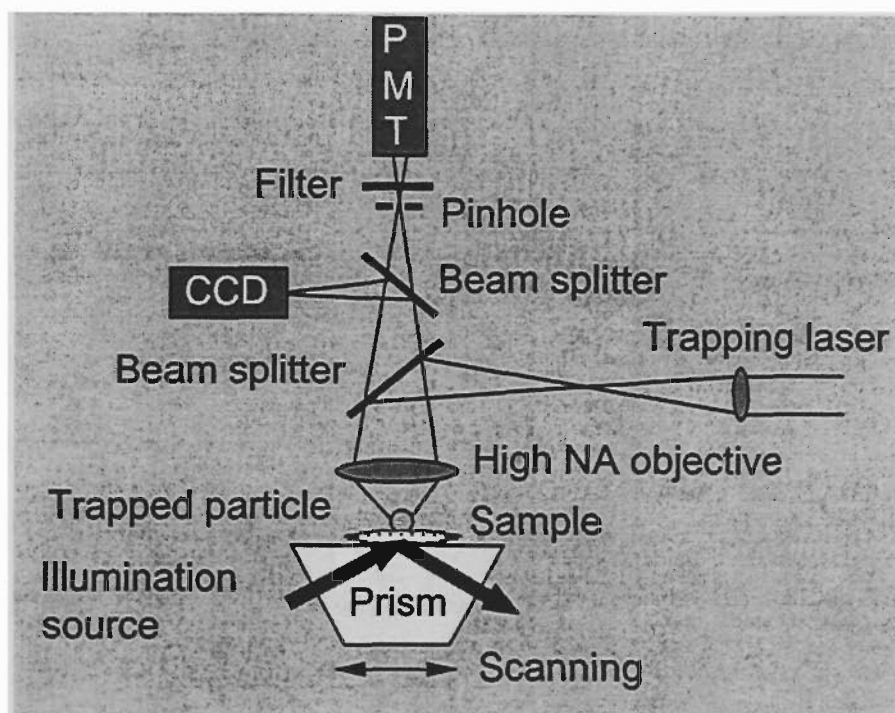


Fig. 2.6 Schematic diagram of particle-trapped NSOM (after Kawata *et al.*, 1994).

In this section, we will introduce the principle of particle-trapped NSOM. As shown in Fig. 2.6, a particle is optically trapped with a laser beam focused by a high NA microscope objective. The particle is laterally pulled toward the optical axis of the focused laser beam, while it is vertically pushed down toward the sample surface by the gradient force of the laser beam. As a result, the distance between the sample and the particle is maintained to be zero.

In addition to the trapping laser beam, another laser beam of a different wavelength is incident at the interface between the sample and its substrate (normally a prism) under the condition of total internal reflection. An evanescent wave from the sample is generated with this illumination laser beam and is scattered by the trapped particle to a photon-multiplier-tube (PMT) placed in the far-field region. This process, i.e., the scattering of evanescent waves by small particles, is termed as near-field Mie scattering in analogy to the concept of Mie scattering. For particle-trapped NSOM, the strength of scattered evanescent waves determines image contrast.

To remove stray light scattered from other locations than the trapped particle and therefore improve signal-to-noise ratio of imaging, a pinhole is mounted at the conjugate point of the particle with respect to the trapping objective. The reflection of the trapping beam on the particle surface is blocked with a band-pass filter. The image of the sample is reconstructed by scanning the particle in 2D across the sample [Kawata *et al.*, 1994].

In comparison with the other forms of NSOM, imaging of particle-trapped NSOM is unique since it relies on collecting evanescent waves scattered by a particle

from a sample for image formation. The strength of scattered evanescent waves is dependent on the scattering efficiency of a particle and the illumination intensity for a sample under study. The performance of laser trapping determines the speed of image acquisition and affects image resolution. The dual-function of a high NA objective in particle-trapped NSOM for signal collection and particle trapping provides such advantages as high signal-to-noise ratio and compactness.

It should be pointed out that in spite of the advantages as have been described, the development of particle-trapped NSOM has encountered some problems such as low scattering efficiency and low scanning speed. However, these problems are associated with laser-trapped dielectric particles and may be overcome by using metallic particles. These issues will be addressed in detail in Chapters 4, 5 and 6.

## **2.4 Laser trapping**

From the introduction of particle-trapped NSOM given in the last section, it is conceivable that the performance of laser trapping may affect image quality of particle-trapped NSOM in many aspects including scanning speed, image resolution, and image contrast. As the trapping performance of a particle is mainly determined by trapping force it experiences, we review in this section the laser trapping technology with a focus on the factors that determine trapping performance.

In the pioneering work of Ashkin, he observed that transparent particles, such as latex spheres and air bubbles freely suspended in liquids and gases, could be accelerated and levitated under the radiation pressure irradiated by a single focused laser beam or multiple focused laser beams [Ashkin, 1970; Ashkin and Dziedzic, 1971]. The radiation

pressure, though in the order of pico-Newtons, is strong enough to levitate and move microparticles against gravity and viscous drag of the solution where these particles are suspended.

In 1986, Ashkin *et al.* proposed and demonstrated that dielectric particles can be optically trapped with a single laser beam focused by a high NA objective lens [Ashkin *et al.*, 1986]. This technique, known as single-beam gradient force trapping or laser tweezers, has generated enormous impact on physical (e.g., self-lasing [Sasaki *et al.*, 1993] and fluorescence sensing [Zhang *et al.*, 1998]), biological (e.g., manipulation of blood cells [Buican *et al.*, 1987] and DNA molecules [Smith *et al.*, 1996]), and chemical (e.g. probing and analysing of chemical compounds [Sasaki *et al.*, 1996]) researches.

### 2.4.1 Principle of laser trapping

Optical trapping is conceptually simple. An object in an electric field of a laser beam is polarised. In the presence of an electric field gradient, the polarised object moves towards the region of highest field due to momentum transfer. The transverse Gaussian intensity profile across the width of the laser beam pulls the object towards the beam axis. In practice, the gradient force of a laser beam, sufficient for trapping a small particle, is generated with the aid of a high NA microscope objective (Fig. 2.7) [Block, 1992].

When an object is optically captured (trapped) in the potential well of a signal laser beam, it experiences conservative gradient, non-conservative absorption and

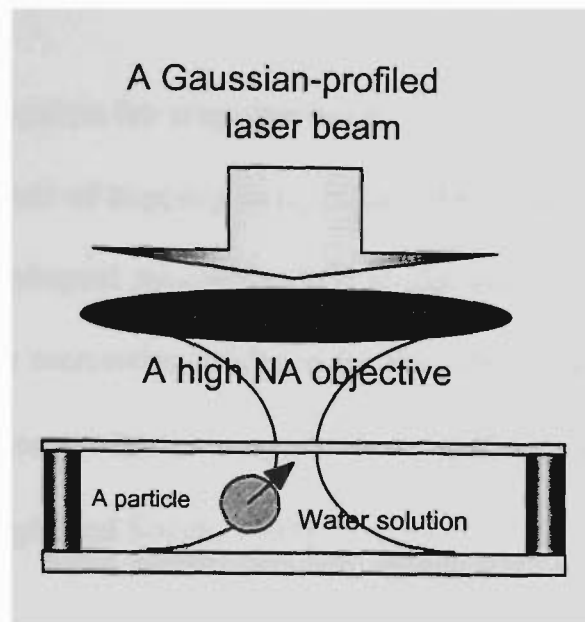


**Fig. 2.7** Schematic diagram of single-beam gradient force trapping.

scattering forces [Svoboda and Block, 1994]. To obtain an effective trap, the gradient force needs to be maximised, while absorption and scattering forces should be minimised as they tend to repel the trapped object away from the focal region of a trapping laser beam in the direction of the local electromagnetic energy flow. The absorption force can be minimised by ensuring that the frequency of a trapping beam is off resonance [Sato *et al.*, 1994].

### 2.4.2 Characterisation of trapping force

An accurate knowledge of trapping force is essential for the applications of laser trapping technique. In this section, the theoretical approaches for the characterisation of trapping force on a dielectric particle are reviewed. In particular, the fundamental differences of the trapping force between a dielectric particle and a metallic particle are pointed out. The factors that affect the performance of laser trapping, such as light distribution in the focal region of a high NA trapping objective and the Brownian motion of a particle inside a solution, are discussed.

### 2.4.2.1 Theoretical approaches for trapping force

Although a general treatment of trapping force on particles is not yet available [Sato and Inaba, 1996], the mostly adopted ray-optics (RO) model and the electromagnetic (EM) wave model do provide a reasonable guidance for the evaluation of trapping force on small spherical particles except for the range between  $\lambda$ - $10\lambda$  ( $\lambda$  is the wavelength of a trapping laser beam) [Wright and Sonek, 1993].

#### 2.4.2.1.1 Ray-optics model

In the ray-optics (RO) model, a trapping laser beam is simply decomposed into individual rays, and the ray density on an objective lens is assumed to be the same as that of the power density. For a dielectric particle, as shown in Fig. 2.8 (a), a single ray of power  $P$  gives rise to a series of reflected and refracted rays. As a result, the particle experiences forces in the  $Y$  and  $Z$  directions due to the net change in momentum per second in the respective directions. These forces can be expressed as [Ashkin, 1992]

$$\begin{cases} F_Y = -\frac{nPR}{c} \sin(\pi + 2\theta) + \sum_{m=0}^{\infty} \frac{nP}{c} T^2 R^m \sin(\alpha_0 + \beta_0), \\ F_Z = \frac{nP}{c} - \left[ \frac{nPR}{c} \cos(\pi + 2\theta) + \sum_{m=0}^{\infty} \frac{nP}{c} T^2 R^m \cos(\alpha_0 + m\beta_0) \right]. \end{cases} \quad (2.2)$$

Here  $R$  and  $T$  are the Fresnel reflectance and transmittance at the incident angle  $\theta$ ,  $n$  is the refractive index of the particle relative to the surrounding medium,  $\alpha_0$  and  $\beta_0$  are the angles relative to the forward direction of the incident ray, and  $c$  is the speed of light in vacuum. Defining the forces parallel (axial) and perpendicular (transverse) to the incident ray as the scattering and gradient forces  $F_s$  and  $F_g$ , we have [Ashkin, 1992]

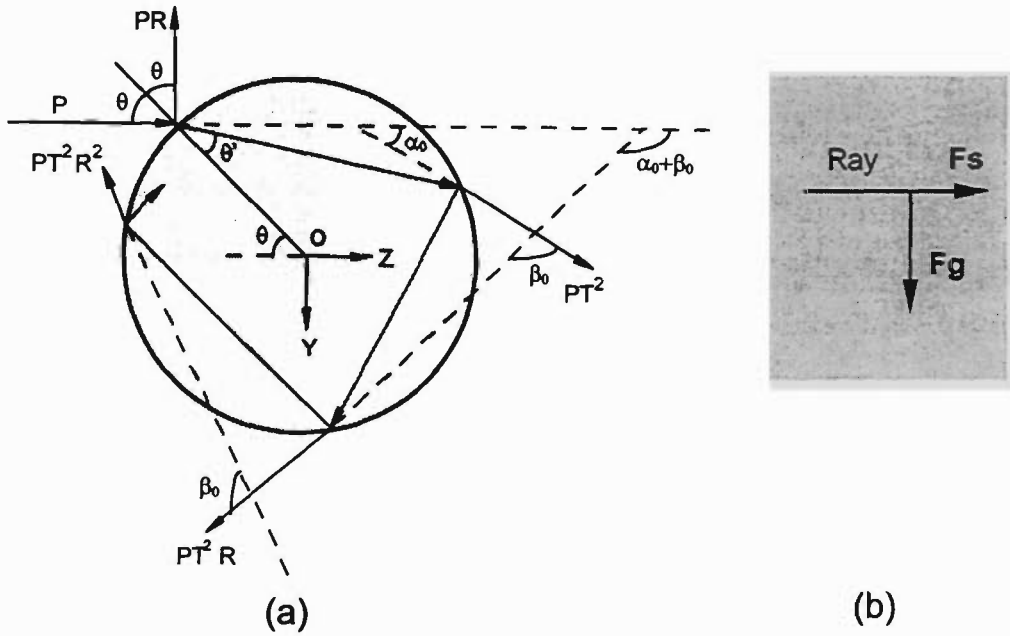


**Fig. 2.8** (a) Geometry for calculating force on a dielectric particle. A single incident ray of power  $P$  causes a series of reflected and refracted rays (after Ashkin, 1992). (b) Relative strength of the gradient and scattering forces of a single ray.

$$\begin{cases} F_g = \frac{nP}{c} \left( 1 + R \cos 2\theta - \frac{T^2 [\cos(2\theta - 2\theta') + R \cos 2\theta]}{1 + R^2 + 2R \cos 2\theta'} \right), \\ F_s = \frac{nP}{c} \left( R \sin 2\theta - \frac{T^2 [\sin(2\theta - 2\theta') + R \sin 2\theta]}{1 + R^2 + 2R \cos 2\theta'} \right), \end{cases} \quad (2.3)$$

where  $\theta'$  is the refractive angle of a single ray.

Assuming the light intensity distribution over the aperture of an objective lens is  $I(\rho)$ , we express the total trapping force on a particle as

$$\mathbf{F}_t = \mathbf{F}_G + \mathbf{F}_S = \frac{\int_0^{2\pi} \int_0^{\rho_{\max}} \mathbf{F}_g \cdot I(\rho) \cdot \rho d\rho d\varphi}{\int_0^{2\pi} \int_0^{\rho_{\max}} I(\rho) \cdot \rho d\rho d\varphi} + \frac{\int_0^{2\pi} \int_0^{\rho_{\max}} \mathbf{F}_s \cdot I(\rho) \cdot \rho d\rho d\varphi}{\int_0^{2\pi} \int_0^{\rho_{\max}} I(\rho) \cdot \rho d\rho d\varphi}, \quad (2.4)$$

where  $\rho$  is the radial position over the objective lens used for trapping,  $\rho_{\max}$  is the maximum radius of the objective aperture,  $\varphi$  is the azimuthal angle (see Fig. 2.9),  $\mathbf{F}_g$

and  $F_s$  are the vectorial gradient and scattering forces of a single ray, and  $F_G$  and  $F_S$  are the vectorial gradient and scattering forces on a particle, respectively. In Eq. (2.4), the gradient and scattering forces of a single ray are weighed by the ray density (proportional to the light intensity) before integration and normalised by the total power entering the back aperture of an objective lens.

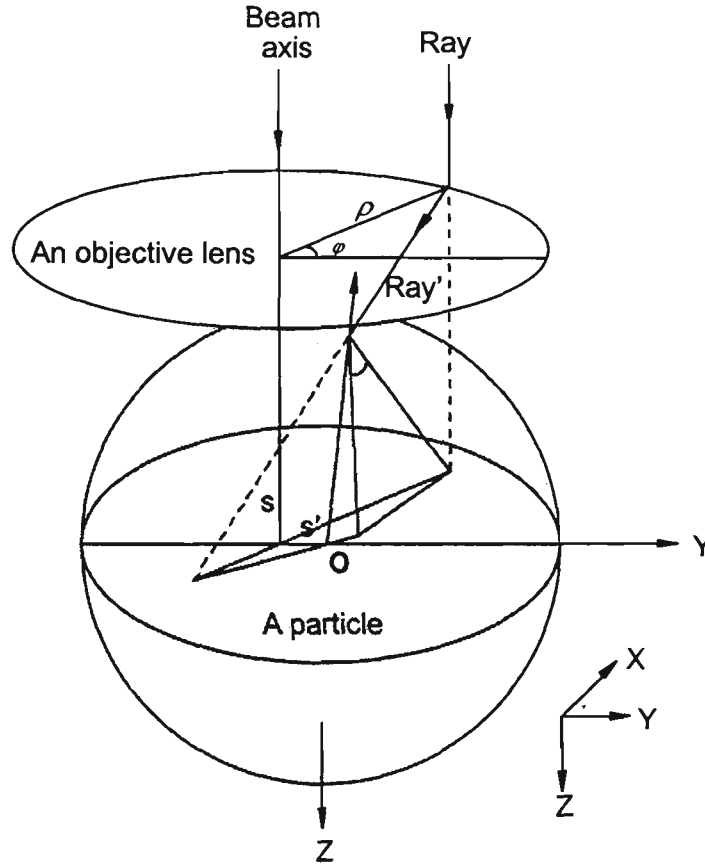
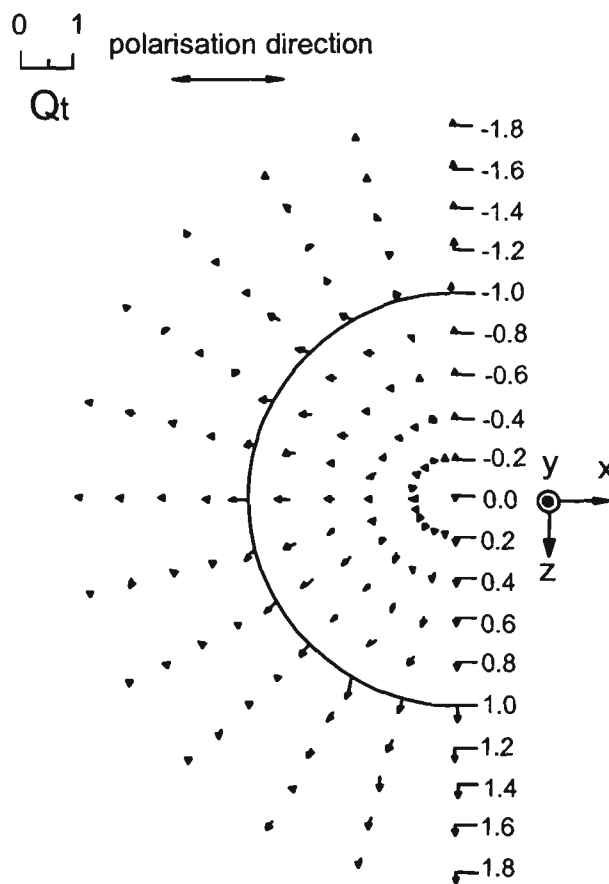


Fig. 2.9 Schematic diagram of the RO model of trapping force (after Ashkin, 1992).  $S$  and  $S'$  are the axial and transverse trapping positions.

The trapping efficiency  $Q_j$ , a parameter independent of trapping power for the evaluation of trapping force  $F_j$ , is defined as

$$Q_j = \frac{F_j c}{n P}, \quad j = g, s. \quad (2.5)$$

Here  $Q_g$  and  $Q_s$  are termed as the gradient and scattering efficiency of a single ray, respectively. The gradient ( $Q_G$ ), scattering ( $Q_S$ ), and total ( $Q_t$ ) trapping efficiency on a particle can be defined in a similar way based on Eq. (2.5) with respect to the gradient ( $F_G$ ), scattering ( $F_S$ ), and total trapping force ( $F_t$ ), respectively. The projections of the total trapping force (efficiency) along the transverse ( $Y$ ) and the axial ( $Z$ ) directions (Fig. 2.9) are defined as the transverse and axial trapping force (efficiency) and represented by  $F_{tr}$  ( $Q_{tr}$ ) and  $F_a$  ( $Q_a$ ), respectively ( $Q_t = \sqrt{Q_{tr}^2 + Q_a^2}$ ).



**Fig. 2.10** Distributions of the total trapping efficiency  $Q_t$  in the  $x$ - $z$  plane for a polystyrene particle. The polarisation direction of the laser beam is parallel to the  $x$ -axis. The laser beam used for trapping is uniform over the aperture of an objective (oil-immersion,  $NA = 1.25$ ) and linearly-polarised ( $\lambda = 488$  nm).

Using Eqs. (2.4) and (2.5), we can calculate the total trapping efficiency  $Q_t$  for a dielectric particle (polystyrene,  $n_p = 1.59$ ) suspended in a water solution ( $n_2 = 1.33$ ). The force diagram is illustrated in Fig. 2.10. In this calculation, the trapping objective (oil-immersion, NA = 1.25) is assumed to obey the sine condition (see section 2.4.2.2.1 or [Stamnes, 1986; Born and Wolf, 1997]). The laser beam used for trapping is uniform over the aperture of the objective and linearly-polarised in parallel to the  $x$ -axis ( $\lambda = 488$  nm). The trapping laser beam propagates in the direction of the  $z$ -axis. The distribution of the total trapping efficiency  $Q_t$  on the right plane is omitted due to its symmetry with respect to the plane at  $x = 0$ . The particle radius is normalised to be unity. Each individual arrow originates from the trapping position of the laser beam and points towards the direction of the total trapping force. The length of the arrow is proportional to the strength of  $Q_t$ .

As shown in Fig. 2.10, in the axial direction, the trapping force on a dielectric particle can be either lifting or pushing depending on the axial trapping position  $S$  (see Fig. 2.9 for definition) is above or below the central equatorial plane of the particle. Along the transverse direction, the force on a dielectric particle tends to attract the particle back to the beam axis. A maximum transverse trapping force occurs for a dielectric particle when the transverse trapping position  $|S'| \rightarrow 1$  (see Fig. 2.9 for definition).

Our study, as will be described in Chapter 3, has found that the maximum transverse trapping efficiency  $Q_{tr}^m$  (i.e., the maximum absolute value of the transverse trapping efficiency) of a dielectric particle decreases when the NA of a trapping

objective increases (Fig. 2.11). This is because the gradient force is dominant over the scattering force for a dielectric particle due to high refraction (refer to Fig. 2.8 (b)).

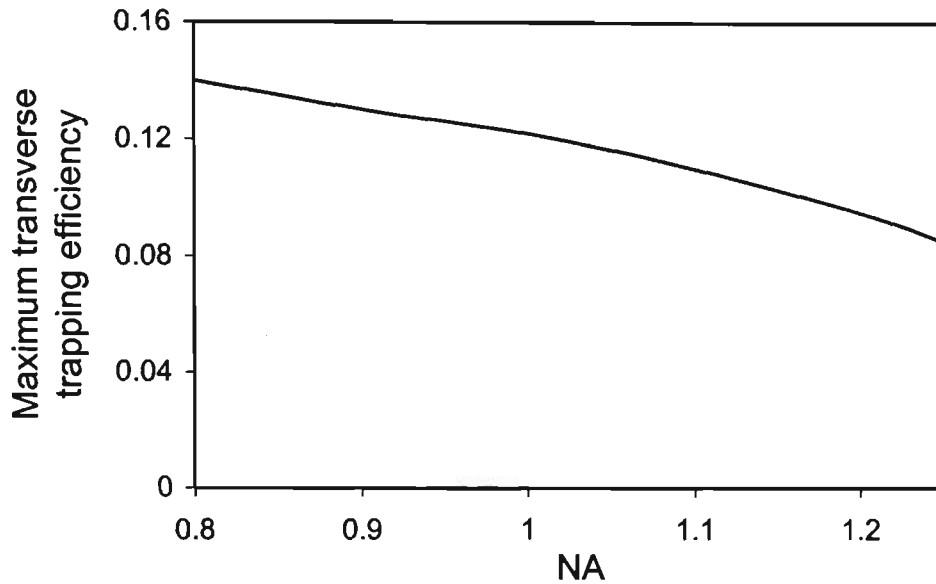


**Fig. 2.11** Maximum transverse trapping efficiency  $Q_r^m$  as a function of the NA of a trapping objective for a polystyrene particle ( $n_p = 1.59$ ). The polarisation direction of the laser beam is parallel to the transverse direction. The light distribution over the aperture of the objective is uniform and linearly-polarised ( $\lambda = 488$  nm). An oil-immersion objective ( $NA = 1.25$ ) is assumed for trapping.

#### 2.4.2.1.2 Electromagnetic wave approach

The electromagnetic (EM) wave approach for the calculation of trapping force on dielectric particles was introduced by Barton *et al.* [Barton *et al.*, 1988; 1989; Barton and Alexander, 1989]. Their results are reasonably consistent with experiments when the particle diameter is smaller than  $\lambda$  [Wright and Sonek, 1993; Wright *et al.*, 1994]. In this model, an incident laser beam is assumed to have a Gaussian intensity profile at the focus of a microscope objective [Barton *et al.*, 1988]. Once expansion coefficients, which are needed to describe the incident and scattered laser fields and expressed in an

infinite series representation, are found, the axial and transverse forces exerted on a micro-sphere can be derived from Maxwell's stress tensor as [Barton *et al.*, 1989]

$$\langle \mathbf{F}_N \rangle = \left\langle \int_{\mathcal{S}} \hat{\mathbf{n}} \cdot \vec{T} d\sigma \right\rangle, \quad (2.6)$$

where  $\langle \rangle$  represents a time average,  $\mathbf{F}_N$  is the net radiation force,  $\hat{\mathbf{n}}$  is an outward normal unit vector,  $\vec{T}$  is Maxwell's stress tensor, and  $\sigma$  is the surface area of the particle.

In order to obtain the expansion coefficients, the EM wave model requires an accurate expression for the radial component of the incident electric field. As the laser beam used to hold the sphere is tightly focused, the paraxial approximation for the incident Gaussian beam is no longer valid [Barton and Alexander, 1989]. Instead, the fifth-order corrected expressions are applied to the incident electromagnetic field components of a monochromatic Gaussian beam (i.e., a focused TEM<sub>00</sub> mode laser beam). Under this approximation, the expressions for general electromagnetic fields (incident, scattered and internal fields) can be obtained by applying boundary conditions at the surface of the sphere. The general electromagnetic field solution is obtained by expressing the field as a sum of two subfields, the electric wave field which is assumed to have a zero radial magnetic field component, and the magnetic wave field which is assumed to have a zero radial electric field component [Barton *et al.*, 1989].

For the steady-state optical condition, the Maxwell's stress tensor can be expressed, in the traditional Minkowski form, as [Barton *et al.*, 1989]

$$\vec{T} = \frac{1}{4\pi} (\epsilon_0 \mathbf{E}\mathbf{E} + \mathbf{H}\mathbf{H} - \frac{1}{2} (\epsilon_0 E^2 + H^2) \vec{I}), \quad (2.7)$$

where  $\mathbf{E}$  and  $\mathbf{H}$  are the electric and magnetic fields at the surface of the particle, and  $\varepsilon_0$  is the permittivity of the particle. The trapping force can be further expressed as

$$\langle \mathbf{F}_N \rangle = \frac{1}{4\pi} \int_0^{2\pi} \int_0^\pi \left\langle \left( \varepsilon_{ext} E_r \mathbf{E} + H_r \mathbf{H} - \frac{1}{2} (\varepsilon_{ext} E^2 + H^2) \hat{\mathbf{r}} \right) \right\rangle r_p^2 \sin\theta_p d\theta_p d\phi_p \Big|_{r_p=r}, \quad (2.8)$$

where  $\varepsilon_{ext}$  is the permittivity of the surrounding medium,  $E_r$  and  $H_r$  are the radial field components,  $\hat{\mathbf{r}}$  is the outward radial vector,  $r$  is the particle radius, and  $(r_p, \theta_p, \phi_p)$  are spherical coordinates. Finally the axial and transverse components of the trapping force can be worked out for different incident fields.

#### 2.4.2.1.3 Comparison of different approaches

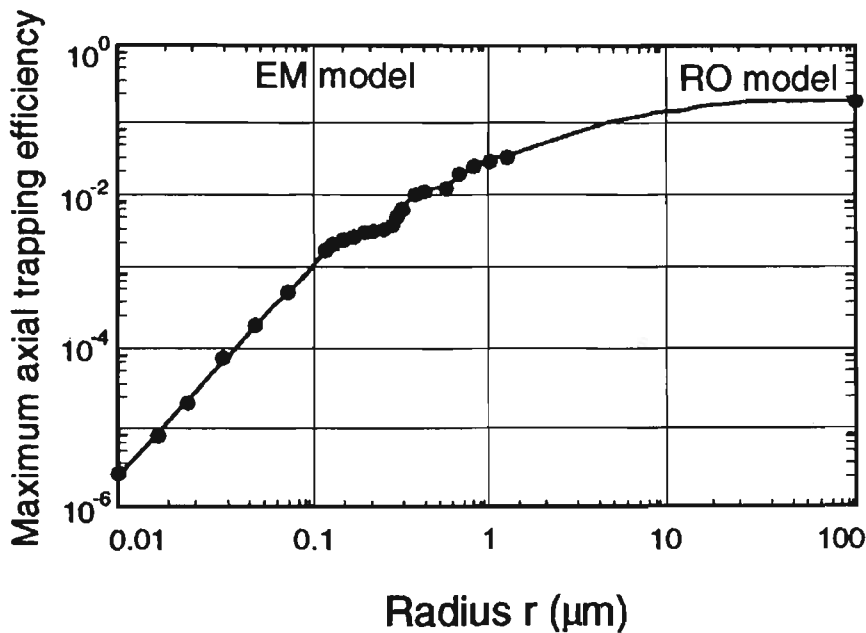


**Fig. 2.12** Maximum axial trapping efficiency  $Q_a^m$  as a function of the microsphere radius  $r$ . The microsphere is assumed to be polystyrene ( $n=1.57$ ) suspended in water ( $n=1.33$ ). For the EM wave model calculation ( $r \leq 1 \mu\text{m}$ ), the wavelength was  $1.06 \mu\text{m}$  and the spot size was  $0.4 \mu\text{m}$ . The RO model calculation ( $r = 100 \mu\text{m}$ ) used a cone angle of  $60^\circ$ . Note the  $r^3$  dependence on  $Q_a^m$  for  $0.01 \leq r < 0.1 \mu\text{m}$ , decreasing to the  $r^0$  dependence as  $r$  becomes large ( $r > 100 \mu\text{m}$ ) (after Wright and Sonek, 1993).

Fig. 2.12 illustrates the maximum axial trapping efficiencies calculated using the EM wave model and the RO model. When compared with experiments, the RO model has proved to be suitable only for large particles (diameter  $\phi > 10\lambda$ ). By contrast, the EM wave model is applicable only to small particles ( $\phi < \lambda$ ) [Wright and Sonek, 1993]. This is due to the fact that the Gaussian beam is not the exact solution to the Maxwell equations near the focus of an objective regardless of the level of approximation adopted. The errors in the predicted forces become more significant when the particle size gets larger [Wright *et al.*, 1994]. One of the remarkable differences between the results of the RO model and the EM wave approach is the existence of an on-axis dip on the force-position curve in the later case. In spite of the similar envelope, the force is zero on the surface of the sphere by the EM wave approach [Barton *et al.*, 1989], whereas it is a maximum by the RO calculation [Ashkin, 1992]. A second difference is that the force curve in the EM wave approach is not simple, but has an oscillating structure [Sato and Inaba, 1996].

When the particle size is in the region between  $\lambda$ - $10\lambda$ , neither the RO model nor the EM wave approach gives the result consistent with the experimental measurement [Wright and Sonek, 1993]. This is because both models have overlooked an important issue in laser trapping, i.e., the light distribution in the focal region of a high NA trapping objective as will be addressed in the following section.

#### **2.4.2.2 Effect of light distribution in the focal region of a trapping objective**

It is evident from the principle of laser trapping that the light distribution in the focal region of a trapping objective determines trapping performance. To improve the positioning sensibility and efficiency of an optical trap, the spatial profile of the force

potential well generated with a trapping objective is desired to be steep and narrow. This can be achieved by increasing the trapping power, reducing the trapping wavelength, or using a high NA trapping objective with different apodization methods.

To evaluate trapping force on a particle, the apodization of a trapping objective must be considered since it determines the ray density (for RO model) and the light distribution in the focal region of the objective (for EM model). In addition, the light distribution in the focal region can be also affected by spherical aberration which arises when a trapping laser beam enters a solution with a refractive index different from that of the original medium. These factors are related to the vectorial properties of a field produced by a high NA trapping objective and will be addressed in this section.

#### 2.4.2.2.1 Sine condition

The sine condition is a basic imaging principle obeyed by commercial microscope objectives for two-dimensional space-invariant imaging [Born and Wolf, 1997; Sheppard and Gu, 1993; Gu, 1999]. This principle is of fundamental importance for the accurate characterisation of trapping force but has been neglected in previous treatments [Ashkin, 1992]. For an example, in the Mie region, the axial trapping efficiency for a particle of diameter  $\phi = 20 \mu\text{m}$  predicted by the RO model was up to 40% larger than the experimental value for a high NA objective [Wright and Sonek, 1993; Wright *et al.*, 1994], while it was approximately 10% smaller than the measured value in the transverse direction [Wright *et al.*, 1994]. This discrepancy is mainly due to an assumption used in the RO theory that a microscope objective used for trapping satisfies the tangent condition.

According to the RO model [Ashkin, 1992], the trapping force exerted on a particle is calculated as a sum of the force produced by each ray passing through the aperture of a microscope objective. When the ray density over the objective aperture is projected into the ray density over the angular aperture of ray convergence, the following condition has been used [Ashkin, 1992]:

$$\rho = f \tan \theta, \quad (2.9)$$

where  $\rho$  is the position of a ray incident upon the objective aperture  $\xi$ ,  $\theta$  is the angle of convergence of a ray after it is refracted by the objective, and  $f$  is the focal length of the objective (see Fig. 2.13). Eq. (2.9) is defined as the tangent condition based on the Helmholtz invariant [Sheppard and Gu, 1993; Born and Wolf, 1997; Gu, 1999]. An objective obeying the tangent condition has a constant magnification factor and the wavefront after the objective is a plane.

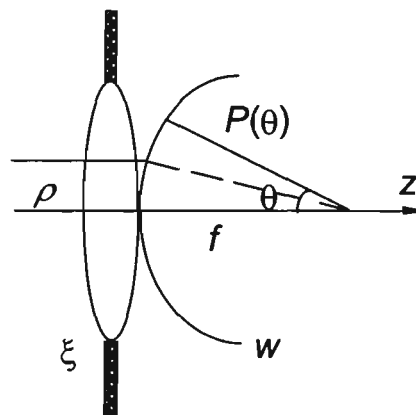


**Fig. 2.13** An incident ray at position  $\rho$  focused by a lens  $\xi$  with an apodization function  $P(\theta)$  and a focal length  $f$ .

In practice, it is extremely difficult to design and manufacture an objective satisfying the tangent condition. Instead, a commercial high NA objective is designed in

such a way that the sine condition [Stamnes, 1986; Born and Wolf, 1997; Gu, 1999], which can be expressed as

$$\rho = f \sin \theta, \quad (2.10)$$

is satisfied. An objective obeying the sine condition produces a spherical wavefront [Sheppard and Gu, 1993; Born and Wolf, 1997] after the incident rays are refracted by the objective, so that all the incident rays can be converged into a single point and the two-dimensional space-invariant condition is satisfied [Sheppard and Gu, 1993].

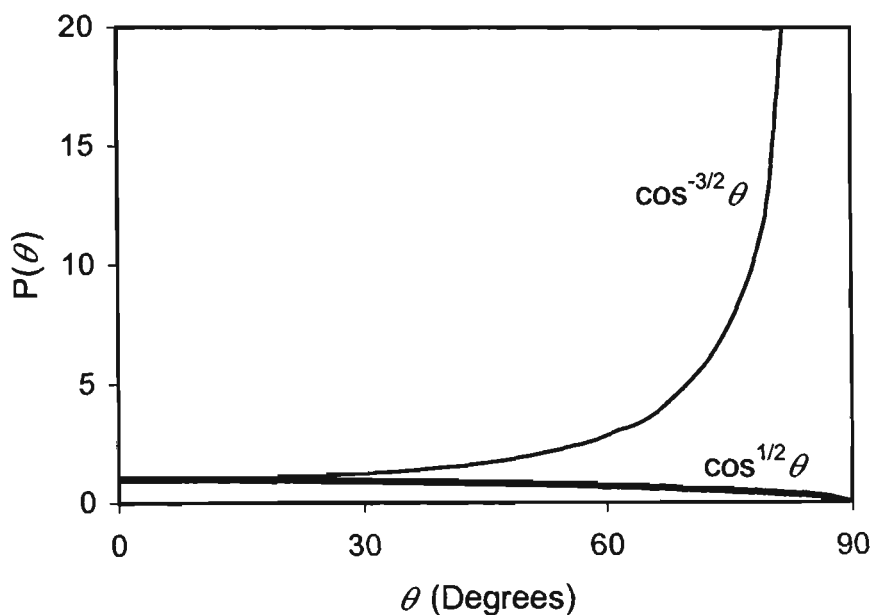


Fig. 2.14 Apodization function  $P(\theta)$  of a lens obeying the sine condition (thick line) and the tangent condition (thin line).

As shown in Fig. 2.13, the relative ray density over the converging wavefront  $w$  of a focusing lens can be represented by an apodization function  $P(\theta)$ . A comparison of the apodization function between the sine ( $P(\theta) = \cos^{1/2} \theta$ ) [Gu, 1999] and tangent ( $P(\theta) = \cos^{-3/2} \theta$ ) [Gu, 1999] conditions is illustrated in Fig. 2.14. For a lens obeying the sine condition, the apodization function decreases monotonically with the

converging angle  $\theta$ , while it approaches infinity when the convergence angle  $\theta$  is close to  $90^\circ$  for a lens satisfying the tangent condition.

The significant difference in the calculation of trapping force between using Eqs. (2.9) and (2.10) is that when the maximum convergence angle of an objective increases, the ray density in the former case approaches infinity while the ray density in the latter case approaches zero. As a result, trapping force in these two cases behaves differently if the NA of an objective is large. This issue will be addressed in detail in section 3.2.

#### 2.4.2.2 Effect of spherical aberration induced by refractive-index mismatch

When a beam is focused into a second medium with a refractive index  $n_2$  different from that of the incident material,  $n_1$ , as illustrated in Fig. 2.15, spherical aberration presents. As a result, the axial position of the main peak intensity is shifted by a negative and positive value under the condition (a)  $n_1 > n_2$  and (b)  $n_1 < n_2$ , respectively.

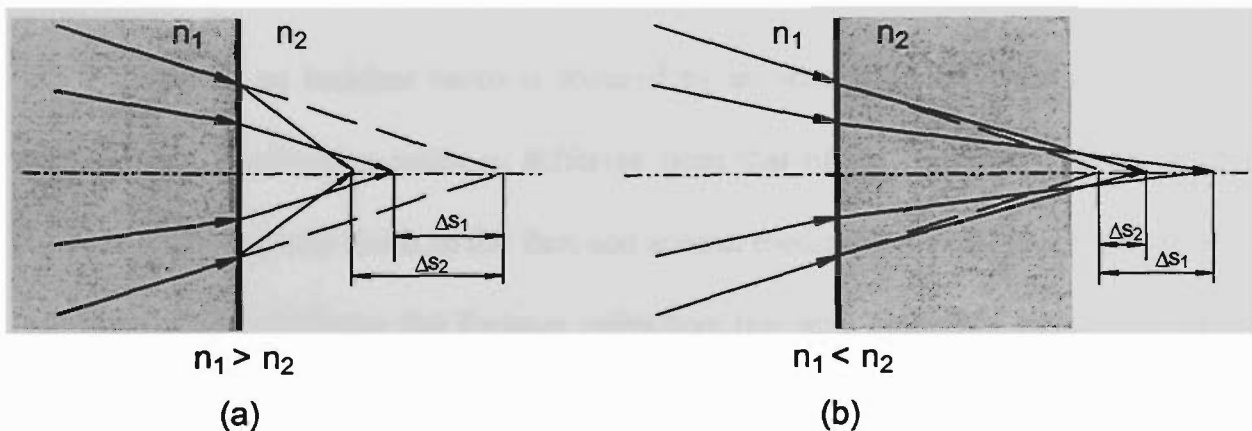


**Fig. 2.15** Illustration of spherical aberration induced by refractive-index mismatch by an interface between medium  $n_1$  and medium  $n_2$ . Negative and positive axial shifts  $\Delta S_i$  ( $i=1,2$ ) are generated under the condition (a)  $n_1 > n_2$  and (b)  $n_1 < n_2$ , respectively.

The effect of spherical aberration on the light distribution in the second medium was investigated in detail by Török *et al.* [Török *et al.*, 1995]. This treatment is applicable to any imaging system involving a high NA objective lens because it is mathematically rigorous and satisfies the homogeneous wave equation. Although only a two-layer media system is considered in this thesis, the formulae obtained can be readily extended to the cases for multiple-layer media [Török and Varga, 1997].

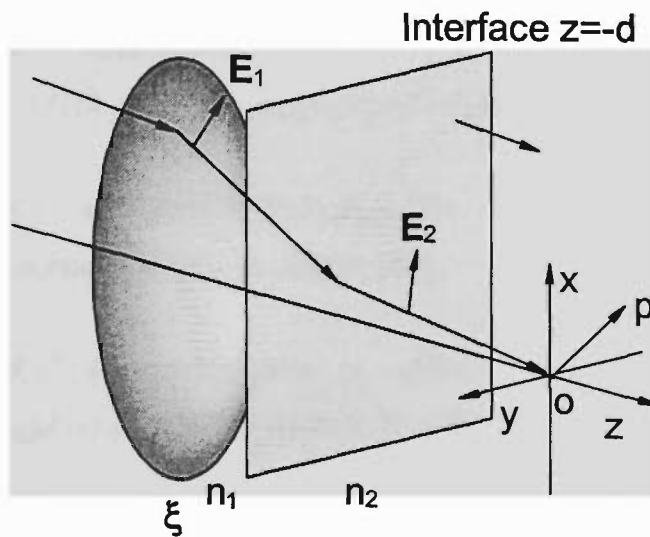


Fig. 2.16 Diagram showing light focused by a lens into two media separated by a planar interface (after Török *et al.*, 1995).

Consider an incident beam is focused by an aberration free lens into a second medium with a refractive index  $n_2$  different from that of the incident medium,  $n_1$  (see Fig. 2.16). The electric fields in the first and second media are represented by  $E_1$  and  $E_2$ , respectively. By applying the Fresnel refraction law and boundary conditions to the interface separating the two media and assuming that the resulting field is constructed as a superposition of refracted plane waves, one can express the electric field components at position  $p$  ( $r_p$ ,  $\theta_p$ ,  $\phi_p$ ) in the second medium as a combination of a set of three integrals,  $I_0$ ,  $I_1$  and  $I_2$  [Török *et al.*, 1995]:

$$\begin{cases} e_{2x} = -iK[I_0 + I_2 \cos(2\theta_p)], \\ e_{2y} = -iKI_2 \sin(2\theta_p), \\ e_{2z} = -2KI_1 \cos\theta_p, \end{cases} \quad (2.11)$$

where  $K = \frac{\pi n_2^2 f l_0}{\lambda}$ ,  $f$  is the focal length of the objective, and  $l_0$  is an amplitude factor.

For a plane-polarised wave, the integrals  $I_0$ ,  $I_1$  and  $I_2$  can be described as [Török *et al.*, 1995]

$$\begin{aligned} I_0 &= \int_0^{\alpha_c} (\cos\theta_1)^{1/2} \sin\theta_1 \exp[ik_0 \Psi(\theta_1, \theta_2, -d)] \times \\ &(\tau_s + \tau_p \cos\theta_2) J_0(k_0 n_1 r \sin\theta_1) \exp(ik_0 n_2 z \cos\theta_2) d\theta_1, \\ I_1 &= \int_0^{\alpha_c} (\cos\theta_1)^{1/2} \sin\theta_1 \exp[ik_0 \Psi(\theta_1, \theta_2, -d)] \times \\ &\tau_p \sin\theta_2 J_1(k_0 n_1 r \sin\theta_1) \exp(ik_0 n_2 z \cos\theta_2) d\theta_1, \\ I_2 &= \int_0^{\alpha_c} (\cos\theta_1)^{1/2} \sin\theta_1 \exp[ik_0 \Psi(\theta_1, \theta_2, -d)] \times \\ &(\tau_s - \tau_p \cos\theta_2) J_2(k_0 n_1 r \sin\theta_1) \exp(ik_0 n_2 z \cos\theta_2) d\theta_1, \end{aligned} \quad (2.12)$$

where  $J_m$  ( $m = 0, 1, 2$ ) is the Bessel function of the first kind, of order  $m$ ,  $k_0$  is the wave number in free space,  $\alpha_c$  is the maximum convergence angle of an objective,  $\theta_1$  and  $\theta_2$  are the incident and the refractive angles in the first and second media, respectively, and  $\tau_s$  and  $\tau_p$  are the Fresnel coefficients for s and p polarisation states. The term  $(\cos\theta_1)^{1/2}$  in each integrand corresponds to the apodization function under the sine condition. The aberration function can be expressed as [Török *et al.*, 1995]

$$\Psi(\theta_1, \theta_2, -d) = -d(n_1 \cos\theta_1 - n_2 \cos\theta_2). \quad (2.13)$$

In the presence of spherical aberration, the intensity distribution in the focal region of a microscope objective becomes broad in both the axial and transverse directions [Török *et al.*, 1996; Sheppard and Török, 1997]. As a result, the laser power

exerted on a particle is attenuated and the trapping performance becomes poor (see section 3.3).

#### 2.4.2.2.3 Compensation for spherical aberration by a change in tube length

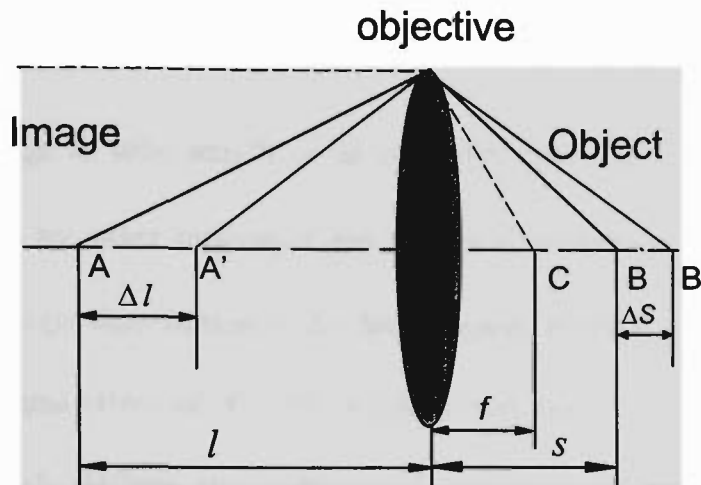


**Fig. 2.17** Tube length  $\overline{AB}$  of an objective.  $l$  and  $s$  are the conjugate distances in image space and object space of the objective, respectively. A change in tube length  $\Delta l$  (from  $A$  to  $A'$ ) produces a shift  $\Delta s$  (from  $B$  to  $B'$ ) in the axial direction. For an objective of a focal length  $f$  used for confocal microscopy, the tube length is  $\infty$  as illustrated by the dashed lines.

As pointed out by Sheppard and Gu [Sheppard and Gu, 1992], the effect of spherical aberration induced by the refractive-index mismatch between two media of different refractive indices can be compensated for by changing the tube length of an objective. The tube length of an objective is defined as the distance  $\overline{AB}$  between an object and its image, where  $l$  and  $s$  are the conjugate distances in image space and object space of the objective, respectively (see Fig. 2.17). For a commercial microscope objective and an objective used for confocal microscopy, the tube length is designed to be 160 mm and infinity, respectively.

The spherical aberration  $\Psi'$  induced by altering the tube length can be expressed as

$$\Psi'(\theta_1) = B \sin^4(\theta_1/2), \quad (2.14)$$

for an objective obeying the sine condition [Sheppard and Gu, 1993]. Here

$$B = -\frac{2k_0 s^2 \Delta l}{l^2}, \quad (2.15)$$

where  $\Delta l$  is the change in tube length of an objective (see Fig. 2.17). Both spherical aberration  $\Psi$  induced by index mismatch and spherical aberration  $\Psi'$  induced by tube length change affect light distribution in the focal region. If the sign of  $\Psi'$  is chosen in such a way that the total effect of  $\Psi + \Psi'$  is minimised, the 3D intensity-point-spread-function (IPSF) which defines the intensity distribution in the focal region of a microscope objective for an ideal point object, can be improved [Sheppard and Gu, 1992]. Because trapping force is dependent on the optical power exerted on a particle, the value of  $B$  can be chosen when the peak intensity of the 3D IPSF reaches the maximum value in the presence of  $\Psi + \Psi'$ , which is called the compensation condition. This method provides useful guidance for the improvement of trapping efficiency and consequently image quality of particle-trapped NSOM (see section 3.3).

#### 2.4.2.3 Effect of Brownian motion

In addition to the light distribution in the focal region of a trapping objective, the performance of laser trapping is also affected by the random movement of a particle in a solution. It is known from statistical physics that for a body immersed in gases, liquids, or solids, random collisions exist between the foreign body and the molecules of the surrounding medium [Besancon, 1974]. This phenomenon, termed as the Brownian motion, can be estimated based on the equi-partition law as [Besancon, 1974]

$$1/2m\bar{v}^2 = 3/2k_B T_a, \quad (2.16)$$

where  $m$  is the mass of the particle,  $k_B$  is the Boltzmann constant,  $T_a$  is the absolute temperature of the surrounding medium, and  $\bar{v}$  is the root-mean-square velocity of the particle.

For a particle trapped in an aqueous solution, the Brownian motion tends to destabilise trapping performance. As a result, a trapped particle is oscillating from the balancing point of a trapping potential well similar to an object attached to a spring. The spring constant  $k_s$  of an optical trap can be estimated as [Higurashi *et al.*, 1999]

$$1/2k_s \langle x_n^2 \rangle = 1/2k_B T_a, \quad (2.17)$$

where  $x_n$  is the dynamic position of the trapped particle. For example for dielectric particles of 0.6  $\mu\text{m}$  to 10  $\mu\text{m}$  in diameters, the lateral spring constant was measured to be in the range from  $10^{-5}$  N/m to  $10^{-3}$  N/m [Kuo and Sheetz, 1993; Svobada *et al.*, 1993; Masuhara *et al.*, 1994; Sasaki *et al.*, 1997]. The lateral trapping potential exerted on a dielectric particle follows a parabolic function, while the longitudinal trapping potential is more complicated dependent on the optical power of a trapping laser beam [Sasaki *et al.*, 1997]. The magnitude of the Brownian motion of a trapped particle is usually in the order of tens of nanometres, and can be suppressed by choosing less absorbing solutions or increasing trapping power. Clearly, the Brownian motion is detrimental to laser trapping and should be minimised for the applications of particle-trapped NSOM.

### 2.4.3 Laser trapping of metallic particles

In this section, we extend our introduction on laser trapping to the subject of laser trapping of metallic particles considering its significance for our research. It was

believed that trapping of a metallic particle can only be achieved for high refractive particles [Sato *et al.*, 1994]. However, it was demonstrated recently that iron, gold (Rayleigh), and gold and silver (Mie) particles can be trapped with a scanned or a fixed single Gaussian laser beam [Sasaki *et al.*, 1992; Sato *et al.*, 1994; Svoboda and Block, 1994]. The key to their successes lies in avoiding the repulsive (scattering) force and maximising the attractive force for a metallic particle by manipulating the scanning modes or the focal positions of trapping laser beams.

In comparison with the theoretical work on trapping force on dielectric particles, the theoretical treatment on trapping force on metallic particles is not comprehensive. Generally speaking, trapping force on metallic particles has been evaluated using the RO model [Sato, 1995] and EM wave theory [Furukawa and Yamaguchi, 1998]. In particular, the RO model has been employed for the evaluation of the trapping force on metallic Mie particles [Sato, 1995]. The multiple-reflection by the inner surface of a metallic particle has been considered for the expression of trapping force. This treatment may not be necessarily true for metallic Mie particles because their skin depths are only of several or tens of nanometres [Born and Wolf, 1997].

To gain an overview on the current status of research on laser trapping of metallic particles, the representative experiments are listed in Table 2.1. It has been demonstrated that a metallic Rayleigh particle can be trapped in 3D with a  $TEM_{00}$  mode laser beam [Svoboda and Block, 1994; Sugiura *et al.*, 1997], while a metallic Mie particle can only be trapped in 2D with a  $TEM_{00}$  mode or a  $TEM_{01}^*$  mode laser beam [Sato *et al.*, 1994; Furukawa and Yamaguchi, 1998].

**Table 2.1** Important experiments on laser trapping of metallic particles

Who	Particle	Trapping Laser	Objective
Sasaki <i>et al.</i> , 1992	iron particles	Caged TEM <sub>00</sub> mode beam from a Nd <sup>3+</sup> : YAG laser of 145 mW, $\lambda=1064$ nm	Oil-immersion
Svoboda and Block, 1994	$\phi=36$ nm gold particles	Polarised TEM <sub>00</sub> mode beam from a Nd: YLF Laser of 2.5 W, $\lambda=1047$ nm	100 $\times$ NA=1.3
Sato <i>et al.</i> , 1994	$\phi=2-5$ $\mu\text{m}$ gold particles, $\phi=2, 3$ $\mu\text{m}$ silver particles, and $\phi=2-15$ $\mu\text{m}$ bronze particles	TEM <sub>00</sub> mode from a Nd <sup>3+</sup> : YAG Laser of 8 mW, $\lambda=1064$ nm	Water-immersion NA=1.2
Sato <i>et al.</i> , 1995	$\phi=38$ nm, and $\phi=2-5$ $\mu\text{m}$ gold particles	TEM <sub>00</sub> or TEM <sub>01</sub> <sup>*</sup> mode from a Nd <sup>3+</sup> : YAG Laser of 30 mW, $\lambda=1064$ nm	Water-immersion NA=1.2
He <i>et al.</i> , 1995	$\phi=10-30$ $\mu\text{m}$ aluminium particles	He-Ne: 633 nm, 7mW, TEM <sub>01</sub> <sup>*</sup>	Oil-immersion

## 2.5 Near-field Mie Scattering

Near-field Mie scattering is a physical process in the imaging of particle-trapped NSOM. The characteristics of the scattered evanescent waves resulting from this process determine signal strength, contrast and resolution of particle-trapped NSOM. In this section, the concept of near-field Mie scattering will be introduced in comparison with that of far-field Mie scattering. Research progress on this topic will be reviewed.

### 2.5.1 Mie scattering and near-field Mie scattering

Solutions to scattering of propagating waves by a spherical particle are generally termed as Mie theory (see Fig. 2.18 (a)). For almost a century, the theory of Mie scattering has been applied extensively to various disciplines including physics, meteorology, chemistry, biochemistry, and astronomy. The formalisms of Mie theory [Born and Wolf, 1997] will not be listed here since they are well known. In particular, when the

particle diameter  $\phi$  is small compared with the wavelength  $\lambda$  of the incident light, i.e., when the dimensionless size parameter  $q = \frac{2\pi n_2}{\lambda} \phi \ll 1$ , Mie scattering reduces to Rayleigh scattering. Here  $n_2$  is the refractive index of the medium surrounding the particle. The interaction of light with a Rayleigh particle can be treated as the interaction of an electric dipole with the incident light [Born and Wolf, 1997].

By comparison, scattering of evanescent waves by a spherical particle is referred to as near-field Mie scattering (see Fig. 2.18 (b)). Near-field Mie scattering was treated for the first time by Chew *et al.* [Chew *et al.*, 1979] in order to attain some guidance to the applications of evanescent wave excitation in Raman spectroscopy. With the recent development of laser trapping technology and near-field optics, research of near-field Mie scattering has become active in analysing optical forces on particles in evanescent wave fields [Almaas and Brevik, 1995; Lester and Nieto-Vesperinas, 1999] and evaluating localised particle-surface interactions [Clapp *et al.*, 1999].

Fig. 2.18 illustrates the schemes of Mie scattering and near-field Mie scattering. The spatial distribution of scattered wave field differs in the two cases resulting from the different characteristics of a plane wave and an evanescent wave. For an evanescent wave, the light intensity decays exponentially along the normal to a boundary, while for a plane wave it remains constant at a particular wavefront. The exponential decay of the evanescent wave above the boundary introduces an asymmetry to the incident field, which results in the presence of certain cross-polarisation components in the scattered field [Chew *et al.*, 1979]. The damping feature of an evanescent wave causes a strong dependence of the strength of scattered evanescent waves on the distance between a

particle and a boundary where an evanescent wave originates. The interaction between a particle and the boundary is not negligible for the scattered field when the distance is small [Lester and Nieto-Vesperinas, 1999; Quinten *et al.*, 1999].

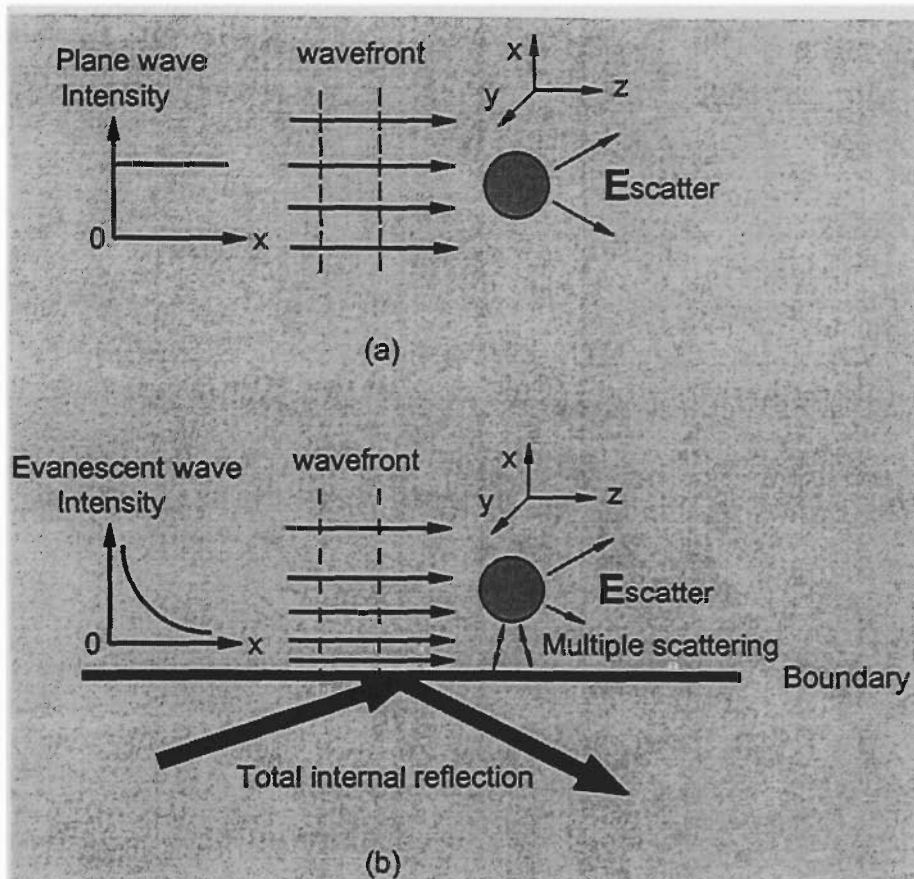


**Fig. 2.18** Schematic diagram for (a) Mie scattering and (b) near-field Mie scattering. The wavefronts of the plane and evanescent waves are illustrated using dashed lines. The distribution of light intensity along the  $x$  direction is shown for the plane and evanescent waves, respectively. In case (b), a beam of light is incident on a boundary separating two different media under the condition of total internal reflection.

## 2.5.2 Theoretical approaches

In this section, the results on near-field Mie scattering obtained with different approaches are described and discussed.

### 2.5.2.1 Multipole expansion method

In the approach of Chew *et al.* [Chew *et al.*, 1979], analytical solutions were provided via the multipole expansion method for the scattered and transmitted fields when a particle is placed in an evanescent wave field. Fig. 2.19 illustrates the system configuration adopted in their approach. Two dielectric media are separated by a plane boundary in the  $y$ - $z$  plane. The refractive indices of the media below and above the boundary are  $n_1$  and  $n_2$  ( $n_1 > n_2$ ), respectively. The incident angle of a plane wave is set at  $\theta > \sin^{-1}(n_2/n_1)$  to generate evanescent waves at the upper surface of the boundary. An isotropic dielectric particle is located at a distance  $\zeta$  away from the boundary. The

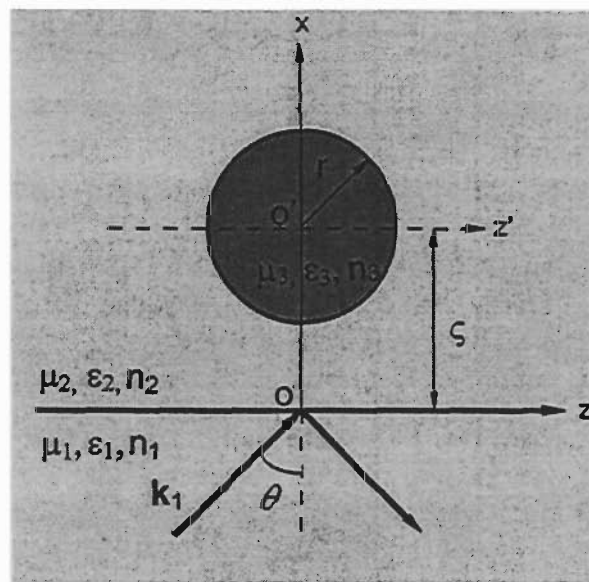


**Fig. 2.19** Propagation of wave  $\mathbf{k}_1$  at incident angle  $\theta$  from a dense medium ( $\mu_1, \epsilon_1, n_1$ ) into a medium ( $\mu_2, \epsilon_2, n_2$ ). A particle ( $\mu_3, \epsilon_3, n_3$ ) with radius  $r$  is located at  $x = \zeta$  in the medium  $n_2$  (after Chew *et al.*, 1979).

distance  $\zeta$  was chosen to be sufficient large so that the particle does not affect the boundary conditions at the plane interface where the evanescent wave is generated, and likewise the plane interface does not perturb the conditions at the surface of the particle.

For an incident wave polarised perpendicular to the plane of incidence, the electric vector of the incident plane wave in the dense medium  $n_1$  can be described as

$$\mathbf{E}_1 = \mathbf{y} \exp(i\mathbf{k}_1 \cdot \mathbf{r}), \quad (2.18)$$

where  $\mathbf{k}_1$  represents the wave vector of the incident plane wave,  $\mathbf{y}$  denotes a unit vector along the  $y$  axis, and  $\mathbf{r}$  is the position vector under inspection. The amplitude of the incident wave is normalised to be unity. Consequently, the electric field in medium  $n_2$  incident on the particle  $(\zeta, 0, 0)$  can be expressed as

$$\mathbf{E}_{inc} = E_{20} \mathbf{y} \exp(i\Lambda z - \Sigma x), \quad (2.19)$$

where  $E_{20}$  is the amplitude of the transmitted wave, and  $\Lambda$  and  $\Sigma$  are expansion coefficients. The first exponential term in Eq. (2.19) represents the propagating property of the field incident on the particle while the second term an evanescent component. It is the second term that causes the differences in Mie scattering and near-field Mie scattering. Once the electric field interacts with a particle, it produces a scattered field as well as a field inside the particle. By expanding the incident field into a series of vector spherical harmonics, one can solve the scattered field and the field inside the particle based on Maxwell boundary conditions [Chew *et al.*, 1979]. The scattered electric field for an incident wave polarised in the plane of incidence can be worked out using the same procedures.

The results by Chew *et al.* show a distinctive difference between near-field Mie scattering and far-field Mie scattering which is the cross-polarisation that occurs in the former case. This is because the damping factor of the incident evanescent wave on the particle, as represented by the second exponential term in Eq. (2.19), destroys the axial symmetry that determines the absence of cross-polarisation in far-field Mie scattering.

The intensity of the spin-flip component induced by cross-polarisation is comparable, in magnitude, to the other component in certain angular ranges [Chew *et al.*, 1979].

### 2.5.2.2 Multiple multipole (MMP) method

Very recently, Quinten and Wannemacher *et al.* investigated the scattering, absorption, and extinction cross-section spectra for dielectric and metallic particles illuminated with evanescent waves [Quinten *et al.*, 1999; Wannemacher *et al.*, 1999a; 1999b] using the multipole expansion method and the multiple multipole (MMP) method [Hafner, 1990]. The cross-sections for scattering and absorption are defined by normalising the scattered or absorbed power with respect to the total power incident on the particle. Accordingly, the extinction cross-section is defined as a sum of the scattering and absorbing cross-sections. The effect of multiple scattering between a particle and a boundary where an evanescent wave is originated was considered in their MMP approach.

The MMP calculations indicate that the p- and s-polarised scattering spectra in the case of evanescent waves differ from those in the case of a plane wave excitation due to the inherent asymmetry of both polarisation states. Furthermore, for a silver particle, the contributions from multipoles of high orders are strongly enhanced, compared with the plane wave excitation, and the enhancement factors are polarisation dependent. The corresponding changes in the scattering and extinction spectra are most pronounced when multipoles of high orders exhibit resonances for the spectral range (0-1000 nm) considered in their approach [Quinten *et al.*, 1999].

### 2.5.2.3 Discussion

In the later work by Liu *et al.* [Liu *et al.*, 1995], the expansion coefficients derived by Chew *et al.* were rectified. In addition to the multipole expansion method, the group-theory method based on the transformation of coordinate systems [Pendleton, 1982] was also adopted for calculating the scattered field for near-field Mie scattering [Zvyagin and Goto, 1998]. Both methods give the same results.

Compared with the results calculated using the multipole expansion method without considering multiple scattering, the results obtained using the MMP method with the inclusion of multiple scattering are significantly different, particle resonances are generally broadened, damped and slightly red-shifted due to multiple scattering [Quinten *et al.*, 1999].

In particle-trapped NSOM, a particle probe is trapped in touch with a sample. Therefore the interactions (multiple scattering) between the particle and an evanescent wave originated from the sample are not negligible [Lester and Nieto-Vesperinas, 1999; Quinten *et al.*, 1999]. In this sense, the MMP approach by Quinten and Wannemacher *et al.* should be advantageous for the characterisation of near-field Mie scattering in particle-trapped NSOM.

### 2.5.3 Experiments on near-field Mie scattering

The experimental characterisation of scattered evanescent waves is not extensive [Prieve and Walz, 1993]. In the experiment by Prieve and Walz, it was found that the dependence of the strength of scattered evanescent waves on the size of dielectric

particles ( $\phi = 7 - 30 \mu\text{m}$ ) is almost linear rather than "radius squared" as followed by Mie scattering under plane wave illumination [Prieve and Walz, 1993; Born and Wolf, 1997]. However, the range of the particle size used in their experiment is beyond the interest of particle-trapped NSOM.

## **2.6 Summary**

In this chapter, we have reviewed the development and principle of NSOM. In particular, we have discussed imaging mechanisms and special features of particle-trapped NOSM utilised in our study. To understand the principle of this technique, detailed introductions to laser trapping and near-field Mie scattering have been given. The information in this chapter has provided instrumental and physical foundations for the investigation into particle-trapped NSOM, which is necessary for comprehending the philosophy of this thesis.

## CHAPTER THREE

# Laser Trapping with a High Numerical-Aperture Objective

### 3.1 Introduction

IT has been known from Chapter 2 that the key component in particle-trapped near-field scanning optical microscopy (NSOM) is a high numerical aperture (NA) microscope objective that focuses a laser beam to form a diffraction limited spot. Laser trapping of a particle probe is obtained in the focal region of the objective, where intensity gradient is usually a maximal. To improve the trapping performance and therefore image quality of particle-trapped NSOM, it is necessary to investigate the light distribution in the focal region of a high NA trapping objective.

In this chapter, several issues discussed in section 2.4.2.2 will be addressed for the applications of laser trapping involving a high NA microscope objective. These issues are apodization of an objective and spherical aberration induced by refractive-index mismatch. Specifically, the effect of the sine condition obeyed by a high NA objective [Ignatowsky, 1919; Richards and Wolf, 1959; Stannnes, 1986; Sheppard and Gu, 1993; Born and Wolf, 1997; Gu, 1999], and the influence of spherical aberration [Török *et al.*, 1995] on laser trapping are discussed in section 3.2 and section 3.3, respectively. It is also demonstrated that this type of spherical aberration can be partially compensated for by a change in tube length of the objective used for trapping [Sheppard

and Gu, 1991; Sheppard *et al.*, 1994]. Discussions and conclusions on the obtained results are presented in section 3.4 and section 3.5, respectively.

## 3.2 Sine condition obeyed by a trapping objective

In this section, the issue of apodization of a high NA objective will be addressed by investigating the effect of the sine condition on trapping force generated [Gu *et al.*, 1997]. The sine condition is obeyed by a high NA objective to perform lateral space-invariant imaging [Born and Wolf, 1997; Gu, 1999]. Our investigation into this topic is based on a comparison of the trapping efficiency between the sine condition and the tangent condition adopted in previous approaches (Ashkin, 1992; refer to section 2.4.2.2.1). To obtain the main property of trapping under the sine condition, the perturbation of a trapped particle to a light field in the focal region of a high NA objective is neglected and only dielectric particles are considered in our treatment. The obtained results are qualitatively applicable to the case of trapping a metallic particle.

### 3.2.1 Axial and transverse trapping forces obeying the sine and tangent conditions

Fig. 3.1 shows the axial trapping efficiency of a particle calculated using Eqs. (2.3)-(2.5) in Chapter 2 as a function of the axial trapping position  $S$ . Here  $Q_a = Q_t = Q_G + Q_S$  (see section 2.4.2.1.1 of Chapter 2 for definitions). The maximum convergence angle of the objective used for trapping is  $70^\circ$  and the particle is trapped with a circularly-polarised uniform beam.

It is clear that the axial trapping efficiency under the sine condition is smaller than that under the tangent condition when the axial trapping position  $|S|$  is approximately less than 1.02. The difference between the two conditions can be up to 50% at the position where the total trapping efficiency is maximal. Outside this axial trapping position, the rays coming from large angles of convergence start missing the particle. Since the trapping force on a dielectric particle is mainly contributed by the gradient force, the axial trapping force experienced by the particle relies more strongly on those rays from large angles of convergence (refer to Fig. 2.8 (b)). For a trapping laser beam of a given power, the ray density at a large angle is lower under the sine condition than that under the tangent condition, leading to the discrepancy of the axial trapping efficiency under the two conditions.

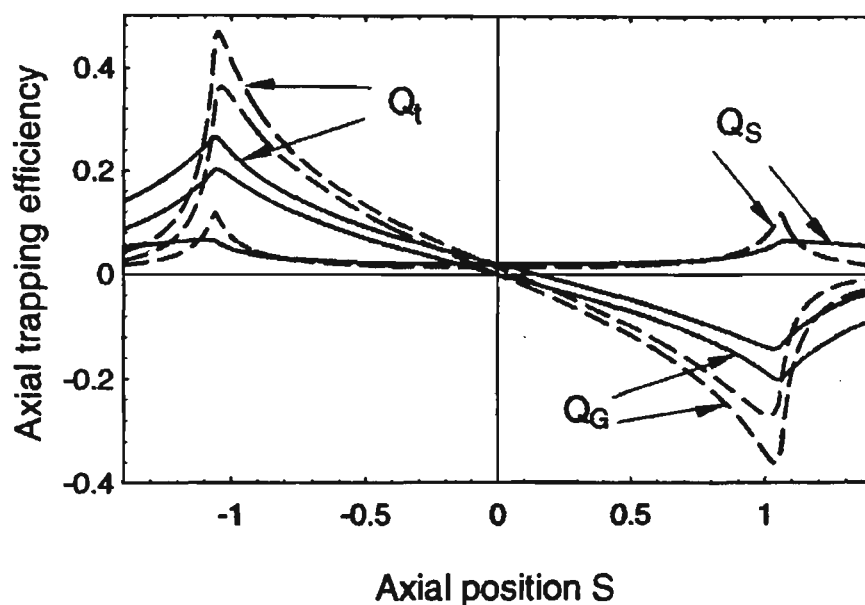


**Fig. 3.1** Axial trapping efficiency as a function of the particle position  $S$  under the illumination of a circularly-polarised uniform beam. The solid curves represent the result with the sine condition, while the dashed curves represent that with the tangent condition.  $Q_t$ ,  $Q_G$ , and  $Q_s$  correspond to the total, gradient, and scattering trapping efficiencies, respectively. The maximum convergence angle of the objective is  $70^\circ$  and the relative refractive index is 1.18.

The light intensity of a Gaussian beam can be expressed as  $I(\rho) = I_0 \exp(-2\rho^2 / w_0^2)$  over the back aperture of an objective (refer to Fig. 2.9 in Chapter 2). Here  $w_0$  is the beam waist. Define a parameter  $a = \frac{w_0}{\rho_{max}}$  for an objective illuminated with a Gaussian beam, where  $\rho_{max}$  is the radius of the objective aperture. Fig. 3.2 illustrates the maximum axial trapping efficiency  $Q_a^m$  calculated using Eqs. (2.3)-(2.5) in Chapter 2 as a function of the NA of the objective for circularly-polarised uniform ( $a = \infty$ ) and Gaussian beam ( $a = 1$ ) illumination. The relative refractive index is 1.18 and the refractive index of the immersion material is 1.33 (water). For both

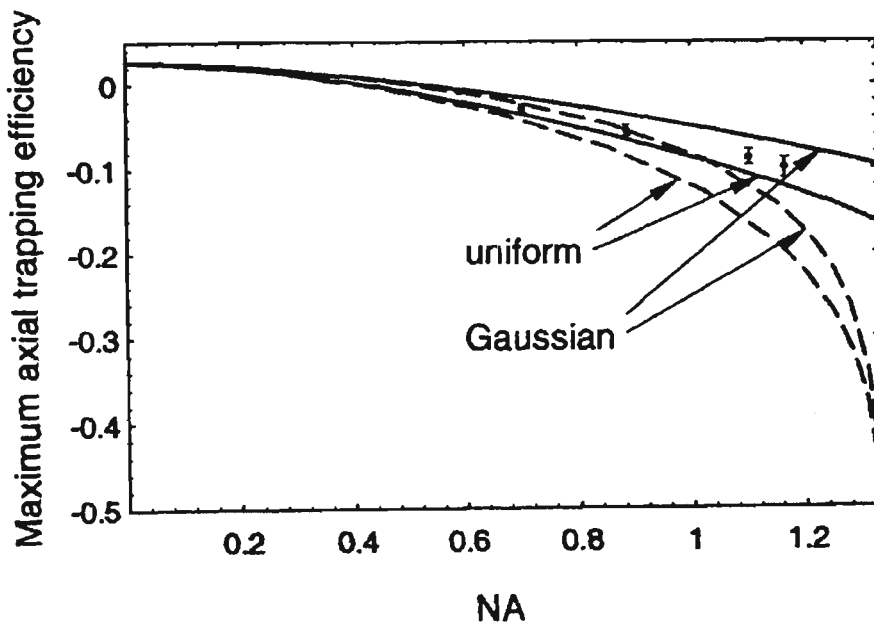
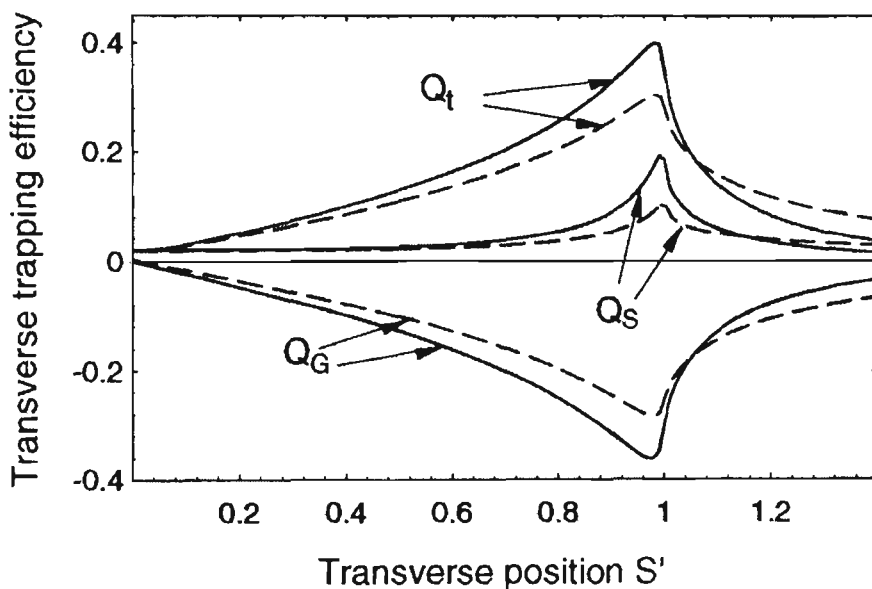


Fig. 3.2 Maximum axial trapping efficiency  $Q_a^m$  as a function of the NA for circularly-polarised uniform and Gaussian beam illumination. For Gaussian beam illumination, the ratio of the beam spot size to the radius of the objective aperture,  $a$ , is assumed to be unity. The solid curves correspond to the sine condition, while the dashed curves satisfy the tangent condition. The relative refractive index is 1.18 and the refractive index of the immersion material is 1.33 (water). The black spots represent the measured values ( $a = 1$ ) of the maximum axial trapping efficiency described by Wright *et al.* [Wright *et al.*, 1994].

uniform and Gaussian beam illumination, when the NA of the objective is low, the difference of the maximum trapping efficiency between the sine and tangent conditions is not significant but it becomes quite pronounced for a high NA objective. In comparison with the measured values of the maximum axial trapping efficiency [Wright *et al.*, 1994], the experimental results fit well the theoretical curves predicted by the sine condition rather than the curves based on the tangent condition, in particular, when the NA is high.



**Fig. 3.3** Transverse trapping efficiency as a function of the particle position  $S'$  under the illumination of a circularly-polarised uniform beam.  $S=0$ ,  $Q_{tr}=Q_G$  and  $Q_a=Q_s$ . The maximum transverse trapping force occurs in the equatorial plane of the particle. The other conditions are the same as those in Fig. 3.1.

A comparison of the transverse trapping efficiency  $Q_{tr}$  (refer to section 2.4.2.1.1 of Chapter 2 for definition) between the sine and tangent conditions is given in Fig. 3.3 for uniform illumination. It is noted that the trapping efficiency under the sine condition is now larger than that under the tangent condition if the transverse trapping position  $S'$  (see Fig. 2.9 of Chapter 2) is approximately less than 1.02. Outside this transverse

trapping position, the rays coming from large angles of convergence start missing the particle. As mentioned above, the trapping force on a dielectric particle is mainly contributed by gradient force. Contrary to the situation as described for the axial trapping efficiency, the transverse trapping force on a dielectric particle relies more strongly on those rays from small angles of convergence (refer to Fig. 2.8 (b)). For a trapping laser beam of a given power, the ray density at a small angle is higher under the sine condition than that under the tangent condition, leading to the discrepancy of the transverse trapping efficiency under the two conditions.

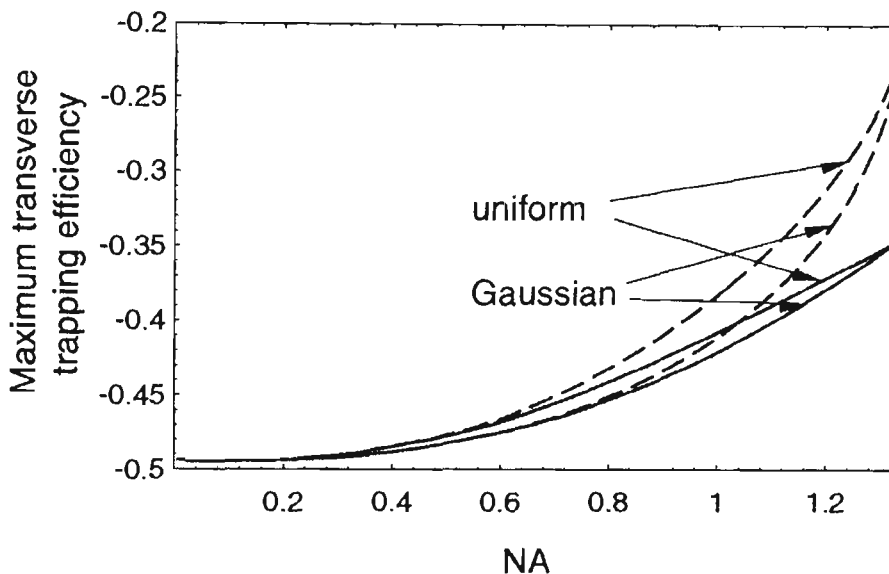


Fig. 3.4 Maximum transverse trapping efficiency  $Q_r^m$  as a function of the NA for circularly-polarised uniform and Gaussian beam illumination.  $S=0$ . The other conditions are the same as those in Fig. 3.2.

The maximum transverse trapping efficiency as a function of the NA for circularly-polarised uniform and Gaussian beam illumination is illustrated in Fig. 3.4. As expected, the difference of the maximum transverse trapping efficiency between the sine and tangent conditions becomes pronounced for a high NA objective. For example, when  $NA = 1.2$ , the absolute value of the maximum trapping efficiency for the sine

condition is approximately 23% larger than that for the tangent condition. Although Wright *et al.* [Wright *et al.*, 1994] reported the measured transverse trapping efficiency for different values of the NA, it is difficult to compare Fig. 3.4 directly with their results. This is because the maximum transverse trapping efficiency was measured when a particle was trapped at a position where the net axial force was zero and the information of this axial position was not given. Nevertheless, in view of the fact that the measured transverse trapping efficiency is larger than that given by the tangent condition, using the sine condition does give the maximum transverse trapping efficiency larger than that predicted by the tangent condition [Gu *et al.*, 1997].

Since the maximum transverse trapping efficiency decreases with the NA for a dielectric particle, the contribution to transverse trapping force by those rays at larger angles of convergence is less significant. Therefore the values of the transverse trapping forces generated with uniform and Gaussian beams approach an equal number when the NA is sufficiently large as shown in Fig. 3.4.

For the applications of laser trapping such as particle-trapped NSOM, it is useful to identify the trapping positions corresponding to the maximum transverse and axial trapping forces. It is found that while  $S_{max}'$  corresponding to the maximum transverse trapping force does not vary significantly with the illumination modes and the NA of a trapping objective under both the sine and the tangent conditions ( $S_{max}'$  is close to the surface of the central equatorial plane of a particle). However,  $S_{max}$  corresponding to the maximum axial trapping force changes dramatically with the NA of a trapping objective but the difference of  $S_{max}$  between the sine and the tangent conditions is negligible (Fig. 3.5).

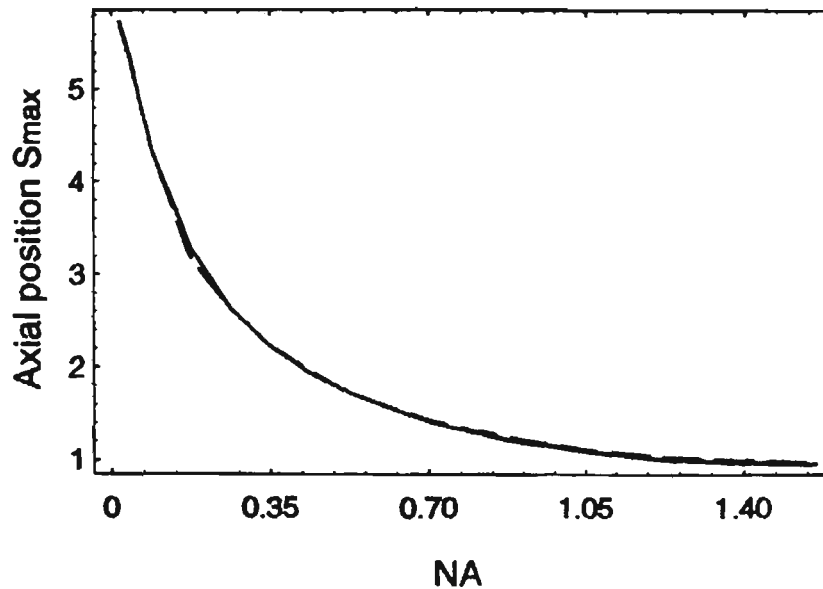


**Fig. 3.5** Axial trapping position  $S_{\max}$  corresponding to the maximum axial trapping force as a function of the NA of a trapping objective for the sine (solid line) and the tangent (dashed line) conditions. Assume that the trapping laser beam is uniform and circularly-polarised. The other conditions are the same as those in Fig. 3.1.

### 3.2.2 Conclusion

In conclusion, the maximum axial and transverse trapping efficiencies for an objective obeying the sine condition are, respectively, smaller and larger than those for an objective obeying the tangent condition. The calculated axial trapping efficiency under the sine condition agrees well with the reported experimental data. Although the discussion in this chapter is restricted to the RO model for large-sized particles, the sine condition also holds in the EM wave model for trapping of small-sized particles if a high NA objective is employed. This effect should also be included when a metallic particle is considered.

### 3.3 Trapping force in the presence of spherical aberration caused by refractive-index mismatch

A common problem in the applications of laser trapping including particle-trapped NSOM is the poor trapping performance when a trapping beam is focused deeply into a medium in which particles are suspended. This degradation of trapping performance is due to spherical aberration caused by refractive-index mismatch between a cover slip and a medium (e.g., water solution) where a particle is suspended (see section 2.4.2.2 or Török *et al.*, 1995). Though noticed [Wright *et al.*, 1994; Felgner *et al.*, 1995], the impact of spherical aberration on trapping force has not been thoroughly investigated. This section is therefore aimed at investigating the effect of spherical aberration induced by refractive-index mismatch on trapping performance and compensating for spherical aberration in terms of a change in tube length of a trapping objective [Ke and Gu, 1998a]. Only transverse trapping force is considered in our treatment since our imaging scheme of particle-trapped NSOM is restricted to 2D.

#### 3.3.1 Experiment

The experimental setup for measuring spherical aberration is illustrated in Fig. 3.6. A linearly-polarised He-Ne laser of output power 17 mW was used as the trapping laser source. This laser beam was expanded and collimated to a size of 20 mm by objective 1 ( $40\times$ , NA = 0.65) and lens 1 ( $f = 100$  mm), respectively. A diaphragm was then used to control the diameter of the collimated beam. Lens 2 ( $f = 400$  mm) was placed after the diaphragm and focused the laser beam to a point  $b$  as shown in Fig. 3.6 after the beam being reflected by mirrors 1 and 2. The laser beam was then sent into a commercial microscope, and reflected downwards by a beam splitter, and re-focused

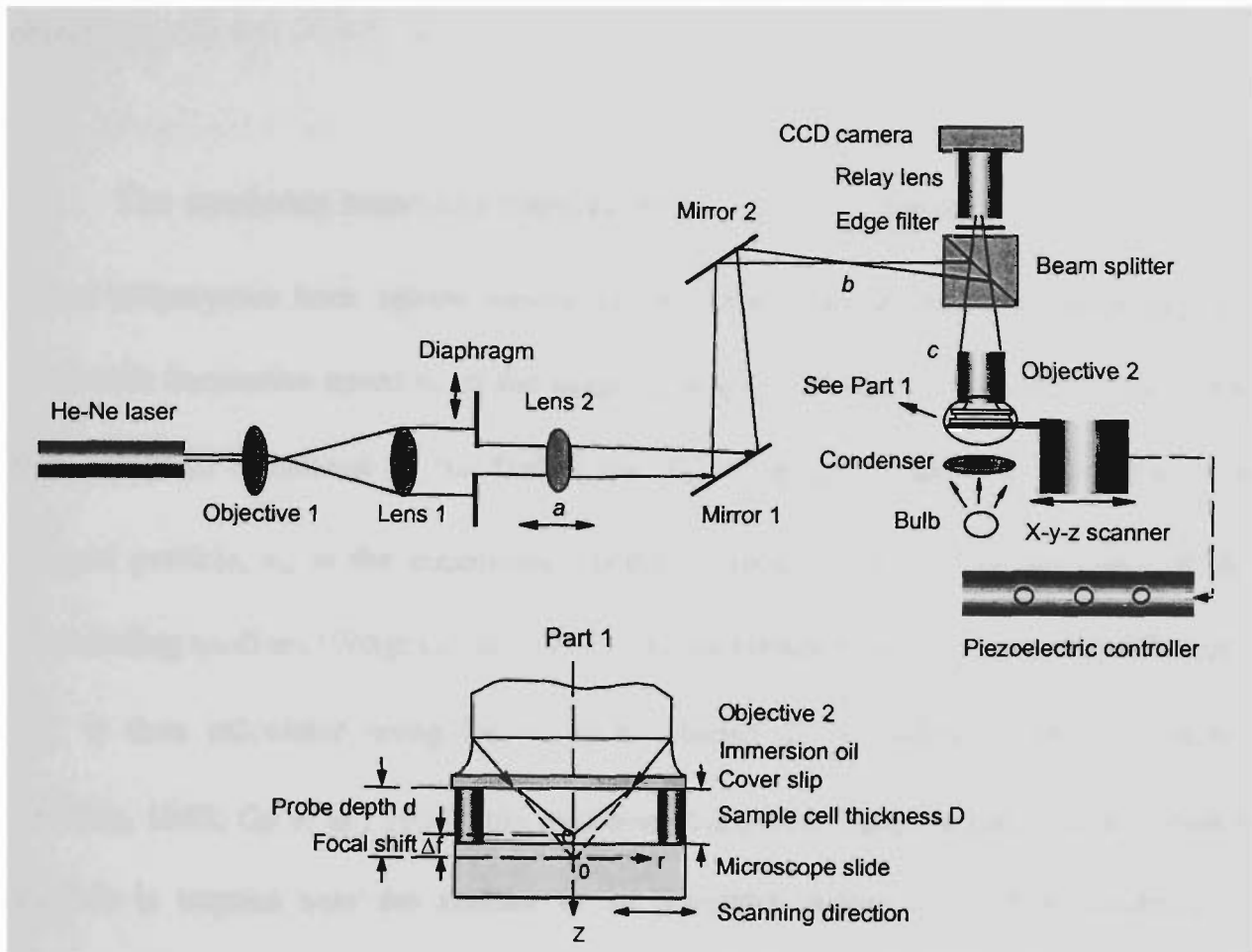


Fig. 3.6 Schematic diagram of a system used for laser trapping. Lens 2 is mounted on a translation stage, and the position of lens 2 determines the effective tube length  $\overline{bc}$  of objective 2.

into a sample cell by microscope objective 2 (oil-immersion,  $100\times$ ,  $NA = 1.25$ ). The tube length  $\overline{bc}$  of objective 2 is designed to be 160 mm. The detailed structure of a sample cell is illustrated in part 1 of Fig. 3.6 which consists of a stretched double-sided tape sandwiched between a cover slip and a microscope slide. A long-pass edge filter was inserted between the beam splitter and a relay lens to block the trapping laser beam, and a CCD camera in conjunction with a computer monitor was used to view a trapping process in real-time. The sample cell was translated by a piezo-driven scanning stage in parallel with the polarisation direction of the laser beam. The trapping power was determined by the power over the entrance aperture  $c$  of the microscope objective,

multiplied by a factor of 81% that was the measured transmittance of the trapping objective.

The maximum transverse trapping force  $F_{tr}^m$  on a trapped particle ( $\phi = 1.893$   $\mu\text{m}$ , a polystyrene latex sphere suspended in water) was measured by searching the maximum translation speed  $v_m$  of the scanning stage at which the particle fell out of the trap, and then calculated by the Stokes law  $F_{tr}^m = 6\pi r v_m \xi$ , where  $r$  is the radius of a trapped particle,  $v_m$  is the maximum translation speed, and  $\xi$  is the viscosity of the surrounding medium [Wright *et al.*, 1994]. The maximum transverse trapping efficiency  $Q_{tr}^m$  is then calculated using Eq. (2.5) in Chapter 2. According to the RO model [Ashkin, 1992; Gu *et al.*, 1997], the maximum transverse trapping force occurs when a particle is trapped near the surface in its equatorial plane. Under this condition, a trapped particle on the computer monitor appeared to be sharp and identical to those adjacent non-moving untrapped particles, and therefore they were in the same focal plane of the trapping objective. To reach this trapping position, the slide in the focal plane of the trapping objective was moved downward by a distance equal to the particle radius. Thus the trapping position was in the central equatorial plane of the trapped particle.

The total transverse force experienced by a laser-trapped particle is determined by the transverse trapping force and the friction between the particle and a microscope slide. The friction is a product of the total axial force, which is a vectorial sum of the gravity, the buoyant force, and the axial trapping force exerted on a trapped particle, and the sliding friction coefficient. For a dielectric particle on a glass slide, the sliding

friction coefficient is between 0.1 to 0.15 [Besancon, 1974]. As a result, the friction for a trapped polystyrene particle of diameter  $\phi = 1.893 \mu\text{m}$  was less than 0.075 pN. A drop of Triton-X100 solution was added to the sample cell to reduce the friction further. The total friction was approximately two orders of magnitude smaller than the maximum transverse trapping force (about 1 pN) and thus negligible.

The effect of spherical aberration induced by the refractive-index mismatch between the cover slip ( $n_1 = 1.5$ ) and the water solution ( $n_2 = 1.33$ ) is affected not only by the thickness of a sample cell  $D$ , but also by the NA of the microscope objective used for trapping. The effective NA of the objective 2,  $\text{NA}'$ , was evaluated by the relation  $\text{NA}' = 1.25 \times \phi_2 / \phi_1$ , where  $\phi_1$  corresponds to the diameter of the diaphragm when the trapping laser beam just fills the aperture of the objective, and  $\phi_2$  is the reduced diameter of the diaphragm.

The measured transverse trapping efficiency as a function of  $\text{NA}'$  for different values of the sample cell thickness  $D$  is shown in Fig. 3.7. For a given value of  $D$ , the transverse trapping efficiency decreases when  $\text{NA}'$  becomes large. This is due to the smaller projection of the gradient force on the transverse direction for an objective of a larger NA [Ashkin, 1992; Gu *et al.*, 1997]. When the thickness of the sample cell increases from 34  $\mu\text{m}$  to 94  $\mu\text{m}$ , the trapping efficiency drops by 25.5% and 66% for  $\text{NA}' = 0.6$  and  $\text{NA}' = 1.25$ , respectively. This reduction of the trapping efficiency is caused by the spherical aberration resulting from the refractive-index mismatch between the cover slip and the water solution. To increase the transverse trapping force of a dielectric particle, one can use an objective of a small NA, or reduce the thickness of a

sample cell. However, these methods will restrict signal level in particle-trapped NSOM and the depth of manipulation inside a biological medium [Sato and Inaba, 1996].

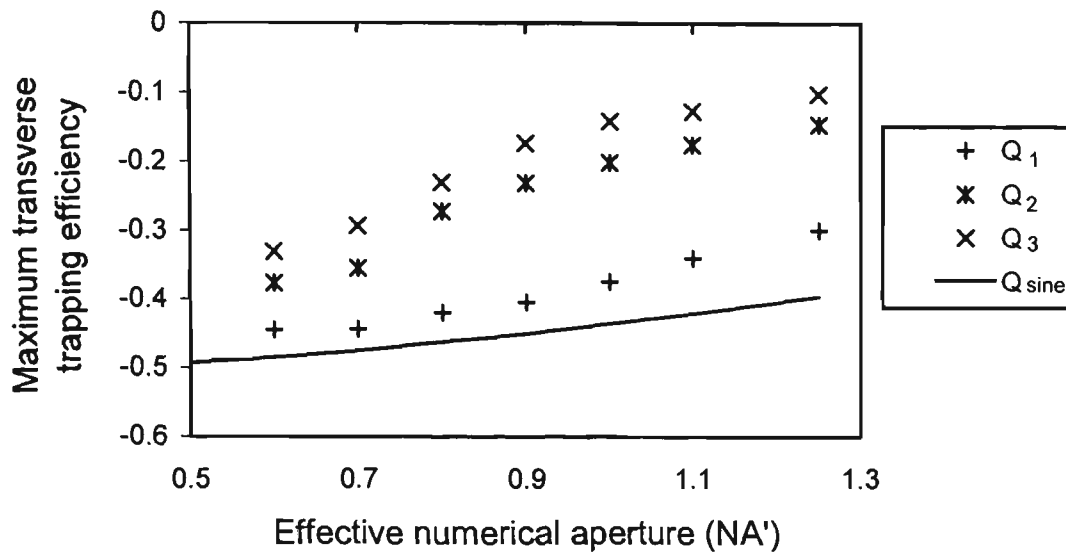


**Fig. 3.7** Maximum transverse trapping efficiency as a function of  $NA'$  for different values of the sample cell thickness  $D$ .  $Q_1$ ,  $Q_2$ , and  $Q_3$  correspond to the maximum transverse trapping efficiencies for  $D=34$   $\mu\text{m}$ ,  $60$   $\mu\text{m}$  and  $94$   $\mu\text{m}$ , respectively.  $Q_{\text{sine}}$  is the theoretical prediction by the RO model under the sine condition.

To improve the transverse trapping efficiency, we introduced the method for aberration compensation used in confocal microscopy [Sheppard and Gu, 1991; Sheppard *et al.*, 1994], which is based on an alteration of the tube length at which a microscope objective is operated (refer to section 2.4.2.2.3 in Chapter 2). In our experiment, the tube length ( $\bar{bc}$  in Fig. 3.6) of the microscope objective was altered from 160 mm, a designed tube length of objective 2, to 140 mm by changing the position of lens 2. The reduction of the tube length is to compensate for the negative focal shift when light from a first medium (cover slip) enters a second medium (water) of lower refractive index. The measured maximum transverse trapping efficiency is

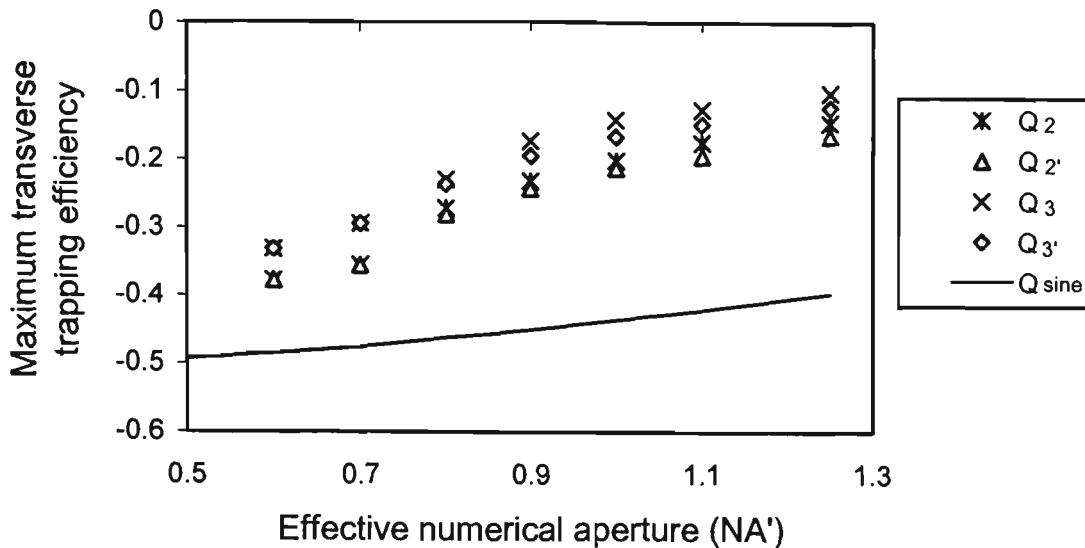


**Fig. 3.8** Maximum transverse trapping efficiency as a function of  $NA'$  for different values of the effective tube length and the sample cell thickness  $D$ .  $Q_2$  and  $Q_3$  correspond to the maximum transverse trapping efficiencies for  $D = 60 \mu\text{m}$  and  $D = 94 \mu\text{m}$  at a tube length of 160 mm,  $Q_2'$  and  $Q_3'$  correspond to the maximum transverse trapping efficiencies for  $D = 60 \mu\text{m}$  and  $D = 94 \mu\text{m}$  at a tube length of 140 mm.  $Q_{\text{sine}}$  is the theoretical prediction by the RO model under the sine condition.

shown in Fig. 3.8. For  $NA'=1.25$ , the improvement in the maximum transverse trapping efficiency for  $D = 34 \mu\text{m}$ ,  $60 \mu\text{m}$  and  $94 \mu\text{m}$  is 6%, 12% and 20%, respectively. A further improvement in the trapping efficiency is possible, as will be discussed in section 3.4.

### 3.3.2 Calculation of light distribution in the focal region

To understand the experimental results, we calculate in this section the diffraction pattern in the focal region of an objective in the presence of spherical aberration caused by refractive-index mismatch. The light distribution over the back aperture of a trapping objective is assumed to follow a Gaussian profile given by  $\exp[-\kappa\rho^2]$ . Here  $\kappa$  is an

attenuation factor of the Gaussian intensity profile and can be determined by the 6% power variation over the objective aperture in the experiment.  $\rho$  is the radial coordinate over the objective aperture, which can be expressed as  $\rho = f \sin \theta$  under the sine condition [Sheppard and Gu, 1993], where  $f$  is the focal length of the objective. Define the cover slip and the water solution as the first and the second medium. For a Gaussian beam which is normally used for trapping, the three-dimensional intensity point spread function (3D IPSF) in the second medium can be evaluated by modifying the first integral of Eq. (2.12) as [Török *et al.*, 1995]

$$I_0 = \int_0^{\alpha_c} \exp[-\kappa \rho^2] (\cos \theta_1)^{1/2} \sin \theta_1 \exp[ik_0 \Psi(\theta_1, \theta_2, -d)] \times (\tau_s + \tau_p \cos \theta_2) J_0(k_0 n_1 r \sin \theta_1) \exp(ik_0 n_2 z \cos \theta_2) d\theta_1. \quad (3.1)$$

Here the term  $(\cos \theta_1)^{1/2}$  is the apodization function of the sine condition obeyed by the objective used for trapping. The depolarisation effect of an objective has been neglected in Eq. (3.1). Compared with the 3D IPSF by the vectorial theory [Török *et al.*, 1995], the peak intensity of the 3D IPSF given by Eq. (3.1) is reduced by approximately 9% when  $d$  increases up to 100  $\mu\text{m}$ , while the full width at half maximum (FWHM) of the 3D IPSF is almost unchanged.

In the experiment, the focus of the laser beam was positioned in the equatorial plane of a trapped particle. Therefore the probe depth  $d$  and the thickness of the sample cell  $D$  should satisfy the following relation:

$$d = D - r - \Delta f \quad (3.2)$$

where  $\Delta f$  is the focal shift of the 3D IPSF as illustrated in part 1 of Fig. 3.6 and is negative in our experiment as the refractive index of the cover slip ( $n_1 = 1.5$ ) is larger than that of the water solution ( $n_2 = 1.33$ ). For the three sample cells used in the

experiment ( $D = 34 \mu\text{m}$ ,  $60 \mu\text{m}$  and  $94 \mu\text{m}$ ), the corresponding probe depth  $d$  is  $39 \mu\text{m}$ ,  $69 \mu\text{m}$  and  $108 \mu\text{m}$ , respectively.

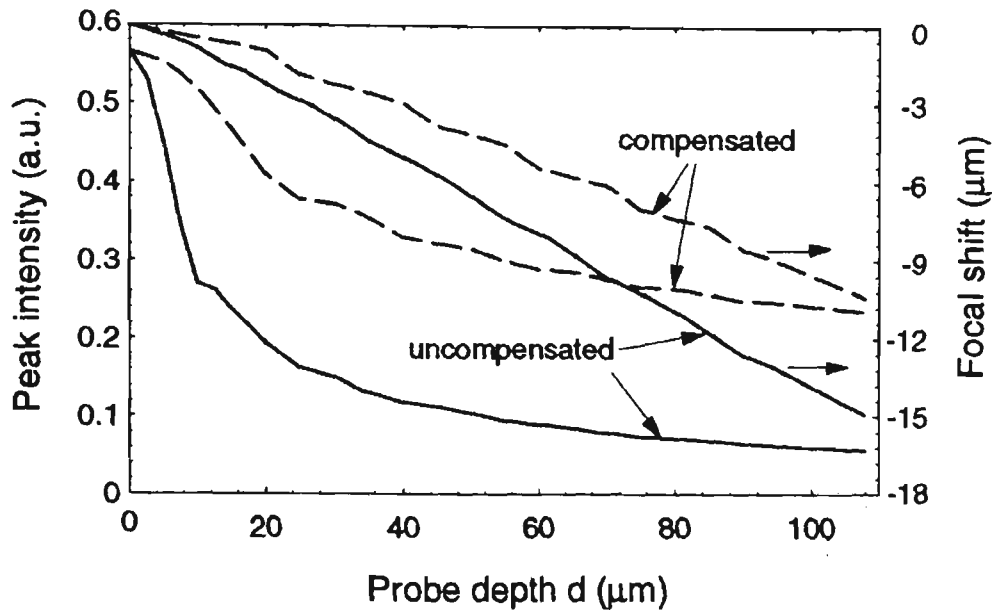


Fig. 3.9 Peak intensity and axial focal shift of the 3D IPSF as a function of the probe depth  $d$  under the uncompensated (solid curves) and compensated (dashed curves) conditions ( $\lambda = 0.633 \mu\text{m}$ ,  $\text{NA}' = 1.25$ ).

When the probe depth  $d$  increases from  $39 \mu\text{m}$  to  $108 \mu\text{m}$ , the peak intensity (a. u.) drops dramatically from 0.1221 to 0.05656 (Fig. 3.9 and Fig. 3.10), and the FWHM of the 3D IPSF along the axial direction,  $\Delta z_{1/2}$ , increases from  $1.86 \mu\text{m}$  to  $3.04 \mu\text{m}$  (Fig. 3.11). When  $d \neq 0$ , the light intensity distribution along the axial direction is no longer symmetric and exhibits a series of strong sidelobes on one side of the main intensity peak (top of Fig. 3.10). The use of the first integral in Eq. (3.1) instead of the three integrals in Eq. (2.12) means that the longitudinal component of the light field is neglected; therefore the diffraction spot becomes circular symmetric.

Compared with the case when  $d = 0$ , the position of the peak light intensity is shifted backwards as illustrated in Fig. 3.10. The FWHM of the 3D IPSF in the

transverse direction,  $\Delta r_{1/2}$ , increases from  $0.346 \mu\text{m}$  to  $0.41 \mu\text{m}$  when the probe depth increases from  $39 \mu\text{m}$  to  $108 \mu\text{m}$ , as shown in Fig. 3.11. It is clear from Figs. 3.9-3.11 that the 3D IPSF in the axial direction is more strongly affected by the aberration effect than that in the transverse direction.

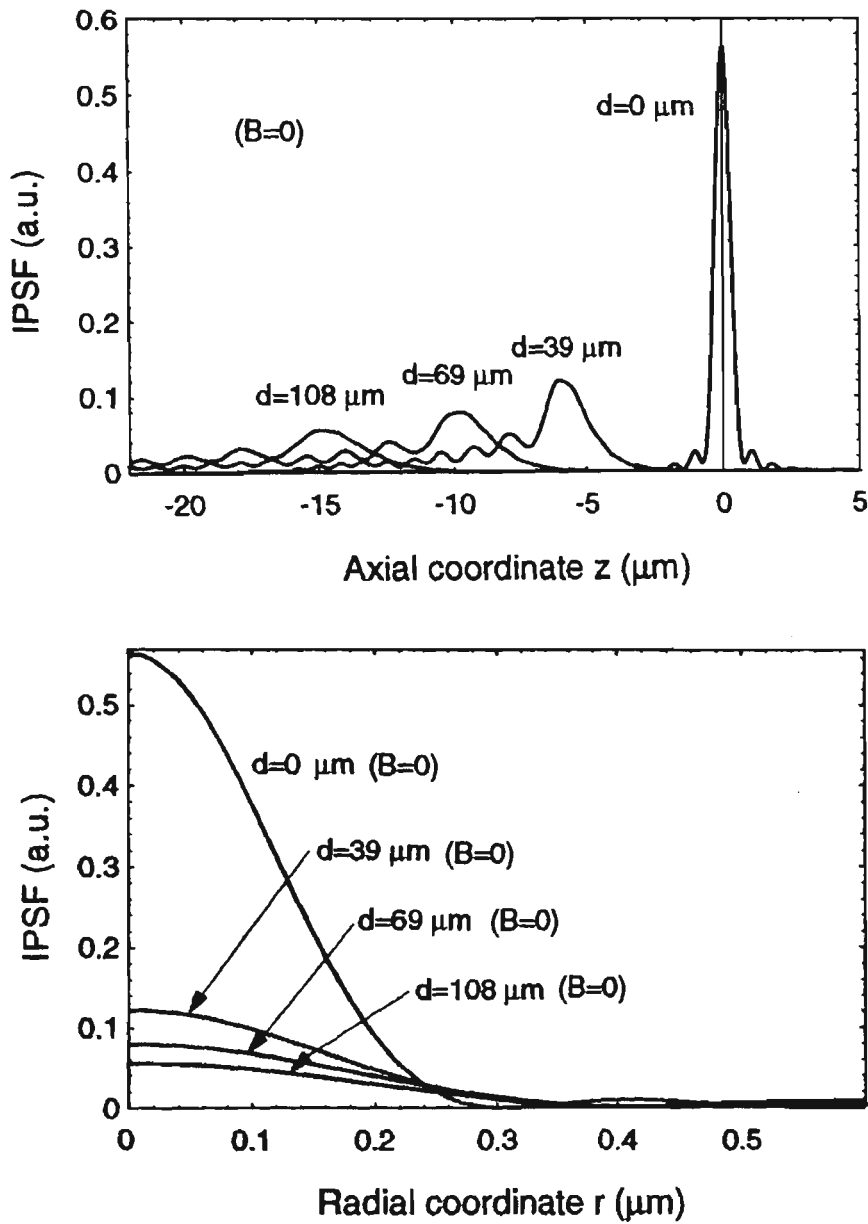


Fig. 3.10 Axial (top) and transverse (bottom) cross-sections of the 3D IPSF for different probe depths under the uncompensated condition ( $\lambda = 0.633 \mu\text{m}$ ,  $\text{NA}' = 1.25$ ).

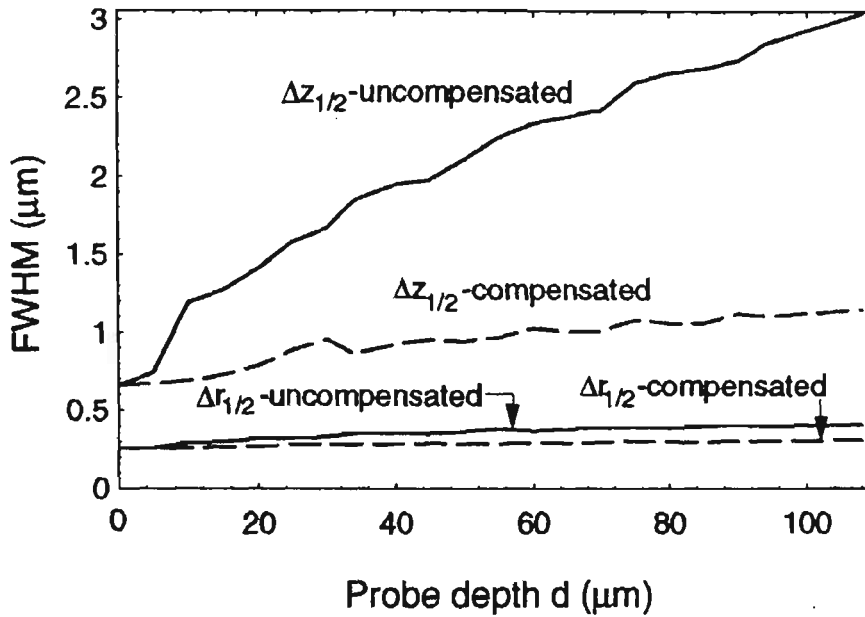


Fig. 3.11 Axial and transverse FWHMs of the 3D IPSF,  $\Delta z_{1/2}$  and  $\Delta r_{1/2}$ , as a function of the probe depth  $d$  under the uncompensated (solid curves) and compensated (dashed curves) conditions ( $\lambda = 0.633 \mu\text{m}$ ,  $\text{NA}' = 1.25$ ).

### 3.3.3 Compensation for spherical aberration in terms of change in tube length

To compensate for the spherical aberration induced by refractive-index mismatch and therefore improve trapping efficiency, we adopt the method of a change in tube length to produce an additional aberration but with a sign opposite to the aberration of refractive-index mismatch. For the three sample conditions as used in our experiment, the probe depth  $d$  [Török *et al.*, 1995] should be chosen to be  $36 \mu\text{m}$ ,  $65 \mu\text{m}$  and  $102 \mu\text{m}$  in order to keep the focus of the laser beam in the equatorial plane of a particle.  $B$  is 815, 1226 and 1812, respectively, under the compensation condition (refer to section 2.4.2.2.3 for definition). The peak light intensity is thus increased from 0.1221 to 0.3505, 0.0801 to 0.2865, and 0.0566 to 0.2390, respectively (Figs. 3.10 and 3.12). Accordingly, the axial FWHM  $\Delta z_{1/2}$  of the 3D IPSF reduces from  $1.86 \mu\text{m}$  to  $0.90 \mu\text{m}$ ,

2.42  $\mu\text{m}$  to 1.006  $\mu\text{m}$ , and 3.04  $\mu\text{m}$  to 1.12  $\mu\text{m}$  (Fig. 3.11). Compared with the uncompensated ( $B = 0$ ) case, the positions of the intensity peak are shifted towards the positive axial direction and the sidelobes of the IPSF in the axial direction become much weaker (Fig. 3.10 and Fig. 3.12).

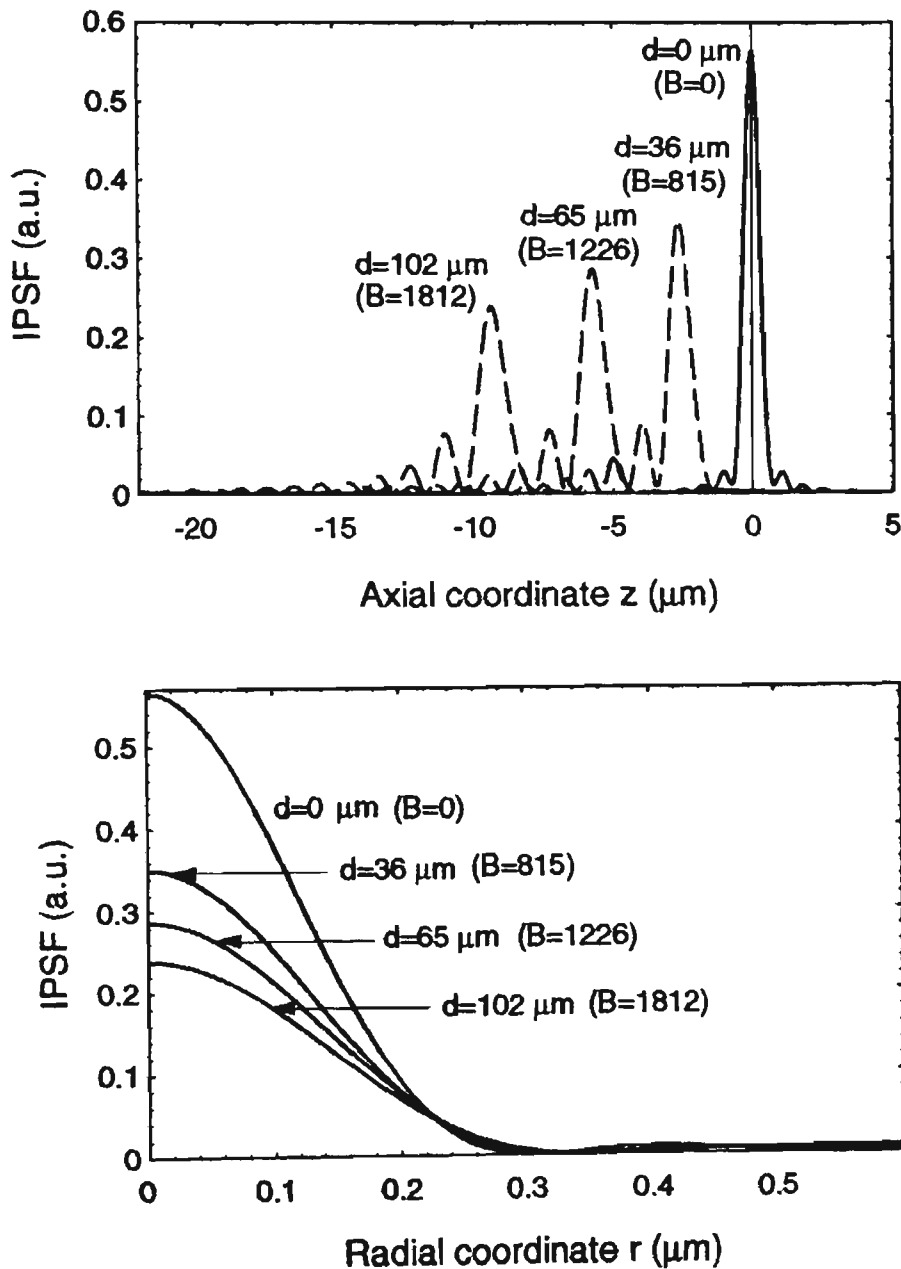


Fig. 3.12 Axial (top) and transverse (bottom) cross-sections of the 3D IPSF for different probe depths under the compensated condition ( $\lambda = 0.633 \mu\text{m}$ ,  $\text{NA}' = 1.25$ ).

### 3.4 Discussion

While trapping force is related to the distribution of the 3D IPSF for an objective according to the EM wave model [Barton *et al.*, 1989], it is directly proportional to the trapping power according to the RO model [Ashkin, 1992]. Based on the 3D IPSF calculated in section 3.3, we can estimate the average trapping power  $P$  on a trapped particle according to the following approximate expression:

$$P = I_m \Delta r_{1/2}^2 \quad (3.3)$$

where  $I_m$  is the peak light intensity at the focus of the objective, and  $\Delta r_{1/2}$  is the transverse FWHM of the 3D IPSF. The average trapping power as a function of the

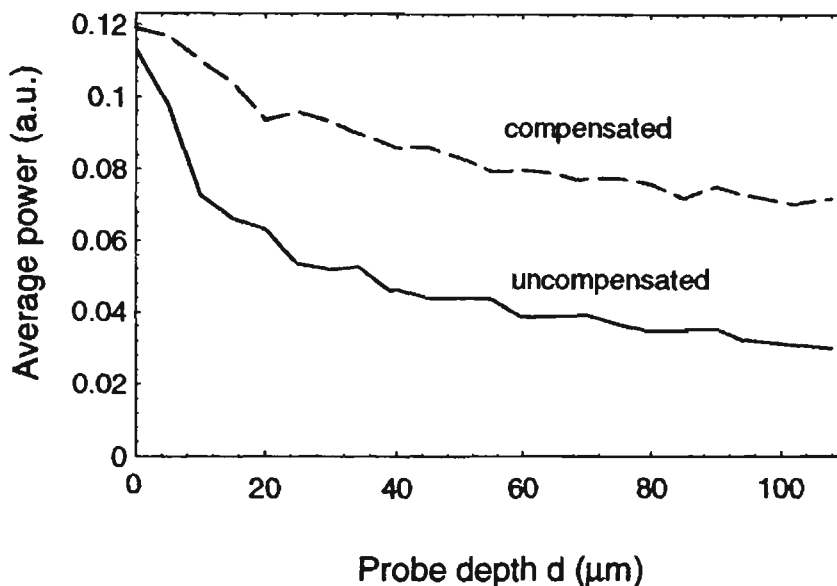


**Fig. 3.13** Average trapping power as a function of the probe depth  $d$  under the uncompensated (solid curve) and compensated (dashed curve) conditions ( $\lambda = 0.633 \mu\text{m}$ ,  $\text{NA}' = 1.25$ ).

probe depth  $d$ , for the uncompensated ( $B = 0$ ) and the compensated ( $B \neq 0$ ) conditions, is illustrated in Fig. 3.13. In particular, the average power under the compensated condition is not constant but decreases with the probe depth, indicating the presence of

high order spherical aberration terms which cannot be completely compensated for by tube length alteration.

Without a change in tube length ( $B = 0$ ), the trapping power (a.u.) drops from 0.0460 to 0.0299 when the probe depth  $d$  increases from 39  $\mu\text{m}$  to 108  $\mu\text{m}$ . After the laser beam penetrates through a sample cell of thickness 34  $\mu\text{m}$ , 60  $\mu\text{m}$  and 94  $\mu\text{m}$ , the average trapping power drops by 59%, 65% and 74%, respectively, while the trapping efficiency is reduced by 25%, 63% and 74% in the experiment compared with the result given by the RO model [Ashkin, 1992; Gu *et al.*, 1997]. The experimental results agree well with the theoretical calculations for thick sample cells, while there is a discrepancy when the sample cell is thin. A possible reason for this discrepancy is the strong perturbation introduced by the boundaries of a thin sample cell. The heating effect on the solution by the trapping laser beam may also become pronounced for a thin sample cell.

When the value of  $B$  satisfies the compensation condition, the effect of the spherical aberration can be minimised as shown in Figs. 3.9-3.12. Under this condition, the average trapping power can be increased by up to 93% ( $B = 815$  and  $d = 36 \mu\text{m}$ ), 94.1% ( $B = 1226$  and  $d = 65 \mu\text{m}$ ) and 135% ( $B = 1812$  and  $d = 102 \mu\text{m}$ ), respectively, for those three sample cells (Fig. 3.13). In comparison with the experimental improvement of 6%, 12% and 20% when the tube length is altered from 160 mm to 140 mm, there is a large difference. The discrepancy between the theory and the experiment is because the objective operated at a tube length of 140 mm is not under the compensation condition. For  $B = 815$ , 1226 and 1812 under the compensation

condition, the corresponding change in the tube length  $\Delta l$  is -294 mm, -443 mm, and -654 mm, according to Eq. (2.15) in Chapter 2. These values mean that the tube length of the objective should be shortened by 294 mm, 443 mm and 654 mm, respectively, for the three sample conditions. Such a large change in tube length is clearly infeasible for an objective designed to be operated at the 160 mm tube length. Instead, a microscope objective of an infinitely-long tube length, which has been used in confocal microscopy [Sheppard and Gu, 1992; Sheppard *et al.*, 1994], should be employed in laser trapping experiments. Using a correction lens in the collimated beam path produced by this kind of objectives can easily result in a large change in tube length. Consequently, a substantial improvement in trapping efficiency can be obtained.

### 3.5 Conclusion

It has been shown that spherical aberration induced by refractive-index mismatch degrades trapping performance. However, this effect can be compensated for by changing the tube length of an objective used for trapping, which leads to an increase of the trapping efficiency by up to 20%. The theoretical prediction suggests that an objective designed for operation at an infinitely-long tube length should be employed for laser trapping applications such as particle-trapped NSOM.

The method for suppressing spherical aberration as demonstrated in the present chapter is valuable for improving the trapping performance and therefore image quality of particle-trapped NSOM. Although only dielectric particles are exemplified in this study, the proposed method for aberration compensation by a change in tube length is applicable to the applications of laser trapping with metallic particles.

## CHAPTER FOUR

# Characterisation of Trapping Force on Metallic Mie Particles

### 4.1 Introduction

It has been pointed out in Chapter 2 that the performance of laser trapping affects imaging quality of particle-trapped near-field scanning optical microscopy (NSOM). An investigation of trapping force on metallic particles is therefore needed for particle-trapped NSOM with a metallic particle.

For laser trapping of metallic particles employing a high numerical aperture (NA) objective, effects of NA and apodization of a trapping objective should be investigated [Ke and Gu, 1999a]. This is because the NA of a trapping objective affects not only trapping performance but also signal collection in particle-trapped NSOM. Apodization of a high NA objective may generate a trapping force more efficiently. Spherical aberration induced by refractive-index mismatch associated with the use of a high NA objective also needs to be considered because it degrades trapping performance. These issues have been considered in Chapter 3 for laser trapping of dielectric particles and will be investigated in this chapter for metallic particles.

This chapter is organised as follows. In section 4.2, the principle of laser trapping of metallic particles is introduced. In section 4.3, an expression for trapping force on metallic Mie particles is derived based on the ray-optics (RO) model. Three

types of metallic Mie particles (gold, nickel and silver), which represent three typical absorption properties of metallic materials, are selected to evaluate trapping force in the transverse and axial directions for different values of the NA of a trapping objective. In section 4.4, detailed measurements of the maximum transverse trapping force on metallic Mie particles (gold, nickel and silver) are described. A discussion on the effect of spherical aberration and thermal heating is presented. Based on this study, an apodization method with the use of an obstructed objective lens (i.e., an annular lens) is introduced in section 4.5 for the improvement of transverse trapping force on a metallic particle. A conclusion on the characterisation of trapping force on metallic Mie particles is presented in section 4.6.

## 4.2 Principle of laser trapping of metallic Mie particles

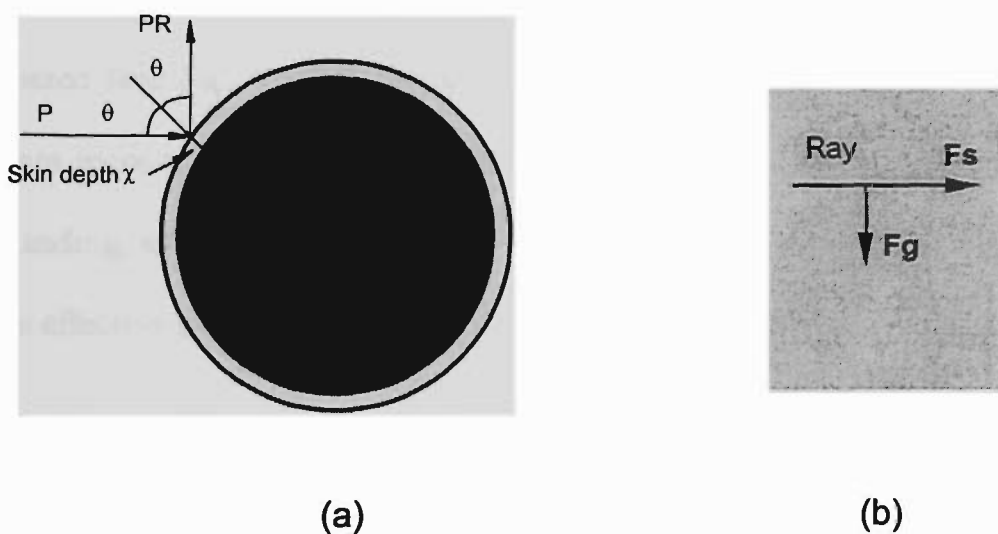


**Fig. 4.1** (a) Geometry for calculating force on a metallic particle of skin depth  $\chi$ . A single incident ray of power  $P$  is mainly reflected. (b) Relative strength of the gradient and scattering forces of a single ray.

When light impinges on a metallic particle, most of light is reflected due to the high reflectance of the metallic surface, while the rest of light penetrates through the particle.

The energy density of the transmitted light falls to  $1/e$  of its original value after the light travels through a skin depth  $\chi$  that is usually of several or tens of nanometres [Born and Wolf, 1997] (see Fig. 4.1 (a)). The momentum change of the incident light, or the optical force experienced by a metallic Mie particle, is mainly determined by the reflection at the surface of the particle. The optical force, caused by the multiple-reflection on the inner surface of the particle, can be neglected for a metallic Mie particle.

As a result of high reflection and small skin depth, the scattering force on a metallic particle is dominant over the gradient force (see Fig. 4.1 (b)), which forms a repulsive potential well for trapping at most of the positions except near the bottom of the particle. However, it can be seen from simple geometry that when the angle  $\theta$  of a ray of convergence is increased, the net transverse trapping force on a metallic particle is increased (see Fig. 4.1 (b)). In other words, rays at larger angles of convergence contribute more to the transverse trapping force on a metallic particle. Based on this understanding, an apodization method based on the use of an annular lens is expected to be more effective in generating transverse trapping force than that of a circular lens.

### 4.3 Calculation of trapping force on metallic Mie particles

The expressions for the scattering force  $F_s$  and the gradient force  $F_g$  caused by a single ray incident on a metallic particle can be expressed according to the RO model as [Ke and Gu, 1999a]

$$\begin{cases} F_s = \frac{nP}{c}(1 + \cos 2\theta \cdot R), \\ F_g = \frac{nPR}{c} \sin 2\theta, \end{cases} \quad (4.1)$$

Eq. (4.1) is actually the first term of Eq. (2.3) for the gradient and scattering force of a dielectric particle. The trapping force experienced by a metallic Mie particle, under the illumination of a highly focused laser beam, can be determined using Eq. (2.4) by integrating the gradient and scattering forces in Eq. (4.1) with respect to the angle of convergence of the trapping objective. The ray density within the maximum angle of convergence determined by the NA of the trapping objective is given according to the sine condition [Stamnes, 1986; Born and Wolf, 1997].

For the applications of laser trapping including particle-trapped NSOM, an oil-immersion objective, more economical than a water-immersion objective, is usually employed. Assume that an oil-immersion objective is illuminated by a uniform linearly-polarised laser beam at a wavelength of 488 nm, and that spherical metallic Mie particles are suspended in water of refractive index 1.33. Three types of metallic particles (gold, nickel and silver) are chosen in our calculation as they exhibit typically high, medium and low absorption properties at this wavelength. Their refractive indices are  $n_g = 0.82 + 1.59i$ ,  $n_n = 1.67 + 2.93i$  and  $n_s = 0.24 + 3.09i$  at  $\lambda = 488$  nm, respectively [Lide, 1996-1997].

Fig. 4.2 shows the distribution of the total trapping efficiency (refer to section 2.4.2.1.1 for definition) calculated using Eqs. (2.4), (2.5) and (4.1) for gold, nickel and silver particles at different trapping positions  $(x, z)$ . Here  $x$  and  $z$  are the transverse and

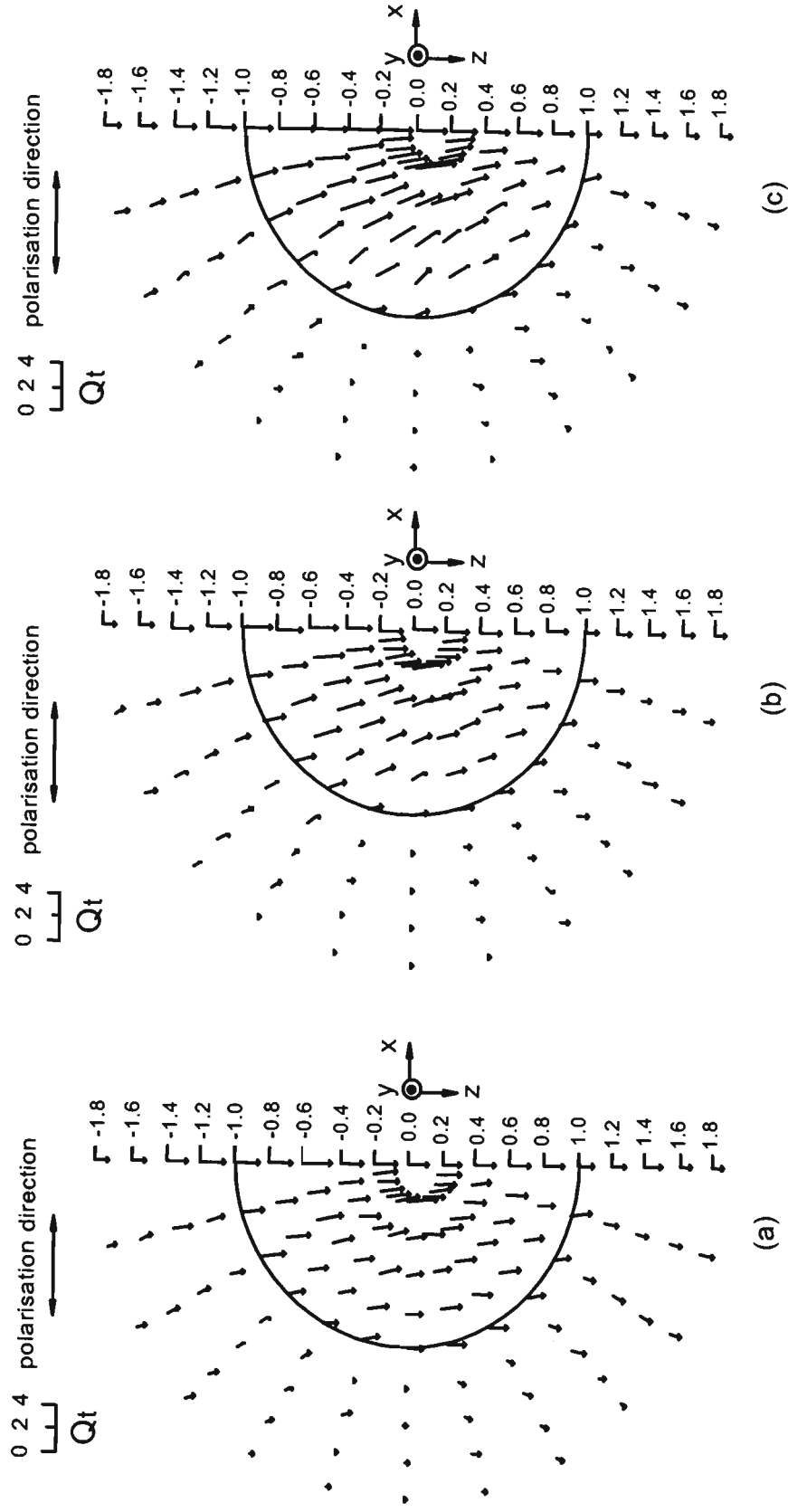


**Fig. 4.2** Distributions of the total trapping efficiency  $Q_t$  in the  $x-z$  plane for gold (a), nickel (b) and silver (c) particles, respectively. The polarisation direction of the laser beam is parallel to the  $x$ -axis. The light distribution over the aperture of the objective is uniform and linearly-polarised ( $\lambda = 488$  nm). An oil-immersion objective (NA = 1.25) is assumed for trapping.

axial trapping positions originating from the centre of the particle, respectively. The polarisation direction of the incident light is assumed to be along the  $x$ -axis. Notice that the particle radius is normalised to be unity. Each individual arrow originates from the trapping position of the laser beam and points towards the direction of the total trapping force. The trapping laser beam propagates in the direction of the  $z$ -axis. The length of the arrow is proportional to the strength of  $Q_i$ .

Unlike a dielectric particle where the axial trapping force can be either a lifting or a pushing force depending on the focal position of the trapping laser beam (refer to Fig. 2.10), the axial trapping force on a metallic particle always pushes the particle along the optical axis regardless of the focal position of the trapping laser beam. On the other hand, when the focal position of a laser beam is shifted downward and away from the centre of the particle, transverse force changes direction with the transverse position. Transverse trapping of a metallic particle only occurs when the projection of the total force along the transverse direction has a negative value (attractive force). Repulsive force dominates otherwise. The area where transverse trapping exists is located below the central equatorial plane of the particle and away from the beam axis. This result is consistent with the experimental observation that a metallic Mie particle can be trapped only in two dimensions (2D) near the bottom of the particle ([Sato *et al.*, 1994; Furukawa and Yamaguchi, 1998]).

To compare the trapping force between gold, nickel and silver particles, the axial and transverse trapping efficiencies are calculated and displayed in Figs. 4.3-4.5. On the axis at  $x = 0$  (Fig. 4.3), a maximum axial trapping efficiency occurs when the

focus of a trapping beam is located approximately at  $z = -0.5$  for all three types of the metallic particles.

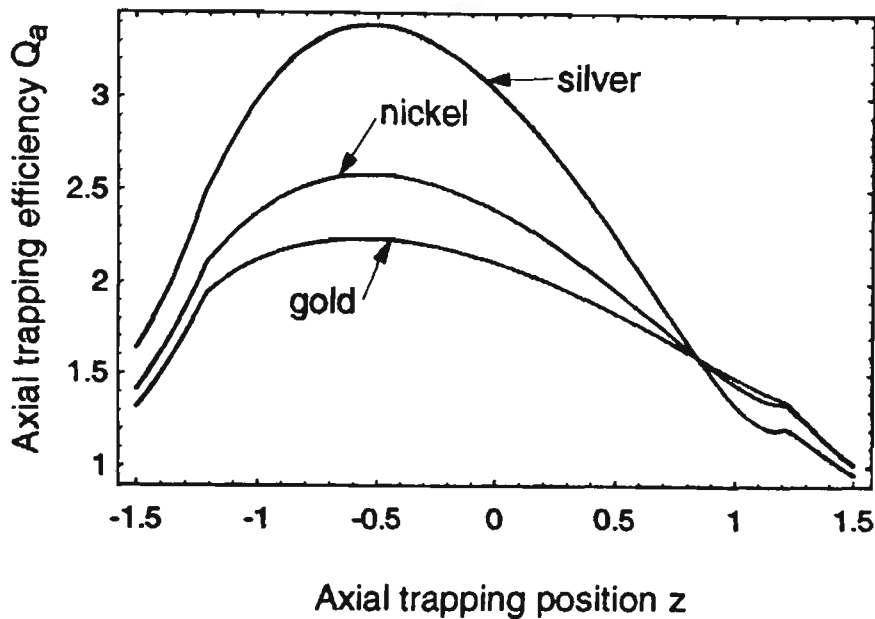
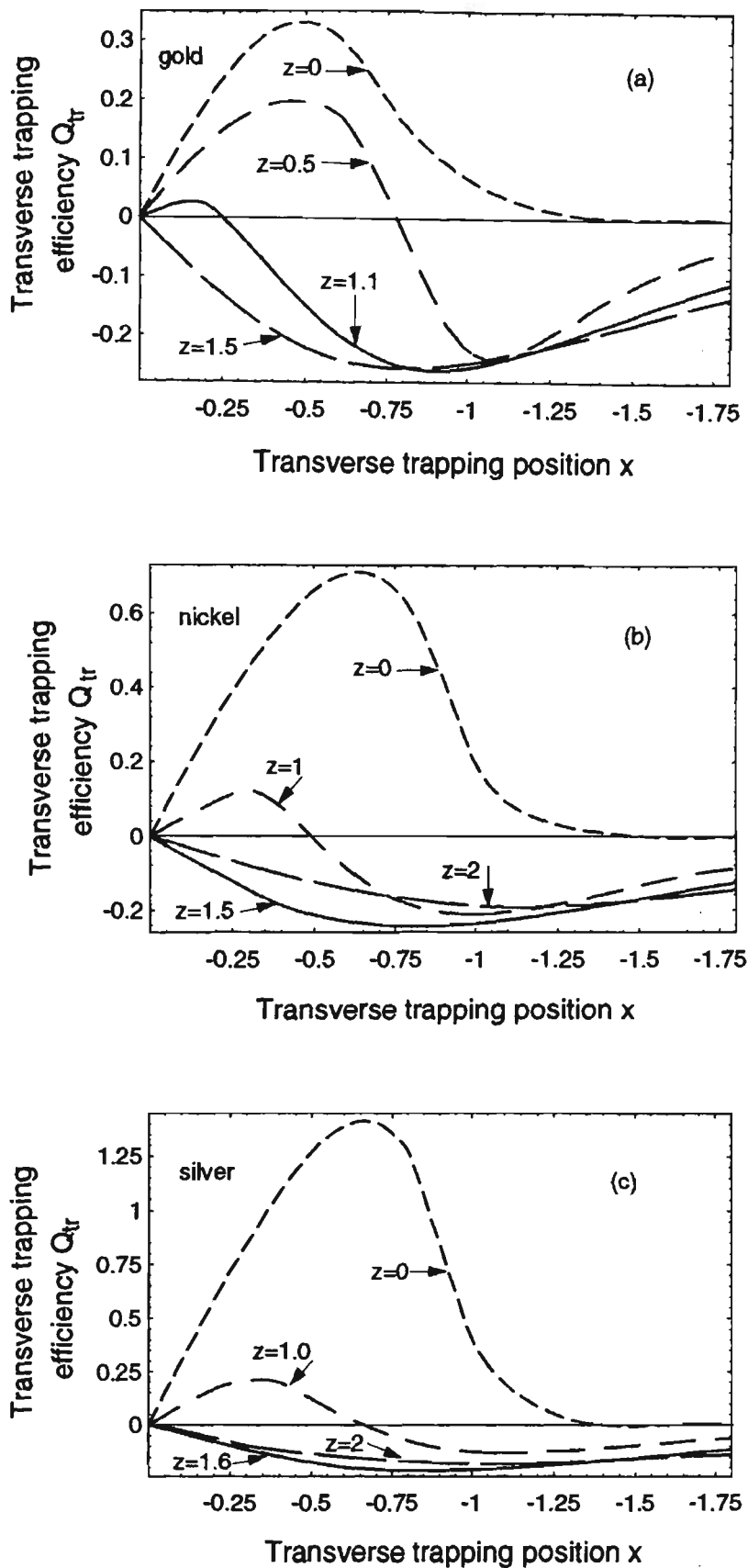


Fig. 4.3 Axial trapping efficiency as a function of the axial trapping position  $z$  when  $x = 0$  for gold, nickel, and silver particles, respectively. The other conditions are the same as those in Fig. 4.2.

For the applications of near-field imaging with a metallic particle trapped in 2D, the transverse trapping force on a particle mainly determines the speed of image acquisition, provided that the axial trapping force is sufficient to keep the particle in touch with a sample. Our attention is therefore focused on the transverse trapping force on metallic particles. As illustrated in Fig. 4.4, when the axial trapping position is above the equatorial plane of a trapped metallic particle, the transverse trapping force in the  $x$ - $z$  plane for gold, nickel and silver particles is predominantly repulsive. This repulsive force becomes weak when the axial trapping position moves downward from the equatorial plane. In the meantime, an attractive transverse trapping force appears. This attractive force increases until it reaches a maximum, which is represented by a



**Fig. 4.4** Transverse trapping efficiency  $Q_{tr}$  as a function of the transverse trapping position  $x$  for gold (a), nickel (b), and silver (c) particles, respectively. The other conditions are the same as those in Fig. 4.2. The solid curves correspond to the situation when a maximum transverse trapping efficiency occurs.

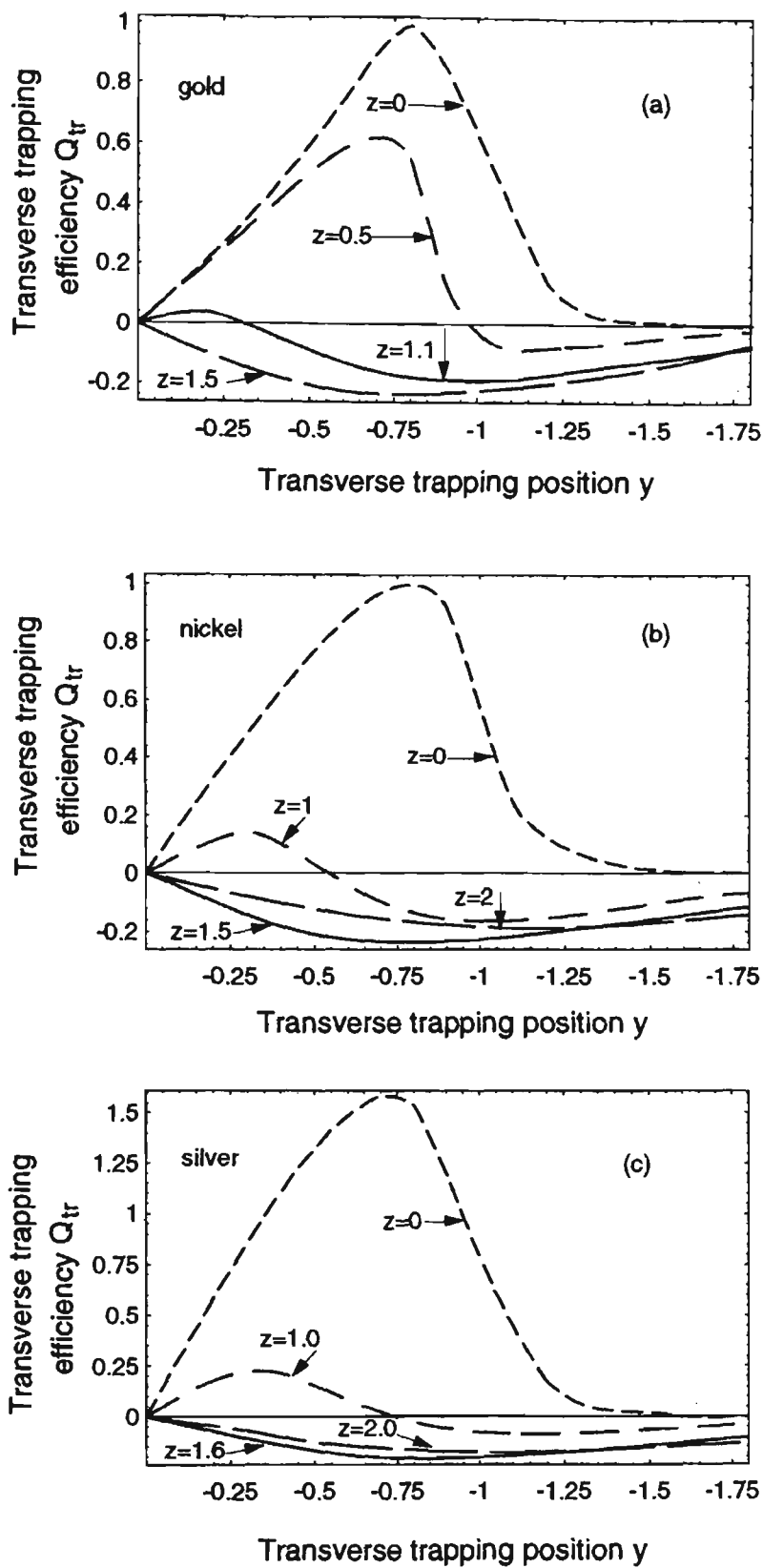


Fig. 4.5 Transverse trapping efficiency  $Q_{tr}$  as a function of the transverse trapping position  $y$  for gold (a), nickel (b), and silver (c) particles, respectively. The trapping position is in the  $y$ - $z$  plane perpendicular to the polarisation direction of the illumination beam and the other conditions are the same as those in Fig. 4.2.

solid curve in Fig. 4.4. For an example, the maximum transverse trapping efficiency occurs at  $z = 1.1$ ,  $z = 1.5$ , and  $z = 1.6$  for gold, nickel and silver particles, respectively. Therefore, Fig. 4.4 suggests that when the axial trapping position is sufficiently low, a metallic particle can be trapped at an on-axis position, while it can be trapped at an off-axis position if the trapping position is slightly below the equatorial plane. This conclusion agrees with the previous experimental observation by Furukawa and Yamaguchi [Furukawa and Yamaguchi, 1998] and our experimental results given in section 4.4.

As a result of using a linearly polarised beam, the trapping efficiency in the  $y$ - $z$  plane is smaller than that in the  $x$ - $z$  plane, as shown in Fig. 4.5. This is due to the slight difference in the trapping power between the two orthogonal planes [Ashkin, 1992]. Compared with the result in Fig. 4.4, the maximum value of the transverse trapping efficiency at  $z = 1.1$ ,  $z = 1.5$ , and  $z = 1.6$  in Fig. 4.5 is reduced by 28%, 3.3%, and 2.1% for gold, nickel and silver particles, respectively. By contrast, the maximum value of the transverse trapping efficiency at  $z = 0$  in Fig. 4.5 is increased by 201%, 40.7% and 10.5% for gold, nickel and silver particles, respectively, compared with that in Fig. 4.4.

## 4.4 Effect of numerical aperture on transverse trapping efficiency

### 4.4.1 Theoretical results

For a given metallic particle, the transverse trapping efficiency changes with the NA of a trapping objective [Ke and Gu, 1999a]. The maximum transverse trapping efficiency  $Q_r^m$  in the  $x$ - $z$  plane for different values of the NA is shown in Tables 4.1-4.3 for gold,

**Table 4.1** Maximum transverse trapping efficiency  $Q_{tr}^m$  as a function of the NA of the trapping objective for a gold particle.

NA	(x, z)	$Q_a$	$Q_{tr}^m$
0.8	(-0.79, 2.8)	0.6788	-0.1638
0.9	(-0.70, 2.3)	0.7569	-0.1883
1.0	(-0.72, 2.0)	0.7445	-0.2089
1.1	(-0.78, 1.7)	0.7232	-0.2308
1.25	(-0.89, 1.1)	0.7444	-0.2595

**Table 4.2** Maximum transverse trapping efficiency  $Q_{tr}^m$  as a function of the NA of the trapping objective for a nickel particle.

NA	(x, z)	$Q_a$	$Q_{tr}^m$
0.8	(-0.86, 3.0)	0.6209	-0.1561
0.9	(-0.85, 2.6)	0.6174	-0.1746
1.0	(-0.80, 2.2)	0.6521	-0.1965
1.1	(-0.80, 1.9)	0.6545	-0.2161
1.25	(-0.80, 1.5)	0.6618	-0.2442

**Table 4.3** Maximum transverse trapping efficiency  $Q_{tr}^m$  as a function of the NA of the trapping objective for a silver particle.

NA	(x, z)	$Q_a$	$Q_{tr}^m$
0.8	(-0.91, 3.1)	0.5920	-0.1483
0.9	(-0.88, 2.7)	0.5852	-0.1641
1.0	(-0.88, 2.3)	0.5931	-0.1817
1.1	(-0.90, 2.0)	0.5775	-0.1948
1.25	(-0.89, 1.6)	0.5751	-0.2133

nickel, and silver particles, respectively. The trapping positions ( $x$ ,  $z$ ) and the axial trapping efficiency  $Q_a$  corresponding to the maximum transverse trapping efficiency  $Q_r^m$  are also listed in Tables 4.1-4.3. The positive and negative signs of the trapping efficiency represent pushing and attractive effects, respectively. When the NA of the objective increases, the maximum transverse trapping efficiency increases accordingly, and the axial trapping position shifts upward although the transverse trapping position does not change appreciably. For a given value of the NA of the objective, the maximum transverse trapping efficiency reduces and the corresponding axial trapping position moves downward, when a metallic material becomes less absorptive.

The fact that the maximum transverse trapping efficiency for a metallic particle increases with the NA is different from the situation of a trapped dielectric particle (refer to Fig. 2.11) in which case the maximum transverse trapping efficiency decreases with the NA. The physical reason for this difference is that a metallic particle has a small skin depth for light transmission and is highly reflective, and therefore the scattering force is stronger than the gradient force for a ray at a given incident angle. As a result, the transverse trapping force increases with the angle of convergence of a trapping objective (Refer to Fig. 4.1 (b)).

#### 4.4.2 Experimental results

To demonstrate the dependence of the transverse trapping efficiency on NA, the transverse trapping force on metallic Mie particles was measured as a function of the NA of a trapping objective. The experimental setup is similar to Fig. 3.6 in Chapter 3 except that a linearly-polarised Ar<sup>+</sup> laser at wavelength  $\lambda = 488$  nm (Spectra-Physics: Stabilite 2017, 5 W) was used for trapping with high power. Three types of metallic

particles used in the experiment were gold ( $\phi = 2 \text{ }\mu\text{m}$ ), nickel ( $\phi = 3 \text{ }\mu\text{m}$ ) and silver particles ( $\phi = 3 \text{ }\mu\text{m}$ ), respectively, suspended in water. Under these conditions, the size parameter  $q = 2\pi n_i \phi / \lambda$  ( $i = g, n, s$ ) for each type of particle is much larger than unity and therefore the RO model should hold. The effective numerical aperture of the trapping objective NA' was determined using the same way as described in section 3.3.1. The trapping power  $P$  was measured at the back aperture of the objective, and multiplied by a factor of 81% which is the measured transmittance of the objective.

The maximum transverse force  $F_{tr}^m$  on a metallic particle was measured using the method prescribed in section 3.3.1 of Chapter 3. The axial trapping position corresponding to the maximum transverse force  $F_{tr}^m$  was achieved by slightly adjusting the axial focal position of the objective until the maximum scanning speed was found. Unlike a dielectric particle in which case the maximum transverse trapping force occurs near the surface of the equatorial plane of the particle (Fig. 3.3 and Ke and Gu, 1998a), the position of the maximum transverse trapping force on a metallic particle is much lower.

It was observed in the experiment that gold and silver particles were easily trapped laterally and scanned at relatively higher speeds, while a nickel particle was trapped at a lower speed due to its larger kinetic friction coefficient. As illustrated in Fig. 4.6, a nickel particle of  $\phi = 3 \text{ }\mu\text{m}$  at the top right corner of the figure was trapped by an  $\text{Ar}^+$  laser beam and stayed at the trapped position when the other particles were moving with the microscope slide. It can be seen that a bright spot on the trapped particle, corresponding to the focal position of the trapping beam, is not located

in the centre of the trapped particle. This phenomenon is caused by the fact that the axial trapping position was slightly below the equatorial plane. Consequently, the balance between the trapping and repulsive forces was not at the centre of the particle, as expected from the theoretical prediction in Fig. 4.4.

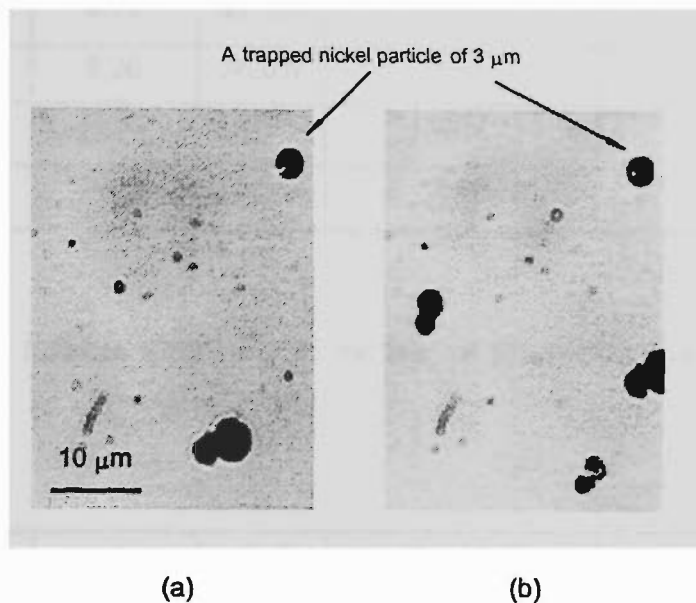


Fig. 4.6 Demonstration of a trapped nickel particle of diameter 3  $\mu\text{m}$ , recorded using a CCD camera. Frames (a) and (b) were recorded at different times.

The measured maximum transverse force  $F_{tr}^m$  is listed in Tables 4.4-4.6 for gold, nickel and silver particles for different values of the NA' of the trapping objective. As the maximum transverse scanning speed of the nickel particle was very small, the NA' of the objective could be adjusted only from 1 to 1.25. For the gold and silver particles the NA' was altered from 0.8 to 1.25. The maximum transverse trapping force  $F_{tr}^t$  calculated using the values of  $Q_{tr}$  in Tables 4.1-4.3 is also displayed in Tables 4.4-4.6. Clearly, the experimental results qualitatively agree with theoretical results  $F_{tr}^t$  in the sense that the larger the value of NA the larger the transverse force. The difference between the theoretical and the experimental results will be discussed in the following.

**Table 4.4** Transverse force as a function of the NA' of the trapping objective for a gold particle.

NA'	$F_{tr}^m$ (pN) measured	$F_{tr}'$ (pN) calculated	$P'/P$	$F_{tr}'$ (pN) calculated with aberration	$F_{tr}^m + F_f$ (pN) estimated transverse trapping force
0.8	0.15	4.35	55.7%	2.42	2.24
0.9	0.27	6.77	41.2%	2.85	2.64
1.0	0.44	9.26	36.0%	3.33	3.33
1.1	0.53	11.56	34.7%	4.00	4.20
1.25	0.69	17.26	25.5%	4.40	4.59

**Table 4.5** Transverse force as a function of the NA' of the trapping objective for a nickel particle.

NA'	$F_{tr}^m$ (pN) measured	$F_{tr}'$ (pN) calculated	$P'/P$	$F_{tr}'$ (pN) calculated with aberration	$F_{tr}^m + F_f$ (pN) estimated transverse trapping force
1.0	0.07	10.02	36.0%	3.61	3.61
1.1	0.09	11.78	34.7%	4.08	4.28
1.25	0.15	17.11	25.5%	4.36	4.74

**Table 4.6** Transverse force as a function of the NA' of the trapping objective for a silver particle.

NA'	$F_{tr}^m$ (pN) measured	$F_{tr}'$ (pN) calculated	$P'/P$	$F_{tr}'$ (pN) calculated with aberration	$F_{tr}^m + F_f$ (pN) estimated transverse trapping force
0.8	0.58	4.01	55.7%	2.23	2.26
0.9	0.78	6.18	41.2%	2.60	2.48
1.0	0.95	8.46	36.0%	3.05	3.05
1.1	1.19	10.36	34.7%	3.59	3.82
1.25	1.50	14.94	25.5%	3.81	4.28

### 4.4.3 Discussion

As shown in Tables 4.4-4.6, there exists a pronounced difference between the theoretical and experimental results. The first reason for this difference is the effect of spherical aberration induced by the refractive-index mismatch between a cover glass and the water solution (refer to section 3.3.2). In the presence of spherical aberration, the distribution of light intensity in the focal region of a trapping objective becomes broad in both the axial and transverse directions, the peak light intensity is reduced and a series of sidelobes occur along the axial direction (see Fig. 3.10). As a result, the effective trapping power on a trapped particle is much less than the incident power through the objective. According to our previous method (see section 3.3.2), the ratio of the effective trapping power  $P'$  at the focus of the objective to the measured incident power  $P$  can be estimated and is shown in Tables 4.4-4.6. Consequently, the maximum transverse trapping force  $F'_{tr}$  is given by  $F'_{tr} = F_{tr} \cdot P' / P$ .

The difference between  $F'_{tr}$  and  $F_{tr}^m$  may be caused by the heating effect of the trapping beam on metallic particles. When the incident laser beam is incident at the surface of an absorptive metallic particle, a temperature gradient could be generated from the front illuminated surface to the back surface of the particle because of intensity gradient and small skin depth [Wood, 1986]. A temperature gradient also occurs in the transverse direction since the trapping laser beam irradiates the particle asymmetrically. But this transverse temperature gradient is negligible because the trapping beam propagates along the z-axis. The energy flow inside the metallic particle and between the particle and the surrounding medium, in a form of heat transferring, leads to a radiometric force opposite to the temperature gradient within the particle

[Wood, 1986; Barber and Chang, 1988; Svoboda and Block, 1994]. As a result, the friction between a trapped metallic particle and the glass slide is increased which may lead to the discrepancy between the measured transverse force and the theoretical predictions.

The radiometric force on a trapped metallic particle is dependent on many factors including the illumination wavelength and intensity, the shape of the trapped particle, and the thermal characteristics of the particle and its surrounding medium [Lewittes *et al.*, 1982; Barber and Chang, 1988]. Adopting the expression for the radiometric force on a particle suspended in a gas medium [Lewittes *et al.*, 1982], we may express the radiometric force  $F_r$  on a metallic particle suspended in water as

$$F_r = C_1 \cdot mg \cdot I / r^2, \quad (4.2)$$

where  $C_1$  is a coefficient depending on the thermodynamic and hydrodynamic features of the metallic particle and the surrounding medium,  $m$  is the mass of the metallic particle, and  $g$  is the acceleration constant of free fall. At a given wavelength, the light intensity on the particle surface,  $I$ , can be estimated by the effective trapping power  $P'$  and NA' of the microscope objective used for trapping. Eq. (4.2) can be rewritten as

$$F_r = C_2 \cdot \rho_p \cdot P' \cdot \text{NA}'^2 \cdot r. \quad (4.3)$$

Here  $\rho_p$  is the density of the metallic material and  $C_2$  is a parameter incorporating the coefficient  $C_1$  and the other constants. The accurate value of  $C_2$  may be obtained by calculating the three-dimensional heat flow inside and outside a metallic particle illuminated by a high NA objective [Lewittes *et al.*, 1982]. However, the value of  $C_2$  may be estimated by a comparison between  $F_{tr}'$  and  $F_{tr}^m$ .

The maximum transverse force  $F_{tr}^m$  on a metallic particle, as measured in the experiment, is given by the difference between the maximum transverse trapping force and the friction:

$$F_{tr}^m = F_{tr}' - F_f. \quad (4.4)$$

Here the friction  $F_f$  is determined by the total axial force  $F_{ta}$ :

$$F_f = F_{ta} \cdot \mu, \quad (4.5)$$

where  $\mu$  is the kinetic friction coefficient between a trapped metallic particle and the microscope slide, and can be chosen to be 0.05, 0.08 and 0.05 for gold, nickel and silver particles, respectively [Besancon, 1974]. The total axial force  $F_{ta}$  on a metallic particle is contributed by the axial trapping force  $F_a$  (downward), gravity  $F_g$  (downward), the buoyant force  $F_b$  (upward), and the radiometric force  $F_r$  (downward), which can be expressed as

$$F_{ta} = F_a + F_g - F_b + F_r. \quad (4.6)$$

The gravity and the buoyant force,  $F_g$  and  $F_b$ , can be easily calculated using the expressions  $F_g = \frac{4}{3}\pi r^3 \rho_p g$  and  $F_b = \frac{4}{3}\pi r^3 \rho_w g$ , where  $\rho_p$  and  $\rho_w$  are the densities of a trapped metallic particle and the water medium, respectively. The density of gold, nickel and silver particles, is 19290 kg/m<sup>3</sup>, 8900 kg/m<sup>3</sup> and 10500 kg/m<sup>3</sup>, respectively [Raznjevic, 1976]. The axial trapping force  $F_a$  can be calculated according to the axial trapping efficiency  $Q_a$  listed in Tables 4.1-4.3.

By applying Eqs. (4.4)-(4.6) to  $F_{tr}'$  and  $F_{tr}^m$  at NA'=1.0, the value of  $C_2$  is estimated to be  $6.60 \times 10^{-7} \text{ m}^3 \text{ s}^2 \text{ W}^{-1}$ ,  $5.65 \times 10^{-7} \text{ m}^3 \text{ s}^2 \text{ W}^{-1}$  and  $5.14 \times 10^{-7} \text{ m}^3 \text{ s}^2 \text{ W}^{-1}$  for gold, nickel and silver particles, respectively. As expected, the stronger the absorption of a

metallic particle the larger the value of  $C_2$ . With the  $C_2$  values, the maximum transverse trapping force ( $F_{tr}^m + F_f$ ) can be evaluated as shown in Tables 4.4-4.6. It can be seen from Tables 4.4-4.6 that the maximum transverse trapping force ( $F_{tr}^m + F_f$ ) increases with the NA of the objective, which is consistent with the theoretical prediction. The difference between  $F_{tr}'$  and  $F_{tr}^m + F_f$  is less than 13%, even for the maximum value of the NA.

The wavelength used in our study is 488 nm. Trapping with a shorter wavelength beam may lead to a higher resolution in particle-trapped NSOM due to the smaller diffraction spot generated, although a near-infrared wavelength is usually selected for trapping in biological applications to prevent possible thermal damage to samples [Buican *et al.*, 1987; Zhang *et al.*, 1998]. If a near-infrared wavelength is used for trapping a metallic particle, the absorption property of metallic particles is different from that discussed in this chapter. For example, a gold particle becomes much less absorptive, which gives rise of a significantly reduced radiometric force.

#### **4.5 Enhancement of transverse trapping efficiency for metallic particles with an annular lens**

As mentioned in section 4.2, the transverse trapping force on a metallic particle can be increased with the use of an annular lens as a trapping objective. This topic will be discussed in the following.

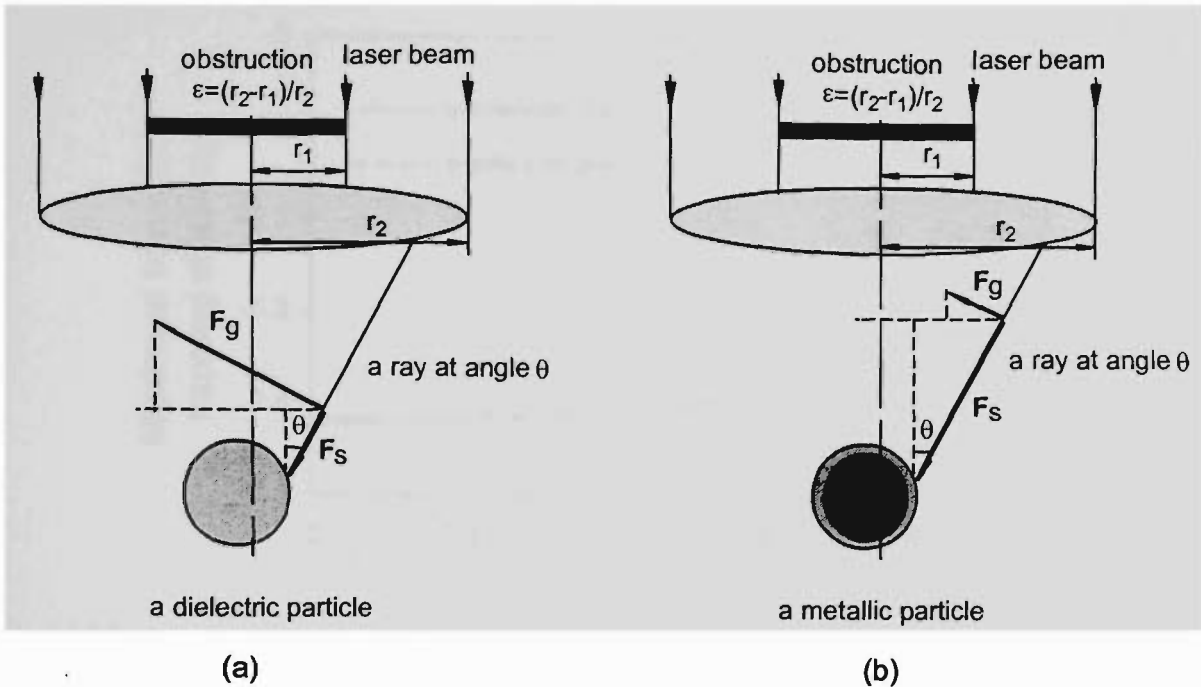
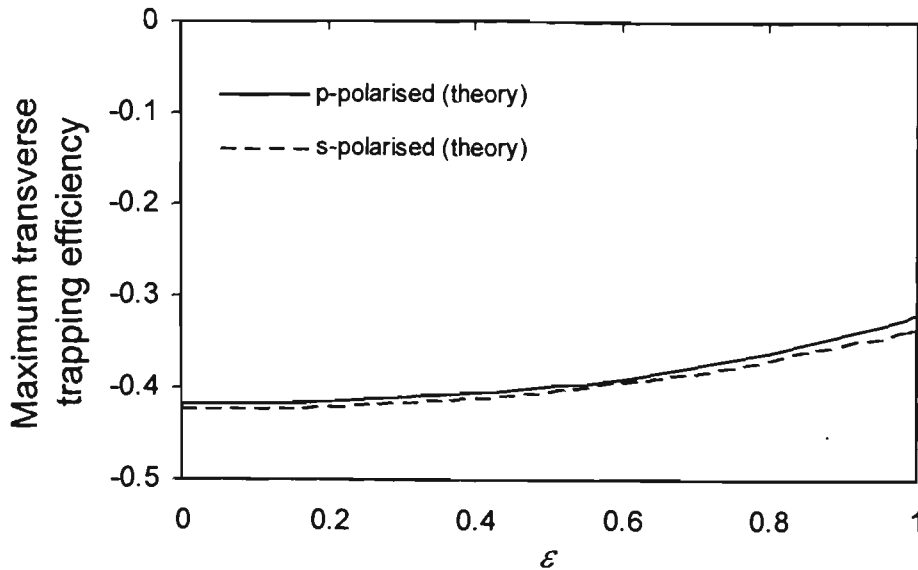


Fig. 4.7 Schematic diagram for demonstrating the difference of trapping force between (a) dielectric and (b) metallic particles.  $F_g$  represents the gradient force and  $F_s$  represents the scattering force.  $\theta$  is the angle of a ray of convergence. The outer ring of the metallic particle indicates its skin depth.

For laser trapping of a dielectric particle, Ashkin has predicated [Ashkin, 1992] that the use of an obstructed beam (i.e., a ring beam) can increase the axial trapping efficiency but reduce the transverse trapping efficiency. The reason for this feature is that the gradient force is dominant due to the refraction on the surface of a trapped dielectric particle. Consequently, the projection of the net trapping force in the transverse direction of the trapping beam is decreased with the angle  $\theta$  of a ray of convergence (Fig. 4.7 (a)). It can be found from the RO model [Ashkin, 1992] that for a given trapping objective, the maximum transverse trapping efficiency for a dielectric particle decreases approximately by up to 23% and 21% for p- and s-polarised trapping beams, respectively (see Fig. 4.8). Here p- and s-polarised trapping beams represent that the polarisation direction of the trapping beam is parallel and perpendicular to the direction of the transverse displacement of a trapped particle, respectively.



**Fig. 4.8** Maximum transverse trapping efficiency as a function of the radius of the central obstruction  $\epsilon$  for a dielectric ( $n_p = 1.59$ ) particle in water ( $n = 1.33$ ), according to the RO model. The NA of the trapping objective is 1.25 at wavelength 488 nm.

Since the net transverse trapping force on a metallic particle increases with the angle  $\theta$  of a ray of convergence, the transverse trapping efficiency for a metallic particle may be enhanced, if a circular obstruction is co-axially placed in the illumination path. Such an enhancement becomes stronger as the radius of the obstruction becomes larger. On the other hand, the reflection coefficient on a metallic surface is complex [Born and Wolf, 1997], which implies the existence of depolarisation of an incident linearly-polarised beam. Thus, the dependence of the transverse trapping efficiency for a metallic particle on the polarisation states of a trapping beam becomes more complicated than that observed for a dielectric particle in Fig. 4.8.

To demonstrate these features, we calculate the maximum transverse trapping efficiency for a gold particle using the RO model (refer to section 4.3). The NA of the

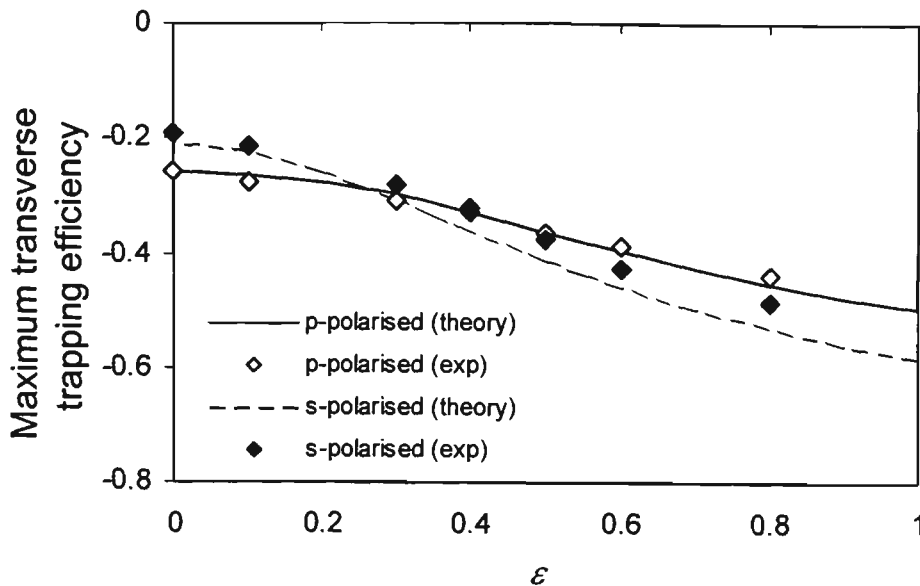


**Fig. 4.9** Maximum transverse trapping efficiency as a function of the radius of the central obstruction  $\varepsilon$  for a gold particle, in water ( $n = 1.33$ ), of diameter  $2 \mu\text{m}$ . The theoretical results are calculated according to the RO model. The NA of the trapping objective is 1.25 at wavelength 488 nm.

objective is assumed to be 1.25 for wavelength 488 nm. The trapping objective obeys the sine condition [Born and Wolf, 1997]. Fig. 4.9 shows the dependence of the maximum transverse trapping efficiency  $Q_{\sigma}^m$  for a gold particle as a function of the radius of the central obstruction  $\varepsilon$ . Here  $\varepsilon$  has been normalised by the outer radius of a uniform illumination beam (see Fig. 4.7).  $Q_{\sigma}^m$  is obtained by varying the focal spot along the axial direction until the maximum value is found. As expected,  $Q_{\sigma}^m$  for  $\varepsilon = 1$ , i.e. for a thin ring beam, is enhanced by factors of 1.9 and 2.8, respectively, for p- and s-polarised trapping beams, compared with that for  $\varepsilon = 0$ . Unlike the situation at  $\varepsilon = 0$  in Fig. 4.8,  $Q_{\sigma}^m$  for a p-polarised beam is 24% larger than that for an s-polarised beam. But the former becomes smaller than the latter as  $\varepsilon > 0.3$ . This phenomenon may be understandable as follows. For an objective of  $\text{NA} = 1.25$ , the angle  $\theta$  of a ray of convergence is approximately  $15^\circ$  when  $\varepsilon = 0.3$ . The reflectance on a gold surface

under s-polarised beam illumination is much stronger than that for p-polarised beam illumination if the incident angle is larger than  $15^\circ$  [Born and Wolf, 1997], which results in the behaviour in Fig. 4.9.

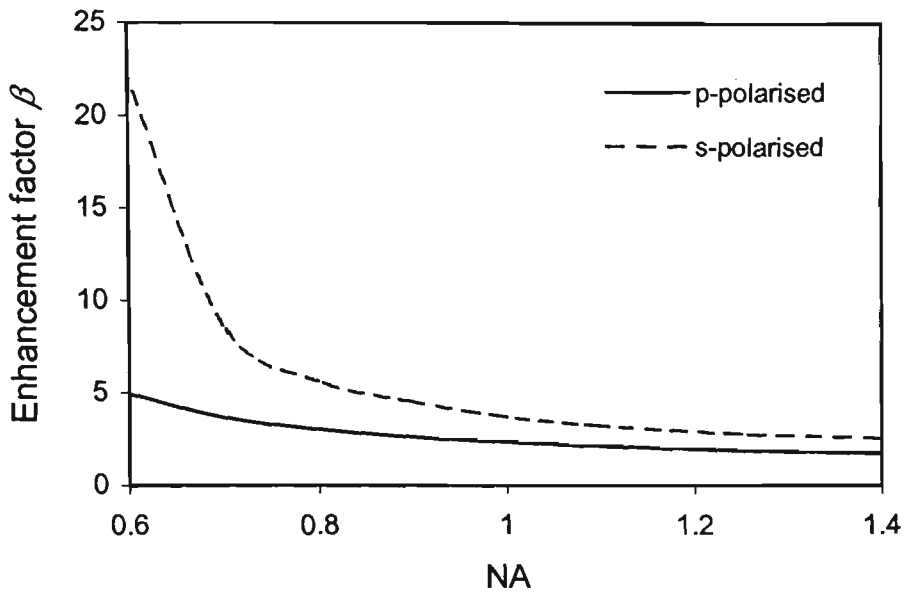


Fig. 4.10 Calculated enhancement factor  $\beta$  as a function of the NA of a trapping objective for a gold particle suspended in water.

It should be pointed out that the enhancement factor  $\beta$ , defined as the ratio of  $Q_r^m(\varepsilon=1)$  to  $Q_r^m(\varepsilon=0)$ , is decreased with the NA of a trapping objective, although  $Q_r^m(\varepsilon=1)$  and  $Q_r^m(\varepsilon=0)$  increase with the NA individually. According to Fig. 4.10, the minimum value of  $\beta$  at  $NA=1.4$  is 1.7 and 2.5 for p- and s-polarised trapping beams, respectively.

In order to confirm the above theoretical prediction, we conducted trapping experiments with gold particles of  $\phi = 2 \mu\text{m}$  in diameter. The experimental setup is similar to Fig. 3.6 in Chapter 3 except an opaque circular disk was co-axially placed

within the entrance aperture to produce a ring illumination beam. An Ar<sup>+</sup> laser at wavelength  $\lambda = 488$  nm (Spectra-Physics: Stabilite 2017, 5 W) was used for trapping. The radius of the obstruction was varied so that the value of  $\varepsilon$  changes from zero to 0.8. The trapping power at the focus of the trapping objective was maintained to be approximately 4.3 mW for all measurements.

The measured dependence of the maximum transverse trapping efficiency  $Q_{tr}^m$  on  $\varepsilon$  is normalised by the calculated value at  $\varepsilon = 0$  for a p-polarised laser beam as depicted in Fig. 4.9. It is seen that the enhancement of  $Q_{tr}^m$  is 1.7 and 2.5, respectively, for p- and s-polarised trapping beams, which agrees well with the theoretical prediction. Fig. 4.9 also confirms the dependence of  $Q_{tr}^m$  on the polarisation states of the trapping beams. When  $\varepsilon$  is small the measured values of  $Q_{tr}^m$  fit well the theoretical values. However, there is a slight discrepancy between the experimental and theoretical results when  $\varepsilon$  becomes large. The discrepancy is caused by light diffraction in the focal region of the trapping objective [Mehta, 1974; Török *et al.*, 1995; Gu, 1999], which is not considered by the RO model.

According to the diffraction theory [Mehta, 1974; Gu, 1999], the concentric power in the focal region of an obstructed beam decreases with the size of the central obstruction. For the particle size used in the experiment, the concentric power on the trapped particle for  $\varepsilon = 0.8$  can be up to 10% lower than that for  $\varepsilon = 0$  [Mehta, 1974], so that the transverse trapping efficiency is accordingly reduced. This estimation is in agreement with the experimental observation in Fig. 4.9.

In summary, the use of an annular lens for trapping a metallic particle leads to a significant enhancement in the maximum transverse trapping efficiency. This enhancement is caused by the fact that scattering force in trapping a metallic particle is much stronger than the gradient force. As a result of the depolarisation upon reflection on the surface of a gold particle, the enhancement factor for an s-polarised trapping beam is larger than that for a p-polarised trapping beam.

## **4.6 Conclusion**

It has been demonstrated that the maximum transverse trapping force on a metallic particle increases with the NA of the trapping objective, while it decreases with the NA of the trapping objective for a dielectric particle. This result is significant for near-field imaging with laser-trapped metallic particles since a high NA objective can lead to high signal-to-noise ratio as well as high transverse scanning speed. Based on this result, our study has also further shown that the use of an annular lens as a trapping objective can effectively improve the transverse trapping efficiency of metallic particles. The use of an annular lens also provides a chance in suppressing radiometric force which degrades the trapping performance of metallic particles. This method is advantageous for imaging with laser-trapped metallic particles as the physical and chemical conditions of a sample under inspection could be less affected due to the reduced heating effect.

## CHAPTER FIVE

# Imaging Enhancement with Laser-Trapped Metallic Particles: Effect of Signal Strength

### 5.1 Introduction

**I**N Chapter 4 we have shown that transverse trapping force on a metallic particle increases with the numerical aperture (NA) of a trapping objective (by contrast, transverse trapping force on a dielectric particle decreases as the NA of the trapping objective increases). As a result, utilising a laser-trapped metallic particle in particle-trapped near-field scanning optical microscopy (NSOM) may increase the scanning speed for image acquisition while maintaining high signal-to-noise ratio.

To improve image resolution, a small-sized metallic particle is needed but may result in a reduced signal strength. Signal strength is an important issue in near-field Mie scattering that may affect image contrast of particle-trapped NSOM. In addition to signal strength, depolarisation of scattered evanescent waves is another issue to be examined for the imaging of particle-trapped NSOM.

This chapter is to give a detailed investigation into signal strength and image contrast in particle-trapped NSOM, with respect to laser-trapped metallic particles of different sizes [Gu and Ke, 1999a; Ke and Gu, 1999b]. This investigation is performed in comparison with that obtained for dielectric particles to demonstrate significant

advantages of using laser-trapped metallic particles in achieving high signal strength, high image contrast, and fast scanning speed. The depolarisation of scattered evanescent waves will be treated as a separate topic in Chapter 6.

This chapter is arranged as follows: In section 5.2, we characterise the dependence of the strength of scattered evanescent waves on the size of laser-trapped particles (dielectric and metallic). In section 5.3, image enhancement with the use of a laser-trapped metallic particle is demonstrated by imaging an evanescent wave interference pattern. This property is further confirmed in section 5.4 according to the image of the surface of a prism. Conclusions on the experimental results are given in section 5.5.

## **5.2 Strength of scattered evanescent waves with laser-trapped metallic particles**

### **5.2.1 Experiment**

To determine the dependence of the signal strength of scattered evanescent waves on the physical size of a laser-trapped particle and demonstrate the associated advantages, dielectric (polystyrene of diameter  $\phi = 0.1-2 \mu\text{m}$ ) and metallic (gold of  $\phi = 0.1, 0.5,$  and  $2 \mu\text{m}$ , and silver of  $\phi = 2 \mu\text{m}$ ) particles were employed. The experimental setup of particle-trapped NSOM is illustrated in Fig. 5.1.

An evanescent wave was generated at the surface of an equilateral prism ( $\text{SF}_{10}$ ,  $n_1 = 1.725$ , surface flatness  $\lambda/10$ ) under the condition of total internal reflection of a He-Ne laser of 17 mW output. The prism was mounted on a three-dimensional (3D)

scanning stage (Melles Griot) driven by a piezoelectric controller (Melles Griot). Particles of different sizes were subsequently suspended in water solution ( $n_2 = 1.33$ ) inside a sample cell. The sample cell was formed of a double-sided tape sandwiched between a cover glass and the prism. The thickness of the sample cell is approximately  $120 \mu\text{m}$ .

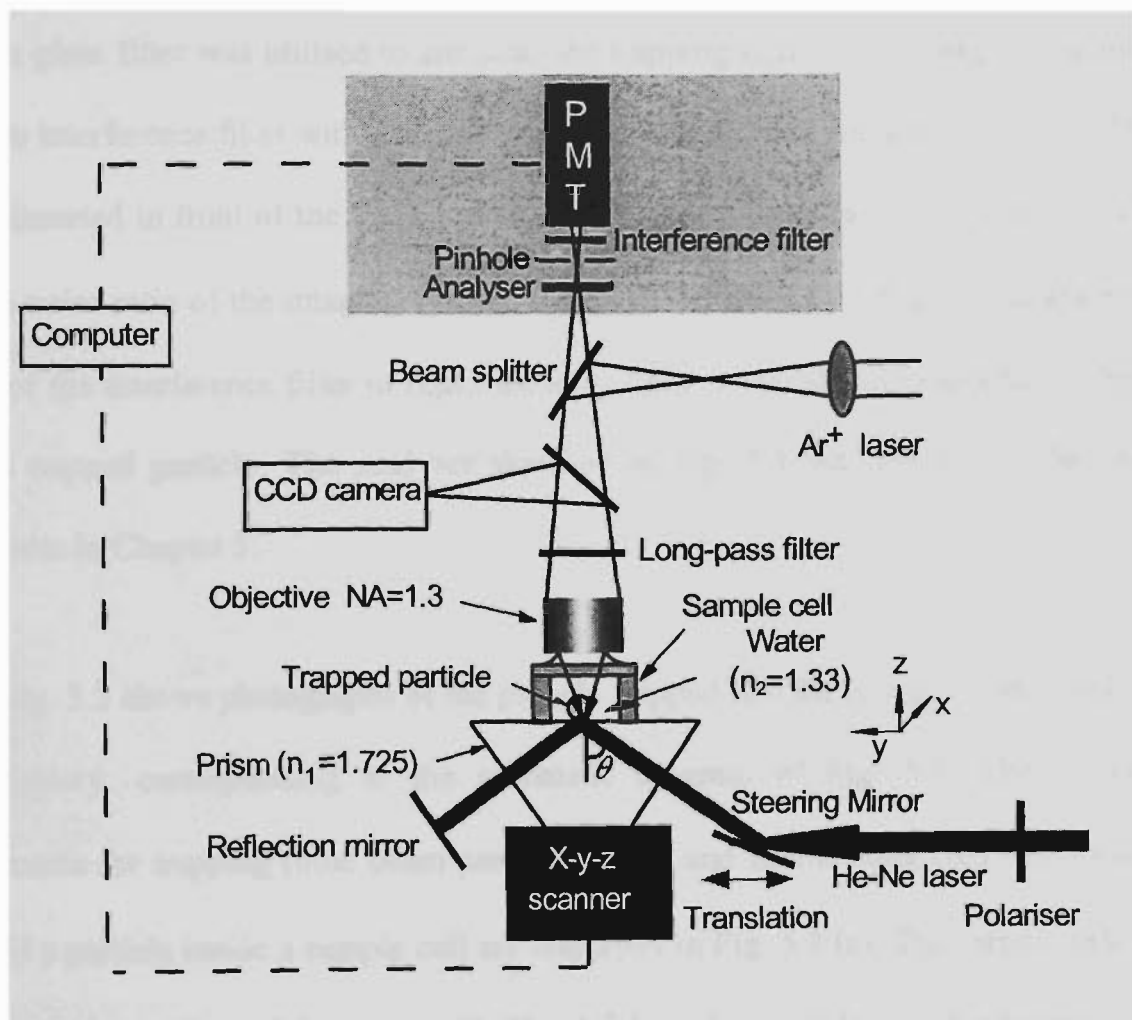
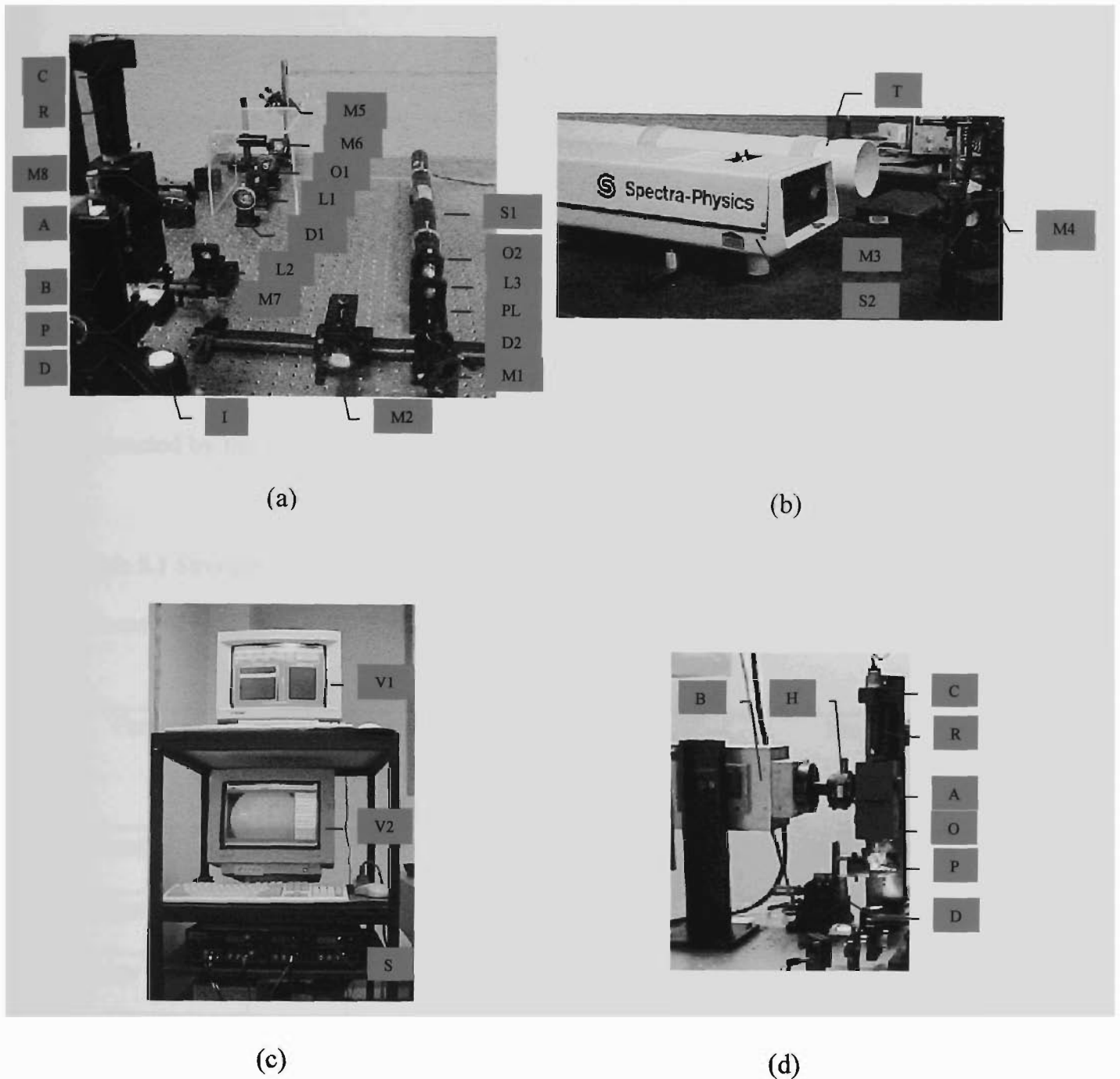


Fig. 5.1 Schematic diagram of particle-trapped NSOM.

An  $\text{Ar}^+$  laser at wavelength  $488 \text{ nm}$  (Spectra-Physics: Stabilite 2017,  $5 \text{ W}$ ) was focused by an oil-immersion objective (Olympus,  $\text{NA} = 1.3$ ,  $160/0.17$ ) for trapping. The short wavelength of  $\text{Ar}^+$  laser produced a sharp focal spot and a stable two-dimensional (2D) trap was achieved for a metallic or dielectric particle by positioning

the focal spot of the trapping laser beam near the bottom of the particle. Under this condition, the trapped particle was held against the surface of the prism. The evanescent wave scattered by the trapped particle was then collected by an air-cooled photomultiplier-tube (PMT, EMI 9658B) mounted at the conjugate imaging point of the trapped particle. A CCD camera (Edmund Scientific) was used to monitor the trapping process under the illumination of a white light source (not shown in the diagram). A long-pass glass filter was utilised to attenuate the trapping light for viewing. A narrow band-pass interference filter with a central wavelength of 633 nm and a bandwidth of 10 nm was inserted in front of the PMT to block the trapping laser beam. To improve the signal-to-noise ratio of the imaging system, a pinhole of diameter 500  $\mu\text{m}$  was aligned in front of the interference filter to reject the stray light scattered from elsewhere other than the trapped particle. The analyser sketched in Fig. 5.1 was not in use for the experiments in Chapter 5.

Fig. 5.2 shows photographs of the particle-trapped NSOM system constructed in the laboratory, corresponding to the schematic diagram of Fig. 5.1. The optical arrangements for trapping (blue beam pass M5 $\rightarrow$ M7) and illuminating (red beam pass S1 $\rightarrow$ M1) a particle inside a sample cell are displayed in Fig. 5.2 (a). The sample cell is mounted on the surface of the prism (P). The Ar<sup>+</sup> laser beam (S2) used for trapping is separated from the system setup as shown in Fig. 5.2 (b). The controlling unit (S) for an  $x$ - $y$ - $z$  scanning stage (D) and the monitors for signal recording (V1) and trapping (V2) are shown in Fig. 5.2 (c). The PMT (B) for signal collection is illustrated in Fig. 5.2 (d).



**Fig. 5.2** Photographs of a particle-trapped NSOM system: (a) optical arrangements for trapping (blue beam pass M5→M7) and illumination (red beam pass S1→M1). A He-Ne laser (S1) for illumination is steered by mirror M2 to a sample cell on top of a prism (P) under the condition of total internal reflection; (b) An Ar<sup>+</sup> laser (S2) used for trapping. The beam is guided by mirrors M3 and M4 into tube T and then passed to M5 shown in (a); (c) a piezoelectric controller (S) for controlling scanning stage D (see (a) and (d)) and monitors for signal recording (V1) and trapping (V2); (d) a PMT (B) for signal collection. M1-M8: mirrors; O, O1, and O2: objectives; L1-L3: lenses; D1 and D2: diaphragms; PL: polariser; I: white light source; A: unit for beam splitters, filter, and analyser; C: CCD camera; R: relay lens; and H: pinhole.

For the measurement of the strength of scattered evanescent waves, the reflection mirror (reflectance  $R = 85\%$ ) parallel to the exit face of the prism was replaced by a beam terminator (not shown in Fig. 5.1). The incident angle of the He-Ne laser inside the prism was set at  $65^\circ$  and the polarisation direction of the He-Ne laser was arranged normal to the plane of incidence (s-polarised). For a particle of given size, the signal was measured three times at a time interval of approximately one-minute and subtracted by the background noise when no particle was trapped.

**Table 5.1** Strength of scattered evanescent waves and image contrast of evanescent interference patterns for different types of laser-trapped particles at the surface of a SF<sub>10</sub> prism.

Particle	Dielectric					Metallic			
	Polystyrene					Gold	Gold	Gold	Silver
Diameter ( $\mu\text{m}$ )	0.1	0.2	0.48	1	2	0.1	0.5	2	2
Signal (a.u.)	0.005	0.01	0.04	0.15	0.25	0.02	0.35	1.95	2.7
Image contrast	1.3%	2.3%	6.2%	10.6%	4.9%	3.9%	6%	12%	14.3%

As shown in Table 5.1, for dielectric particles, when the particle size  $\phi$  is small ( $\phi \leq 1 \mu\text{m}$ ), the dependence of the strength of scattered evanescent waves  $\eta$  (a.u.) on the particle size follows a "radius squared" relation of  $\eta \approx 0.15\phi^2$ . When the particle size becomes large ( $\phi \geq 1 \mu\text{m}$ ), the signal strength displays an almost linear dependence on the size of a laser-trapped dielectric particle.

### 5.2.2 Discussion

The monotonic dependence of the strength of scattered evanescent waves on the size of a dielectric particle is due to the increasing interaction (reflection and multiple scattering) between the particle and an evanescent wave when the particle size is increased. The interaction area is mainly located near the bottom of the particle due to the exponential decaying feature of the evanescent wave field.

The enhancement of signal strength with the particle size may be also related to the morphology dependent resonance (MDR) of a particle illuminated by an evanescent wave [Barber and Chang, 1988]. The physical interpretation of MDR is that rays or beams propagating around the sphere, confined by an almost total internal reflection. After circumnavigating the sphere, the beam returns to the original position in phase [Barber and Chang, 1988]. MDR occurs for a particle when size parameter  $q = 2\pi\phi n_2 / \lambda > 1$ , where  $\lambda$  is the illumination wavelength, and  $n_2$  is the refractive index of the medium [Wannemacher *et al.*, 1999b]. Under the experiment condition ( $\lambda = 633$  nm, and  $n_2 = 1.33$ ), a particle of  $\phi > 76$  nm is capable of generating MDR, which is satisfied in our experiment (refer to Table 5.1). Due to the excitation of MDR, the local fields within, near and on the particle surface become enhanced at the incident frequency, causing the extinction, scattering and absorption to exhibit sharp peaks [Messinger *et al.*, 1981].

MDR also exists for metallic particles and is associated with the surface plasmon (SP) resonance of metallic particles. SP resonance is known as sensitive to the size of a metallic particle. For small particles in the Rayleigh limit ( $\phi \ll \lambda$ ), dipolar SP

resonance may occur, while for large metallic particles outside the Rayleigh limit (as is the case in our experiment), SP resonances of multipolar orders may be excited with phase retardation occurring from different parts of the particle [Messinger *et al.*, 1981]. The enhancement of signal strength due to the excitation of SP resonance will be further discussed in Chapter 6.

As shown in Table 5.1, for polystyrene and gold particles, the scattered signal is increased by a factor of approximately 24 and 96, respectively, when the particle size is increased from 0.1  $\mu\text{m}$  to 2  $\mu\text{m}$ . For a particle of diameter 2  $\mu\text{m}$ , the scattered signal from a gold and a silver particle is approximately 8 and 12 times stronger than that from a polystyrene particle, respectively. The difference of the scattered signal strength between metallic and dielectric particles becomes small as the particle size reduces. It can be concluded from Table 5.1 that for a given particle size, metallic particles show greater signal strength than dielectric particles, as a result of higher reflection, and the possible MDR and SP resonance of metallic particles [Messinger *et al.*, 1981; Barber and Change, 1988; Born and Wolf, 1997]. These results suggest that image quality of particle-trapped NSOM may be enhanced with a metallic particle.

### **5.3 Enhanced image contrast of particle-trapped NSOM with laser-trapped metallic particles**

In this section, we conduct an investigation into the dependence of image contrast on the size of laser-trapped dielectric and metallic particles. The outcome of this study is to quantify the relationship between the signal strength of scattered evanescent waves and

image contrast of particle-trapped NSOM, and therefore demonstrate the significant improvement of image contrast in particle-trapped NSOM with metallic particles.

### 5.3.1 Image contrast of particle-trapped NSOM with dielectric particles

#### 5.3.1.1 Measurement of image contrast with trapped dielectric particles of different sizes

To characterise image contrast of particle-trapped NSOM, we utilise an evanescent wave interference pattern as a test object. In the experiment, the evanescent wave interference pattern was formed at the surface of the prism by aligning the reflection mirror in parallel with the exit face of an equilateral SF<sub>10</sub> prism and setting the incident angle of the He-Ne laser (s-polarised) at  $\theta = 60^\circ$  (see Fig. 5.1). The prism was scanned in the  $x$ - $y$  plane using an  $x$ - $y$ - $z$  scanning stage at a speed of 1  $\mu\text{m/s}$ . The acquisition time for each image (60×132 pixels) was approximately 2 min (top part of Fig. 5.3). The

image contrast  $C$  is defined by  $C = \frac{I_{\max} - I_{\min}}{I_{\max} + I_{\min}}$ , where  $I_{\max}$  and  $I_{\min}$  are the measured

maximum and minimum light intensities, respectively. The image contrast measured from the intensity cross-section (bottom part of Fig. 5.3) of the images at the marked position is 1.3%, 2.3%, 6.2%, 10.6%, and 4.9%, for a particle of diameter  $\phi = 0.1, 0.2, 0.5, 1, \text{ and } 2 \mu\text{m}$ , respectively (see Table 5.1). The crooked area in Fig. 5.3 (d) is possibly due to the drift of the trapping position or the alignment of the prism. A maximum value of image contrast,  $C = 10.6\%$ , was obtained for a particle of  $\phi = 1 \mu\text{m}$  (Fig. 5.4).

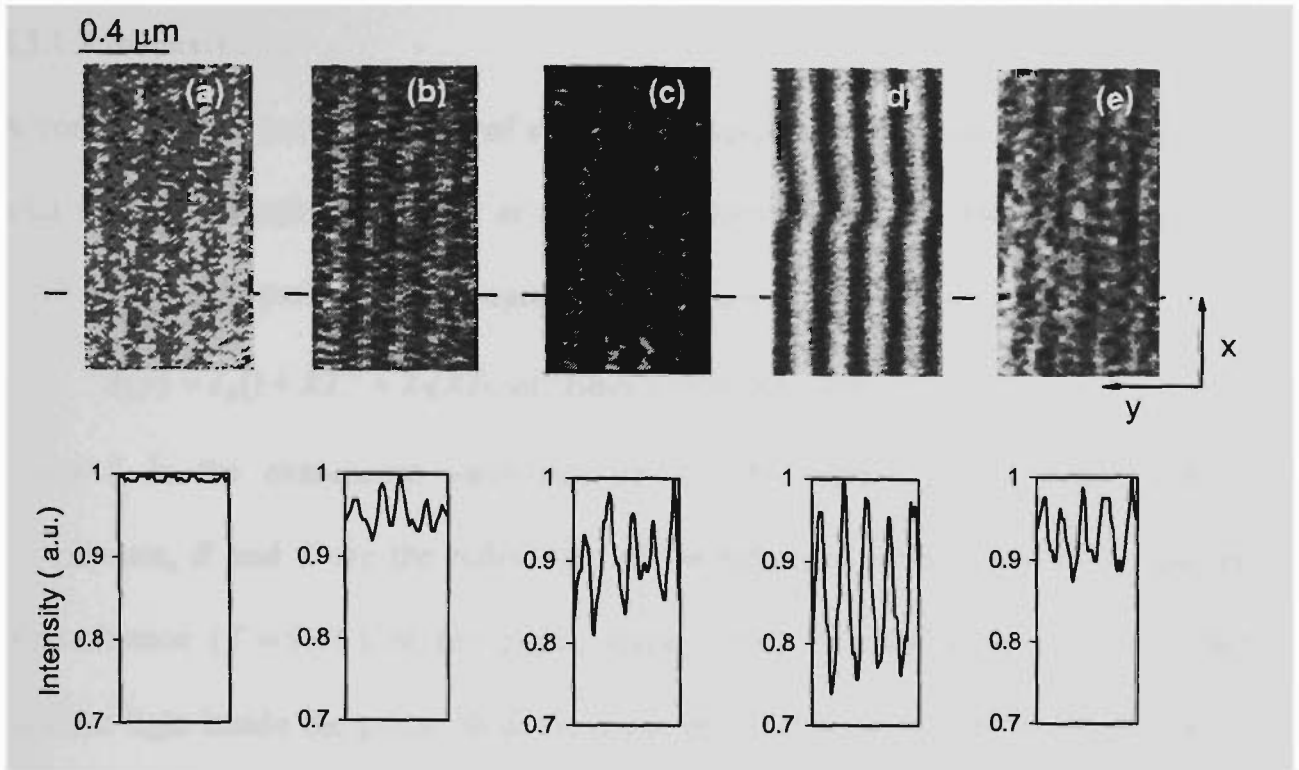


Fig. 5.3 (Top) Images of evanescent wave interference patterns obtained with a laser-trapped particle of (a)  $\phi = 0.1 \mu\text{m}$ ; (b)  $\phi = 0.2 \mu\text{m}$ ; (c)  $\phi = 0.5 \mu\text{m}$ ; (d)  $\phi = 1 \mu\text{m}$  and (e)  $\phi = 2 \mu\text{m}$ , respectively. (Bottom) The intensity cross-sections corresponding to the marked position of each image.

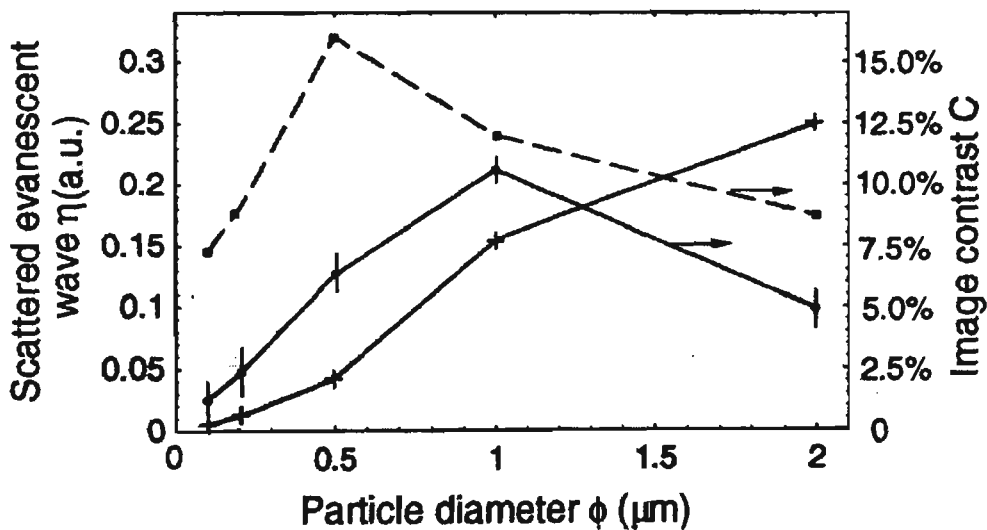


Fig. 5.4 Dependence of the strength of scattered evanescent waves and the image contrast of the evanescent wave interference pattern on the size of a laser-trapped polystyrene particle. The estimated image contrast as a function of the particle size is illustrated as the dashed curve.

### 5.3.1.2 Discussion

According to the previous study of evanescent waves on the surface of a prism upon total internal reflection [Reddick *et al.*, 1990; Meixner *et al.*, 1994], the evanescent wave interference pattern can be expressed as [Bainier *et al.*, 1996]

$$I(y) = I_0 [1 + RT^2 + 2\sqrt{RT}\cos(2kysin\theta + \Phi)]\exp(-2\alpha z) \quad (5.1)$$

where  $I_0$  is the evanescent wave intensity on the surface of the prism without interference,  $R$  and  $T$  are the reflectance of the reflection mirror ( $R = 85\%$ ) and the transmittance ( $T \approx 96\%$ ) of the prism, respectively,  $k$  is the wave number of the incident light inside the prism,  $\Phi$  is the phase constant between two interfered waves, and  $\alpha$  is the attenuating factor of the evanescent wave in the water medium where particles were suspended and can be expressed as  $\alpha = 2\pi / \lambda \sqrt{n_1^2 \sin^2 \theta - n_2^2}$ .

Consequently the fringe visibility  $\tau$  of the evanescent wave interference pattern can be expressed as [Paesler and Moyer, 1996]

$$\tau = \frac{I_{\max} - I_{\min}}{I_{\max} + I_{\min}}, \quad (5.2)$$

where  $I_{\max}$  and  $I_{\min}$  are the maximum and minimum light intensities on the surface of the prism respectively. The value of  $\tau$  is approximately 98% under our experimental condition. The detected light intensity  $I_D$  in Fig. 5.3 can be estimated by a convolution of  $I(y)$  in Eq. (5.1) with the light intensity  $I_c$  distributed on the cap of a trapped particle in contact with the evanescent wave field

$$I_D = I(y) \otimes I_c. \quad (5.3)$$

An accurate solution to Eq. (5.3) is not straightforward due to the lack of information of  $I_c$ . However, as an approximation, the description of  $I_c$  can be considered

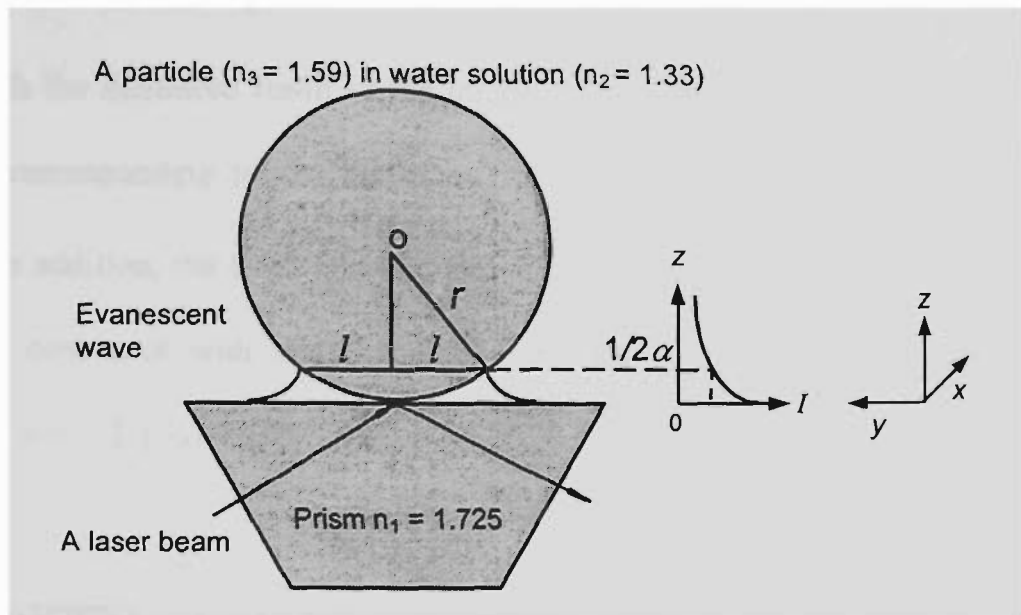


Fig. 5.5 Schematic diagram of a particle of radius  $r$  in contact with an evanescent wave field. The particle is immersed in water solution ( $n_2 = 1.33$ ) on the top of a prism ( $n_1 = 1.725$ ).

to be the same as the tip shape. Because the interference pattern is extended in the  $y$  direction, the cap in contact with the evanescent wave field can be approximate as a simple one-dimensional rectangular function and its size (see Fig. 5.5) is given by

$$I_c = \begin{cases} 1 & |y| < l \\ 0 & \text{otherwise} \end{cases} \quad (5.4)$$

Eq. (5.3) can be further simplified as a nonlinear function

$$I_D(y') = \int_{-l}^l I(y - y') dy' \quad (5.5)$$

The size of the cap can be estimated according to the condition under which the evanescent wave intensity decays to  $1/e$  its value on the surface of the prism, i.e.,  $2l = 2 \cdot \sqrt{r^2 - [r - 1/(2\alpha)]^2}$ . According to Eq. (5.5), the estimated contrast  $C$  for the five particles under our experimental conditions is 7.3%, 9%, 16%, 12% and 8.7%, respectively (dashed curve in Fig. 5.4). In particular, a maximum value of contrast,

$C = 16\%$ , is obtained for a particle of  $\phi = 0.5 \mu\text{m}$ . This behaviour is qualitatively consistent with the measured result of the image contrast except for the fact that the particle size corresponding to the maximum value of contrast is  $\phi = 1 \mu\text{m}$  in the experiment. In addition, the fringe spacing measured in Fig. 5.3 is approximately  $0.21 \mu\text{m}$  which is consistent with that calculated from Eq. (5.1) under the experiment condition ( $\Delta y = 0.212 \mu\text{m}$ ).

The occurrence of a maximum image contrast is due to the competition of two adverse factors, the signal strength and the background level. Although a larger particle can lead to stronger signal strength that may result in better image contrast, it produces simultaneously a larger background that may degrade image contrast. The situation is more complicated in practice as the noise level of an imaging system also contributes to the background. Even for a given noise level, the effect of noise is more pronounced for a smaller particle as the signal strength becomes weaker. As a result, the position corresponding to the maximum image contrast is shifted towards the large particle size as shown in Fig. 5.4. This result indicates that if a small particle is used for high-resolution imaging, a high sensitivity detector is needed in order to achieve an optimal image contrast.

## 5.3.2 Image contrast of particle-trapped NSOM with metallic particles

### 5.3.2.1 Measurement of image contrast with trapped metallic particles of different sizes

In this section, we turn to image contrast of evanescent wave interference patterns with metallic particles of different sizes.

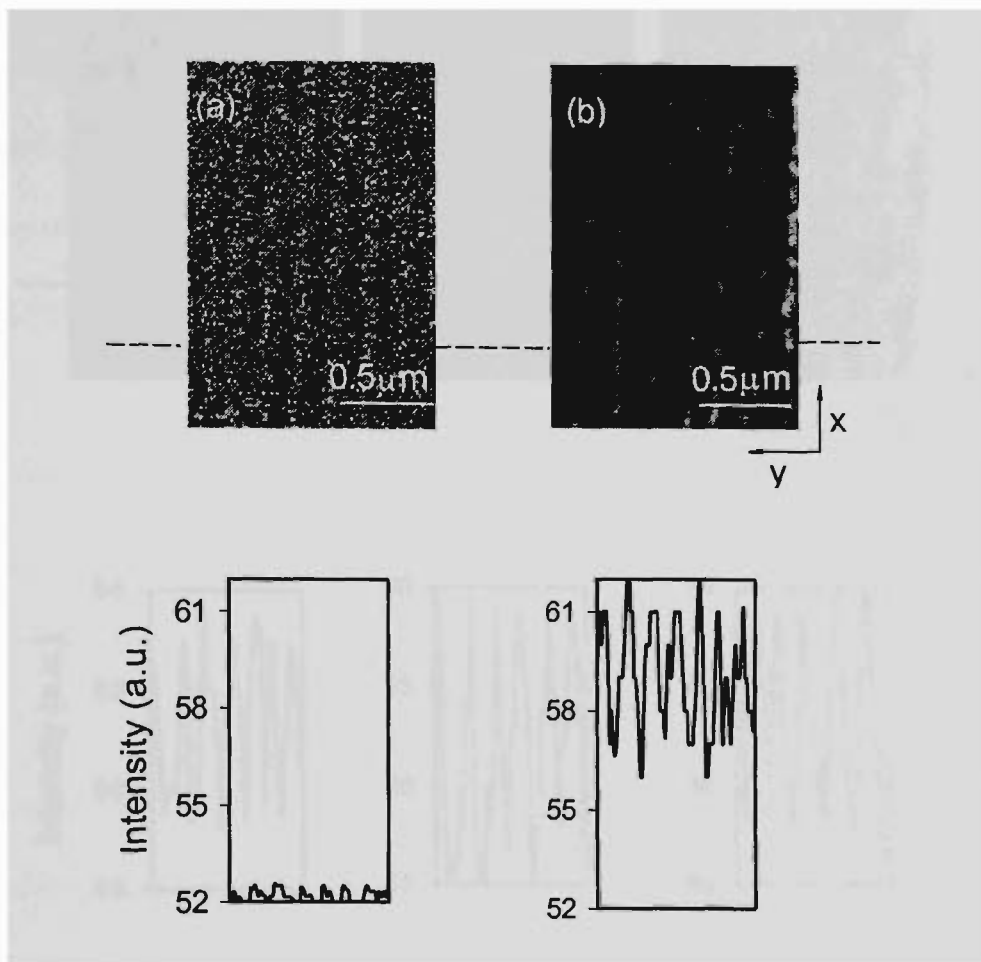


**Fig. 5.6** (Top) Images of evanescent wave interference patterns recorded with a trapped particle of diameter  $0.1 \mu\text{m}$ : (a) polystyrene; (b) gold. (Bottom) The intensity cross-sections corresponding to the marked position of each image.

Fig. 5.6 shows the images of the evanescent wave interference pattern recorded with a trapped polystyrene or gold particle of diameter  $0.1 \mu\text{m}$ . The scanning speed of a trapped polystyrene and gold particle was  $1 \mu\text{m}/\text{sec}$  and  $1.5 \mu\text{m}/\text{sec}$ , respectively, and the corresponding image acquisition time ( $70 \text{ pixels} \times 100 \text{ pixels}$ ) was 2.2 min and 1.6 min. As expected, a trapped gold particle of  $100 \text{ nm}$  exhibits an improvement in image contrast from 1.3% to 3.9% due to its higher scattered signal strength.

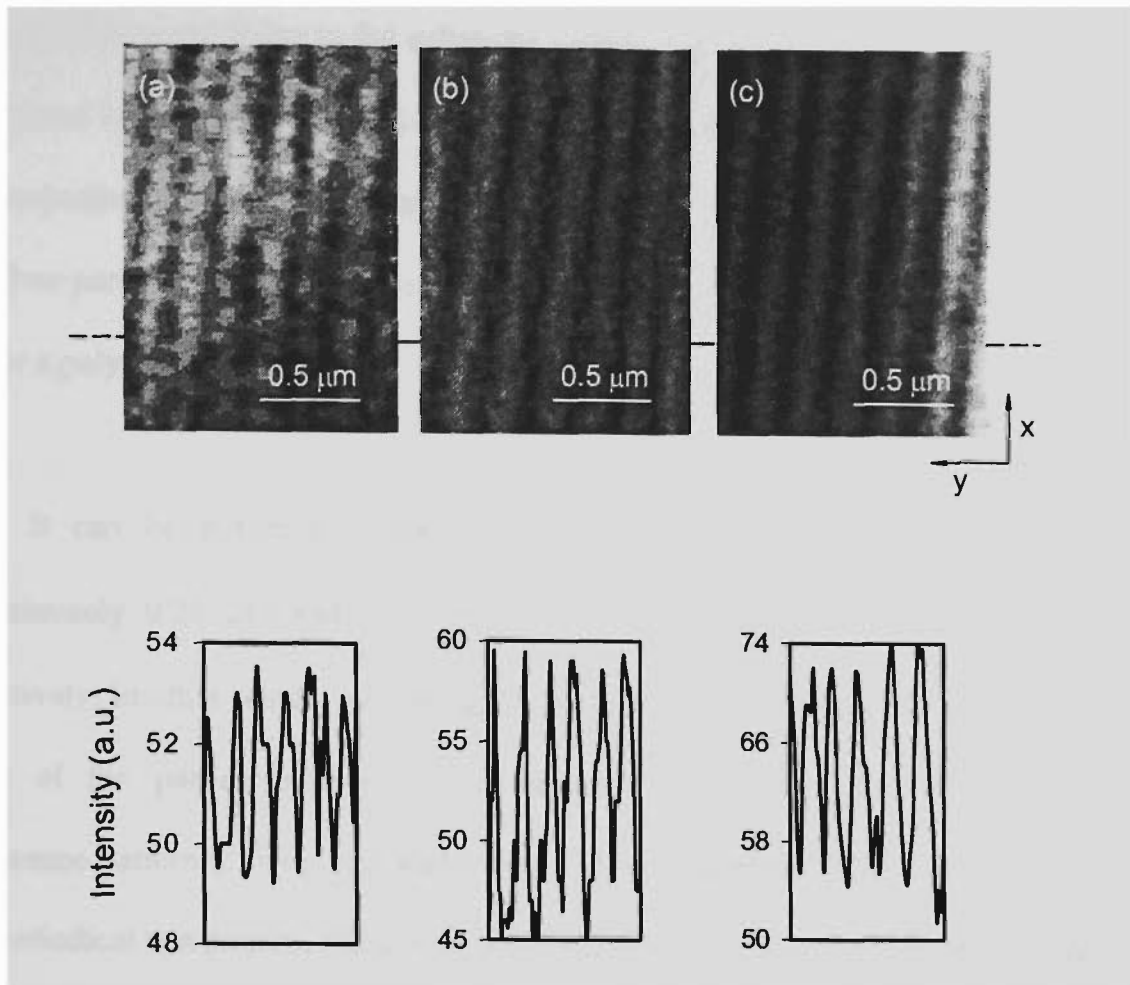


**Fig. 5.7** (Top) Images of evanescent wave interference patterns recorded with a trapped particle of diameter  $2\ \mu\text{m}$ : (a) polystyrene; (b) gold; (c) silver. (Bottom) The intensity cross-sections corresponding to the marked position of each image.

According to Table 5.1 the scattered signal strength increases significantly with the particle size. Therefore the evanescent wave interference patterns were also recorded with trapped particles of diameter  $2\ \mu\text{m}$  and the measured images are displayed in Fig. 5.7. The images were acquired with scanning speeds of  $1\ \mu\text{m}/\text{sec}$ ,  $1.5\ \mu\text{m}/\text{sec}$  and  $1.5\ \mu\text{m}/\text{sec}$  for polystyrene, gold and silver particles, respectively. Consequently, the image contrast measured at the marked position for polystyrene, gold and silver particles of diameter  $2\ \mu\text{m}$  is 4.9%, 12% and 14.3% respectively. A comparison between Fig. 5.6 and Fig. 5.7 confirms that for a given material image contrast is improved by the use of

a large particle mainly due to the enhanced signal strength. For example, image contrast is increased by factors of 2.8 and 2.1 for larger polystyrene and gold particles (see Fig. 5.7), respectively. It is also demonstrated from Fig. 5.7 that the image contrast for gold and silver particles is improved by factors of 1.5 and 1.9 respectively as compared with that for a polystyrene particle.

It can be determined from Figs. 5.6 and 5.7 that the fringe spacing is approximately 0.21  $\mu\text{m}$  and 0.22  $\mu\text{m}$  for a trapped particle of 0.1  $\mu\text{m}$  and 2  $\mu\text{m}$ , respectively. In other words, increasing the particle size by 20 times does not reduce the ability of the particle-trapped NSOM system in resolving the evanescent wave interference pattern at the given wavelength. This is understandable from Eq. (5.5) that for a periodical test pattern, the size of a particle that determines the range of integration only affects the signal strength and contrast of an obtained image. Image resolution can be high for a periodical pattern provided that the difference between signal maximum and minimum is detectable by a given detector.

### **5.3.2.2 Discussion**

According to Eq. (5.5), the image contrast of evanescent interference pattern acquired with a particle of 2  $\mu\text{m}$  in diameter is calculated to be  $C = 16\%$  and the fringe spacing is 0.212  $\mu\text{m}$ . The latter is in good agreement with the measured fringe spacings, whereas the former agrees with the measured image contrast for gold and silver particles. In general, the larger the size of a trapped particle the better the image contrast is. However, it should be pointed out that the contrast of the measured periodic fringes is also affected by the scattered signal strength when the noise of the experimental system is given. Therefore, the image contrast in Fig. 5.7 (a) is poorer than that in Figs. 5.7 (b)

and 5.7 (c) because of the lower scattered signal strength from a polystyrene particle in Fig. 5.7 (a) and the image contrast in Fig. 5.6 is poorer than that in Fig. 5.7 resulting from the lower signal strength from smaller particles.

#### **5.4 Image enhancement for a prism surface with laser-trapped metallic particles**

The enhancement of image contrast with the use of a metallic particle is confirmed by imaging the surface of a BK7 prism (surface flatness  $\lambda/4$ ,  $n = 1.51$ ). The surface structure was first recorded with a Fluoview confocal microscope (Fig. 5.8 (a)), and then with a particle-trapped NSOM system (Figs. 5.8 (b) and (c)). The image in Fig. 5.8 (a) was recorded in a reflection mode with a single-line  $\text{Ar}^+$  laser of 3 mW ( $\lambda = 488$  nm) and an oil-immersion objective ( $\text{NA} = 1.25$ ,  $60\times$ ). The experimental setup used for Figs. 5.8 (b) and (c) was the same as that in Fig. 5.1 except that the  $\text{SF}_{10}$  prism was replaced by a BK7 prism of lower refractive index and the incident angle was increased to  $70^\circ$  to satisfy the total internal reflection condition. The particle probes used for Figs. 5.8 (b) and (c) are dielectric polystyrene and metallic gold particles of  $\phi = 100$  nm in diameter, respectively. The images were acquired with scanning speeds of  $1 \mu\text{m}/\text{sec}$  and  $1.5 \mu\text{m}/\text{sec}$  for polystyrene and gold particles, respectively. To strengthen the SP resonance associated with the gold particle, the He-Ne laser used for illumination was fixed at a p-polarised state (polarised in the plane of incidence) in Figs. 5.8 (b) and (c).

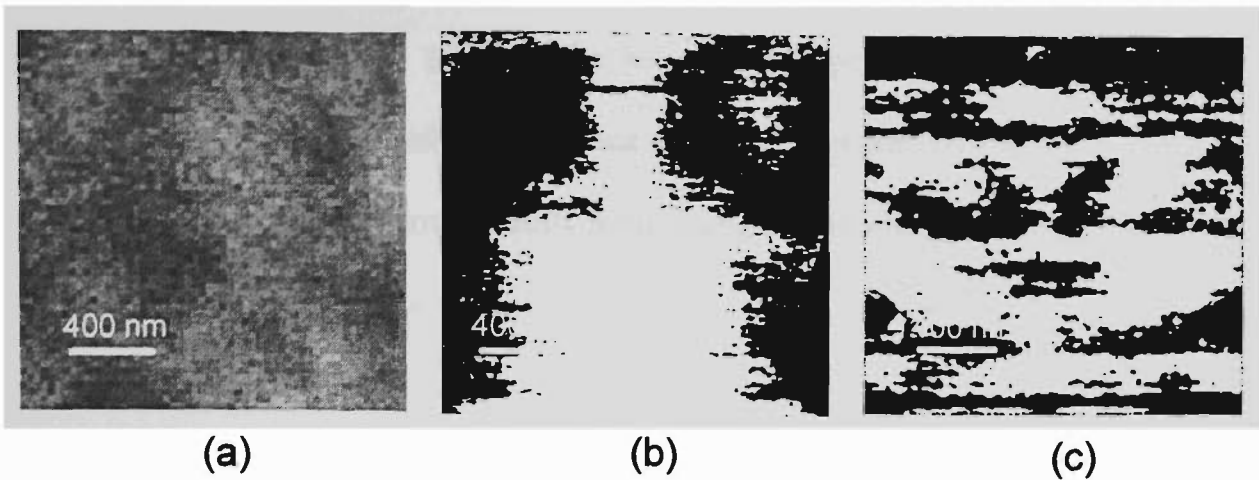


**Fig. 5.8** Images of the surface structures of a BK7 prism recorded with: (a) a Fluoview confocal microscope; (b) a polystyrene particle of 100 nm in diameter; and (c) a gold particle of 100 nm in diameter. The images in (b) and (c) were recorded with an illumination He-Ne laser of a p-polarised state.

Clearly, Figs. 5.8 (b) and (c) show more detail than Fig. 5.8 (a) owing to the superior resolution of the particle-trapped NSOM system over that of a confocal microscope. Fig. 5.8 also indicates that the image obtained with a metallic particle (Fig. 5.8 (c)) shows more details than that acquired with a dielectric particle (Fig. 5.8 (b)) because of the increased signal strength resulting from high scattering efficiency of a trapped metallic particle. The improvement of image quality may be also related to the surface structure of the BK7 prism which could benefit MDR and SP resonance [Wannemacher *et al.*, 1999a].

## 5.5 Conclusion

In conclusion, it has been found that the strength of scattered evanescent waves increases monotonically with the size of a laser-trapped particle (dielectric or metallic), while a maximum image contrast of an evanescent interference pattern is obtained for a particle of particular size. This result implies that an optimal image contrast can be achieved for a small particle by employing a high sensitivity detector. Compared with

imaging with a dielectric particle, the use of a trapped metallic particle leads to enhanced image contrast and increased scanning speed in particle-trapped NSOM. This enhancement of image contrast results from strong signal strength scattered by metallic particles.

## CHAPTER SIX

# Imaging Enhancement with Laser-Trapped Metallic Particles: Effect of Depolarisation

### 6.1 Introduction

THE use of polarisation information of evanescent waves offers a new dimension for image improvement in near-field scanning optical microscopy (NSOM) [Keller *et al.*, 1993, 1995; Adelman *et al.*, 1999; Aigouy *et al.*, 1999]. This method has proved advantageous for apertureless NSOM using a metallic needle probe since it is effective in retrieving the original information of a sample with little distortion.

In Chapter 5, we have examined the issue of signal strength in near-field Mie scattering. It has been demonstrated that the use of a metallic particle instead of a dielectric particle for particle-trapped NSOM can result in better image contrast owing to enhanced signal strength. Mie scattering theory states that scattering of a propagating wave by a small particle leads to depolarisation [Born and Wolf, 1997]. By analogy, scattering of an evanescent wave may also introduce depolarisation that could affect particle-trapped NSOM. Our study on this issue as will be presented in the current chapter is conducted initially for dielectric particles and then extended to that for metallic particles because of the complicity in the latter case. Similar to the methodology adopted in Chapter 5, our investigation into the depolarisation of near-field Mie scattering is

focused on the effect of particle size on the degree of polarisation and particle-trapped NSOM.

This chapter is arranged as follows. Section 6.2 is concentrated on investigating the dependence of phase shift of evanescent waves on the polarisation direction of an illumination laser beam. In section 6.3, the degree of polarisation of scattered evanescent waves is characterised in detail for dielectric and metallic particles, respectively. The polarisation-gating method, a technique previously employed in confocal microscopy [Schmitt *et al.*, 1992; Schilders *et al.*, 1998], is adopted in section 6.4 for image enhancement of particle-trapped NSOM based on section 6.3. The polarisation-gating method is then applied to the imaging of a prism surface in section 6.5 to show its effect on image contrast. A conclusion on the experimental characterisation is finally given in section 6.6.

## **6.2 Evanescent waves on a prism surface on the polarisation states of illumination**

### **6.2.1 Phase shift of evanescent waves**

In the following, we inspect the phase shift of evanescent waves under the illumination of a laser beam of different polarisation states [Ke and Gu, 1998b].

As demonstrated by other researchers, an evanescent wave, generated at the surface of a prism with a laser beam under the condition of total internal reflection, experiences a phase shift when the polarisation state of an illuminated laser beam is

altered [Courjon *et al.*, 1994]. This phase shift can be analytically solved based on Maxwell boundary conditions.

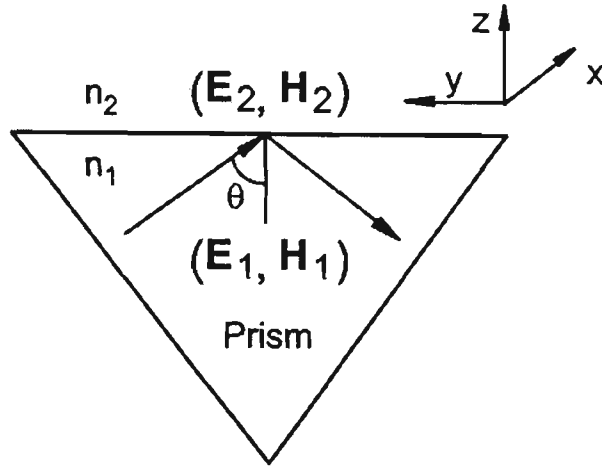


**Fig 6.1** Schematic diagram of a prism illuminated with an incident laser beam under the condition of total internal reflection. The electromagnetic fields in the prism ( $n_1$ ) and the medium ( $n_2$ ) are represented by  $(\mathbf{E}_1, \mathbf{H}_1)$  and  $(\mathbf{E}_2, \mathbf{H}_2)$ , respectively. The electromagnetic field in medium  $n_2$  is evanescent ( $n_1 > n_2$ ).

As shown in Fig. 6.1, a prism (refractive index  $n_1$ ) is illuminated with a p-polarised beam (polarised in parallel to the plane of incidence for an illumination beam) under the condition of total internal reflection. The refractive index of the medium above the prism is  $n_2$  ( $n_2 < n_1$ ). Assume  $b_1 = k_0 n_1 \cos \theta$  and  $p_2 = \sqrt{k_0^2 n_1^2 \sin^2 \theta - k_0^2 n_2^2}$ , where  $k_0$  is the wave number of light in free space. The tangential fields can be expressed as

$$\begin{cases} E_{y1} = -\cos \theta / n_1 \cdot A_1 \exp(-ib_1 z) + \cos \theta / n_1 \cdot B_1 \exp(ib_1 z), \\ H_{x1} = A_1 \exp(-ib_1 z) + B_1 \exp(ib_1 z), \end{cases} \quad (6.1)$$

in the prism, and

$$\begin{cases} E_{y2} = iC_1 p_2 / (k_0 n_2^2) \cdot \exp(-p_2 z), \\ H_{x2} = C_1 \exp(-p_2 z), \end{cases} \quad (6.2)$$

in the medium. Here  $A_1$  and  $B_1$  are amplitude coefficients of the incident and reflected beams inside the prism, and  $C_1$  is the amplitude coefficient of the evanescent wave field in the medium, respectively [Ke and Gu, 1998b]. Applying Maxwell boundary conditions to Eqs. (6.1) and (6.2), we obtain

$$\begin{cases} \cos \theta / n_1 \cdot B_1 - \cos \theta / n_1 \cdot A_1 = iC_1 p_2 / (k_0 n_2^2), \\ A_1 + B_1 = C_1. \end{cases} \quad (6.3)$$

The amplitude coefficients can be solved using Eq. (6.3) and given by

$$\begin{cases} B_1 / A_1 = \frac{k_0 n_2^2 \cos \theta + i n_1 p_2}{k_0 n_2^2 \cos \theta - i n_1 p_2}, \\ C_1 / A_1 = \frac{2k_0 n_2^2 \cos \theta}{k_0 n_2^2 \cos \theta - i n_1 p_2}. \end{cases} \quad (6.4)$$

Hence for a p-polarised beam, the phase shift  $\phi_{1p}$  of the reflected and the phase shift  $\phi_{2p}$  of the transmitted wave (evanescent wave) in relation to the incident wave can be described as

$$\begin{cases} e^{i\phi_{1p}} = -B_1 / A_1, \\ e^{i\phi_{2p}} = C_1 / A_1, \end{cases} \quad (6.5)$$

which can be further explicitly expressed as

$$\begin{cases} \phi_{1p} = 2 \tan^{-1} \left( \frac{n_1 \sqrt{n_1^2 \sin^2 \theta - n_2^2}}{n_2^2 \cos \theta} \right), \\ \phi_{2p} = \tan^{-1} \left( \frac{n_1 \sqrt{n_1^2 \sin^2 \theta - n_2^2}}{n_2^2 \cos \theta} \right). \end{cases} \quad (6.6)$$

Using the same approach, the tangential fields for an s-polarised laser beam (polarised in perpendicular to its incident plane) can be expressed as

$$\begin{cases} E_{x1} = A_1' \exp(-ib_1z) + B_1' \exp(ib_1z), \\ H_{y1} = n_1 \cos \theta \cdot A_1' \exp(-ib_1z) - n_1 \cos \theta \cdot B_1' \exp(ib_1z), \end{cases} \quad (6.7)$$

in the prism, and

$$\begin{cases} E_{x2} = C_1' \exp(-p_2z), \\ H_{y2} = -iC_1' p_2 / k_0 \cdot \exp(-p_2z), \end{cases} \quad (6.8)$$

in the medium. Here again  $A_1'$  and  $B_1'$  are amplitude coefficients of the incident and the reflected beams inside the prism, and  $C_1'$  is the amplitude coefficient of the evanescent wave field in the medium, respectively [Ke and Gu, 1998b]. For an s-polarised laser beam, the phase shift  $\phi_{1s}$  of the reflected wave and the phase shift  $\phi_{2s}$  of the transmitted wave can be finally expressed as

$$\begin{cases} \phi_{1s} = 2 \tan^{-1} \left( \frac{\sqrt{n_1^2 \sin^2 \theta - n_2^2}}{n_1 \cos \theta} \right), \\ \phi_{2s} = \tan^{-1} \left( \frac{\sqrt{n_1^2 \sin^2 \theta - n_2^2}}{n_1 \cos \theta} \right). \end{cases} \quad (6.9)$$

It is obviously seen from Eqs. (6.6) and (6.9) that for both s- and p-polarised incident beams, the phase shift of the reflected wave is exactly twice as large as that for the transmitted evanescent wave. Secondly, the phase shift on the surface of the prism (transmission or reflection) is related to the incident angle of an illumination laser beam and the refractive indices of the media forming the boundary. From Eqs. (6.6) and (6.9), the difference of the phase shift of the reflected and the transmitted light between the s-

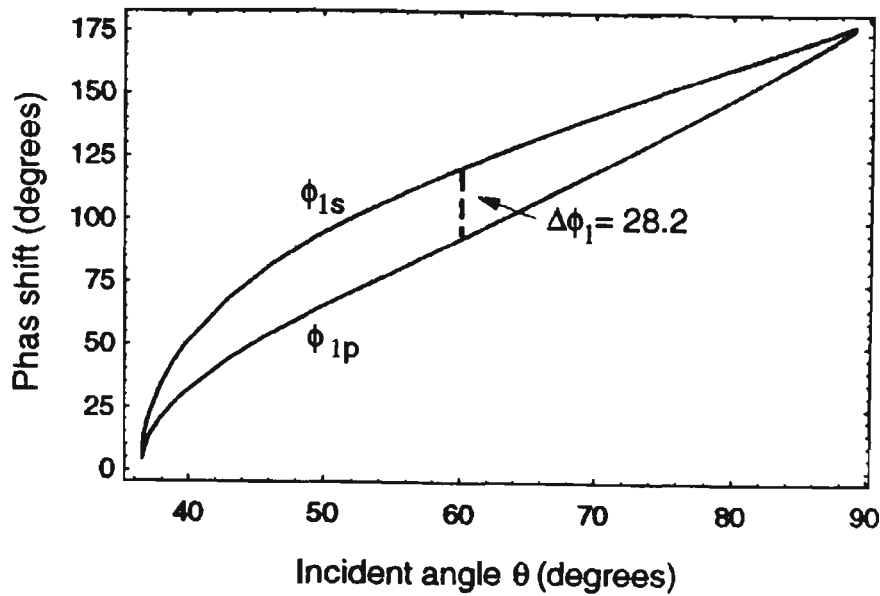


**Fig. 6.2** Phase shift of a reflected propagating wave under the s- and p-polarised laser beam illumination. The refractive indices of the prism and the medium above the prism are 1.75 and 1.33 (water), respectively.  $\phi_{1s}$  and  $\phi_{1p}$  are the phase shifts of the reflected propagating wave for s- and p-polarised incident beams, respectively.

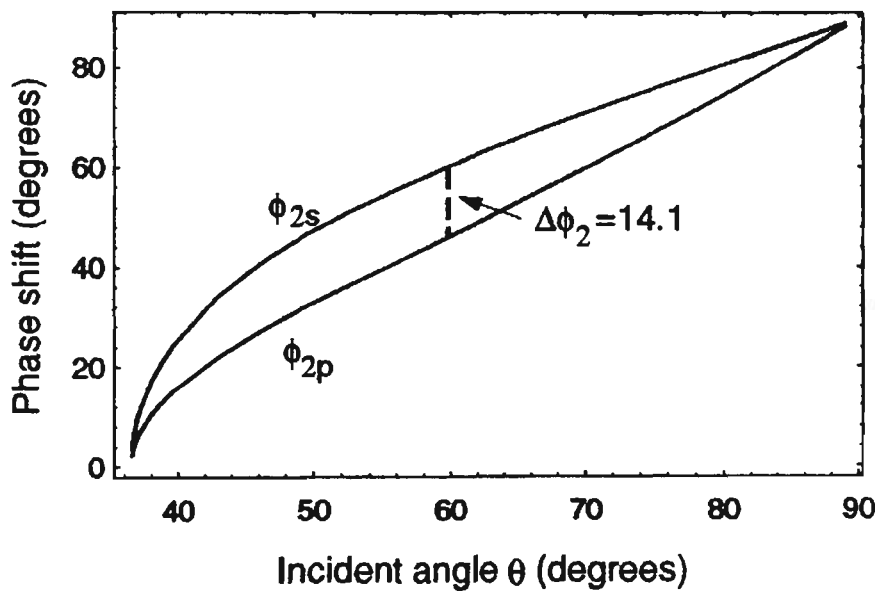


**Fig. 6.3** Phase shift of a transmitted evanescent wave under the s- and p-polarised laser beam illumination. The refractive indices of the prism and the medium above the prism are 1.75 and 1.33 (water), respectively.  $\phi_{2s}$  and  $\phi_{2p}$  are the phase shifts of the transmitted evanescent wave for s- and p-polarised incident beams, respectively.

and p-polarised beam illumination,  $\Delta\phi_1$  and  $\Delta\phi_2$ , can be calculated and are illustrated in Fig. 6.2 and Fig. 6.3, respectively. At an incident angle of  $\theta = 60^\circ$ ,  $\Delta\phi_1$  for the reflected propagating wave and  $\Delta\phi_2$  for the transmitted evanescent wave is  $\Delta\phi_1 = 28.2^\circ$  and  $\Delta\phi_2 = 14.1^\circ$ , respectively.

### 6.2.2 Measurement of the phase shift of evanescent waves

In practice, the phase-shift difference of the evanescent waves may be evaluated by detecting the evanescent wave interference fringes under s- and p-polarised beam illumination. This detection can be implemented using scanning tunnelling optical microscopy [Courjon *et al.*, 1994]. However, we have used a trapped particle as a near-field probe to detect the evanescent wave interference fringe [Gu and Ke, 1999b]. The experimental setup is the same as that in Fig. 5.1 but without the use of the analyser. Following the method as described in section 5.3 of Chapter 5, we obtained images of evanescent wave interference patterns with a laser-trapped particle of 2  $\mu\text{m}$  in diameter (see Fig. 6.4). The incident illumination laser beam was altered from an s- to a p-polarised state. The signal strength under p-polarised beam illumination is weaker than that under s-polarised beam illumination due to the lower reflectance of the steering mirror (see Fig. 5.1) in the former case. The phase-shift difference of the evanescent waves can be determined as  $\Delta\phi = 10.47^\circ$  from Fig. 6.4 according to  $\Delta\phi = 2\pi(L - L')/L$ . The measured value of the phase-shift difference is different from the calculated value ( $\Delta\phi = 14.1^\circ$ ) for an evanescent wave at the surface of the prism as described in section

6.2.1. This discrepancy indicates that depolarisation occurs during the scattering of evanescent waves by small particles.

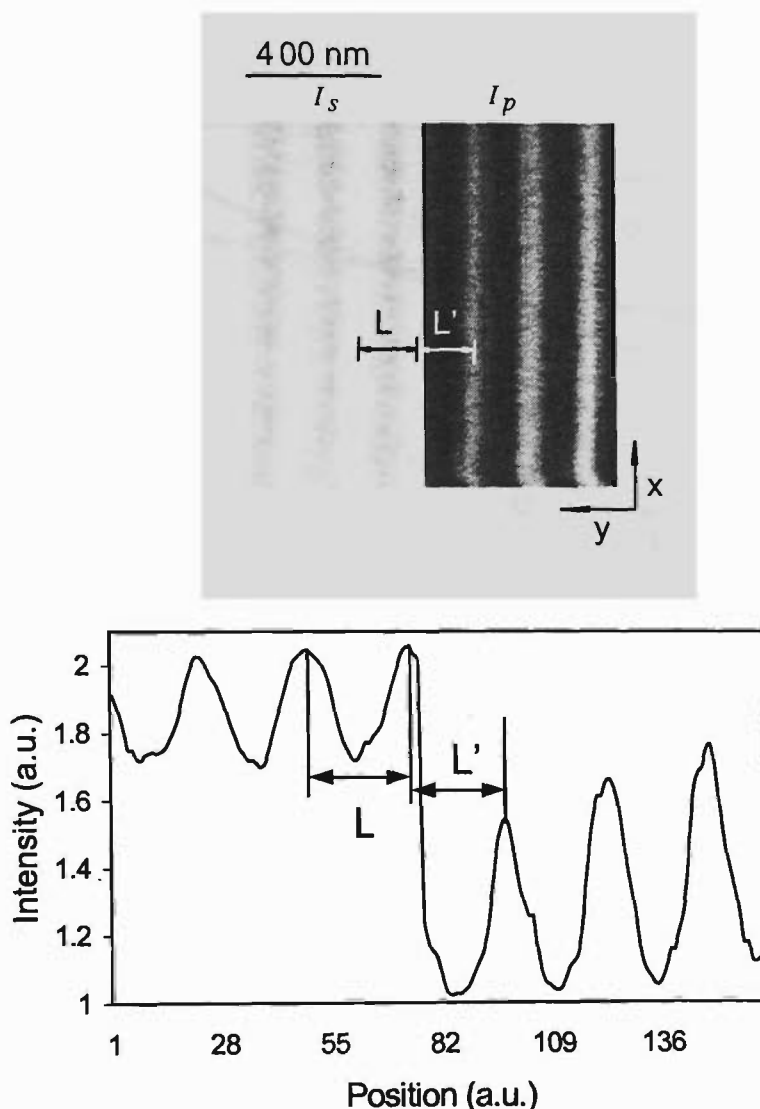
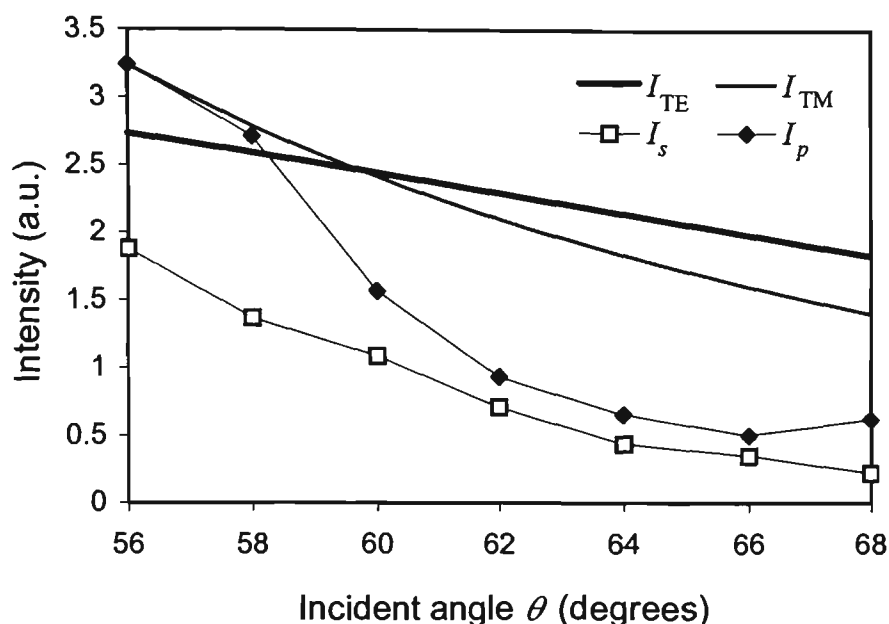


Fig. 6.4 (Top) Images of evanescent wave interference patterns under s- and p-polarised beam illumination (He-Ne laser beam). (Bottom) Intensity cross-sections correspond to the images.

Fig. 6.5 shows the measured strength of scattered evanescent waves as a function of the incident angle under s- and p-polarised He-Ne laser beam illumination. The evanescent wave intensity at the surface of the prism  $I_M$ , normalised by the incident light intensity  $I_0$ , can be expressed as

$$I_M / I_0 = \frac{4n_1^2 \cos^2 \theta}{(n_1^2 - n_2^2)} \left[ \frac{n_2^2}{n_1^2 - (n_1^2 + n_2^2) \cos^2 \theta} \right]^j, \quad (6.10)$$



**Fig. 6.5** Measured strength of scattered evanescent waves as a function of the incident angle  $\theta$ .  $I_{TE}$  and  $I_{TM}$ : calculated intensity of the evanescent wave at the surface of the prism under s- and p-polarised beam illumination;  $I_s$  and  $I_p$ : measured scattered signal under s- and p-polarised beam illumination.

where  $\theta$  is the incident angle of the He-Ne laser, and  $j$  is 0 and 1 for s- and p-polarised incident beams, respectively [Mahan and Bitterli, 1978]. However, the measured signals of the scattered evanescent wave by a trapped particle of  $\phi = 2 \mu\text{m}$  under s- and p-polarised beam illumination (curves  $I_s$  and  $I_p$  in Fig. 6.5) show a different tendency from the results (curves  $I_{TE}$  and  $I_{TM}$  in Fig. 6.5) calculated by Eq. (6.10). This discrepancy indicates the occurrence of depolarisation during the scattering of the evanescent waves by small particles. This effect will be further examined in the next section.

## 6.3 Depolarisation of scattered evanescent waves

### 6.3.1 Depolarisation of evanescent waves scattered by trapped dielectric particles

In this section, we conduct a detailed experimental investigation into the depolarisation of scattered evanescent waves using laser-trapped dielectric particles of different sizes. The experimental setup is similar to that illustrated in Fig. 5.1 of Chapter 5. The reflection mirror was blocked in this experiment. The degree of polarisation of scattered evanescent waves,  $\gamma$ , can be evaluated according to the following definition:

$$\gamma = \frac{I_{\parallel} - I_{\perp}}{I_{\parallel} + I_{\perp}}, \quad (6.11)$$

where subscripts  $\parallel$  and  $\perp$  denote an analyser parallel or perpendicular to the polarisation state of the illumination He-Ne beam. The larger the  $\gamma$  value, the weaker the effect of depolarisation.

Fig. 6.6 illustrates the light intensities measured with a polariser and an analyser for particles of diameters  $\phi = 0.1, 0.2, 0.5, 1$  and  $2 \mu\text{m}$ .  $I_s$  and  $I_p$  were measured for s- and p-polarised beams without an analyser,  $I_{ss}$  and  $I_{sp}$  were measured with an analyser parallel and perpendicular to the incident s-polarised beam, and  $I_{pp}$  and  $I_{ps}$  were measured with an analyser parallel and perpendicular to the incident p-polarised beam, respectively. According to the signal strength and the noise level of the imaging system, the incident angle  $\theta$  of the He-Ne laser was chosen to be  $56^\circ$  to  $58^\circ$  for a particle of  $0.1 \mu\text{m}$  in diameter,  $56^\circ$  to  $62^\circ$  for particles of  $0.2$  and  $0.5 \mu\text{m}$  in diameters, and  $56^\circ$  to  $68^\circ$  for particles of  $1$  and  $2 \mu\text{m}$  in diameters, respectively.

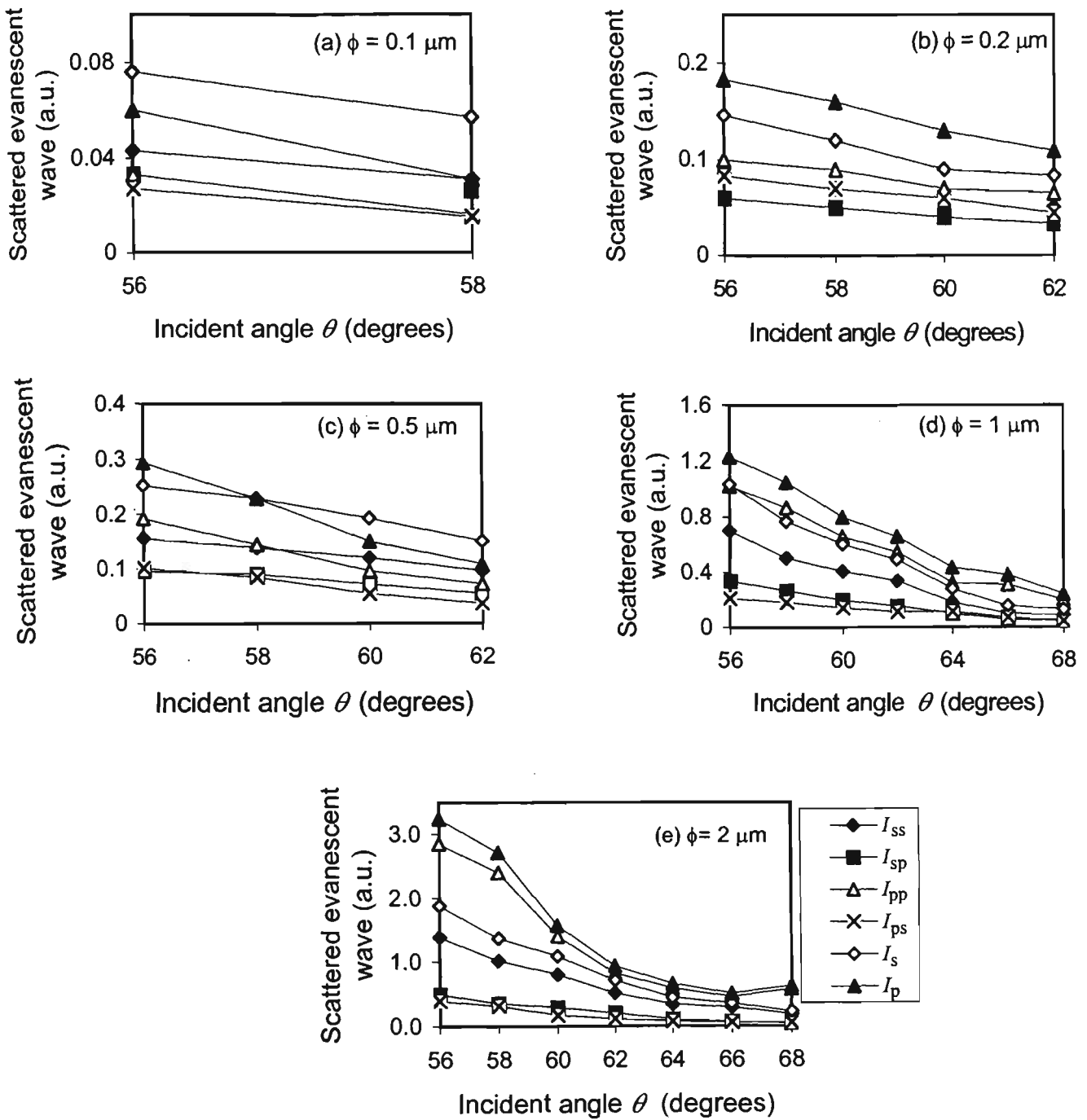


**Fig. 6.6** Dependence of the signal strength of scattered evanescent waves on the incident angle  $\theta$  of an illumination He-Ne laser beam for dielectric particles of (a)  $\phi=0.1 \mu\text{m}$ ; (b)  $\phi=0.2 \mu\text{m}$ ; (c)  $\phi=0.5 \mu\text{m}$ ; (d)  $\phi=1 \mu\text{m}$ ; and (e)  $\phi=2 \mu\text{m}$ .  $I_s$  and  $I_p$ : measured scattered signal without using an analyser under s- and p-polarised beam illumination;  $I_{ss}$  and  $I_{sp}$ : measured scattered signal with an s-analyser and a p-analyser under s-polarised beam illumination, respectively;  $I_{ps}$  and  $I_{pp}$ : measured scattered signal with an s-analyser and a p-analyser under p-polarised beam illumination, respectively.

As expected, for both s and p-polarised illumination beams, the scattered signals decrease when the incident angle  $\theta$  increases due to the weaker interaction between a particle and an evanescent wave. Further the intensity of scattered evanescent waves changes with the polarisation directions of the polariser and the analyser. This indicates that for a linearly-polarised incident beam, cross-polarisation components appear in the scattered wave field in the process of near-field Mie scattering as a result of depolarisation.

Using Eq. (6.11), the degree of polarisation of scattered evanescent waves for individual particles shown in Fig. 6.6 can be evaluated and is plotted in Fig. 6.7. For an s-polarised illumination beam, the averaged degree of polarisation of scattered evanescent waves is approximately  $\gamma = 0.11, 0.17, 0.25, 0.31,$  and  $0.51$  for particles of diameters  $\phi = 0.1, 0.2, 0.5, 1$  and  $2 \mu\text{m}$ , respectively. By contrast, for a p-polarised illumination light, the averaged degree of polarisation of scattered evanescent waves is approximately  $\gamma = 0.06, 0.12, 0.30, 0.65,$  and  $0.78$  for particles of diameters  $\phi = 0.1, 0.2, 0.5, 1$  and  $2 \mu\text{m}$ , respectively. The averaged degree of polarisation of scattered evanescent waves as a function of the size of a trapped particle is summarised in Fig. 6.8 for both s- and p-polarised beam illumination.

Several features of scattered evanescent waves can be summarised from Figs. 6.6-6.8. Firstly, the degree of polarisation of scattered evanescent waves increases with the particle size for both s- and p-polarised incident beams. This property is similar to that of

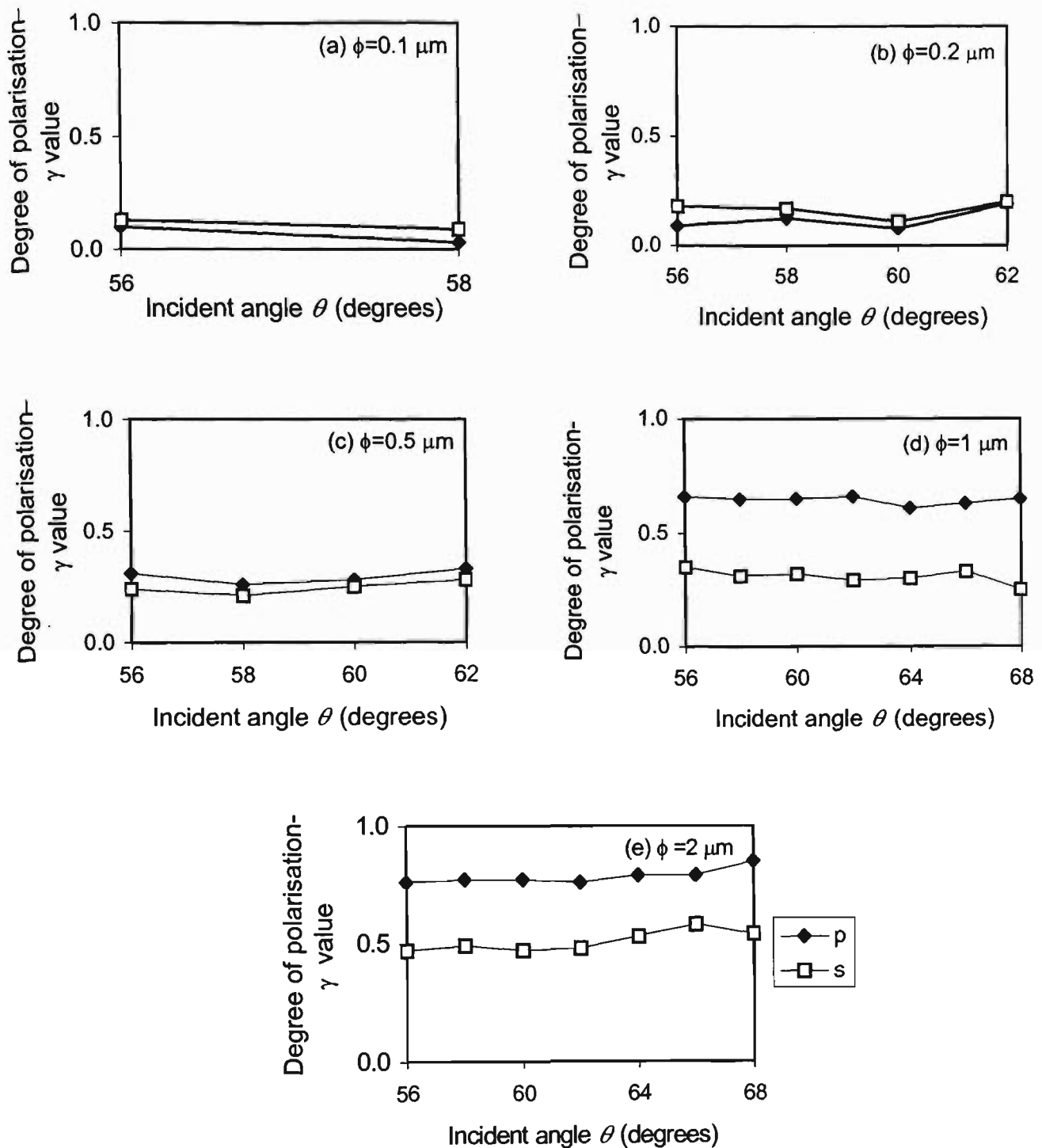


**Fig. 6.7** Dependence of the degree of polarisation of scattered evanescent waves on the incident angle  $\theta$  of an illumination He-Ne laser beam for dielectric particles of (a)  $\phi = 0.1 \mu\text{m}$ ; (b)  $\phi = 0.2 \mu\text{m}$ ; (c)  $\phi = 0.5 \mu\text{m}$ ; (d)  $\phi = 1 \mu\text{m}$ ; and (e)  $\phi = 2 \mu\text{m}$ .

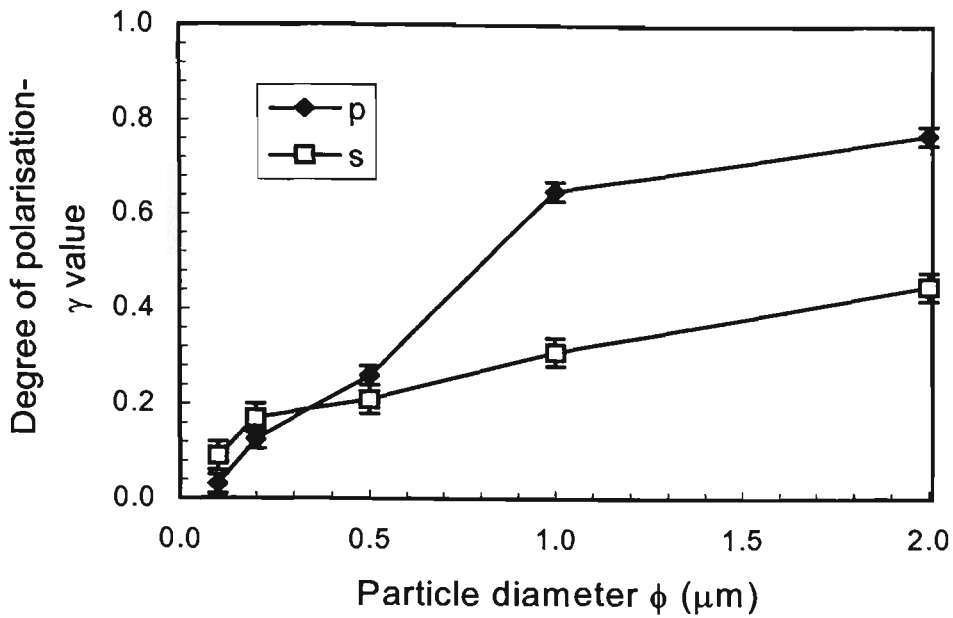


**Fig. 6.8** The averaged degree of polarisation of scattered evanescent waves as a function of the size of a polystyrene particle for an illumination beam of both s- and p-polarised states.

Mie scattering where the depolarisation of a propagating wave is stronger for a smaller particle [Born and Wolf, 1997]. This is due to the difference in scattering cross-section for Rayleigh and Mie particles. Secondly, the degree of polarisation is insensitive to the incident angle of the illumination He-Ne laser since the interaction between a particle and an evanescent wave is highly localised at the bottom of the particle. Thirdly, the depolarisation of scattered evanescent waves is more significant for s-polarised light than p-polarised light when the particle size is approximately  $\phi \geq 0.5 \mu\text{m}$ . However this situation reverses for a smaller particle ( $\phi < 0.5 \mu\text{m}$ ). This may be related to the scattering cross-section of a dielectric particle that has different dependences on the particle size for s and p-polarised illumination beams [Wannemacher *et al.*, 1999a].

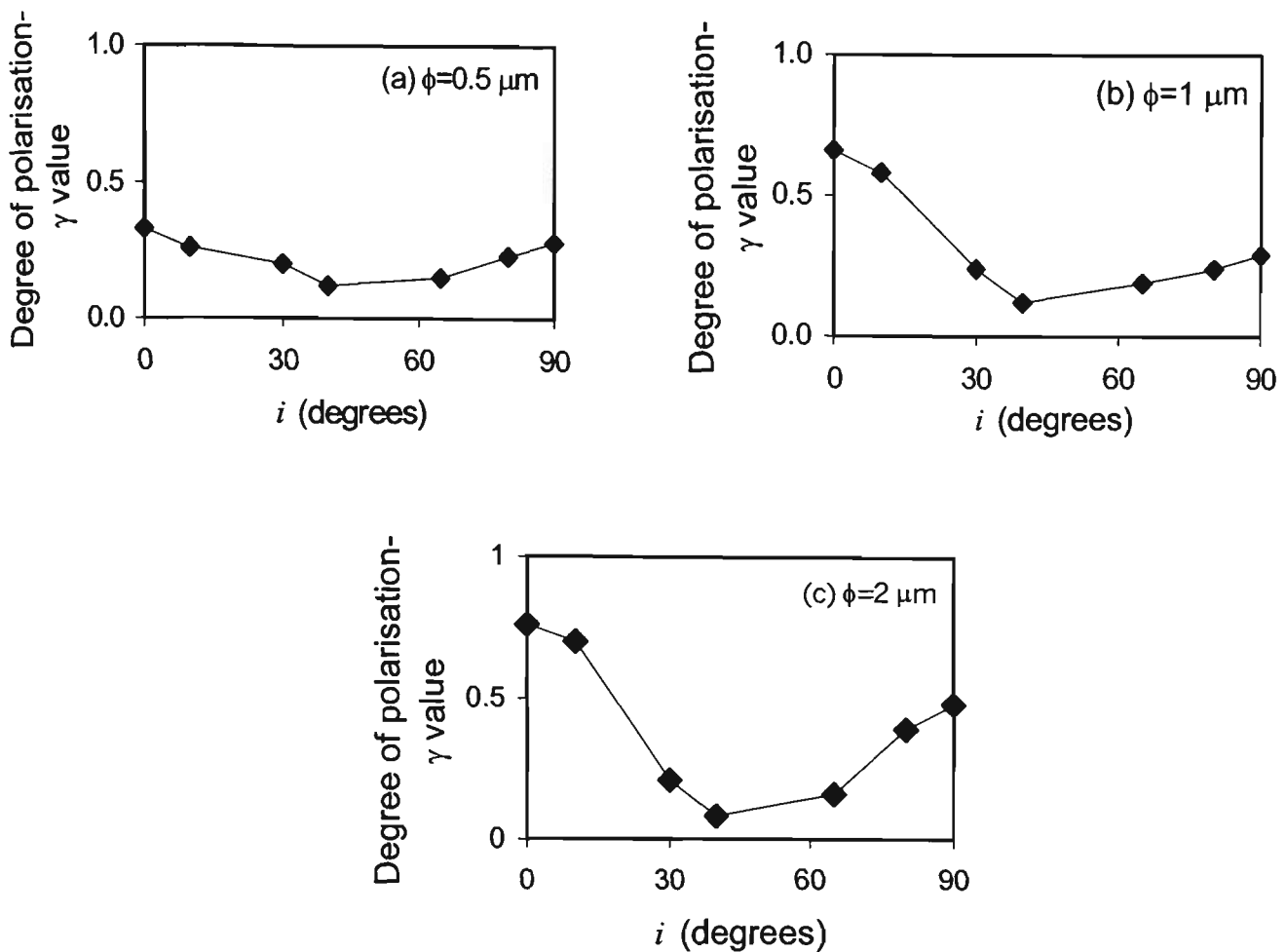


**Fig. 6.9** Degree of polarisation of scattered evanescent waves as a function of the polarisation direction  $i$  of incident light relative to the incident plane for polystyrene latex particles of (a)  $\phi = 0.5 \mu\text{m}$  (b)  $\phi = 1 \mu\text{m}$  and (c)  $\phi = 2 \mu\text{m}$ , respectively.  $\theta = 62^\circ$ .

It is difficult to provide a theoretical explanation on the depolarisation effect associated with small dielectric particles due to the complicity in theoretical treatment involving a high NA objective for signal collection. However, the results shown in Fig. 6.8 can be indirectly confirmed by measuring the degree of polarisation of scattered evanescent waves at different polarisation angle  $i$  of an incident beam relative to the incident plane. Results are shown in Figs. 6.9 (a), (b) and (c) for particles of  $\phi = 0.5, 1$

and  $2\ \mu\text{m}$  at  $\theta = 62^\circ$ , respectively. In each case, a “v” shaped pattern of the degree of polarisation is seen when the polarisation angle of the incident light  $i$  is altered from  $0^\circ$  to  $90^\circ$ , indicating that strong depolarisation occurs near  $i = 45^\circ$ . This result has demonstrated the evolution of depolarisation of scattered evanescent waves when the polarisation state of an illumination laser beam is altered.

### **6.3.2 Depolarisation of evanescent waves scattered by trapped metallic particles**

Similar to the approach adopted for dielectric particles as described in the last section, our investigation into the depolarisation of evanescent waves scattered by metallic particles starts with a measurement of signal strength for the different polarisation directions of the polariser and the analyser. Figs. 6.10 (a), (b) and (c) illustrate the signal strength of scattered evanescent waves measured as a function of the incident angle of an illumination laser beam for metallic gold particles of  $\phi = 0.1, 0.5$  and  $2\ \mu\text{m}$ , respectively. The incident angle of the illumination He-Ne laser was varied from  $56^\circ$  to  $62^\circ$  in each case.

It is seen from Fig. 6.10 that the signal strength of scattered evanescent waves decreases with the incident angle of an illumination laser for different polarisation directions of a polariser and an analyser. This result is similar to that obtained for dielectric particles (Fig. 6.6). It can be understood that as the incident angle of an illumination He-Ne laser is increased, the decay length of an evanescent wave at the

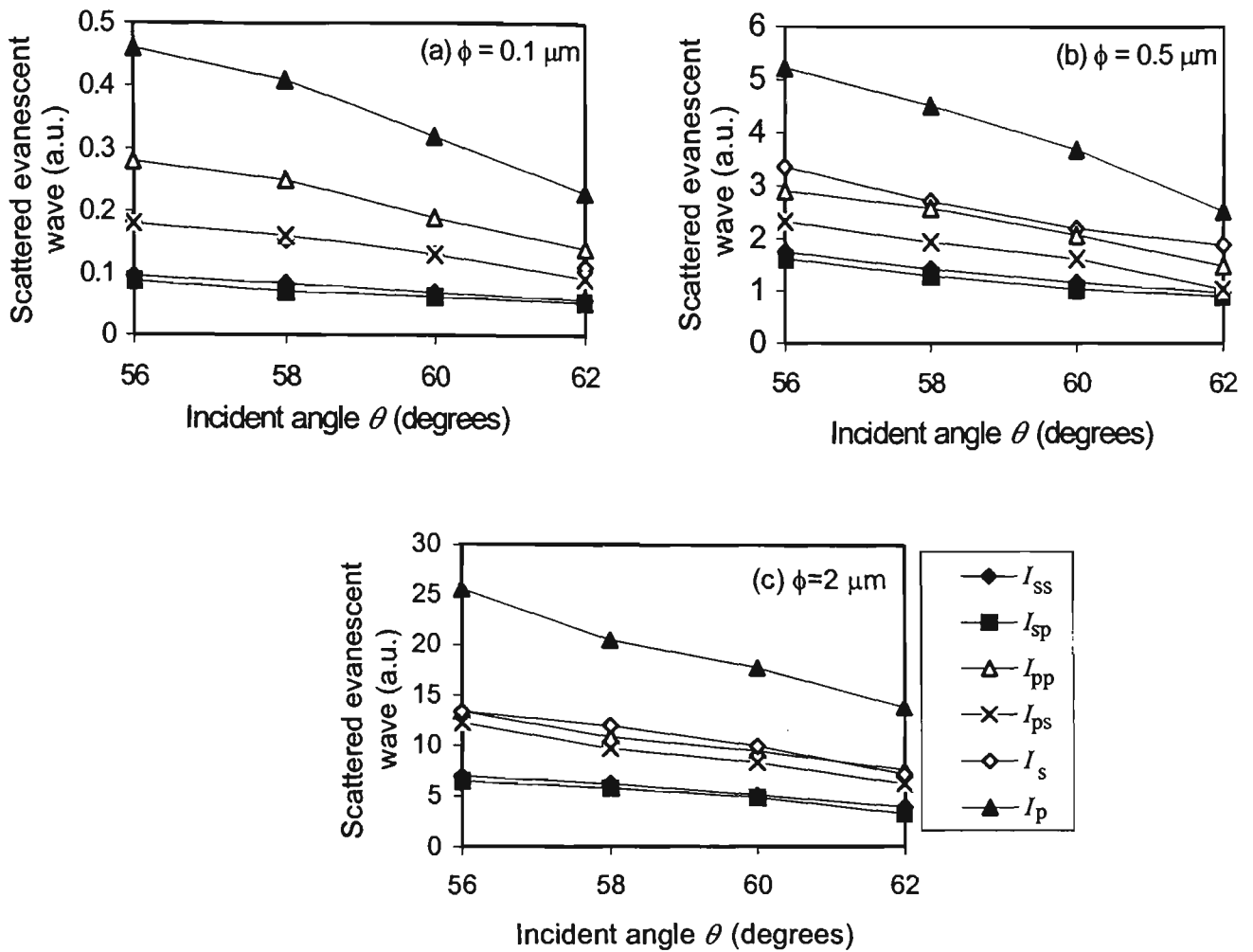


**Fig. 6.10** Dependence of the signal strength of scattered evanescent waves on the incident angle  $\theta$  of an illumination He-Ne laser beam for metallic gold particles of (a)  $\phi = 0.1 \mu\text{m}$ ; (b)  $\phi = 0.5 \mu\text{m}$ ; and (c)  $\phi = 2 \mu\text{m}$ . The definitions of  $I_s$ ,  $I_p$ ,  $I_{ss}$ ,  $I_{sp}$ ,  $I_{pp}$  and  $I_{ps}$  are the same as those in Fig. 6.6.

surface of a prism is decreased and as a result the interaction between the particle and the evanescent field is weakened.

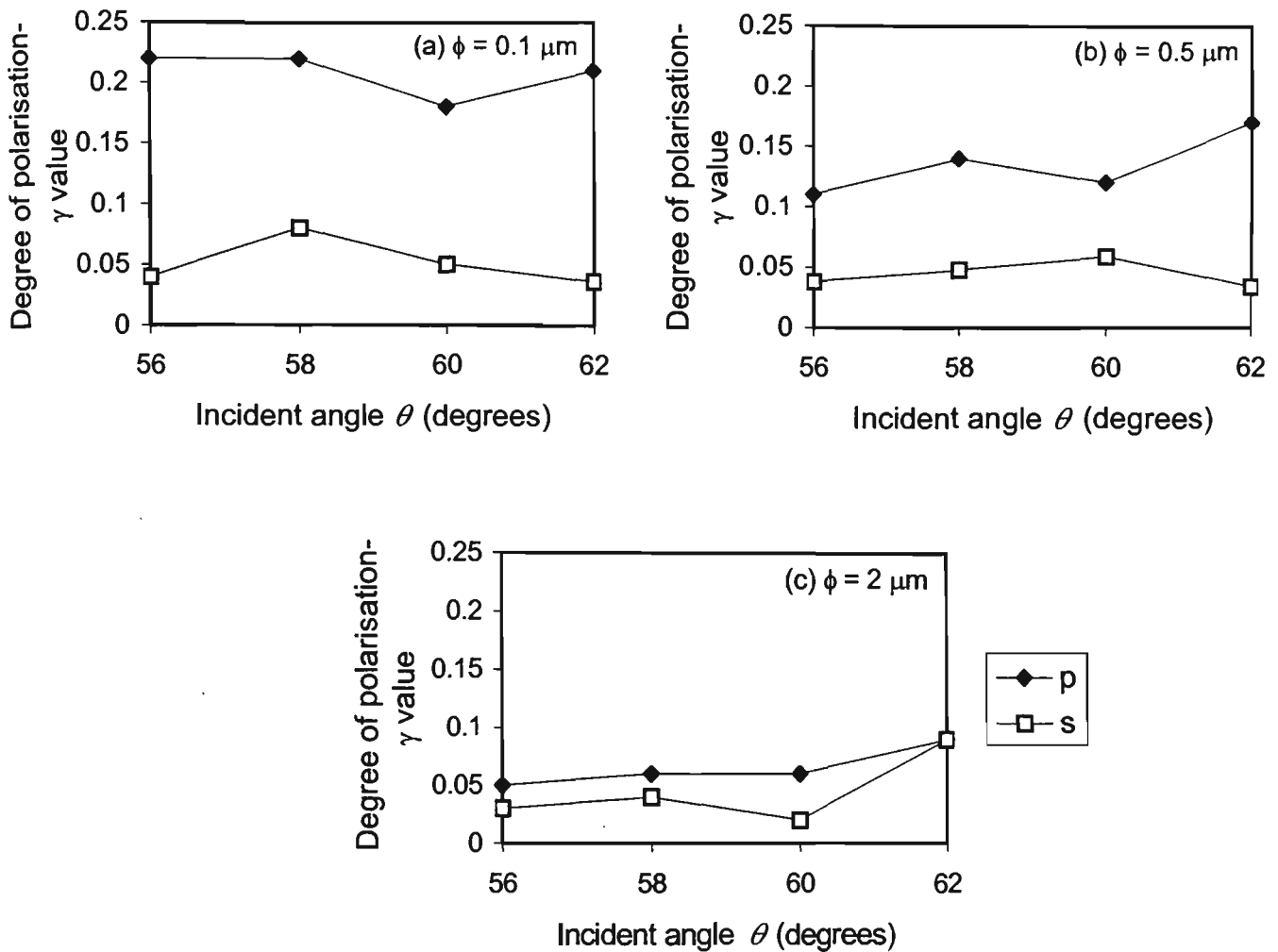


**Fig. 6.11** Dependence of the degree of polarisation of scattered evanescent waves on the incident angle  $\theta$  of an illumination He-Ne laser beam for gold particles of (a)  $\phi=0.1 \mu\text{m}$ ; (b)  $\phi = 0.5 \mu\text{m}$ ; and (c)  $\phi = 2 \mu\text{m}$ .

To evaluate the depolarisation effect induced by near-field Mie scattering of metallic particles, we calculate in Fig. 6.11 the degree of polarisation for gold particles based on Fig. 6.10 and Eq. (6.11). It is indicated in Fig. 6.11 that the interaction between a metallic particle and an evanescent wave is dependent on the incident angle as well as the polarisation state of an illumination laser beam.

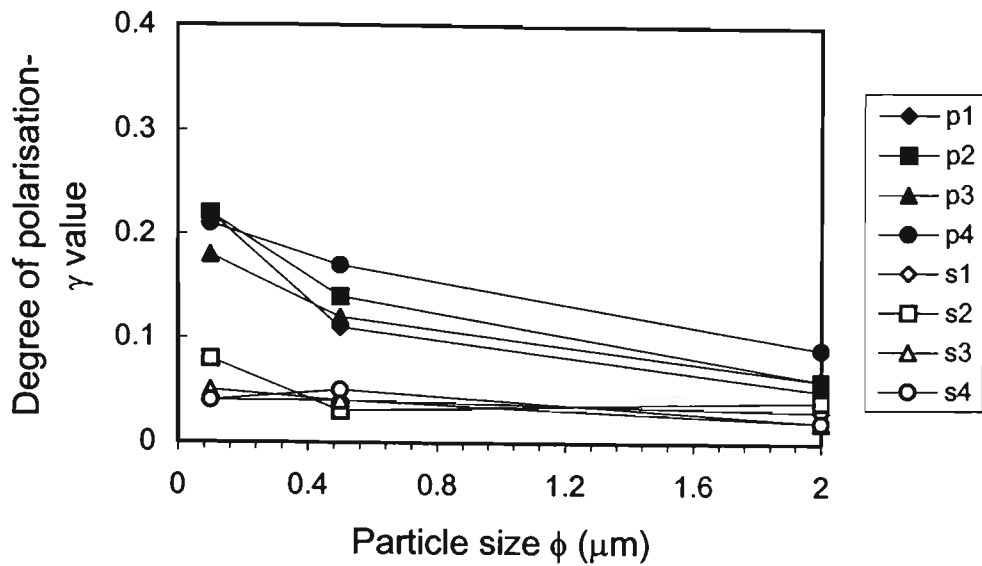


**Fig. 6.12** Degree of polarisation as a function of the size of a gold particle under s- and p-polarised beam illumination. Here p1, p2, p3, and p4 represent the results measured for p-polarised beam illumination at incident angles of  $\theta = 56^\circ$ ,  $58^\circ$ ,  $60^\circ$ , and  $62^\circ$ , respectively, while s1, s2, s3, and s4 correspond to the results measured for s-polarised beam illumination at incident angles of  $\theta = 56^\circ$ ,  $58^\circ$ ,  $60^\circ$ , and  $62^\circ$ , respectively.

The degree of polarisation of scattered evanescent waves for metallic gold particles of different sizes is summarised in Fig. 6.12 for both s- and p-polarised beam illumination. Here p1, p2, p3, and p4 represent the results measured for p-polarised beam illumination at incident angles of  $\theta = 56^\circ$ ,  $58^\circ$ ,  $60^\circ$ , and  $62^\circ$ , respectively, while s1, s2, s3, and s4 correspond to the results measured for s-polarised beam illumination at incident angles of  $\theta = 56^\circ$ ,  $58^\circ$ ,  $60^\circ$ , and  $62^\circ$ , respectively. It is striking to see that the degree of polarisation of scattered evanescent waves decreases with the size of metallic particles particularly for p-polarised illumination. For an s-polarised illumination beam, the averaged degree of polarisation is  $\gamma = 0.052$ ,  $0.04$ , and  $0.028$  for a gold particle of

$\phi = 0.1, 0.5$  and  $2 \mu\text{m}$ , respectively, while for a p-polarised illumination beam, the averaged degree of polarisation is  $\gamma = 0.208, 0.135,$  and  $0.065$  for a gold particle of  $\phi = 0.1, 0.5,$  and  $2 \mu\text{m}$ , respectively. This result differs from that attained for dielectric particles in which case the degree of polarisation increases monotonically with the size of a dielectric particle (see Fig. 6.8).

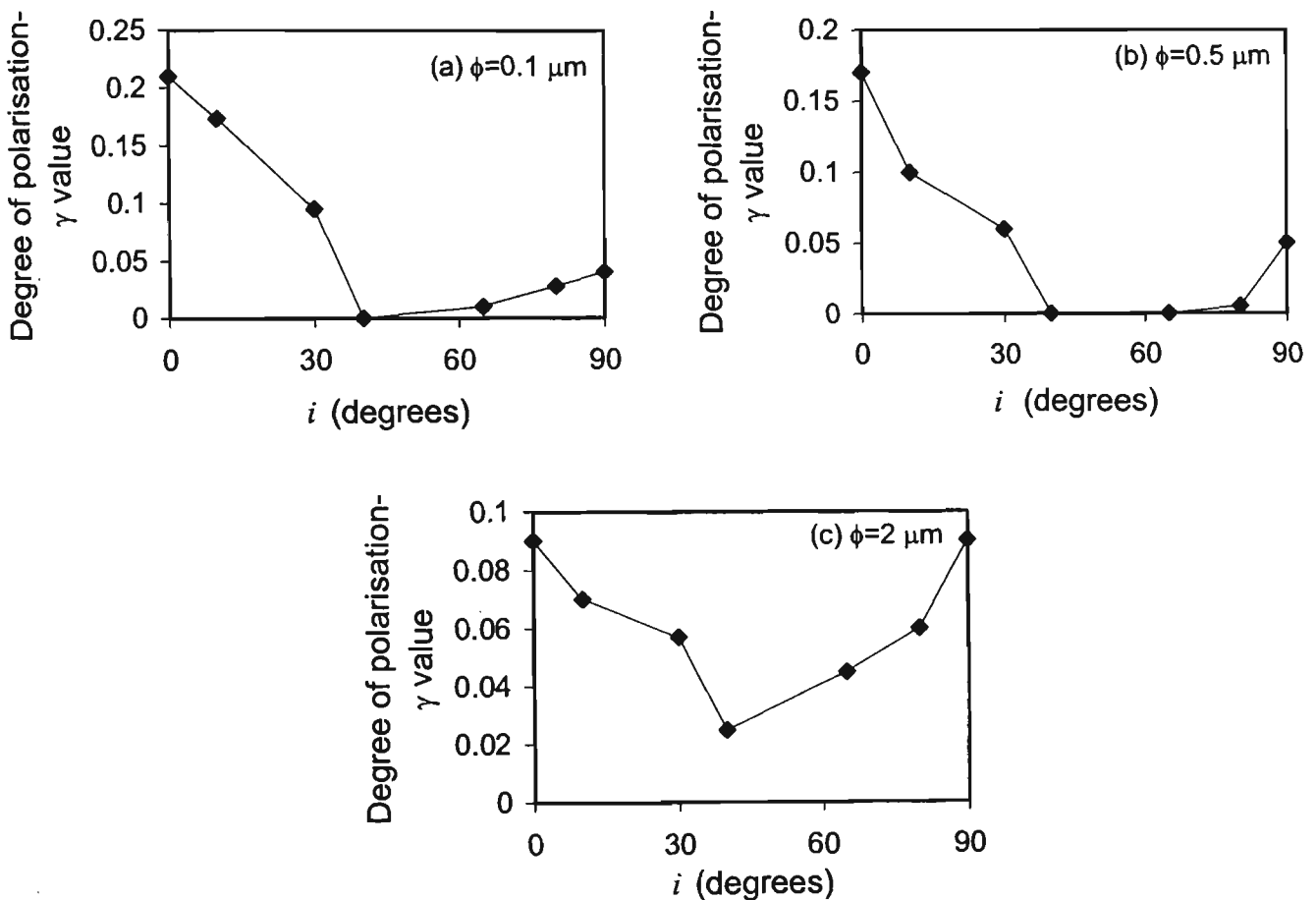


**Fig. 6.13** Degree of polarisation of scattered evanescent waves as a function of the polarisation direction  $i$  of an incident beam relative to the incident plane for gold particles of (a)  $\phi = 0.1 \mu\text{m}$  (b)  $\phi = 0.5 \mu\text{m}$  and (c)  $\phi = 2 \mu\text{m}$ , respectively.  $\theta = 62^\circ$ .

To confirm our results, the degree of polarisation of scattered evanescent waves was measured as a function of the polarisation angle  $i$  of an incident beam relative to the incident plane. Results are shown in Figs. 6.13 (a), (b) and (c) for gold particles of  $\phi = 0.1, 0.5$  and  $2 \mu\text{m}$  at  $\theta = 62^\circ$ , respectively. Similar to Fig. 6.9 obtained for dielectric particles, a “v” shaped pattern of the degree of polarisation is shown in each case when the polarisation angle of the incident light  $i$  is altered from  $0^\circ$  to  $90^\circ$ , indicating that strong depolarisation occurs near  $i = 45^\circ$ . This result exhibits the variance of the depolarisation of scattered evanescent waves for metallic particles when the polarisation state of an illumination laser beam is altered.

For metallic particles illuminated by an evanescent wave, the scattered light field may be enhanced due to the strong surface charge density; the incident light drives the free electrons in a metallic particle along the direction of polarisation, leaving ions accumulated on the surface of the particle. The charge density is zero inside the particle. The distribution of surface charges oscillates under the evanescent wave illumination (see Fig. 6.14).

The oscillating charge distribution leads to radiation of electromagnetic waves and can be approximately described as that of an electric dipole. As shown in Fig. 6.14, for an s-polarised illumination beam, the electric field radiated from the dipole along the  $x$  direction is symmetric about the  $x$  and  $y$  axes in the plane parallel to the prism surface. Consequently, the magnitude of the electric field components in the far-field region along

the  $x$  ( $E_{\perp}$ ) and  $y$  ( $E_{\parallel}$ ) directions may not differ significantly, leading to a low degree of polarisation of the scattered evanescent waves,  $\gamma_s$ .

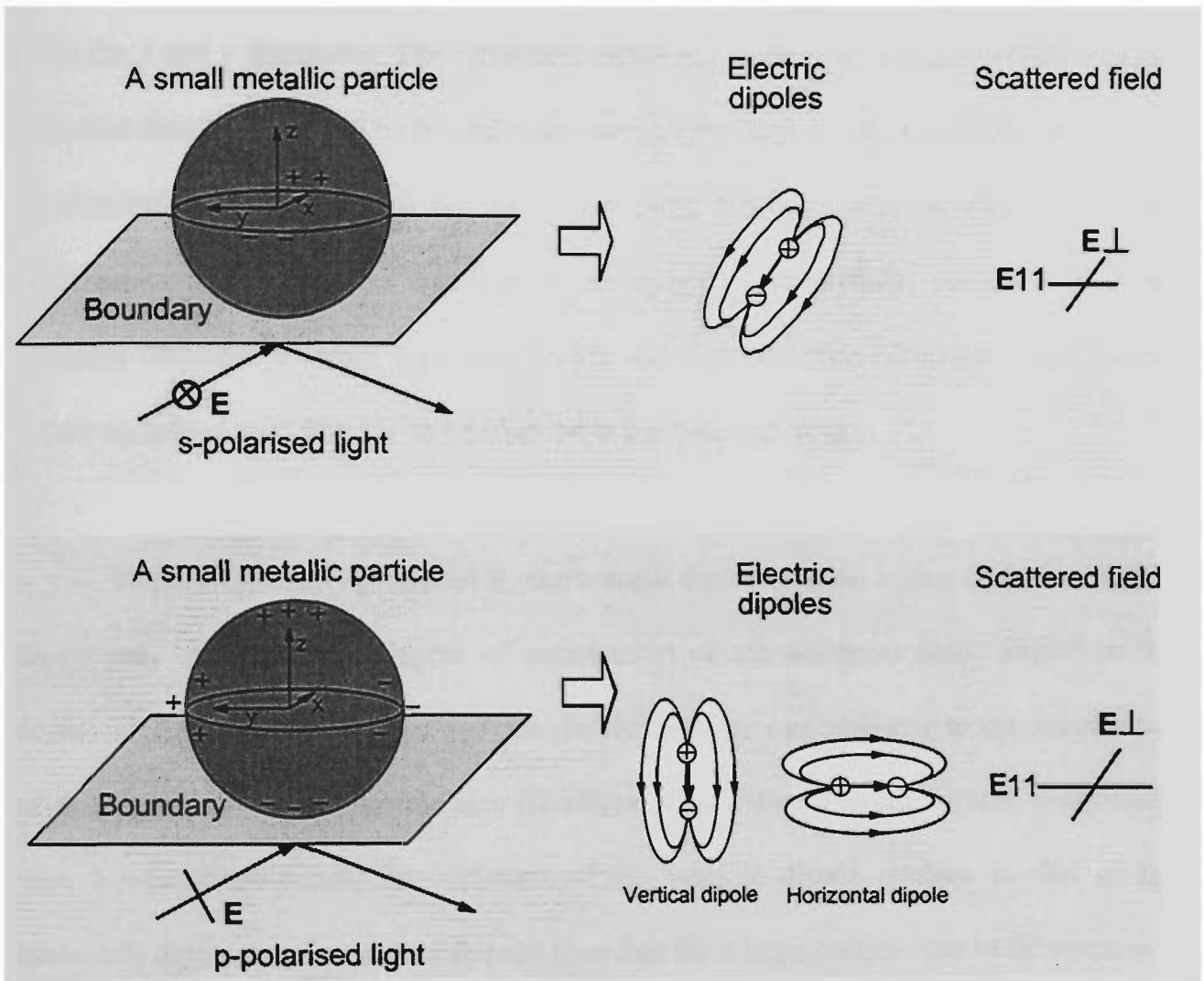


Fig. 6.14 A model for evaluating the depolarisation effect with a metallic particle illuminated with s- and p-polarised evanescent waves. The electrons (-) and ions (+) accumulated on the surface of the particle are illustrated.

For a p-polarised illumination beam, the radiation generated by surface charges may be simulated by two dipoles (vertical and horizontal) as illustrated in Fig. 6.14. The electric field produced by each dipole is stronger than that with an s-polarised illumination beam due to the enhancement of surface plasmon (SP) resonance [Kerker,

1969]. The electric field generated by the vertical dipole is symmetric about the  $z$ -axis and may contribute equally to the scattered field in the incident plane and that perpendicular to the incident plane. The radiation of the horizontal dipole is symmetric about the  $x$  and  $y$  directions. The difference between the electric field components along these two directions caused by the SP resonance may contribute largely to the variance of the detected signal by a high NA objective along the corresponding directions. This experimental result suggests that the SP resonance for a metallic particle with a p-polarised illumination beam may result in the less depolarisation of scattered evanescent waves compared with that for an s-polarised beam (see Fig. 6.12).

The light intensity produced by the vertical dipole relative to that of the horizontal dipole may determine the degree of polarisation of the scattered field. Therefore the degree of polarisation may vary with the physical size of a particle due to the dependence of the SP resonance on particle size [Griffiths, 1981]. For a small particle illuminated with a p-polarised beam, the radiation of the vertical dipole relative to that of the horizontal dipole may be more enhanced than that for a large particle due to SP resonance [Messinger *et al.*, 1981]. As a result, the degree of polarisation of the scattered field may decrease more quickly with the particle size for a p-polarised illumination beam than that for an s-polarised illumination beam (see Fig. 6.12).

## **6.4 Imaging of particle-trapped NSOM by polarisation-gating**

It has been demonstrated in our study that depolarisation is an important feature of near-field Mie scattering. It is necessary to evaluate the impact of depolarisation of near-field

Mie scattering on particle-trapped NSOM. This section is aimed at solving this task with the aid of the polarisation-gating technique.

The polarisation-gating mechanism is one of the methods for efficiently selecting unscattered and/or less scattered photons which are less depolarised and carry more information of a sample than multiply scattered photons [Schmitt *et al.*, 1992; Schilders *et al.*, 1998]. Based on the same physical intuition, one can assume that less depolarised photons of scattered evanescent waves carry more information of a sample. Practically this is achieved by deploying a polariser and an analyser in the illumination and collection passes of an imaging system, respectively, to filter out the depolarised components of the signal [Schmitt *et al.*, 1992].

#### **6.4.1 Polarisation-gating for imaging with laser-trapped dielectric particles**

Recall that the scattered signal for a dielectric particle of 1  $\mu\text{m}$  in diameter under p-polarised illumination exhibits less depolarisation than that under s-polarised beam illumination (Fig. 6.7 (d)). In the following, we shall utilise the polarisation-gating method to evaluate the impact of this result on near-field imaging.

Using the procedures as described in section 5.3 of Chapter 5, we constructed an evanescent interference field at the prism surface by aligning the reflection mirror in parallel with the exit face of the prism and setting the incident angle of the He-Ne laser at

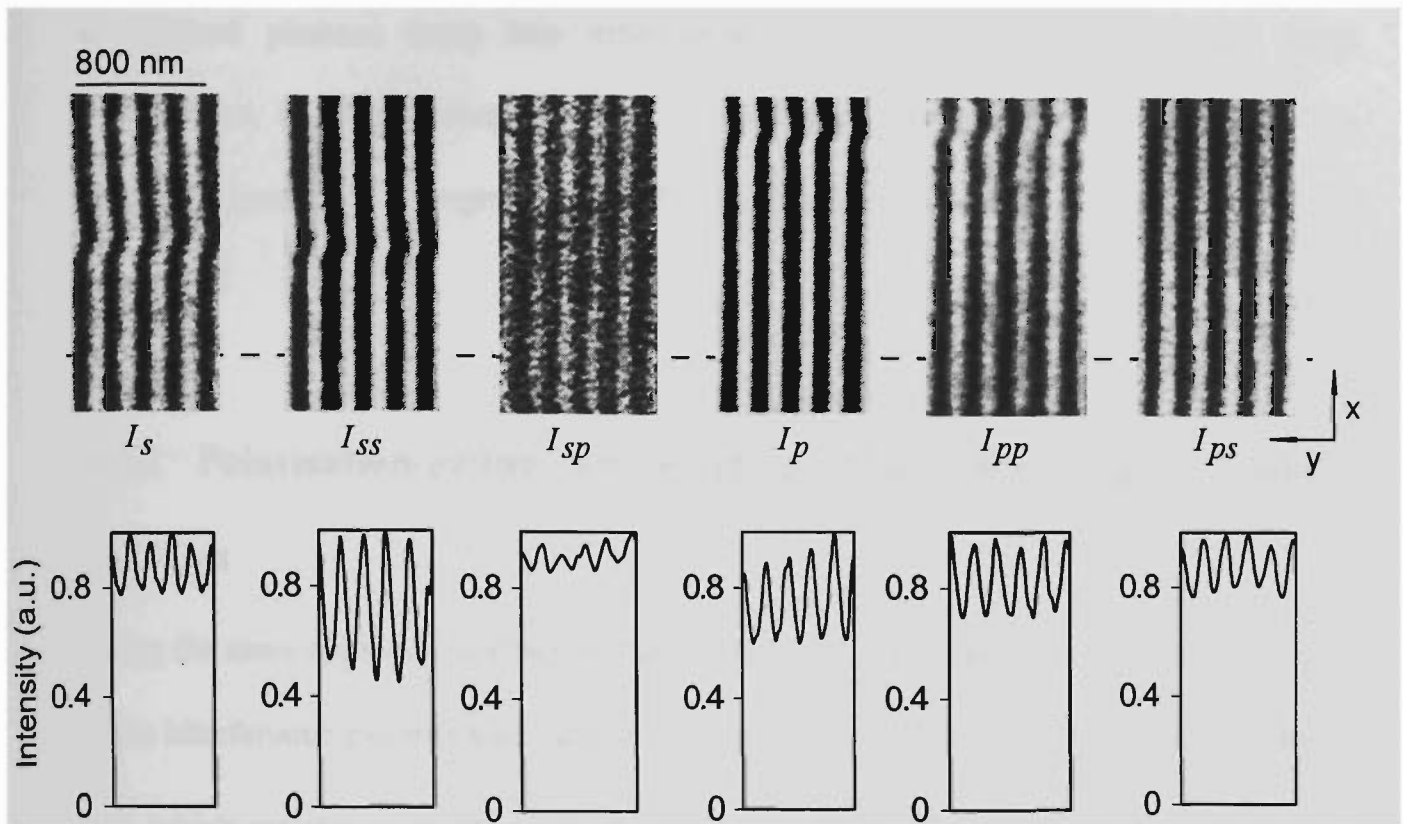


**Fig. 6.15** Images (top) and the corresponding cross-sections (bottom) of the evanescent wave interference patterns for different polarisation directions of the polariser and the analyser. The images have been normalised by the maximum intensity.

$\theta = 60^\circ$  (refer to Fig. 5.1 for the experimental setup). A polystyrene particle of  $\phi = 1 \mu\text{m}$  was used and the scanning speed for imaging was maintained at  $1 \mu\text{m/s}$  in  $x$ - $y$  directions. The definitions of  $I_s$ ,  $I_{ss}$ ,  $I_{sp}$ ,  $I_p$ ,  $I_{pp}$  and  $I_{ps}$  in Fig. 6.15 are the same as those adopted before (refer to section 6.3). The top part of Fig. 6.15 shows images of  $110 \times 256$  pixels, normalised by the maximum intensity, while the intensity cross-sections corresponding to the marked position are placed in the bottom part of Fig. 6.15. According to these cross-sections, the contrast for images constructed with  $I_s$ ,  $I_{ss}$ ,  $I_{sp}$ ,  $I_p$ ,  $I_{pp}$  and  $I_{ps}$  is approximately 9%, 28%, 6%, 18%, 12% and 14%, respectively. As expected, the image created with  $I_{ss}$  shows the best contrast. This result confirms the prediction that more strongly

depolarised photons carry less information of an object. For p-polarised beam illumination, the image contrast for  $I_{pp}$  is slightly poorer than that for  $I_p$  because the scattered signal  $I_p$  is stronger than  $I_{pp}$  (Fig. 6.15) and the noise level is increased in the latter case.

### 6.4.2 Polarisation-gating for imaging with laser-trapped metallic particles

Using the same approach as described in section 6.2.2, we obtained images of evanescent wave interference patterns with laser-trapped gold particles of  $\phi = 0.1 \mu\text{m}$ ,  $0.5 \mu\text{m}$  and  $2 \mu\text{m}$ , which are shown in Fig. 6.16, Fig. 6.17, and Fig. 6.18, respectively. The scanning speed for imaging was maintained at  $1.5 \mu\text{m/s}$  in  $x$ - $y$  directions for three different sized particles. According to the intensity cross-sections, for a gold particle of  $\phi = 0.1 \mu\text{m}$ , the image contrast constructed with  $I_s$ ,  $I_{ss}$ ,  $I_{sp}$ ,  $I_p$ ,  $I_{pp}$  and  $I_{ps}$  is approximately 4.2%, 6.2%, 2%, 3.1%, 7.0% and 2.5%, respectively. The improvement in image contrast is more obvious under the illumination of a p-polarised illumination beam possibly due to the increased signal strength (see Fig. 6.10). For a gold particle of  $\phi = 0.5 \mu\text{m}$ , the image contrast, in the order same as that for a gold particle of  $\phi = 0.1 \mu\text{m}$ , is approximately 8.3%, 13.4%, 5.0%, 7.0%, 14.1%, and 3.0%, respectively. For a gold particle of  $\phi = 2 \mu\text{m}$ , the image contrast constructed with  $I_s$ ,  $I_{ss}$ ,  $I_{sp}$ ,  $I_p$ ,  $I_{pp}$  and  $I_{ps}$  is approximately 9%, 11%, 4%, 6%, 13%, and 3%, respectively.

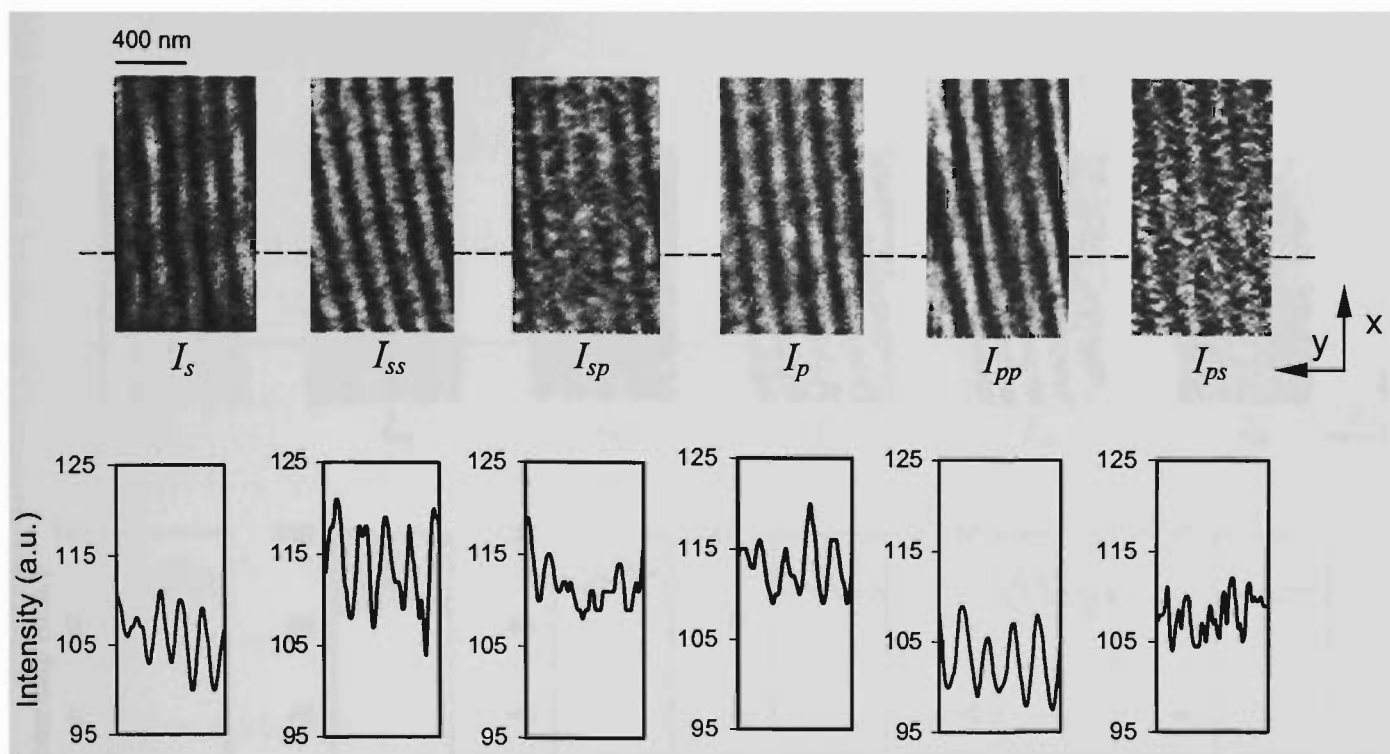


**Fig. 6.16** Images (top) and the corresponding cross-sections (bottom) of evanescent wave interference patterns for different polarisation directions of a polariser and an analyser. The images were recorded with a gold particle of  $\phi = 0.1 \mu\text{m}$ .

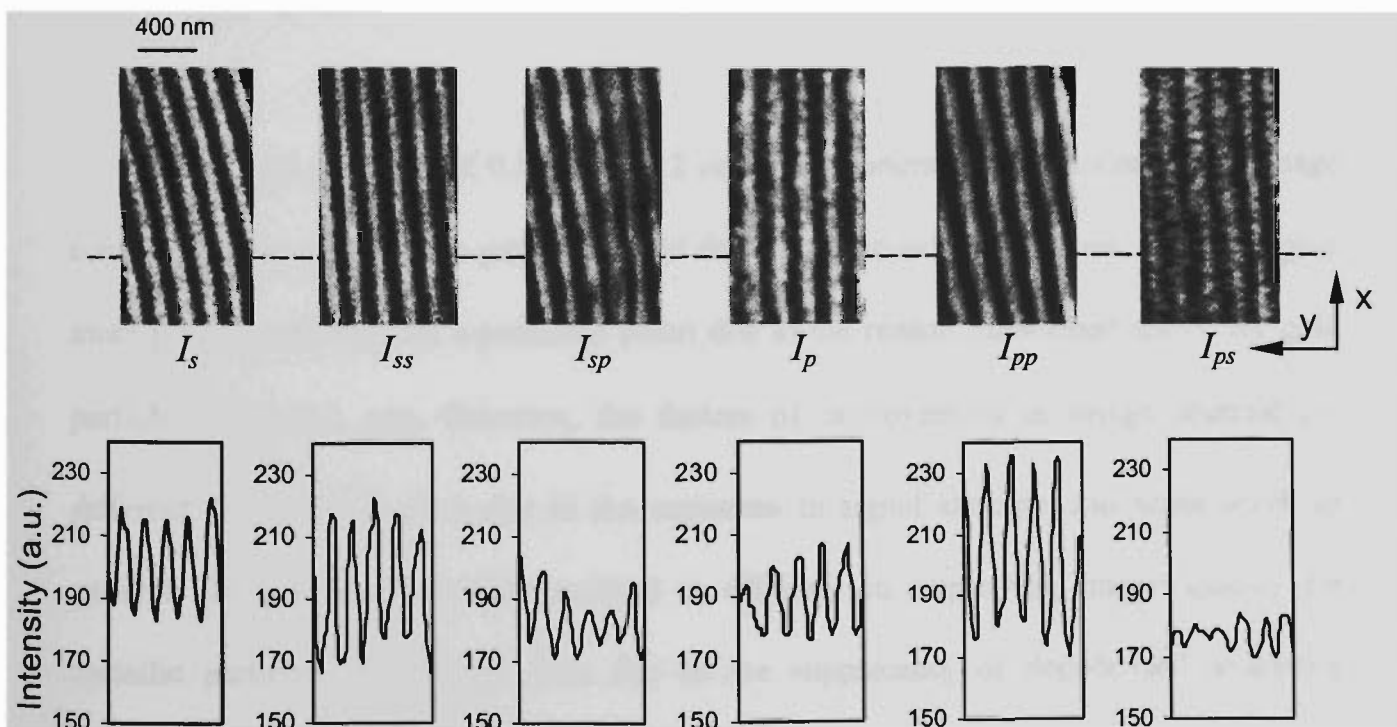


**Fig. 6.17** Images (top) and the corresponding cross-sections (bottom) of evanescent wave interference patterns for different polarisation directions of a polariser and an analyser. The images were recorded with a gold particle of  $\phi = 0.5 \mu\text{m}$ .

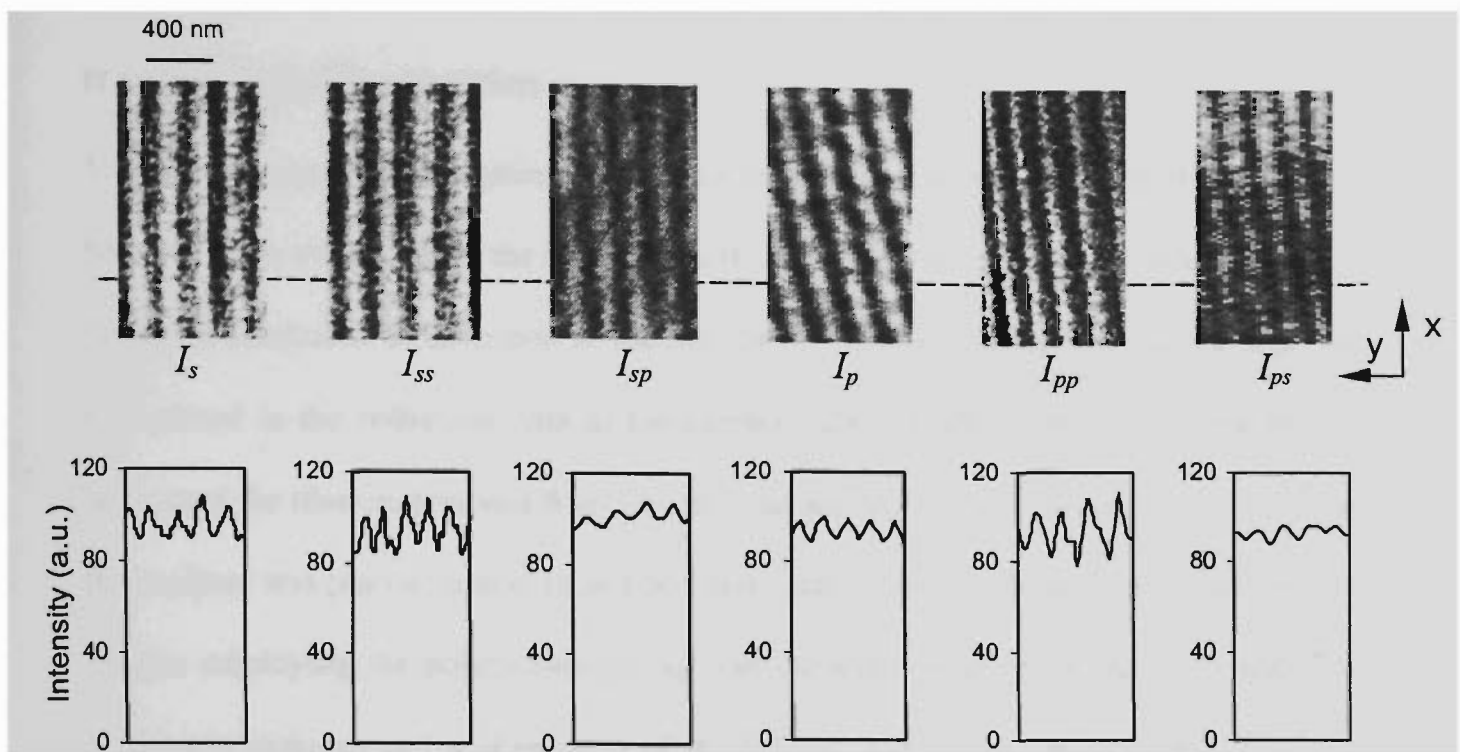


**Fig. 6.18** Images (top) and the corresponding cross-sections (bottom) of evanescent wave interference patterns for different polarisation directions of a polariser and an analyser. The images were recorded with a gold particle of  $\phi=2 \mu\text{m}$ .

For gold particles of  $0.5 \mu\text{m}$  and  $2 \mu\text{m}$  in diameters, the enhancement of image contrast by the polarisation-gating method for a p-polarised illumination beam is again more pronounced than an s-polarised beam due to the reason mentioned above for gold particle of  $\phi = 0.1 \mu\text{m}$ . However, the factors of improvement in image contrast are different for different sizes due to the variances in signal strength and noise level. In general, the polarisation-gating method is effective in improving image quality for metallic particles of varying sizes due to the suppressing of depolarised scattering photons.

## **6.5 Polarisation-gating for imaging of a prism surface with laser-trapped metallic particles**

The use of the polarisation-gating method for improving image quality of particle-trapped NSOM is also examined for the surface of a BK7 prism. The images were recorded under the same conditions as described in section 5.4 of Chapter 5 except for that an analyser was placed in the collection pass in the current case. For easy comparison, the He-Ne laser used for illumination was fixed at a p-polarised state. The polarisation direction of the analyser was placed parallel to and perpendicular to that of the polariser, respectively. Images employing the polarisation-gating method were recorded in Fig. 6.19 and Fig. 6.20 for polystyrene and gold particles of  $\phi = 0.1 \mu\text{m}$  in diameter, respectively.

Compared with the images recorded without the use of an analyser (Figs. 6.19 (a) and 6.20 (a)), the image contrasts in Figs. 6.19 (b) and 6.20 (b) are obviously better when the polarisation direction of the analyser is parallel to that of the polariser. By contrast, images are degraded when the polarisation direction of the analyser is perpendicular to that of the polariser as shown in Figs. 6.19 (c) and 6.20 (c). This result is consistent with that obtained with evanescent wave interference patterns showing that depolarisation in near-field Mie scattering is crucial for image formation and that polarisation-gating is effective for image enhancement. In addition, imaging with a laser-trapped metallic particle is advantageous over a dielectric particle in that better image contrast and resolution can be obtained in the former case. This result agrees with that reported in Chapter 5.

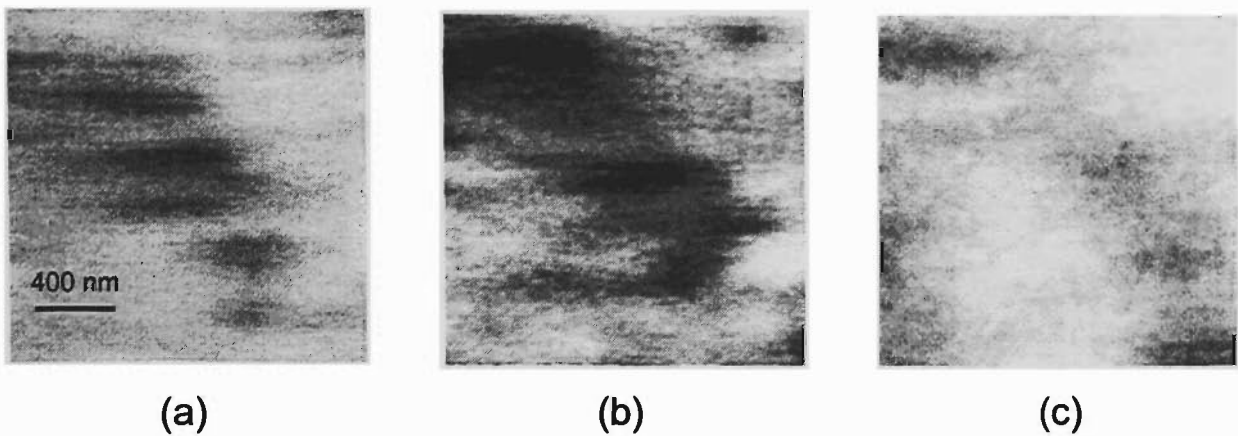


**Fig. 6.19** Images of the surface structure of a BK7 prism recorded with a polystyrene particle of 100 nm in diameter under the condition: (a) no analyser; (b) with an analyser of the polarisation direction parallel to that of the polariser; and (c) with an analyser of the polarisation direction perpendicular to that of the polariser.

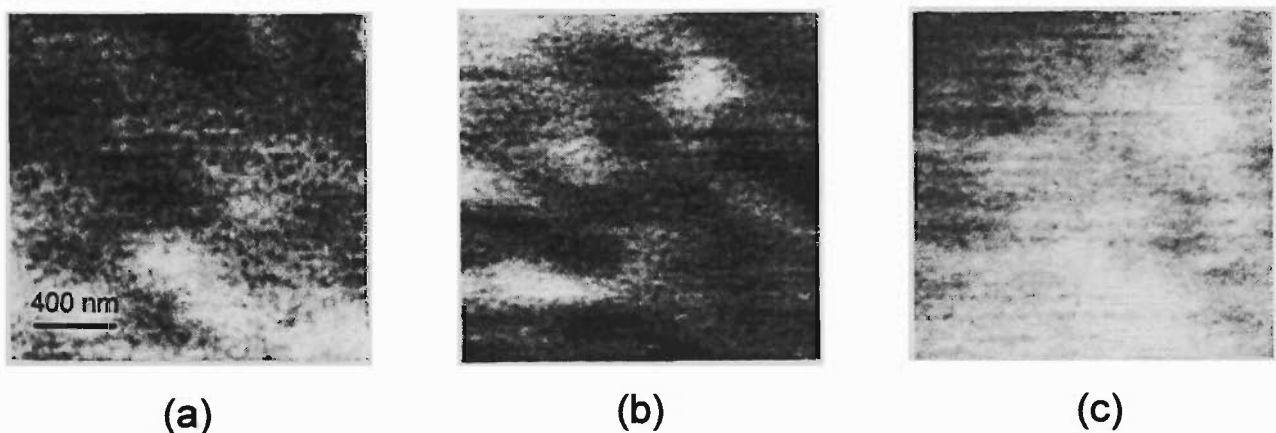


**Fig. 6.20** Images of the surface structure of a BK7 prism recorded with a gold particle of 100 nm in diameter under the condition: (a) no analyser; (b) with an analyser of the polarisation direction parallel to that of the polariser; and (c) with an analyser of the polarisation direction perpendicular to that of the polariser.

## 6.6 Conclusion

In conclusion, near-field Mie scattering is a depolarisation process for both dielectric and metallic particles. Our study has found that the degree of polarisation in this process increases with the size of a laser-trapped dielectric particle for both s- and p-polarised illumination beams. The depolarisation effect is stronger for an s-polarised illumination than a p-polarised illumination for a large particle but this tendency reverses for a particle of small size. However, a different behaviour has been observed for the depolarisation of near-field Mie scattering by metallic particles. The degree of polarisation decreases with the particle size possibly due to the strong enhancements of SP resonance associated with small metallic particles.

In our study, the effect of depolarisation on image quality has been examined in terms of the employment of the polarisation-gating method. It has been found that for a dielectric particle of  $\phi = 1 \mu\text{m}$ , the image contrast of an evanescent wave interference pattern is improved approximately by a factor of 3 if a parallel analyser is used under s-polarised beam illumination. Similarly for a metallic gold particle of  $\phi = 0.1 \mu\text{m}$  illuminated with s- and p-polarised beams, enhancement factors of 1.5 and 2.2 have been, respectively, obtained for the image contrast of the evanescent wave interference patterns with the use of analysers in parallel to the polarisation direction of a polariser. These results suggest that less depolarised scattered evanescent photons carry more information of an object and that the polarisation-gating technique is effective in suppressing the depolarised photons in image formation. In this sense, a metallic particle of small size

may provide more advantages in that it scatters evanescent waves with less depolarisation.

## CHAPTER SEVEN

# Conclusion

### 7.1 Thesis conclusion

**R**EPORTED in this thesis is a detailed characterisation of particle-trapped near-field scanning optical microscopy (NSOM), resulting from the employment of laser-trapped metallic particles. The use of a laser-trapped metallic particle has proved efficient for resolving the major problems of particle-trapped NSOM such as the low scattering efficiency and slow transverse scanning speed associated with a dielectric particle. Consequently, near-field imaging has been performed with laser-trapped metallic particles and image enhancement has been observed.

Considering image formation in particle-trapped NSOM, we have treated laser trapping and near-field Mie scattering as two major issues in our investigation. Since laser trapping is mainly determined by the light distribution in the focal region of a high numerical aperture (NA) trapping objective, the apodization of a high NA objective and spherical aberration induced by refractive-index mismatch have been examined in detail. It has been demonstrated that the sine condition obeyed by a commercial high NA objective used for trapping increases the transverse trapping force on a dielectric particle. A metallic particle can be trapped stably in two dimensions by focusing a single laser beam near its bottom. The maximum transverse efficiency of a metallic particle increases with the NA of a trapping objective while it decreases for a dielectric

particle. Therefore high scanning speed and high signal-to-noise ratio can be obtained simultaneously for metallic particles with the use of a high NA trapping objective for imaging. It has been proved theoretically and experimentally that the presence of spherical aberration affects the trapping force on a particle and degrades trapping performance. However, spherical aberration can be compensated for and trapping force can be improved based on a change in tube length of a trapping objective. A further improvement of the trapping efficiency is possible if a microscope objective of infinitely-long tube length is employed. It is also demonstrated that the use of an annular lens is effective in improving transverse trapping force for metallic particles.

Regarding near-field Mie scattering, we have shown that signal strength is improved with the use of a metallic particle, and that the improved signal can result in better image contrast. This improvement is due to high reflection and the possible surface plasmon resonance and morphology dependence resonance. Although the signal strength increases monotonically with the particle size, a maximum image contrast is obtained with a particle of given size. This result indicates that if a small particle is used for high-resolution imaging, a high sensitivity detector should be employed to achieve an optimal image contrast. In addition to signal strength, the effect of depolarisation has also been examined in our study. It has been found that the degree of polarisation of scattered evanescent waves increases with the size of laser-trapped dielectric particles while it decreases for metallic particles. The depolarisation of scattered evanescent waves is more significant for an s-polarised illumination beam than a p-polarised beam for a large dielectric particle, but this situation reverses for a small dielectric particle. In the case of a metallic particle, the degree of polarisation for a p-polarised illumination beam is higher in comparison with that for an s-polarised beam.

Based on the investigation of depolarisation of near-field Mie scattering, the polarisation-gating method has been introduced for image improvement of particle-trapped NSOM. It has been shown that for a constructed evanescent wave interference pattern and a prism surface, the polarisation-gating method is effective in improving image quality of particle-trapped NSOM. This result has suggested that depolarised photons carry less information of a sample and should be relinquished for imaging.

In conclusion, we have examined the fundamental issues of particle-trapped NSOM. Our study has shown that the use of a laser-trapped metallic particle is advantageous for high quality near-field imaging. The introduction of a laser-trapped metallic particle has proved effective not only for resolving the problems of particle-trapped NSOM with a dielectric particle, but also for achieving fast scanning speed, enhanced signal strength, improved image contrast and resolution. These advantages, together with the noninvasive approach of laser trapping, enable particle-trapped NSOM an alternative tool for the future applications of near-field imaging. Although our treatment is mainly within the frame of microscopic imaging, the knowledge obtained in this research is beneficial to the application of laser trapping and the study of near-field physics.

## 7.2 Future work

Our research on particle-trapped NSOM has led to the future work in the following aspects:

- The investigation of trapping forces on dielectric and metallic particles of  $\lambda$ - $10\lambda$  in diameters. By applying Török's theory [Török *et al.*, 1995] of focusing light through different media to a practical trapping system, the exact solution to the light distribution in the focal region of a high NA trapping objective may be solved. Based on a combination of this approach with the electromagnetic wave theory by Barton *et al.* [Barton *et al.*, 1989], the value of trapping force on a laser-trapped particle of a given size may be solvable.
- The study of the improvement of transverse performance with the use of an annular lens under the doughnut beam ( $\text{TEM}_{01}^*$ ) illumination. This is because the phase singularity of a doughnut beam results in an intensity-minimal on optical axis and may reduce the thermal effect, while an annular lens only allows rays at high angles of convergence coming through a trapping objective that produce sufficient transverse trapping force. This investigation requires the employment of the rigorous diffraction theory, as well as the consideration of spherical aberration induced by refractive-index mismatch.
- Near-field Mie scattering by small particles. This study includes the theoretical and experimental characterisations on the interactions between a particle (dielectric or metallic) and an evanescent wave in both the spectral and temporal aspects. The theoretical characterisation of the strength and depolarisation of scattered evanescent waves by metallic particles, in the presence of a high NA objective for signal collection, needs to be further

explored with the multiple multipole (MMP) method or the finite-difference time domain (FDTD) method [Umashankar and Taflove, 1982].

# Bibliography

- Adelmann Ch., Hetzler J., Scheober G., Schimmel Th., Wegener M., Weber H.B., and v. Löhneysen H., "Experiments on the depolarization near-field scanning optical microscopy", *Appl. Phys. Lett.* **74**, 179 (1999).
- Aigouy L., Lahrech A., Grésillon S., Cory H., Boccara A.C., and Rivoal J.C., "Polarization effects in an apertureless scanning near-field optical microscopy: an experimental study", *Opt. Lett.* **24**, 187 (1999).
- Almaas E. and Brevik I., "Radiation forces on a micrometer-sized sphere in an evanescent field", *J. Opt. Soc. Am. B* **12**, 2429 (1995).
- Ashkin A., "Acceleration and trapping of particles by radiation pressure", *Phys. Rev. Lett.* **24**, 156 (1970).
- Ashkin A. and Dziedzic J.M., "Optical levitation by radiation pressure", *Appl. Phys. Lett.* **19**, 283 (1971).
- Ashkin A., Dziedzic J.M., Bjorkholm J.E., and Chu S., "Observation of a single-beam gradient force optical trap for dielectric particles", *Opt. Lett.* **11**, 288 (1986).
- Ashkin A., Schütze K., Dziedzic J.M., Euteneuer U., and Schliwa, "Force generation of organelle transport measured *in vivo* by an infrared laser trap", *Nature* **348**, 346 (1990).
- Ashkin A., "Forces of a single-beam gradient laser trap on a dielectric sphere in the ray optics regime", *J. Biophys.* **61**, 569 (1992).
- Bachelot R., Gleyzes P., and Boccara A.C., "Near-field optical microscope based on local perturbation of a diffraction spot", *Opt. Lett.* **20**, 1924 (1995).
- Bainier C., Courjon D., and Baida F., "Evanescent interferometry by scanning optical tunnelling detection", *J. Opt. Soc. Am. A* **13**, 267 (1996).
- Barber P.W. and Chang R.K., *Optical effects associated with small particles* (World Scientific Publishing, Singapore, 1988).
- Barton J.P., Alexander D.R., and Schaub S.A., "Internal and near-surface electromagnetic fields for a spherical particle irradiated by a focused laser beam", *J. Appl. Phys.* **64**, 1632 (1988).

- Barton J.P., Alexander D.R., and Schaub S.A., "Theoretical determination of net radiation force and torque for a spherical particle illumination by a focused laser beam", *J. Appl. Phys.* **66**, 4594 (1989).
- Barton J.P. and Alexander D.R., "Fifth-order corrected electromagnetic field components for a fundamental Gaussian beam", *J. Appl. Phys.* **66**, 2800 (1989).
- Besancon R.M., *The Encyclopedia of Physics* (second edition) (Van Nostrand Reinhold, New York, 1974).
- Betzig E., Trautman J.K., Harris T.D., Weiner J.S., and Kostelak R.L., "Breaking the diffraction barrier: optical microscopy on a nanometric scale", *Science* **251**, 1468 (1991).
- Betzig E. and Trautman J.K., "Near-field optics: microscopy, spectroscopy, and surface modification beyond the diffraction limit", *Science* **257**, 189 (1992).
- Binnig G., Quate C.F., and Gerber Ch., "Atomic force Microscope", *Phys. Rev. Lett.* **56**, 930 (1986).
- Block S.M., Goldstein, L.S.B., and Schnapp B.J., "Bead movement by single kinesin molecules studied with optical tweezers", *Nature* **348**, 348 (1990).
- Block S.M., "Making light work with optical tweezers", *Nature* **360**, 492 (1992).
- Born M. and Wolf E., *Principles of Optics* (6<sup>th</sup> edition, Pergamon, Cambridge University Press, 1997).
- Buican T.N., Smyth M.J., Crissman H.A., Salzman G.C., Stewart C.C., and Martin J.C., "Automated single-cell manipulation and sorting by light trapping", *Appl. Opt.* **26**, 5311 (1987).
- Chew H., Wang D.S., and Kerker M., "Elastic scattering of evanescent electromagnetic waves", *Appl. Opt.* **18**, 2679 (1979).
- Clapp A.R., Ruta A.G., and Dickinson R.B., "Three-dimensional optical trapping and evanescent wave light scattering for direct measurement of long range forces between a colloidal particle and a surface", *Rev. Sci. Instrum.* **70**, 2627 (1999).
- Courjon D., Bainier C., and Baida F., "Seeing inside a Fabry-Perot resonator by means of a scanning tunneling optical microscope", *Optics Commun.* **110**, 7 (1994).

- de Fornel F., Lesniewska E., Salomon L., and Goudonnet J.P., "First image obtained in the near infrared spectrum with the photon scanning tunneling microscope", *Optics Commun.* **102**, 1 (1993).
- Felgner H., Müller O., and Schliwa M., "Calibration of light forces in optical tweezers", *Appl. Opt.* **34**, 977 (1995).
- Finer J.T., Simmons R.M., and Spudich J.A., "Single myosin molecule mechanics: piconewton forces and nanometre steps", *Nature* **368**, 113 (1994).
- Florin E.L., Hörber J.K.H., and Stelzer E.H.K., "High resolution axial and lateral position sensing using two-photon excitation of fluorophores by a continuous-wave Nd: YAG laser", *Appl. Phys. Lett.* **69**, 446 (1996).
- Friese M.E., Truscott A.G., Rubinsztein-Dunlop H., and Heckenberg N.R., "Three-dimensional imaging with laser tweezers", *Appl. Opt.* **38**, 6597 (1999).
- Furukawa H. and Yamaguchi I., "Optical trapping of metallic particles by a fixed Gaussian beam", *Opt. Lett.* **23**, 216 (1998).
- Ghislain L.P. and Webb W.W., "Scanning force microscope based on an optical trap", *Opt. Lett.* **18**, 1678 (1993).
- Girard C. and Dereux A., "Near-field optics theories", *Rep. Prog. Phys.* **59**, 657 (1996).
- Gleyzes P., Boccara A.C., and Bachelot R., "Near field optical microscopy using a metallic vibrating tip", *Ultramicroscopy* **57**, 318 (1995).
- Griffiths D.J., *Introduction to Electrodynamics* (Prentice-Hall, London, 1981).
- Gu, M., Ke P.C., and Gan X.S., "Trapping force by a high numerical-aperture microscope objective obeying the sine condition", *Rev. Sci. Instrum.* **68**, 3666 (1997).
- Gu M. and Ke P.C., "Image enhancement in near-field scanning optical microscopy with laser-trapped metallic particles", *Opt. Lett.* **24**, 74 (1999a).
- Gu M. and Ke P.C., "Effect of depolarisation of scattered evanescent waves on particle-trapped near-field scanning optical microscopy", *Appl. Phys. Lett.* **75**, 175 (1999b).
- Gu M., *Advanced Optical Imaging Theory* (Springer, Heidelberg, 1999).

- Hafner Ch., *The Generalized Multipole Technique for Computational Electromagnetics* (Artech House Books, 1990).
- Hatano H., Inouye Y., and Kawata S., "A near-field scanning optical microscope which measures both constant-height and constant-gap images", *Jpn. J. Appl. Phys.* **37**, L1008 (1998).
- He H., Heckenberg N.R., and Rubinsztein-Dunlop H., "Optical particle trapping with higher order doughnut beams produced using high efficiency computer generated holograms", *J. Mod. Opt.* **42**, 217 (1995).
- Higurashi E., Sawada R., and Ito T., "Nanometer-displacement detection of optically trapped metallic particles based on critical angle method for small force detection", *Rev. Sci. Instrum.* **70**, 3068 (1999).
- Ignatowsky V.S., "Diffraction by a lens of arbitrary aperture", *Trans. Opt. Inst. Petrograd* **1**, 1 (1919).
- Inouye Y. and Kawata S., "Near-field scanning optical microscope with a metallic probe tip", *Opt. Lett.* **19**, 159 (1994).
- Kawata S., Inouye Y., and Sugiura T., "Near-field scanning optical microscopy with a laser-trapped probe", *Jpn. J. Appl. Phys.* **33**, L1725 (1994).
- Ke P.C. and Gu M., "Characterisation of trapping force in the presence of spherical aberration", *J. Mod. Opt.* **45**, 2159 (1998a).
- Ke P.C. and Gu M., "Effect of the sample condition on the enhanced evanescent waves used for laser trapping near-field microscopy", *Optik* **109**, 104 (1998b).
- Ke P.C. and Gu M., "Characterization of trapping force on metallic Mie particles", *Appl. Opt.* **38**, 160 (1999a).
- Ke P.C. and Gu M., "Dependence of strength and depolarisation of scattered evanescent waves on the size of laser-trapped dielectric particles", *Optics Commun.* **171**, 205 (1999b).
- Keller O., Xiao M., and Bozhevolnyi S., "Optical diamagnetic polarizability of a mesoscopic metallic sphere transverse self-field approach", *Optics Commun.* **102**, 238 (1993).
- Keller O., Xiao M., and Bozhevolnyi S., "Optical paramagnetic polarizability of mesoscopic particles: a study of local field corrections", *Optics Commun.* **114**, 491 (1995).

- Kerker M., *The Scattering of Light and Other Electromagnetic Radiation*, (Academic, New York, 1969).
- Kuo S.C. and Sheetz M.P., "Force of single kinesin molecules measured with optical tweezers", *Science* **260**, 232 (1993).
- Lester M. and Nieto-Vesperinas M., "Optical forces on microparticles in an evanescent laser field", *Opt. Lett.* **24**, 936 (1999).
- Leviatan Y., "Study of near-zone fields of a small aperture", *J. Appl. Phys.* **60**, 1577 (1986).
- Lewittes M., Arnold S., and Oster G., "Radiometric levitation of micron sized spheres", *Appl. Phys. Lett.* **40**, 455 (1982).
- Lide D.R., *CRC Handbook of Chemistry and Physics*, 77<sup>th</sup> ed. (CRC Press, Boca Raton, 1996-1997), Sec. 12, pp. 130-143.
- Liu C., Kaiser T., Lange S., and Schweiger G., "Structural resonances in a dielectric sphere illuminated by an evanescent wave", *Optics Commun.* **117**, 521 (1995).
- Mahan A.I. and Bitterli C.V., "Total internal reflection: a deeper look", *Appl. Opt.* **17**, 509 (1978).
- Malmqvist L. and Hertz M., "Trapped particle optical microscopy", *Optics Commun.* **94**, 19 (1992).
- Malmqvist L. and Hertz M., "Two-color trapped particle optical microscopy", *Opt. Lett.* **19**, 853 (1994).
- Masuhara H., de Schryver F.C., Kitamura N., and Tamai N., *Microchemistry* (Elsevier, Amsterdam, 1994).
- Mehta B. L., "Total illumination in an aberration free annular aperture", *Appl. Opt.* **13**, 736 (1974).
- Meixner A.J., Bopp M.A., and Tarrach G., "Direct measurement of standing evanescent waves with a photon-scanning tunneling microscope", *Appl. Opt.* **34**, 7995 (1994).
- Mertz J., Hipp M., Mlynek J., and Marti O., "Optical near-field imaging with a semiconductor probe tip", *Appl. Phys. Lett.* **64**, 2338 (1994).

- Messinger B.J., von Raben K.U., Chang R.K., and Barber P.W., "Local fields at the surface of noble-metal microspheres", *Phys. Rev. B* **24**, 649 (1981).
- Minsky M., U. S. patent 3013467, Microscopy Apparatus, Dec. 19, 1961 (Filed Nov. 7, 1957).
- Miyata H., Yoshioka H., Hakozaki H., Suzuki N., Furuno T., Ikegami A., Kinoshita K. Jr., Nishizaka T., and Ishiwata S., "Mechanical measurements of single actomyosin motor force", *Biophys. J.* **68**, S286 (1995).
- Novotny L., Sánchez E.J., and Xie X.S., "Near-field optical imaging using metal tips illuminated by higher-order Hermite-Gaussian beams", *Ultramicroscopy* **71**, 21 (1998).
- Ohta S. and Kusumi A., "Near-field fluorescence microscopy of actin cytoskeleton in cultured cells", *Handbook of near-field nano-photonics* (Ohtsu and Kawata, Eds, 1997), Chap. 3, 125-128.
- Paesler M.A. and Moyer P.J., *Near-field optics: Theory, Instrumentation, and applications* (John Wiley & Sons, Inc., New York, 1996).
- Partovi A., Peale D., Wuttig M., Murray C.A., Zydzik G., Hopkins L., Baldwin K., Hobson W.S., Wynn J., Lopata J., Dhar L., Chichester R., and Yeh J. H-J, "High-power laser light source for near-field optics and its application to high-density optical data storage", *Appl. Phys. Lett.* **75**, 1515 (1999).
- Prieve D.C. and Walz J.Y. "Scattering of an evanescent surface wave by a microscopic dielectric sphere", *Appl. Opt.* **32**, 1629 (1993).
- Pendleton J.D., "Mie scattering into solid angles", *J. Opt. Am. A* **72**, 1029 (1982).
- Pohl D.W., Denk W., and Lanz M., "Optical Stethoscopy: imaging recording with resolution  $\lambda/20$ ", *Appl. Phys. Lett.* **44**, 651 (1984).
- Quinten M., Pack A., and Wannemacher, "Scattering and extinction of evanescent waves by small particles", *Appl. Phys. B.* **68**, 87 (1999).
- Raznjevic K., *Handbook of Thermodynamic Tables and Charts* (Hemisphere Publishing, Washington, 1976), pp. 3.
- Reddick R., Warmack R., Chilcott D., Sharp S., and Ferrell T., "Photon scanning tunnelling microscopy", *Rev. Sci. Instrum.* **61**, 3669 (1990).

- Richards B. and Wolf E., "Electromagnetic diffraction in optical systems II. Structure of the image field in an aplanatic system", *Proc. Roy. Soc. London A* **253**, 358 (1959).
- Sasaki K., Koshioka M., Misawa H., Kitamura N., and Masuhara H., "Optical trapping of a metal particle and a water droplet by a scanning laser beam", *Appl. Phys. Lett.* **60**, 807 (1992).
- Sasaki K., Misawa H., Kitamura N., Fujisawa R., and Masuhara H., "Optical micromanipulation of a lasing polymer particle in water", *Jpn. J. Appl. Phys.* **32**, L1144 (1993).
- Sasaki K., Shi Z., Kopelman R., and Masuhara H., "Three-dimensional pH microprobing with an optically-manipulated fluorescent particle", *Chem. Lett.* **2**, 141 (1996).
- Sasaki K., Tsukima M., and Masuhara H., "Three-dimensional potential analysis of radiation pressure exerted on a single microparticle", *Appl. Phys. Lett.* **71**, 37 (1997).
- Sato S., Harada Y., and Waseda Y., "Optical trapping of microscopic metal particles", *Opt. Lett.* **19**, 1807 (1994).
- Sato S., Harada Y., and Waseda Y., "Optical trapping of micrometer-sized gold particles", *Optics (in Japanese)* **24**, 40 (1995).
- Sato S., "Calculation of optical trapping forces for micrometer-sized particles with complex refractive index", *Technical Digest Series Conference Edition, QELS 16*, (1995).
- Sato S. and Inaba H., "Optical trapping and manipulation of microscopic particles and biological cells by laser beams", *Optical and Quantum Electrics* **28**, 1 (1996).
- Schilders S., Gan X.S., and Gu M., "Resolution improvement in microscopic imaging through turbid media based on differential polarization gating", *Appl. Opt.* **37**, 4300 (1998).
- Schmitt J.M., Gandjbakhche A.H., and Bonner R.F., "Use of polarized light to discriminate short-path photons in a multiply scattering medium", *Appl. Opt.*, **31**, 6535 (1992).
- Sheppard C.J.R. and Gu M., "Aberration compensation in confocal microscopy", *Appl. Opt.* **30**, 3563 (1991).
- Sheppard C.J.R. and Gu M., "Axial imaging through an aberrating layer of water in confocal microscopy", *Optics Commun.* **88**, 180 (1992).

- Sheppard C.J.R. and Gu M., "Imaging by a high aperture optical system", *J. Mod. Opt.* **40**, 1631 (1993).
- Sheppard C.J.R., Gu M., Brain K., and Zhou H., "Influence of spherical aberration on axial imaging of confocal reflection microscopy", *Appl. Opt.* **33**, 616 (1994).
- Sheppard C.J.R. and Török P., "Effects of specimen refractive index on confocal imaging", *J. Microscopy* **185**, 366 (1997).
- Simmons R.M., Finer J.T., Chu S., and Spudich J.A., "Quantitative measurements of force and displacement using an optical trap", *Biophys. J.* **70**, 1831 (1996).
- Smith S.B., Cui Y., and Bustamante C., "Overstretching B-DNA: the elastic response of individual double-stranded and single-stranded DNA molecules", *Science* **271**, 795 (1996).
- Stamnes J.J., *Waves in Focal Regions* (Adam Hilgar, Bristol, 1986).
- Sugiura T., Okada T., Inouye Y., Nakamura O., and Kawata S., "Gold-bead scanning near-field optical microscope with laser-force position control", *Opt. Lett.* **22**, 1663 (1997).
- Svoboda K., Schmidt C.F., Schnapp B.J., and Block S.M., "Direct observation of kinesin stepping by optical trapping interferometry", *Nature* **365**, 721 (1993).
- Svoboda K. and Block S.M., "Optical trapping of metallic Rayleigh particles", *Opt. Lett.* **19**, 930 (1994).
- Török P., Varga P., Laczik Z., and Booker G.R., "Electromagnetic diffraction of light focused through a planar interface between materials of mismatched refractive indices: an integral representation", *J. Opt. Soc. Am, A* **12**, 325 (1995).
- Török P., Varga P., Konkol A., and Booker G.R., "Electromagnetic diffraction of light focused through a planar interface between materials of mismatched refractive indices - structure of the electromagnetic field. II", *J. Opt. Soc. Am, A* **13**, 2232 (1996).
- Török P. and Varga P., "Electromagnetic diffraction of light focused through a stratified medium", *Appl. Opt.* **36**, 2305 (1997).
- Tsai D.P. and Guo W.R., "Near-field optical recording on the cyanine dye layer of a commercial compact disk-recordable", *J. Vac. Sci. Technol. A* **15**, 1442 (1997).

- Umashankar K. and Taflove A., "Novel method to analyze electromagnetic scattering of complex objects", IEEE Trans. Electromagn. Compat. EMC-24, 397 (1982).
- Vikram C.S. and Witherow W.K., "Chemical silver coating of fibre tips in near-field scanning optical microscopy", Opt. Lett. 24, 682 (1999).
- van Labeke D., and Barchiesi D., "Probes for scanning tunneling optical microscopy: a theoretical comparison", J. Opt. Soc. Am. A 10, 2193 (1993).
- Visscher K., Gross S.P., and Block S.M., "Construction of multiple-beam optical traps with nanometer-resolution position sensing" IEEE J. Sel. Top. Quantum Electron. 2, 1066 (1996).
- Wannemacher R., Pack A., and Quinten M., "Resonant absorption and scattering in evanescent fields", Appl. Phys. B 68, 225 (1999a).
- Wannemacher R., Quinten M., and Pack A., "Evanescent-wave scattering in near-field optical microscopy", J. Microscopy 194, 260 (1999b).
- Wei P.K., Hsu J.H., Fann W.S., and Tsai K.T., "Dual-optical mode near-field scanning optical microscopy", Appl. Opt. 35, 6727 (1996).
- Wood R.M., *Laser Damage in Optical Materials* (GEC Research, Hirst Research Centre, UK, 1986), Chap. 1, pp. 24-25.
- Wright W.H. and Sonek G.J., "Radiation trapping forces on microspheres with optical tweezers", Appl. Phys. Lett. 63, 715 (1993).
- Wright W.H., Sonek G.J., and Berns M.W., "Parametric study of the forces on microspheres held by optical tweezers", Appl. Opt. 33, 1735 (1994).
- Zenhausen F., O'Boyle M.P., and Wickramasinghe H.K., "Apertureless near-field optical microscope", Appl. Phys. Lett. 65, 1623 (1994).
- Zhang Z., Sonek G.J., Liang H., Berns M.W., and Tromberg B.J., "Multiphoton fluorescence excitation in continuous-wave infrared optical traps", Appl. Opt. 37, 2766 (1998).
- Zvyagin A.V. and Goto K., "Mie scattering of evanescent waves by a dielectric sphere: comparison of multipole expansion and group-theory methods", J. Opt. Am. A 15, 3003 (1998).

# List of Figures

## Chapter 2

- Fig. 2.1 Concepts of near-field and far-field (after Betzig and Trautman, 1992) .....9
- Fig. 2.2 Schematic diagram of photon-tunnelling NSOM.....12
- Fig. 2.3 Schematic diagram of vibrating metallic tip NSOM (after Inouye and Kawata, 1994).....13
- Fig. 2.4 Scheme of atomic force microscopy-based NSOM (after Ohta and Kusumi, 1997).....14
- Fig. 2.5 Schematic diagram of the essential optical elements of NSOM (after Paesler and Moyer, 1996).....16
- Fig. 2.6 Schematic diagram of particle-trapped NSOM (after Kawata *et al.*, 1994)...19
- Fig. 2.7 Schematic diagram of single-beam gradient force trapping.....23
- Fig. 2.8 (a) Geometry for calculating force on a dielectric particle. A single incident ray of power  $P$  causes a series of reflected and refracted rays (after Ashkin, 1992). (b) Relative strength of the gradient and scattering forces of a single ray.....25
- Fig. 2.9 Schematic diagram of the RO model of trapping force (after Ashkin, 1992).  $S$  and  $S'$  are the axial and transverse trapping positions.....26
- Fig. 2.10 Distributions of the total trapping efficiency  $Q_t$  in the  $x$ - $z$  plane for a polystyrene particle. The polarisation direction of the laser beam is parallel to the  $x$ -axis. The laser beam used for trapping is uniform over the aperture of an objective (oil-immersion, NA = 1.25) and linearly-polarised ( $\lambda = 488$  nm)..27
- Fig. 2.11 Maximum transverse trapping efficiency  $Q_t^m$  as a function of the NA of a trapping objective for a polystyrene particle ( $n_p = 1.59$ ). The polarisation direction of the laser beam is parallel to the transverse direction. The light distribution over the aperture of the objective is uniform and linearly-

- polarised ( $\lambda = 488 \text{ nm}$ ). An oil-immersion objective ( $\text{NA} = 1.25$ ) is assumed for trapping.....29
- Fig. 2.12 Maximum axial trapping efficiency  $Q_a^m$  as a function of the microsphere radius  $r$ . The microsphere is assumed to be polystyrene ( $n = 1.57$ ) suspended in water ( $n = 1.33$ ). For the EM model calculation ( $r \leq 1 \text{ }\mu\text{m}$ ), the wavelength was  $1.06 \text{ }\mu\text{m}$  and the spot size was  $0.4 \text{ }\mu\text{m}$ . The RO model calculation ( $r = 100 \text{ }\mu\text{m}$ ) used a cone angle of  $60^\circ$ . Note the  $r^3$  dependence on  $Q_a^m$  for  $0.01 \leq r < 0.1 \text{ }\mu\text{m}$ , decreasing to the  $r^0$  dependence as  $r$  becomes large ( $r > 100 \text{ }\mu\text{m}$ ) (after Wright and Sonek, 1993).....31
- Fig. 2.13 An incident ray at position  $\rho$  focused by a lens  $\xi$  with an apodization function  $P(\theta)$  and a focal length  $f$ .....34
- Fig. 2.14 Apodization function  $P(\theta)$  of a lens obeying the sine condition (thick line) and the tangent condition (thin line).....35
- Fig. 2.15 Illustration of spherical aberration induced by refractive-index mismatch by an interface between medium  $n_1$  and medium  $n_2$ . Negative and positive axial shifts  $\Delta s_i$  ( $i=1,2$ ) are generated under the condition (a)  $n_1 > n_2$  and (b)  $n_1 < n_2$ , respectively.....36
- Fig. 2.16 Diagram showing light focused by a lens into two media separated by a planar interface (after Török *et al.*, 1995).....37
- Fig. 2.17 Tube length  $\overline{AB}$  of an objective.  $l$  and  $s$  are the conjugate distances in image space and object space of the objective, respectively. A change in tube length  $\Delta l$  (from A to A') produces a shift  $\Delta s$  (from B to B') in the axial direction. For an objective of a focal length  $f$  used for confocal microscopy, the tube length is  $\infty$  as illustrated by the dashed lines.....39
- Fig. 2.18 Schematic diagram for (a) Mie scattering and (b) near-field Mie scattering. The wavefronts of the plane and evanescent waves are illustrated using dashed lines. The distribution of light intensity along the  $x$  direction is shown for the plane and evanescent waves, respectively. In case (b), a beam of light is incident on a boundary separating two different media under the condition of total internal reflection.....45

Fig. 2.19 Propagation of wave  $\mathbf{k}_1$  at incident angle  $\theta$  from a dense medium ( $\mu_1, \varepsilon_1, n_1$ ) into a medium ( $\mu_2, \varepsilon_2, n_2$ ). A particle ( $\mu_3, \varepsilon_3, n_3$ ) with radius  $r$  is located at  $x = \zeta$  in the medium  $n_2$  (after Chew *et al.*, 1979).....46

### Chapter 3

Fig. 3.1 Axial trapping efficiency as a function of the particle position  $S$  under the illumination of a circularly-polarised uniform beam. The solid curves represent the result with the sine condition, while the dashed curves represent that with the tangent condition.  $Q_t$ ,  $Q_G$ , and  $Q_S$  correspond to the total, gradient, and scattering trapping efficiencies, respectively. The maximum convergence angle of the objective is  $70^\circ$  and the relative refractive index is 1.18.....53

Fig. 3.2 Maximum axial trapping efficiency  $Q_a^m$  as a function of the NA for circularly-polarised uniform and Gaussian beam illumination. For Gaussian beam illumination, the ratio of the beam spot size to the radius of the objective aperture,  $a$ , is assumed to be unity. The solid curves correspond to the sine condition, while the dashed curves satisfy the tangent condition. The relative refractive index is 1.18 and the refractive index of the immersion material is 1.33 (water). The black spots represent the measured values ( $a = 1$ ) of the maximum axial trapping efficiency described by Wright *et al.* [Wright *et al.*, 1994].....54

Fig. 3.3 Transverse trapping efficiency as a function of the particle position  $S'$  under the illumination of a circularly-polarised uniform beam.  $S=0$ ,  $Q_{tr}=Q_G$  and  $Q_a=Q_S$ . The maximum transverse trapping force occurs in the equatorial plane of the particle. The other conditions are the same as those in Fig. 3.1.....55

Fig. 3.4 Maximum transverse trapping efficiency  $Q_{tr}^m$  as a function of the NA for circularly-polarised uniform and Gaussian beam illumination.  $S=0$ . The other conditions are the same as those in Fig. 3.2.....56

Fig. 3.5 Axial trapping position  $S_{\max}$  corresponding to the maximum axial trapping force as a function of the NA of a trapping objective for the sine (solid line) and the tangent (dashed line) conditions. Assume that the trapping laser beam

- is uniform and circularly-polarised. The other conditions are the same as those in Fig. 3.1.....58
- Fig. 3.6 Schematic diagram of a system for laser trapping. Lens 2 is mounted on a translation stage, and the position of lens 2 determines the effective tube length  $\overline{bc}$  of objective 2.....60
- Fig. 3.7 Maximum transverse trapping efficiency as a function of NA' for different values of the sample cell thickness  $D$ .  $Q_1$ ,  $Q_2$ , and  $Q_3$  correspond to the maximum transverse trapping efficiencies for  $D = 34 \mu\text{m}$ ,  $60 \mu\text{m}$  and  $94 \mu\text{m}$ , respectively.  $Q_{\text{sine}}$  is the theoretical prediction by the RO model under the sine condition.....63
- Fig. 3.8 Maximum transverse trapping efficiency as a function of NA' for different values of the effective tube length and the sample cell thickness  $D$ .  $Q_2$  and  $Q_3$  correspond to the transverse trapping efficiencies for  $D = 60 \mu\text{m}$  and  $D = 94 \mu\text{m}$  at a tube length of 160 mm,  $Q_2'$  and  $Q_3'$  correspond to the transverse trapping efficiencies for  $D = 60 \mu\text{m}$  and  $D = 94 \mu\text{m}$  at a tube length of 140 mm.  $Q_{\text{sine}}$  is the theoretical prediction by the RO model under the sine condition.....64
- Fig. 3.9 Peak intensity and axial focal shift of the 3D IPSF as a function of the probe depth  $d$  under the uncompensated (solid curves) and compensated (dashed curves) conditions ( $\lambda = 0.633 \mu\text{m}$ ,  $\text{NA}'=1.25$ ).....66
- Fig. 3.10 Axial (top) and transverse (bottom) cross-sections of the 3D IPSF for different probe depths under the uncompensated condition ( $\lambda = 0.633 \mu\text{m}$ ,  $\text{NA}'=1.25$ ).....67
- Fig. 3.11 Axial and transverse FWHMs of the 3D IPSF,  $\Delta z_{1/2}$  and  $\Delta r_{1/2}$ , as a function of the probe depth  $d$  under the uncompensated (solid curves) and compensated (dashed curves) conditions ( $\lambda = 0.633 \mu\text{m}$ ,  $\text{NA}'=1.25$ ).....68
- Fig. 3.12 Axial (top) and transverse (bottom) cross-sections of the 3D IPSF for different probe depths under the compensated condition ( $\lambda = 0.633 \mu\text{m}$ ,  $\text{NA}'=1.25$ ).....69
- Fig. 3.13 Average trapping power as a function of the probe depth  $d$  under the uncompensated (solid curve) and compensated (dashed curve) conditions ( $\lambda = 0.633 \mu\text{m}$ ,  $\text{NA}'=1.25$ ).....70

## Chapter 4

- Fig. 4.1 (a) Geometry for calculating force on a metallic particle of skin depth  $\chi$ . A single incident ray of power  $P$  is mainly reflected. (b) Relative strength of the gradient and scattering forces of a single ray .....74
- Fig. 4.2 Distributions of the total trapping efficiency  $Q_t$  in the  $x$ - $z$  plane for gold (a), nickel (b) and silver (c) particles, respectively. The polarisation direction of the laser beam is parallel to the  $x$ -axis. The light distribution over the aperture of the objective is uniform and linearly-polarised ( $\lambda = 488$  nm). An oil-immersion objective (NA = 1.25) is assumed for trapping.....77
- Fig. 4.3 Axial trapping efficiency as a function of the axial trapping position  $z$  when  $x = 0$  for gold, nickel, and silver particles, respectively. The other conditions are the same as those in Fig. 4.2.....79
- Fig. 4.4 Transverse trapping efficiency  $Q_r$  as a function of the transverse trapping position  $x$  for gold (a), nickel (b), and silver (c) particles, respectively. The other conditions are the same as those in Fig. 4.2. The solid curves correspond to the situation when a maximum transverse trapping efficiency occurs .....80
- Fig. 4.5 Transverse trapping efficiency  $Q_r$  as a function of the transverse trapping position  $y$  for gold (a), nickel (b), and silver (c) particles, respectively. The trapping position is in the  $y$ - $z$  plane perpendicular to the polarisation direction of the illumination beam and the other conditions are the same as those in Fig. 4.2.....81
- Fig. 4.6 Demonstration of a trapped nickel particle of diameter 3  $\mu\text{m}$ , recorded using a CCD camera. Frames (a) and (b) were recorded at different times .....86
- Fig. 4.7 Schematic diagram for demonstrating the difference of trapping force between (a) dielectric and (b) metallic particles.  $F_g$  represents the gradient force and  $F_s$  represents the scattering force.  $\theta$  is the angle of a ray of convergence. The outer ring of the metallic particle indicates its skin depth....  
.....92

- Fig. 4.8 Maximum transverse trapping efficiency as a function of the radius of the central obstruction  $\varepsilon$  for a dielectric ( $n_p = 1.59$ ) particle in water ( $n = 1.33$ ), according to the RO model. The NA of the trapping objective is 1.25 at wavelength 488 nm .....93
- Fig. 4.9 Maximum transverse trapping efficiency as a function of the radius of the central obstruction  $\varepsilon$  for a gold particle, in water ( $n = 1.33$ ), of diameter 2  $\mu\text{m}$ . The theoretical results are calculated according to the RO model. The NA of the trapping objective is 1.25 at wavelength 488 nm.....94
- Fig. 4.10 Calculated enhancement factor  $\beta$  as a function of the NA of a trapping objective for a gold particle suspended in water.....95

## Chapter 5

- Fig. 5.1 Schematic diagram of particle-trapped NSOM.....100
- Fig. 5.2 Photographs of a particle-trapped NSOM system: (a) optical arrangements for trapping (blue beam pass M5→M7) and illumination (red beam pass S1→M1). A He-Ne laser (S1) for illumination is steered by mirror M2 to a sample cell on top of a prism (P) under the condition of total internal reflection; (b) An  $\text{Ar}^+$  laser (S2) used for trapping. The beam is guided by mirrors M3 and M4 into tube T and then passed to M5 shown in (a); (c) a piezoelectric controller (S) for controlling scanning stage D (in (a) and (d)) and monitors for signal acquisition (V1) and trapping (V2); (d) a PMT (B) for signal collection. M1-M8: mirrors; O, O1, and O2: objectives; L1-L3: lenses; D1 and D2: diaphragms; PL: polariser; I: white light source; A: unit for beamsplitters, filter, and analyser; C: CCD camera; R: relay lens; and H: pinhole.....102
- Fig. 5.3 (Top) Images of evanescent wave interference patterns obtained with a laser-trapped particle of (a)  $\phi = 0.1 \mu\text{m}$ ; (b)  $\phi = 0.2 \mu\text{m}$ ; (c)  $\phi = 0.5 \mu\text{m}$ ; (d)  $\phi = 1 \mu\text{m}$  and (e)  $\phi = 2 \mu\text{m}$ , respectively. (Bottom) The intensity cross-sections corresponding to the marked position of each image.....107
- Fig. 5.4 Dependence of the strength of scattered evanescent waves and the image contrast of the evanescent wave interference pattern on the size of a laser-

- trapped polystyrene particle. The estimated image contrast as a function of the particle size is illustrated as the dashed curve.....107
- Fig. 5.5 Schematic diagram of a particle of radius  $r$  in contact with an evanescent wave field. The particle is immersed in water solution ( $n_2 = 1.33$ ) on the top of a prism ( $n_1 = 1.725$ ).....109
- Fig. 5.6 (Top) Images of evanescent wave interference patterns recorded with a trapped particle of diameter  $0.1 \mu\text{m}$ : (a) polystyrene; (b) gold. (Bottom) The intensity cross-sections corresponding to the marked position of each image.....111
- Fig. 5.7 (Top) Images of evanescent wave interference patterns recorded with a trapped particle of diameter  $2 \mu\text{m}$ : (a) polystyrene; (b) gold; (c) silver. (Bottom) The intensity cross-sections corresponding to the marked position of each image.....112
- Fig. 5.8 Images of the surface structures of a BK7 prism recorded with: (a) a Fluoview confocal microscope; (b) a polystyrene particle of  $100 \text{ nm}$  in diameter; and (c) a gold particle of  $100 \text{ nm}$  in diameter. The images in (b) and (c) were recorded with an illumination He-Ne laser of a p-polarised state.....115

## Chapter 6

- Fig 6.1 Schematic diagram of a prism illuminated with an incident laser beam under the condition of total internal reflection. The electromagnetic fields in the prism ( $n_1$ ) and the medium ( $n_2$ ) are represented by  $(\mathbf{E}_1, \mathbf{H}_1)$  and  $(\mathbf{E}_2, \mathbf{H}_2)$ , respectively. The electromagnetic field in medium  $n_2$  is evanescent ( $n_1 > n_2$ )...  
..... 119
- Fig. 6.2 Phase shift of a reflected propagating wave under the s- and p-polarised laser beam illumination. The refractive indices of the prism and the medium above the prism are 1.75 and 1.33 (water), respectively.  $\phi_{1s}$  and  $\phi_{1p}$  are the phase shifts of the reflected propagating wave for s- and p-polarised incident beams, respectively.....122
- Fig. 6.3 Phase shift of a transmitted evanescent wave under the s- and p-polarised laser beam illumination. The refractive indices of the prism and the medium above the prism are 1.75 and 1.33 (water), respectively.  $\phi_{2s}$  and  $\phi_{2p}$  are the

- phase shifts of the transmitted evanescent wave for s- and p-polarised incident beams, respectively.....122
- Fig. 6.4 (Top) Images of evanescent wave interference patterns under s- and p-polarised beam illumination (He-Ne laser beam). (Bottom) Intensity cross-sections correspond to the images.....124
- Fig. 6.5 Measured strength of scattered evanescent waves as a function of the incident angle  $\theta$ .  $I_{TE}$  and  $I_{TM}$ : calculated intensity of the evanescent wave at the surface of the prism under s- and p-polarised beam illumination;  $I_s$  and  $I_p$ : measured scattered signal under s- and p-polarised beam illumination.....125
- Fig. 6.6 Dependence of the signal strength of scattered evanescent waves on the incident angle  $\theta$  of an illumination He-Ne laser beam for dielectric particles of (a)  $\phi = 0.1 \mu\text{m}$ ; (b)  $\phi = 0.2 \mu\text{m}$ ; (c)  $\phi = 0.5 \mu\text{m}$ ; (d)  $\phi = 1 \mu\text{m}$ ; and (e)  $\phi = 2 \mu\text{m}$ .  $I_s$  and  $I_p$ : measured scattered signal without using an analyser under s- and p-polarised beam illumination;  $I_{ss}$  and  $I_{sp}$ : measured scattered signal with an s-analyser and a p-analyser under s-polarised beam illumination, respectively;  $I_{ps}$  and  $I_{pp}$ : measured scattered signal with an s-analyser and a p-analyser under p-polarised beam illumination, respectively.....127
- Fig. 6.7 Dependence of the degree of polarisation of scattered evanescent waves on the incident angle  $\theta$  of an illumination He-Ne laser beam for dielectric particles of (a)  $\phi = 0.1 \mu\text{m}$ ; (b)  $\phi = 0.2 \mu\text{m}$ ; (c)  $\phi = 0.5 \mu\text{m}$ ; (d)  $\phi = 1 \mu\text{m}$ ; and (e)  $\phi = 2 \mu\text{m}$ .....129
- Fig. 6.8 The averaged degree of polarisation of scattered evanescent waves as a function of the size of a polystyrene particle for an illumination beam of both s- and p-polarised states.....130
- Fig. 6.9 Degree of polarisation of scattered evanescent waves as a function of the polarisation direction  $i$  of an incident light relative to its incident plane for polystyrene latex particles of (a)  $\phi = 0.5 \mu\text{m}$  (b)  $\phi = 1 \mu\text{m}$  and (c)  $\phi = 2 \mu\text{m}$ , respectively.  $\theta = 62^\circ$  .....131
- Fig. 6.10 Dependence of the signal strength of scattered evanescent waves on the incident angle  $\theta$  of an illumination He-Ne laser beam for metallic gold

- particles of (a)  $\phi = 0.1 \mu\text{m}$ ; (b)  $\phi = 0.5 \mu\text{m}$ ; and (c)  $\phi = 2 \mu\text{m}$ . The definitions of  $I_s$ ,  $I_p$ ,  $I_{ss}$ ,  $I_{sp}$ ,  $I_{pp}$  and  $I_{ps}$  are the same as those in Fig. 6.6.....133
- Fig. 6.11 Dependence of the degree of polarisation of scattered evanescent waves on the incident angle  $\theta$  of an illumination He-Ne laser beam for gold particles of (a)  $\phi = 0.1 \mu\text{m}$ ; (b)  $\phi = 0.5 \mu\text{m}$ ; and (c)  $\phi = 2 \mu\text{m}$ .....134
- Fig. 6.12 Degree of polarisation as a function of the size of a gold particle under s- and p-polarised beam illumination. Here p1, p2, p3, and p4 represent the results measured for p-polarised beam illumination at incident angles of  $\theta = 56^\circ$ ,  $58^\circ$ ,  $60^\circ$ , and  $62^\circ$ , respectively, while s1, s2, s3, and s4 correspond to the results measured for s-polarised beam illumination at incident angles of  $\theta = 56^\circ$ ,  $58^\circ$ ,  $60^\circ$ , and  $62^\circ$ , respectively.....135
- Fig. 6.13 Degree of polarisation of scattered evanescent waves as a function of the polarisation direction  $i$  of an incident beam relative to the incident plane for gold particles of (a)  $\phi = 0.1 \mu\text{m}$  (b)  $\phi = 0.5 \mu\text{m}$  and (c)  $\phi = 2 \mu\text{m}$ , respectively.  $\theta = 62^\circ$  .....136
- Fig. 6.14 A model for evaluating the depolarisation effect with a metallic particle illuminated with s- and p-polarised evanescent waves. The electrons (-) and ions (+) accumulated on the surface of the particle are illustrated.....138
- Fig. 6.15 Images (top) and the corresponding cross-sections (bottom) of the evanescent wave interference patterns for different polarisation directions of a polariser and an analyser. The images have been normalised by the maximum intensity.....141
- Fig. 6.16 Images (top) and the corresponding cross-sections (bottom) of evanescent wave interference patterns for different polarisation directions of a polariser and an analyser. The images were recorded with a gold particle of  $\phi = 0.1 \mu\text{m}$  .....143
- Fig. 6.17 Images (top) and the corresponding cross-sections (bottom) of evanescent wave interference patterns for different polarisation directions of a polariser and an analyser. The images were recorded with a gold particle of  $\phi = 0.5 \mu\text{m}$ .....143
- Fig. 6.18 Images (top) and the corresponding cross-sections (bottom) of evanescent wave interference patterns for different polarisation directions of a polariser

and an analyser. The images were recorded with a gold particle of  $\phi = 2$   $\mu\text{m}$ .....144

Fig. 6.19 Images of the surface structure of a BK7 prism recorded with a polystyrene particle of 100 nm in diameter under the condition: (a) no analyser; (b) with an analyser of the polarisation direction parallel to that of the polariser; and (c) with an analyser of the polarisation direction perpendicular to that of the polariser.....146

Fig. 6.20 Images of the surface structure of a BK7 prism recorded with a gold particle of 100 nm in diameter under the condition: (a) no analyser; (b) with an analyser of the polarisation direction parallel to that of the polariser; and (c) with an analyser of the polarisation direction perpendicular to that of the polariser.....146

# List of Tables

## Chapter 2

Table 2.1 Important laser trapping experiments with metallic particles.....	43
-----------------------------------------------------------------------------	----

## Chapter 4

Table 4.1 Maximum transverse trapping efficiency $Q_{tr}^m$ as a function of the NA of the trapping objective for a gold particle.....	83
Table 4.2 Maximum transverse trapping efficiency $Q_{tr}^m$ as a function of the NA of the trapping objective for a nickel particle.....	83
Table 4.3 Maximum transverse trapping efficiency $Q_{tr}^m$ as a function of the NA of the trapping objective for a silver particle.....	83
Table 4.4 Transverse force as a function of the NA' of the trapping objective for a gold particle.....	87
Table 4.5 Transverse force as a function of the NA' of the trapping objective for a nickel particle.....	87
Table 4.6 Transverse force as a function of the NA' of the trapping objective for a silver particle.....	87

## Chapter 5

Table 5.1 Strength of scattered evanescent waves and image contrast of evanescent interference patterns for different types of laser-trapped particles at the surface of a SF <sub>10</sub> prism.....	103
--------------------------------------------------------------------------------------------------------------------------------------------------------------------------------------------------------	-----

# List of Symbols

$\lambda$ - wavelength	$\epsilon_{\text{ext}}$ - permittivity of a surrounding medium
$c$ - speed of light in vacuum	$\mu_i$ - permeability
$n$ - relative refractive index	$k_B$ - Boltzmann constant
$n_i$ - refractive indices ( $i = 1,2,3$ )	$k_s$ - spring constant
$n_p$ - refractive index of polystyrene	$\theta$ - incident angle
$n_g$ - refractive index of gold	$\theta'$ - refractive angle
$n_s$ - refractive index of silver	$\theta_1$ - incident angle in the first medium
$n_n$ - refractive index of nickel	$\theta_2$ - refractive angle in the second medium
$\mathbf{E}$ - electric field	$(r_p, \theta_p, \phi_p)$ - spherical coordinates
$\mathbf{H}$ - magnetic field	$\varphi$ - azimuthal angle
$\mathbf{E}_1, \mathbf{E}_2$ - electric fields in the first and second media	$\rho$ - radial coordinate over an objective aperture
$\mathbf{H}_1, \mathbf{H}_2$ - magnetic fields in the first and second media	$\rho_{\text{max}}$ - maximum radius of an objective aperture
$\mathbf{E}_{\text{inc}}$ - incident field	$\alpha_c$ - maximum convergence angle
$\mathbf{E}_{\text{sc}}$ - scattered field	$\alpha_0, \beta_0$ - angles relative to the forward direction of an incident ray
$\mathbf{E}_{\text{int}}$ - internal field	$R$ - Fresnel reflectance
$\mathbf{E}_{\perp}$ - electric field component along $x$ -axis in far-field region	$T$ - Fresnel transmittance
$\mathbf{E}_{\parallel}$ - electric field component along $y$ -axis in far-field region	TM - transverse magnetic mode
$E_r$ - radial component of electric field	TE - transverse electric mode
$H_r$ - radial component of magnetic field	$\tau_s$ - Fresnel coefficient for s polarisation state
$E_{20}$ - amplitude of transmitted wave	$\tau_p$ - Fresnel coefficient for p polarisation state
$k$ - wave number of light in a prism	$I$ - intensity
$k_0$ - wave number of light in free space	$I_0$ - incident light intensity
$\mathbf{k}_1$ - wave vector in the first medium	$I_D$ - detected light intensity
$\mathbf{y}$ - unit vector along the $y$ axis	$I(y)$ - light intensity of an evanescent wave interference pattern
$\epsilon$ - normalised radius of the central obstruction of an annular lens	$I_c$ - light distributed on the cap of a particle
$\epsilon_i$ - permittivity ( $i = 0,1,2,3$ )	

$I_m$ - peak intensity	$\hat{\mathbf{n}}$ - outward normal unit vector
$I_M$ - intensity at the surface of a prism	$\vec{\mathbf{T}}$ - Maxwell's stress tensor
$I_{TE}$ - calculated light intensity at the surface of a prism for an s-polarised beam	$\mathbf{r}$ - position vector
$I_{TM}$ - calculated light intensity at the surface of a prism for a p-polarised beam	$\xi$ - exit aperture
$I_{\max}$ - measured maximum light intensity	$l_0$ - amplitude factor
$I_{\min}$ - measured minimum light intensity	$\phi$ - particle diameter
$I_{11}$ - measured scattered signal with the polarisation direction of an analyser parallel to that of a polariser	$r$ - particle radius
$I_{\perp}$ - measured scattered signal with the polarisation direction of an analyser perpendicular to that of a polariser	$\phi_1$ - diameter of a diaphragm
$I_s$ - measured scattered signal without an analyser under s-polarised beam illumination	$\phi_2$ - reduced diameter of a diaphragm
$I_p$ - measured scattered signal without an analyser under p-polarised beam illumination	$a$ - ratio of beam spot size to the radius of an objective aperture
$I_{ss}$ - measured scattered signal with an s-analyser under s-polarised beam illumination	$q$ - size parameter
$I_{sp}$ - measured scattered signal with a p-analyser under s-polarised beam illumination	$\sigma$ - surface area
$I_{pp}$ - measured scattered signal with a p-analyser under p-polarised beam illumination	$S$ - axial trapping position
$I_{ps}$ - measured scattered signal with an s-analyser under p-polarised beam illumination	$S'$ - transverse trapping position
$P$ - trapping power	$S_{\max}$ - axial trapping position corresponds to maximum axial trapping force
$P'$ - effective trapping power	$S_{\max}'$ - transverse trapping position corresponds to maximum transverse trapping force
$\hat{\mathbf{r}}$ - outward radial vector	$\chi$ - skin depth
	$f$ - focal length
	$\Delta f$ - focal shift
	$P(\theta)$ - apodization function
	NA - numerical aperture
	NA' - effective numerical aperture
	$d$ - probe depth
	$\zeta$ - distance between a particle and a boundary
	$l, s$ - conjugate distances in image space and object space
	$\Delta l$ - tube length change
	$\Delta s, \Delta s_1,$ and $\Delta s_2$ - axial shifts
	$D$ - sample thickness

$\Delta r_{1/2}$ - FWHM of the 3D ISPF in the transverse direction	$F'_{tr}$ - calculated maximum transverse trapping efficiency without aberration
$\Delta z_{1/2}$ - FWHM of the 3D ISPF in the axial direction	$F_{tr}$ - calculated maximum transverse trapping efficiency with aberration
$B$ - compensation factor	$F_r$ - radiometric force
$T_a$ - absolute temperature	$F_f$ - friction
$\bar{v}$ - root-mean-square velocity	$F_g$ - gravity
$v_m$ - maximum translation speed	$F_b$ - buoyant force
$x_n$ - dynamic position	$Q_g$ - gradient trapping efficiency of a single ray
$w_0$ - beam waist	$Q_s$ - scattering trapping efficiency of a single ray
$\xi$ - viscosity	$Q_G$ - gradient trapping efficiency
$\rho_p$ - density of a particle	$Q_S$ - scattering trapping efficiency
$\rho_w$ - density of water	$Q_t$ - total trapping efficiency
$m$ - mass	$Q_{tr}$ - transverse trapping efficiency
$g$ - acceleration constant of free fall	$Q_a$ - axial trapping efficiency
$\mu$ - kinetic friction coefficient	$Q_{tr}^m$ - maximum transverse efficiency
$\alpha$ - attenuating factor of evanescent wave	$Q_a^m$ - maximum axial efficiency
$\kappa$ - attenuation factor of Gaussian intensity profile	$Q_{\text{sine}}$ - theoretical prediction using the sine condition
$\Psi$ - aberration function	$J_m$ ( $m = 0,1,2$ ) - Bessel function of the first kind, of order $m$
$\Psi'$ - spherical aberration by tube length change	$\eta$ - signal strength
$C_1, C_2$ - coefficients for radiometric force	$C$ - image contrast
$\Lambda, \Sigma$ - expansion coefficients	$\tau$ - visibility
$\varepsilon$ - normalised central obstruction of an annular lens	$A_1, B_1, C_1$ - amplitude coefficients of incident, reflected and evanescent fields for p-polarised light
$\beta$ - enhancement factor	$A_1', B_1', C_1'$ - amplitude coefficients of incident, reflected and evanescent fields for s-polarised light
$F_s$ - scattering force of a single ray	$\Phi$ - phase constant
$F_g$ - gradient force of a single ray	
$F_t$ - total trapping force	
$F_G$ - gradient force	
$F_S$ - scattering force	
$F_{tr}$ - transverse trapping force	
$F_a$ - axial trapping force	
$F_N$ - net radiation force	

$\phi_{1p}$  - phase shift of reflected wave for p-polarised light

$\phi_{2p}$  - phase shift of transmitted wave for p-polarised light

$\phi_{1s}$  - phase shift of reflected wave for s-polarised light

$\phi_{2s}$  - phase shift of transmitted wave for s-polarised light

$\Delta\phi_1$  - phase-shift difference of a reflected wave

$\Delta\phi_2$  - phase-shift difference of a transmitted wave

$\Delta\phi$  - phase-shift difference

$\gamma$  - degree of polarisation

$\gamma_s$  - degree of polarisation for s-polarised light

$\gamma_p$  - degree of polarisation for p-polarised light

# Publications of the Author

## ● Refereed Journal Papers

1. *Optimising the strength of an evanescent wave generated from a prism coated with a double-layer thin-film stack*, P. C. Ke, X. S. Gan, J. Szajman, S. Schilders, and M. Gu, *Bioimaging* **5** (1997), 1-8.
2. *Trapping force by a high numerical-aperture microscope objective*, M. Gu, P. C. Ke, and X. S. Gan, *Rev. Sci. Instrum.* **68** (1997), 3666-3668.
3. *Effect of the sample condition on the enhanced evanescent waves used for laser trapping near-field microscopy*, P. C. Ke and M. Gu, *Optik* **109** (1998), 104-108.
4. *Characterisation of trapping force in the presence of spherical aberration*, P. C. Ke and M. Gu, *J. Mod. Opt.* **45** (1998), 2159-2168.
5. *Characterisation of trapping force on metallic Mie particles*, P. C. Ke and M. Gu, *Appl. Opt.* **38** (1999), 160-167.
6. *Image enhancement in near-field scanning optical microscopy with laser-trapped metallic particles*, M. Gu and P. C. Ke, *Opt. Lett.* **24** (1999), 74-76.
7. *Effect of depolarisation of scattering evanescent waves on near-field imaging with laser-trapped particles*, M. Gu and P. C. Ke, *Appl. Phys. Lett.* **75** (1999), 175-177.

8. *Dependence of strength and depolarisation of scattered evanescent waves on the size of laser-trapped dielectric particles*, P. C. Ke and M. Gu, *Optics Commun.* **171** (1999), 205-211.
9. *Enhancement of transverse trapping efficiency for metallic particles with an obstructed laser beam*, M. Gu, D. Morrish, and P. C. Ke, *Appl. Phys. Lett.* **77** (2000), 34-36.
10. *Depolarization of evanescent waves scattered by laser-trapped gold particles: effect of particle size*, M. Gu and P. C. Ke, *J. Appl. Phys.* (accepted).

#### ● Article

1. *Particle-trapped near-field scanning optical microscopy*, M. Gu and P. C. Ke, *Australia Optical Society News* **12**, (1998), 9-12.

#### ● Proceedings

1. *Optimisation of the enhanced evanescent wave for near-field microscopy*, P. C. Ke, J. Szajman, X. S. Gan and M. Gu, *Proc. SPIE* **2984** (1997), 42-49.
2. *Enhanced evanescent wave generated from a prism coated with an optimised double-layer thin-film stack*, M. Gu and P. C. Ke, *Cell Vision* **4** (1997), 110-111.

3. *Near-field imaging with trapped metallic particles*, P. C. Ke and M. Gu, Technical Digest of NFO-5, (5<sup>TH</sup> International Conference on Near-field Optics and Related Techniques, nfo-5, Shirahama, Japan), (1998), 109-110.
  
4. *Direct measurement of evanescent wave interference patterns with laser-trapped dielectric and metallic particles*, M. Gu and P. C. Ke, Proc. SPIE (1<sup>st</sup> Joint OSJ-SPIE Conference on Optical Engineering for Sensing and Nanotechnology, ICOSN'99, Yokohama, Japan) **3740** (1999), 323-326.
  
5. *Study of the mechanism of super resolution optical near-field structure*, D. P. Tsai, F. H. Ho, C. W. Yang, M. Gu and P. C. Ke, Proc. SPIE (Joint International Symposium on Optical Memory and Optical Data Storage 1999, ISOM/ODS'99, Hawaii, USA) **3864** (1999), 315-317.
  
6. *Polarisation imaging in particle-trapped near-field scanning optical microscopy*, P. C. Ke and M. Gu, The Second Asia-Pacific Workshop on Near-Field Optics 1999 (Beijing, China), (1999), 87-88.

### ● Conference Papers

1. *Characterisation of trapping force for trapped particle optical microscopy*, P. C. Ke and M. Gu, XI Conference of Australian Optical Society (Adelaide, Australia), 12/1997.

2. *Fabrication and characterisation of optical fibre probes*, J. Mukerjee, P. C. Ke and M. Gu, XI Conference of Australian Optical Society (Adelaide, Australia), 12/1997.
3. *Trapped particle near-field microscopy with a metal particle probe*, P. C. Ke and M. Gu, Focus on Microscopy (Sydney, Australia), 3/1998.
4. *Characterisation of scattered evanescent waves for particle-trapped near-field optical microscopy*, P. C. Ke and M. Gu, XII Conference of Australian Optical Society (Sydney, Australia), 7/1999.
5. *Three-dimensional laser trapping of metallic Mie particles*, D. Morrish, P. C. Ke and M. Gu, XII Conference of Australian Optical Society (Sydney, Australia), 7/1999.